Structural and microstructural neuroimaging for diagnosis and tracking of neurodegenerative diseases

Junhao Wen

STRUCTURAL AND MICROSTRUCTURAL NEUROIMAGING FOR DIAGNOSIS AND TRACKING OF NEURODEGENERATIVE DISEASES

JUNHAO WEN

Image credit : generated by deep dream

Sorbonne Université

École Doctorale d'Informatique, de Télécommunication et d'Électronique (EDITE)

ARAMIS LAB à l'Institut du Cerveau et de la Moelle épinière (ICM)

STRUCTURAL AND MICROSTRUCTURAL NEUROIMAGING FOR DIAGNOSIS AND TRACKING OF NEURODEGENERATIVE DISEASES

NEUROIMAGERIE STRUCTUREL ET MICROSTRUCTUREL POUR LE DIAGNOSTIC ET LE SUIVI DE MALADIES NEURODEGENERATIVES

JUNHAO WEN

Thèse de doctorat d'informatique

Dirigée par *Olivier Colliot, Stanley Durrleman* et *Anne Bertrand*

Présentée et soutenue publiquement le 4 *Juillet 2019*

Devant un jury composé de :

- *M. Frederik BARKHOF*
  Professeur, Vrije University, Rapporteur
- *M. Pierrick COUPÉ*
  Chargé de recherche, Bordeaux Université, Rapporteur
- *M. Matthieu CORD*
  Professeur, Sorbonne Université, Examinateur
- *M. Olivier COMMOWICK*
  Chargé de recherche, INRIA, Examinateur
- *M. Olivier COLLIOT*
  Directeur de recherche, CNRS, Directeur de thèse
- *M. Stanley DURRLEMAN*
  Directeur de recherche, INRIA, Co-Directeur de thèse

Abstract

STRUCTURAL AND MICROSTRUCTURAL NEUROIMAGING FOR DIAGNOSIS AND TRACKING OF NEURODEGENERATIVE DISEASES

by Junhao WEN

Biomarker identification and tracking in dementia are essential to better understand the pathological mechanism and disease trajectory. For this purpose, various types of data, including cognitive and clinical tests, neuroimaging and fluid biomarkers, have been used. Another challenge is early diagnosis of dementia. It is of great importance to diagnose patients in an early stage at which brain damage is not yet severe and may be reversible. Tracking and diagnosis at an early stage ultimately ensures a proper care of patients, and monitoring of disease-modifying therapeutic treatment.

The current PhD aims has two main objectives. First, we aim to identify the most promising biomarkers at the presymptomatic stage of dementia. More specifically, we studied this in the case of genetic frontotemporal lobar degeneration (FTLD) due to C9orf72 mutation. The second objective is to advance early diagnosis and prognosis by using machine learning (ML) methods with magnetic resonance imaging (MRI) data. We tackle this in the context of sporadic Alzheimer's disease (AD).

According to these two objectives, the thesis consists of two main parts, each part comprising two studies. In the first study, biomarkers were identified from conventional T1-weighted MRI and diffusion tensor imaging (DTI) model. The second study compared the sensitivity and specificity of the advanced Neurite Orientation Dispersion and Density Imaging (NODDI) model and to that of conventional techniques, namely T1-weighted MRI and DTI. The second part focuses on early diagnosis of AD and comprises the last two studies. The third study proposes an open source framework for reproducible evaluation of AD classification using diffusion MRI and conventional ML methods. The last study extends this framework to deep learning methods and demonstrates its use on T1-weighted MRI. Generally, we aim to improve the transparency and reproducibility in the field, including clarifying the bad practices, sharing the tools and source code for reproducible research and rigorously comparing different approaches.

Résumé

by Junhao WEN

L'identification et le suivi de biomarqueur de la démence sont essentiels pour mieux comprendre les mécanismes pathologiques et la trajectoire de la maladie. À cette fin, divers types de données, tests cognitifs et cliniques, neuroimagerie et biomarqueurs des fluides périphériques, ont été utilisés. Le diagnostic précoce de la démence constitue un autre défi. Il est très important de diagnostiquer les patients à un stade précoce auquel les lésions cérébrales ne sont pas encore sévères et peuvent être réversibles. Le suivi et le diagnostic à un stade précoce permettent une prise en charge adéquate des patients et de mesurer l'efficacité de nouveaux traitements.

Cette thèse a deux objectifs principaux. Premièrement, nous cherchons à identifier les biomarqueurs les plus prometteurs au stade présymptomatique de la démence. Plus spécifiquement, nous avons étudié ce phénomène dans le cas de la dégénérescence lobaire frontotemporale (FTLD) due à la mutation C9orf72. Le deuxième objectif est de faire progresser le diagnostic et le pronostic précoces en utilisant des méthodes d'apprentissage machine et des données d'imagerie par résonance magnétique (IRM). Nous abordons cette question dans le contexte de la maladie d'Alzheimer sporadique (MA).

Suivant ces deux objectifs, la thèse se compose de deux parties principales, chaque partie comprenant deux études. Dans la première étude, les biomarqueurs ont été identifiés à partir de l'IRM conventionnelle pondérée T1 et du modèle d'imagerie du tenseur de diffusion (DTI). La deuxième étude a comparé la sensibilité et la spécificité du modèle NODDI (Advanced Neurite Orientation Dispersion and Density Imaging) et celle de techniques conventionnelles, à savoir l'IRM pondérée en T1 et le DTI. La deuxième partie porte sur le diagnostic précoce de la MA et comprend les deux dernières études. La troisième étude propose un cadre open source pour une évaluation reproductible de la classification de la MA à l'aide de l'IRM de diffusion et des méthodes classiques d'apprentissage. La dernière étude étend ce cadre aux méthodes d'apprentissage profond et démontre son utilisation sur l'IRM pondérée en T1. Généralement, nous visons à améliorer la transparence et la reproductibilité de ces recherches, notamment en mettant en évidence les mauvaises pratiques, en partageant les outils et le code source pour une recherche reproductible et en comparant rigoureusement différentes approches.

Acknowledgements

This wonderful journey heads to the end. I am very grateful to all the beautiful things that I have ever encountered during this PhD.

Firstly, I thank the financial support from China Scholarship Council (CSC) and ARAMIS laboratory during my PhD.

Secondly, I would like to thank myself, who had enough courage to pursue a PhD at the very beginning, with knowing almost nothing about machine learning, neuroscience and French, little about English. I am so grateful for the 4-year life in Paris: I have been intensively emerged into the scientific topics that attract me; I have mastered English, French and Spanish; I have traveled to 18 countries all over the world; I have experienced too many my-first-time, such as surfing and skate. As Ernest Hemingway said, "*Paris est une fête*", Paris will always accompany me.

Thirdly, I am so grateful to my three supervisors during my PhD: Olivier Colliot, Anne Bertrand and Stanley Durrleman. Thank you for guiding me into this field.

Fourthly, I would like to thank my families for all their supports: my father, mother and big brother. Especially my father, who has always high expectations for me.

Fifthly, I want to thank all my friends and colleagues. I am so happy to meet "Mi hermano comunista" Jorge and "Mon fiston" Alex, I can not imagine a PhD without you. I enjoyed all the jokes, gyms, saunas and parties that we experienced together. I remember all the wonderful moments with Aleix and Susana at Cité Universitaire de Paris and also during our trips to Grans Canaria and Iceland. I thank Mingyue for accompanying me to come to ICM in the weekends. I appreciate all the time with Cata and Jérémy being around my place in ARAMIS. We went through this wonderful journey together. I thank all the help for my French learning, especially Alex for the bad words, Jérémy for the grammar correction and Martina and Marie for the practicing time. For my Spanish learning (a lot of thanks to Marie, Juliana, Jorge and Cata), I would like to especially thank Juliana because I have an Argentina accent thanks to you! I enjoyed each time for the skate patrolling in the streets of Paris with Benoît and Raphaël. Also, I hope we will make it work for our first surfing trip.

Finally, longing for a new journey, I hope that I can always find happiness and satisfaction in science and always be myself.

Scientific production

JOURNAL PAPERS

1. **Wen, J.**, Zhang, H., Alexander, D.C., Durrleman, S., Routier, A., Rinaldi, D., Houot, M., Couratier, P., Hannequin, D., Pasquier, F. and Zhang, J., Colliot, O., Le Ber., I. and Bertrand, A. Neurite Density is Reduced in the Presymptomatic Phase of C9orf72 Disease, **J Neurol Neurosurg Psychiatry**, pp.jnnp-2018. https://hal.inria.fr/hal-01907482/file/WEN_NODDI-R1_manuscript_2018_10_27_postprint.pdf. **(Chapter 2 of the dissertation)**

2. Bertrand, A., **Wen, J. (Co-first author)**, Rinaldi, D., Houot, M., Sayah, S., Camuzat, A., Fournier, C., Fontanella, S., Routier, A., Couratier, P. and Pasquier, F., Habert, M., Hannequin, D., Martinaud, O., Caroppo, P., Levy, R., Dubois, B., Brice, A., Durrleman, S. and Colliot, O., Le Ber. Early Cognitive, Structural, and Microstructural Changes in Presymptomatic C9orf72 Carriers Younger Than 40 Years. **JAMA Neurology**, 75(2), pp.236-245, 2018. https://hal.inria.fr/hal-01654000/document **(Chapter 1 of the dissertation)**

3. Samper-González, J., Burgos, N., Bottani, S., Fontanella, S., Lu, P., Marcoux, A., Routier, A., Guillon, J., Bacci, M., **Wen, J.** and Bertrand, A., Bertin, H., Habert, M., Durrleman, S., Evgeniou, T. and Colliot, O. Reproducible evaluation of classification methods in Alzheimer's disease : framework and application to MRI and PET data. **Neuroimage**, 183, pp.504-521.2018. https://hal.inria.fr/hal-01858384/document

4. Marcoux, A., Burgos, N., Bertrand, A., Teichmann, M., Routier, A., **Wen, J.**, Samper-González J, Bottani S, Durrleman S, Habert M-O, and Colliot O. An Automated Pipeline for the Analysis of PET Data on the Cortical Surface, **Frontiers in Neuroinformatics**, 12, 2018. https://hal.inria.fr/hal-01950933.

SUBMITTED JOURNAL PAPERS

1. **Wen, J.**, Thibeau–Sutre, Jorge S., Routiere A., Bottanie, S., Durrlemane, S., Burgos, N., Colliot, O. Convolutional Neural Networks for Classification of Alzheimer's Disease: Overview and Reproducible Evaluation, Submitted to **Medical Image Analysis**. https://arxiv.org/pdf/1904.07773.pdf. **(Chapter 4 of the dissertation)**

2. **Wen, J.**, Samper-González, J., Bottani, S., Routier, A., Burgos, N., Jacquemont, T., Fontanella, S., Durrleman, S., Epelbaum, S., Bertrand, A., and Colliot, O. Reproducible evaluation of diffusion MRI features for automatic classification of patients with Alzheimer's disease, Submitted to **Neuroinformatics**. https://arxiv.org/pdf/1812.11183.pdf. **(Chapter 3 of the dissertation)**

3. Yue, L., Hu, D., Zhang, H., **Wen, J.**, Wu, Y., Wang, T., Shen D., Xiao, S. Prediction of 7-year MCI progression from subjective cognitive decline: Evidence from the China Longitudinal Ageing Study (CLAS), Submitted to **Alzheimer's & Dementia**.

4. Routier, A., Burgos, N., Guillon, J., Samper-González, J., **Wen, J.**, Bottani, S., Marcoux, A., Bacci, M., Fontanella, S., Jacquemont, T., Gori, P., Guyot, A., Lu, P., Diaz Melo, D., Thibeau—Sutre, E., Moreau, T., Teichmann, M., Habert, M.-O., Durrleman, S., Colliot, O. Submitted to **Frontiers in Neuroinformatics**.

CONFERENCE ABSTRACTS

1. **Wen, J.**, Samper-Gonzalez, J., Routier, A., Bottani, S., Durrleman, S., Burgos, N. and Colliot, O. Beware of feature selection bias! Example on Alzheimer's disease classification from diffusion MRI. **Organization for Human Brain Mapping Annual Meeting, OHBM 2019**, Rome, June 2019. https://hal.inria.fr/hal-02105134/document

2. **Wen, J.**, Elina Thibeau–Sutre, Samper-Gonzalez, J., Routier, A., Bottani, S., Didier Dormont, Durrleman, S., Colliot, O and Burgos, N. How serious is data leakage in deep learning studies on Alzheimer's disease classification? **Organization for Human Brain Mapping Annual Meeting, OHBM 2019**, Rome, June 2019. https://hal.inria.fr/hal-02105133/document

3. **Wen, J.**, Samper-González, J., Bottani, S., Routier, A., Burgos, N., Jacquemont, T., Fontanella, S., Durrleman, S., Bertrand, A. and Colliot, O. Using diffusion MRI for classification and prediction of Alzheimer's Disease : a reproducible study. **Alzheimer's Association International Conference, AAIC 2018**, Chicago, USA, July, 2018. https://www.alzheimersanddementia.com/article/S1552-5260(18)32351-3/fulltext

4. **Wen, J.**, Samper-Gonzalez, J., Bottani, S., Routier, A., Burgos, N., Jacquemont, T., Fontanella, S., Durrleman, S., Bertrand, A. and Colliot, O. Comparison of DTI Features for the Classification of Alzheimer's Disease : A Reproducible Study. **Organization for Human Brain Mapping Annual Meeting, OHBM 2018**, Singapore, June 2018. https://hal.inria.fr/hal-01758206/document

5. **Wen, J.**, Zhang, H., Alexander, D., Durrleman, S., Routier, A., Rinaldi, D., Houot, M., Zhang, J., Colliot, O., Le Ber, I. and Bertrand, A. NODDI Highlights Promising New Markers In Presymptomatic C9orf72 Carriers. **Organization for Human Brain Mapping Annual Meeting, OHBM 2018**, Singapore, June 2018. https://hal.inria.fr/hal-01758137/document

6. **Wen, J.**, Thibeau–Sutre, E., Samper-González, J., Routier, S., Bottani, S., Dormont, D., Durrleman, S., Colliot, O., Burgos, N. How serious is data leakage in deep learning studies on Alzheimer's disease classification? **Organization for Human Brain Mapping Annual Meeting, OHBM 2019**, Italy, Roma 2019.

7. **Wen, J.**, Samper-González, J., Routier, A., Bottani, S., Durrleman S., Burgos, N., Colliot, O. Beware of feature selection bias! Example on Alzheimer's disease classification from diffusion MRI **Organization for Human Brain Mapping Annual Meeting, OHBM 2019**, Italy, Roma 2019.

8. Samper-González, J., Bottani, S., Burgos, N., Fontanella, S., Lu, P., Marcoux, A., Routier, A., Guillon, J., Bacci, M., **Wen, J.**, Bertrand, A., Bertin, H., Habert, M-O., Durrleman, S., Evgeniou, T., and Colliot, O. Reproducible evaluation of Alzheimer's Disease classification from MRI and PET data, **In Annual meeting of the Organization for Human Brain Mapping - OHBM 2018**, Singapore, June 2018, https://hal.inria.fr/hal-01761666

9. Marcoux, A., Burgos, N., Bertrand, A., Teichmann, M., Routier, A., **Wen, J.**, Samper-González, J., Bottani, S., Durrleman, S., Habert, M-O. and Colliot, O. A pipeline for the analysis of 18F-FDG PET data on the cortical surface and its evaluation on ADNI, **In Annual meeting of the Organization for Human Brain Mapping - OHBM 2018**, Singapore, June 2018, https://hal.archives-ouvertes.fr/hal-01757646

10. Routier, A., Guillon, J., Burgos, N., Samper-González, J., **Wen, J.**, Fontanella, S., Bottani, S., Jacquemont, T., Marcoux, A., Gori, P., Lu, P., Moreau, T., Bacci, M., Durrleman, S., and Colliot, O. Clinica: an open source software platform for reproducible clinical neuroscience studies. **In Annual meeting of the**

Organization for Human Brain Mapping - OHBM 2018, Singapore, June 2018, https://hal.inria.fr/hal-01760658

11. Yue, L., **Wen, J.** and Xiao, S. Asymmetry of Medial Temporal Lobe Associated with Cognitive Deterioration in Sub- jective Memory Decline : A Chinese Community Study with One Year Follow-up. **Alzheimer's Association International Conference, AAIC 2018**, Chicago, USA, July, 2018. https://www.alzheimersanddementia.com/article/S1552-5260(18)30557-0/abstract

12. Bertrand, A., **Wen, J.**, Rinaldi, D., Camuzat, A., Fontanella, S., Routier, A., Couratier, P., Pasquier, F., Martinaud, O., Durrleman, S. and Brice, A., Colliot, O. and Le Ber., I. Accelerated Subcortical Atrophy During Aging Presymptomatic Carriers of C9orf72 Mutation. **In Annual meeting of the Organization for Human Brain Mapping - OHBM 2017**, UK, London, July 2017. https://www.alzheimersanddementia.com/article/S1552-5260(17)31814-9/fulltext

TALKS AND POSTERS

1. Poster – Annual meeting of the Organization for Human Brain Mapping-OHBM, Italy, Rome, June 2019.
2. Oral – ICM - IoN Workshop, Paris, France, October 2018.
3. Poster – Annual meeting of the Organization for Human Brain Mapping-OHBM, Singapore, June 2018.
4. Poster – Alzheimer's Association International Conference, AAIC 2017, USA, Chicago, July 2018.
5. Poster – Alzheimer's Association International Conference, AAIC 2017, UK, London, July 2017.

SCIENTIFIC POPULARIZATION

1. Fête de la science, Campus Jussieu, Paris, France, 2016
2. Salon Culture et Jeux Mathématiques, Paris France, 2016
3. Fête de la science, ICM, Paris, France, 2017
4. Exchange internship at CIMC lab at UCL, London, 2018

Contents

List of Figures

List of Tables

List of Abbreviations

AD	Alzheimer's disease
FTLD	Fronto-temporal lobar degeneration
ALS	Amyotrophic lateral sclerosis
C9orf72	Chromosome 9 open reading frame 72
PGRN	progranulin gene mutations
MAPT	Microtubule-associated protein tau
ADNI	Alzheimer's Disease Neuroimaging Initiative
AIBL	Australian Imaging, Biomarker and Lifestyle Flagship Study of Ageing
OASIS	Open Access Series of Imaging Studies
BIDS	Brain Imaging Data Structure
ILSVRC	ImageNet Large Scale Visual Recognition Challenge
MCI	Mild cognitive impairment
pMCI	Progressive mild cognitive impairment
CN	Cognitively normal
sMCI	Stable mild cognitive impairment
MRI	Magnetic Resonance Imaging
T1w MRI	T1-weighted magnetic resonance imaging
T1w	T1-weighted
PET	Positron emission tomography
DWI	Diffusion-weighted image
ASL	Arterial spin labeling
DTI	Diffusion tensor imaging
fMRI	Functional magnetic resonance imaging
NODDI	Neurite Orientation Dispersion and Density Imaging
FA	Fractional anisotropy
MD	Mean diffusivity
RD	Radial diffusivisity
AD	Axial diffusivisity
MO	Mode of anisotropy
WM	White matter
GM	Gray matter
CSF	Cerebrospinal fluid
JHU	John Hopkins University
MNI	Standard space of the Montreal Neurological Institute
TR	repetition time
TE	echo time
MMSE	Mini-mental state examination
CDR	Clinical dementia rating
AUC	Area under the receiver operating characteristic curve
CV	Cross-validation
ML	Machine learning

DL	Deep Learning
SVM	Support vector machine
RF	Random Forest
NN	Nearest Neighbors
LR	Logistic Regression
NB	Native Bayes
SGD	stochastic gradient descent
ResNet	Residual Neural Network
GANs	Generative Adversarial Networks
AE	autoencoder
FWHM	Full width at half maximum
ROI	Region Of Interest
QC	Quality check
SNR	signal-to-noise ratio
MSE	mean squared error
dof	degree of freedom
EPI	echo-planar imaging

To my father.

Introduction

Dementia is a syndrome, usually of a chronic or progressive nature, in which there are impairments in different cognitive functions, including difficulty in memory, disturbances in language, behavior, and impairments in activities of daily living (Burns and Iliffe, 2009b). Worldwide, about 12 million people have dementia, and this total is likely to increase to 25 million by 2040 (Ferri et al., 2005). Only in France, there were about 1,175,000 patients with dementia in 2012[1]. The burden of caring for dementia patients is heavy. Annual costs per patient have been estimated at $57,000 in the United States, $64,000 in Italy, $24,000 in Sweden and $14,000 in Canada (Burns and Iliffe, 2009b).

The most common type of dementia is Alzheimer's disease (AD), representing 50% to 70% of cases (Burns and Iliffe, 2009b). Other major forms include frontotemporal lobar degeneration (FTLD), vascular dementia and dementia with Lewy bodies. There are no strict boundaries between different forms of dementia and mixed forms often co-exist, meaning that one patient may be affected by different forms of dementia simultaneously. A small proportion of families have a genetic form of dementia, mainly caused by a mutation in one of the dementia genes. For instance, APP, PSEN1 and PSEN2 genes for AD; MAPT, GRN, C9orf72, and other genes for FTLD (Loy et al., 2014).

There is currently no effective treatment to cure dementia or to alter its progressive course. The main obstacles are as follows. First, early and accurate diagnosis of dementia is difficult. Given that the disease trajectory usually starts many years before the symptoms appear, it is of great importance to identify, as early as possible, if a certain subject will develop dementia. The stages before dementia consist in the presymptomatic (no symptoms) and prodromal (mild symptoms but no dementia) stages. For instance, the progression of mild cognitive impairment (MCI) subjects into AD attracts more and more attention to the community (Rathore et al., 2017). The benefits of early diagnosis and biomarker identification include identification of treatable physical and psychiatric causes, treatment of comorbid conditions, initiation of psychosocial support, and instigation of pharmacological symptomatic treatments (Burns and Iliffe, 2009b). Secondly, one needs to have robust markers to track disease progression and to monitor the effect of potential

[1] www.alzheimer-europe.org

therapeutic treatments. This is particularly important during the presymptomatic stage. The presymptomatic stage represents the best time-window for the medical intervention before irreversible brain damage is present. A large body of studies has looked at the automatic classification for early diagnosis, and biomarkers identification and tracking during different stages of dementia. Refer to (Rathore et al., 2017; Floeter and Gendron, 2018) for more details on related topics.

In this work, we consider two types of dementia: sporadic AD and genetic forms of FTLD. The needs in terms of early diagnosis and biomarker tracking are quite different. On the one hand, in genetic forms of dementia where the causal mutation is known, identification of individuals who will become demented is relatively straightforward since the mutations usually have complete penetrance. However, for genetic forms of FTLD, biomarkers of the presymptomatic phase are still lacking. These are crucially needed to identify the best therapeutic window and to monitor new treatments. On the other hand, there has been a huge progress in the development of biomarkers of AD, in particular the ability to measure amyloid and tau in the CSF and using positron emission tomography (PET) imaging. However, in sporadic AD, identifying future demented patients remains challenging.

FTLD and amyotrophic lateral sclerosis (ALS) are neurodegenerative diseases with common genetic causes, the most frequent being a GGGGCC repeat expansion in the chromosome 9 open reading frame 72 (C9orf72) gene. Currently, the pathological mechanism behind this disease is still unclear (DeJesus-Hernandez et al., 2011). Several studies focused on identifying biomarkers at the presymptomatic stage (Rohrer et al., 2015; Walhout et al., 2015; Lee et al., 2016; Cash et al., 2017; Papma et al., 2017; Popuri et al., 2018; Burns and Iliffe, 2009b; Lee et al., 2016). Researchers have demonstrated that biomarkers change up to 25 years before estimated symptom onset (Rohrer et al., 2015), suggesting that the presymptomatic phase is the best time-window to monitor the potential therapeutic treatment since the pathological damage is at its minimum and potentially still reversible (Rohrer et al., 2013). However, limitations exist and advances are needed. First, most studies focused on gray matter (GM) analysis based on anatomical MRI and only a few studies have assessed white matter (WM) with diffusion MRI. Besides, no consensus reached among these studies. For instance, one study (Lee et al., 2016) detected disruptions of white matter (WM) integrity using diffusion tensor imaging (DTI), whereas another study (Walhout et al., 2015) failed to identify such changes. Lastly, the data sample of participants in these studies was relatively small, meaning that the statistical power of their studies were limited. Efforts have also been made to identify biomarkers using other modalities. This includes functional MRI,

perfusion by arterial spin labeling (ASL) and PET imaging, and neuropsychological tests (see (Jiskoot, 2018) for details). However, robust biomarkers of familial FTLD are urgently needed for staging, prognosis, onset prediction, and treatment monitoring.

Early diagnosis and prediction of the progression of the disease are critical from the clinical perspective. In genetic forms of dementia, a genetic consultation can easily identify carriers of mutation (when the patients have a known mutation). For sporadic cases, such as sporadic AD, this diagnosis still mainly relies on clinical evaluation and cognitive assessment using neuropsychological tests. In recent years, diagnosis has evolved thanks to advances in biomarker technology and neuroimaging. Currently, besides the clinical assessment, neuroimaging-based biomarkers are also integrated into the diagnosis criteria. T1-weighted (T1w) MRI and diffusion MRI provide macroscopic spatial patterns of atrophy and microscopic white matter integrity, respectively. These neuroimaging-based markers are used to describe the topography of neurodegeneration within the brain. Moreover, pathophysiological markers, reflecting the presence of specific abnormal protein deposits, conveyed by PET imaging are also available.

Diagnosis of dementia at its late stage has limited value. Researchers are currently challenging early and accurate diagnosis or prediction of the progression from mild to severe stage of the disease trajectory. However, this remains a difficult task. To that objective, machine learning (ML) techniques are of interest due to their ability to learn relevant patterns within the data, providing promising performances for classification and prediction. In the past years, large publicly available datasets have been made available. These datasets provide multimodal data, including MRI, PET and also neuropsychological data. The most well known is the Alzheimer's Disease Neuroimaging Initiative[2] (ADNI) but other publicly available datasets exist, including the Open Access Series of Imaging Studies[3] (OASIS) and the Australian Imaging, Biomarker and Lifestyle Flagship Study of Ageing[4] (AIBL). These open-access datasets considerably advanced the development of ML for AD diagnosis, including both conventional ML and deep learning (DL) methods (LeCun, Bengio, and Hinton, 2015). One can note that more than several hundreds of papers have been published on that topic and new papers are continuously coming out.

With such intensive research, one may wonder why there has been very little translation of these methods to clinical routine. The underlying reasons are as follows. First, bad practices, due to the lack of knowledge from medical imaging to ML techniques, are unfortunately often present. Several studies (see (O'Dwyer et

[2] http://adni.loni.usc.edu/
[3] https://www.oasis-brains.org/
[4] https://aibl.csiro.au/

al., 2012; Wang et al., 2019) for example) reporting promising performances confounded by data leakage, which refers to the use of test data in any part of the training process (Kriegeskorte et al., 2009; Rathore et al., 2017). Secondly, it is very hard, even for the solid papers without data leakage, to assess and compare the performances across studies and approaches. This is due to the fact that they differ in terms of participant selection, image preprocessing procedures for feature extraction or selection, classification models and evaluation procedures. It is thus hard to tell which method performs best and which component of the approach (e.g., feature extraction or classification algorithm) has the most influence on the results. Moreover, these studies are difficult to reproduce. Reproducibility has recently become an intensively debated issue in areas of science such as neuroimaging (Gorgolewski et al., 2016; Poldrack et al., 2017) and ML (Sonnenburg et al., 2007; Stodden, Leisch, and Peng, 2014; Vanschoren et al., 2014). Finally, most of the published works have achieved competitive performances for discriminating AD patients from cognitively normal (CN) subjects. However, the clinical value of this task may be limited since the patient is already demented. More interesting challenge tasks for early diagnosis still remain unsolved.

* *
*

The current dissertation has two main objectives.

First, we aim to advance the identification of biomarkers of the presymptomatic phase of genetic FTLD, focusing on the C9orf72 mutation, using multimodal neuroimaging data. To that purpose, we studied a relatively large population of presymptomatic C9orf72 carriers (N=41), using various neuroimaging modalities. We first used classical anatomical MRI and diffusion MRI applied to DTI model. We then used advanced models of multi-shell diffusion MRI data, specifically the neurite orientation dispersion and density imaging (NODDI) model. For these different modalities, we developed specific image processing pipelines that were used for the study and released publicly.

Secondly, we hope to advance the steps towards the future translation to clinical practice of ML approaches for diagnosis and prognosis of AD. To that purpose, we first proposed a framework for reproducible evaluation of AD classification methods from diffusion MRI data. This extended a previous framework devoted to T1w MRI and PET data (Samper-González et al., 2018). In this study, we used conventional ML models. We then went one step further and checked the potential of DL models in AD classification. As mentioned above, bad practices exist in this field. We performed an exhaustive literature survey and critically reviewed the potential flaws of these studies. We then proposed an open-access framework

and studied the influence of the key components of the framework on classification performances. By doing this, we hope to facilitate the future research on AD classification and improve the research transparency, reproducibility and objectivity.

To summarize, the current thesis tries make progress towards answering the following questions:

- What are the most promising candidate of biomarkers in presymptomatic stage of C9orf72 diseases?
- How far are we away from the translation to clinical practice of AD classification using ML techniques?

The main contributions of this thesis are:

- Identification of early alterations in the presymptomatic stage of C9orf72 disease using conventional anatomical and diffusion MRI.
- Identification of more sensitive biomarkers using an advanced model (NODDI) of diffusion MRI.
- The development of a framework for reproducible evaluation of classification of AD and its application to diffusion MRI with conventional ML methods, and to anatomical MRI with DL methods.
- The development and release of open source software packages, focusing on image processing, statistics and ML techniques.

* *
*

The dissertation consists of five chapters.

First, Chapter 1 introduces the background related to this thesis. This covers: i) the basic knowledge of frontotemporal lobar degeneration and its genetic forms, and Alzheimer's disease, ii) different modalities of neuroimaging data, iii) image processing procedures and iv) two types of analysis approaches (i.e., classical statistics and ML methods), and datasets used in the current thesis.

Chapter 2 presents the study of a cohort of first-degree relatives of C9orf72 patients. T1w MRI, DTI and neuropsychological test were examined for identifying potential biomarkers at the presymptomatic stage.

Chapter 3 extends the previous paper by studying the potential of NODDI and comparing it sensitivity to that of DTI. It aims to clarify the added value of NODDI compared to conventional techniques such as DTI and T1w MRI.

Chapter 4 describes our open source framework for AD classification from diffusion MRI data and applies it to study the value of this modality for these diagnostic and prediction tasks.

Chapter 5 extends the previous chapter to DL models and demonstrates its use on anatomical MRI.

Finally, the main results are recalled and future work directions are presented.

In addition, we present, in appendices, the supplementary materials for Chapter 2, Chapter 3 and Chapter 5, respectively.

Chapter 1

Background

In this chapter, we aim to provide a straightforward introduction to the main concepts involved in this dissertation. Specifically, this chapter contains the background knowledge regarding: i) the neurodegenerative diseases that we studied (Section 1.1); ii) neuroimaging modalities (Section 1.2); iii) main steps for image preprocessing and feature extraction (Section 1.3); iv) classical statistical models (Section 1.4), v) machine learning models (Section 1.5), vi) neuroimaging biomarkers of C9orf72 carriers (Section 1.6), vii) neuroimaging for classification of AD (Section 1.7) and viii) datasets used in this dissertation (Section 1.8).

1.1 Neurodegenerative diseases

Neurodegenerative diseases are characterized by the progressive loss of structure or function of neurons, due to for instance, the death of neurons. Neurons normally don't reproduce or replace themselves, thus such diseases are irreversible[5]. Examples of neurodegenerative diseases are AD, FTLD and ALS. In the section, we briefly introduce the three diseases involved in this PhD.

1.1.1 Alzheimer's disease

AD is the first cause and represents 60–70% of cases of dementia (Burns and Iliffe, 2009a). Currently, the epidemic situation of AD is becoming more and more grievous. In 2015, there were approximately 29.8 million people worldwide with AD (Vos et al., 2016). It affects most often elderly people. Among the general population, it affects about 6% of people over 65 years of age (Burns and Iliffe, 2009a). Especially in developed countries, AD is one of the most financially costly diseases (Bonin-Guillaume et al., 2005).

The underlying cause of Alzheimer's disease is still poorly understood (Burns and Iliffe, 2009a). For instance, about 70% of the cases are believed to be influenced by different genes inherited from patients' parents (Ballard et al., 2011). Other risk

[5] https://en.wikipedia.org/wiki/Neurodegeneration

factors include a history of head injuries, depression, and hypertension (Burns and Iliffe, 2009a). The disease trajectory is divided into three main stages, with a progressive pattern of cognitive and functional impairment.

- Presymptomatic: the stage during which pathological changes accumulate in the absence of any symptoms (Dubois et al., 2016; Sperling et al., 2011);
- mild cognitive impairment (MCI): the stage during which the patient has mild cognitive deficits, mainly memory troubles, but is not demented (Dubois and Albert, 2004; Albert et al., 2011);
- AD: the final stage during which the presence of the memory problems, language, executive and motor functions is severe enough to make it impossible to carry out everyday tasks for the patients (McKhann et al., 1984; McKhann et al., 2011).

Several competing hypotheses exist and try to explain the cause of the disease (Duyckaerts, Delatour, and Potier, 2009). The first one is the amyloid hypothesis. It postulates that extracellular amyloid beta ($A\beta$) deposits are the fundamental cause of AD (Mudher and Lovestone, 2002; Hardy and Allsop, 1991). This accumulation can start up to 20 years before the diagnosis. Another popular hypothesis is the so-called tau hypothesis (Mudher and Lovestone, 2002). This hypothesis proposed that tau protein abnormalities initiate the disease cascade. The formation of neurofibrillary tangles made of tau proteins links to each other inside neurons and causes the death of neurons. Other hypotheses also exist in the community (Zlokovic, 2007).

AD is usually diagnosed based on clinical assessment (e.g., person's medical history, history from relatives) and neuropsychological tests (e.g., mini mental state examination, MMSE). This is usually performed once the symptoms occur. Earlier diagnosis of AD is critical because it not only would allow providing adequate care to the patient, but also provides the best time window for development of disease-modifying drugs. Until now, there is no definitive evidence to support that any particular measure is effective in preventing or curing AD. In recent decades, new criterias have been proposed to achieve an earlier and more accurate diagnosis (Dubois et al., 2007; Dubois et al., 2014; Albert et al., 2011). These criterias integrated biomarkers, established thanks to different techniques including neuroimaging and fluid biomarkers (Hampel et al., 2014), into clinical and cognitive tests.

1.1.2 Frontotemporal lobar degeneration

FTLD is a clinically and pathologically heterogeneous syndrome, which is characterized by progressive decline in behaviour or language associated with degeneration of the frontal and anterior temporal lobes (Floeter et al., 2016). FTLD is considered as an important cause of dementia, in particular in patients younger than 65 years of age.

There are three main distinct clinical phenotypes of FTLD: (i) behavioural variant frontotemporal dementia (bvFTD), characterized by changes in behaviour and personality and cortical degeneration focusing on frontal-predominant regions; (ii) semantic dementia, showing the loss of knowledge about words and objects involving anterior temporal regions and (iii) progressive nonfluent aphasia, resulting in difficulty in language output and grammar associated with left perisylvian cortical atrophy (Rabinovici and Miller, 2010). FTLD is also pathologically heterogeneous. Like most neurodegenerative diseases, FTLD is accompanied with the presence of insoluble protein in neurons (Le Ber et al., 2008). Three subtypes exist depending on the type of the protein that aggregates in neuronal inclusions: i) FTLD-Tau, accounting for 30–40% of FTLD. They are characterized by the accumulation of tau protein in neurons. ii) FTLD-TDP, representing 50–60% of FTLD cases. TDP-43 (TAR DNA-binding protein) is witnessed to be aggregated in neurons (Neumann et al., 2006); iii) FTLD-FUS, a rare form (10% of FTLD cases). It is characterized by the presence of FUS-positive inclusions (Neumann et al., 2007).

1.1.2.1 Genetic forms of FTLD

FTLD is also genetically heterogeneous. For the last decade, researchers shed more light on the genetic forms of FTLD since the identification of two major genes, progranulin gene mutations (PGRN) (Snowden et al., 2006; Baker et al., 2006; Cruts et al., 2006) and chromosome 9 open reading frame 72 (C9orf72) (DeJesus-Hernandez et al., 2011), but also with other genes which are less frequently witnessed. Until 2013, more than twelve genes were identified in the literature explaining 50-60% of familial cases (see (Le Ber, 2013) for details). Here, we present three main genes representing a familial form of FTLD.

Microtubule-associated protein tau (MAPT) mutation was the firstly identified in 1998 (Hutton et al., 1998) and helps encode the tau protein. In France, the frequency of MAPT mutations is approximately 3% of patients with FTLD and close to 10% in familial forms of the disease (Le Ber et al., 2008). In 2006, PGRN mutations were identified. This mutation is associated with the TDP-43 positive inclusions in neurons (Snowden et al., 2006; Baker et al., 2006; Cruts et al., 2006). In France, the relative frequency of PGRN mutations is 13% in familial

FTLD (Le Ber et al., 2008). Progranulin promotes the growth of neurons and increases the survival of cortical and spinal motor neurons, and could therefore have a neurotrophic effect. The pathophysiological mechanisms associated with PGRN mutations are still unknown. In 2011, a GGGGCC repeat expansion in C9orf72 gene was identified in 9p-linked families (c9FTLD/ALS) (DeJesus-Hernandez et al., 2011). In France, the prevalence rate differed according to the phenotype: 13% in familial bvFTD (without ALS), but up to 66% in familial FTLD-ALS (Le Ber et al., 2013). The function of the protein coded by C9orf72 and the pathogenic effect of the non-coding expansion are still unclear.

Each mutation has a distinct pattern of brain atrophy (Figure 1.1). MAPT and GRN mutations showed striking temporal and temporoparietal atrophy, respectively. The C9orf72 mutation showed a signature of wide grey matter loss over the whole brain, with the most striking loss in frontal lobes.

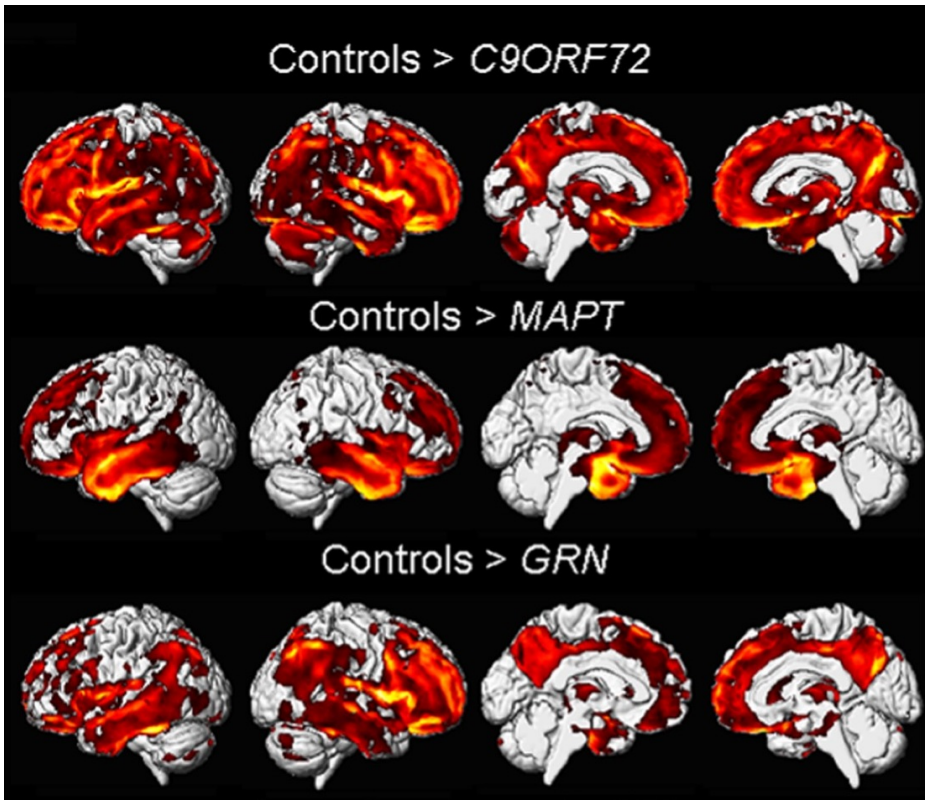

Figure 1.1: Atrophy pattern of three main genetic form of FTLD. Mutation carriers was compared to the control group in the voxel-based morphometry analysis of grey matter volume. Permission was obtained from (Whitwell et al., 2012)

1.2 Neuroimaging data

When studying neurodegenerative disease based on brain neuroimaging data, three main steps are involved: i) image acquisition using various modalities; ii)

image preprocessing to extract features and iii) applying different data analysis methods, for instance classical statistical models for group comparison or more advanced machine learning models, on the extracted quantitative features.

In this section, we review the two data modalities that are relevant to this dissertation and provide a basic explanation of these techniques. Specifically, section 1.2.1 presents the anatomical MRI and section 1.2.2 introduces the diffusion MRI. Note that we only briefly introduce these techniques. One can refer to (Susumu Mori and J-Donald Tournier, 2013; McRobbie, 2006; Schmitt, Stehling, and Turner, 1998) for more details on different MRI modalities.

1.2.1 Anatomical MRI

T1w MRI uses a short repetition time (TR) and echo time (TE) to enhance the tissue contrast, thus allowing to study the patient's brain morphology. T1w MRI usually offers excellent contrast: fluids are very dark such as CSF in ventricle, GM is grey and WM is more brighter. This MRI sequence is known as anatomical MRI because it shows clearly the boundaries between different tissues (Figure 1.2). T1w MRI is widely used in neurodegenerative diseases to assess brain atrophy or tissue damage.

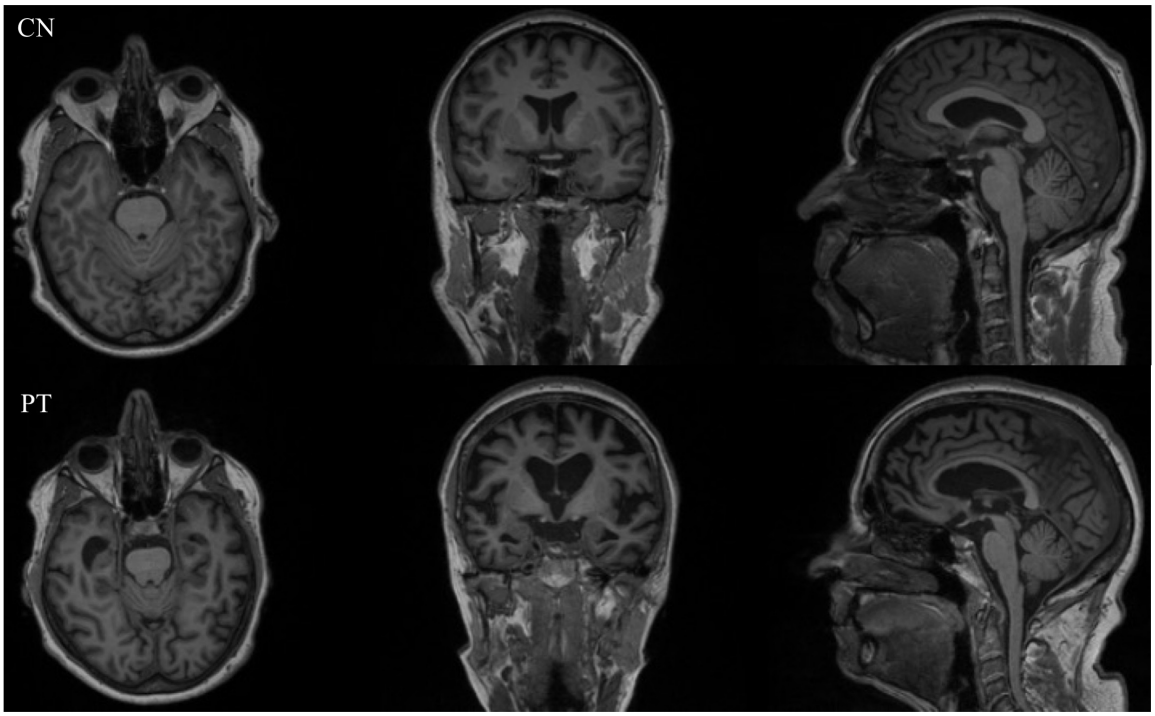

Figure 1.2: T1w MRI for a cognitively normal subject (CN) and for a patient with C9orf72 mutation (PT). One can note the whole brain atrophy and the enlargement of the ventricles.

1.2.2 Diffusion MRI

Diffusion MRI (Le Bihan et al., 1986) uses the diffusion of water molecules to generate contrast in MR images. It allows the mapping of the Brownian motion process of molecules, mainly water, in biological tissues (e.g., GM and WM) in vivo and non-invasively. The motion of water in the brain is not totally isotropic because the mobility of water is constrained by its cellular environment. The intensity of each voxel reflects the rate of water diffusion at that location in the brain. When there is no constraint as in free water (e.g., CSF), the motion of water is randomly diffused in all directions (isotropy). When the water motion is constrained by the tissues (e.g., WM and GM), the diffusion is anisotropic (Merboldt, Hanicke, and Frahm, 1985). This quality makes diffusion MRI sensitive to the microstructural damage and indicative for early pathological changes.

The amplitude and anisotropy of the diffusion depends on several parameters, such as the direction, density or diameter of the fibre bundles. In order to measure these diffusion parameters (amplitude and anisotropy), one should first acquire an image with the diffusion-sensitizing gradients turned off (b-value=0 s/mm^2) or set to a very low value (e.g., b-value=5 s/mm^2). This is usually referred to as b0 image and serves as a baseline for later calculated maps. The diffusion-weighted images (DWI) are then run with different combination of b-value and b-vec (the gradients' direction), generating the source images sensitized to diffusion in multiple directions. For illustration purpose, three diffusion images using b-values of 5, 300, 700 and 2200 s/mm^2 are shown in Figure 1.3. One can observe that higher b-value shows progressively more diffusion weighting but also more noise (lower signal-to-noise ratio, SNR). As a practical matter, most routine clinical diffusion sequence currently use b-values between 0 and 1000 s/mm^2). Note that we denote one image sequence with multiple b-values as multi-shell data. Conversely, we note the image sequence with a single b-value as single-shell data in this dissertation.

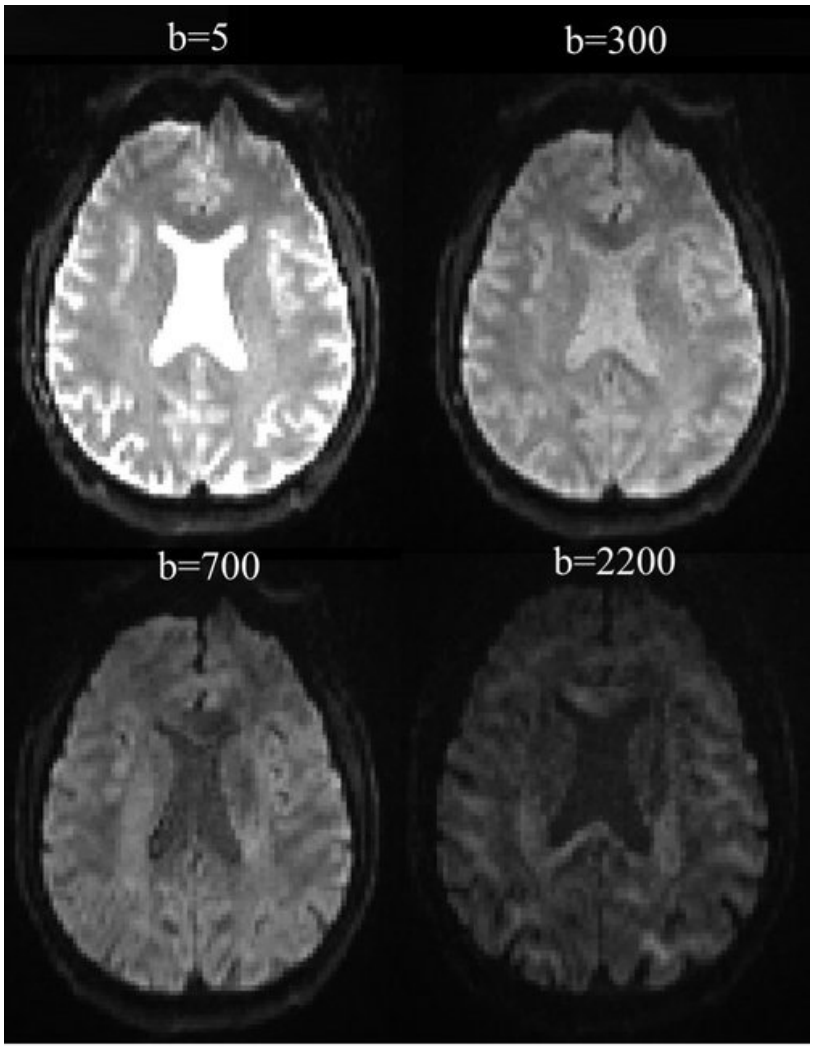

Figure 1.3: Multi-shell diffusion MRI for a cognitively normal subject (CN). Images using different b-values, 5, 300, 700, and 2200 s/mm^2, are shown here.

1.2.2.1 Diffusion tensor imaging

Different models can be applied to the preprocessed diffusion MRI data (the details of image preprocessing will be introduced in section 1.3). One of the most widely used models is DTI (Basser et al., 1994). DTI is popular for imaging the white matter of the brain and has been applied to a tremendous variety of neuroimaging studies (O'Donnell and Westin, 2011). DTI modelizes each voxel as a diffusion tensor. The derived tensor anisotropy measures are ratios of the eigenvalues that are used to quantify the shape of the diffusion. The most common metrics are fractional anisotropy (FA, often referred to as the measure of "white matter integrity"), mean diffusivity (MD), axial diffusivity (AD) and radial diffusivity (RD). Figure 1.4 shows the DTI metric maps. DTI metrics are computed according to the following formulas:

$$FA = \frac{\sqrt{3\left[(\lambda_1 - \lambda)^2 + (\lambda_2 - \lambda)^2 + (\lambda_3 - \lambda)^2\right]}}{\sqrt{2(\lambda_1^2 + \lambda_2^2 + \lambda_3^2)}}$$

$$MD = \frac{\lambda_1 + \lambda_2 + \lambda_3}{3}$$

$$AD = \lambda_1$$

$$RD = \frac{\lambda_2 + \lambda_3}{2}$$

where $\lambda = \frac{\lambda_1+\lambda_2+\lambda_3}{3}$, λ_1, λ_2, λ_3 are the eigenvalues of the diffusion tensor.

Although widely used in neuroimaging studies, the DTI model has limitations. First, DTI metrics lack specificity. They are hard to interpret from the biophysical point of view. For instance, the change of FA could be caused by numerous factors (e.g., cell death or change in myelination) (Alexander et al., 2007; O'Donnell and Westin, 2011). Secondly, DTI is limited when an image voxel suffers from partial volume effect (e.g., the voxels near to ventricle). Lastly, DTI is able to model only the major fibre direction. On the other hand, in the brain, a high proportion of WM voxels are localizing where crossing or fanning fibres are present (Behrens et al., 2007). This may confound the following analyses dependent on DTI results, such as DTI tractography.

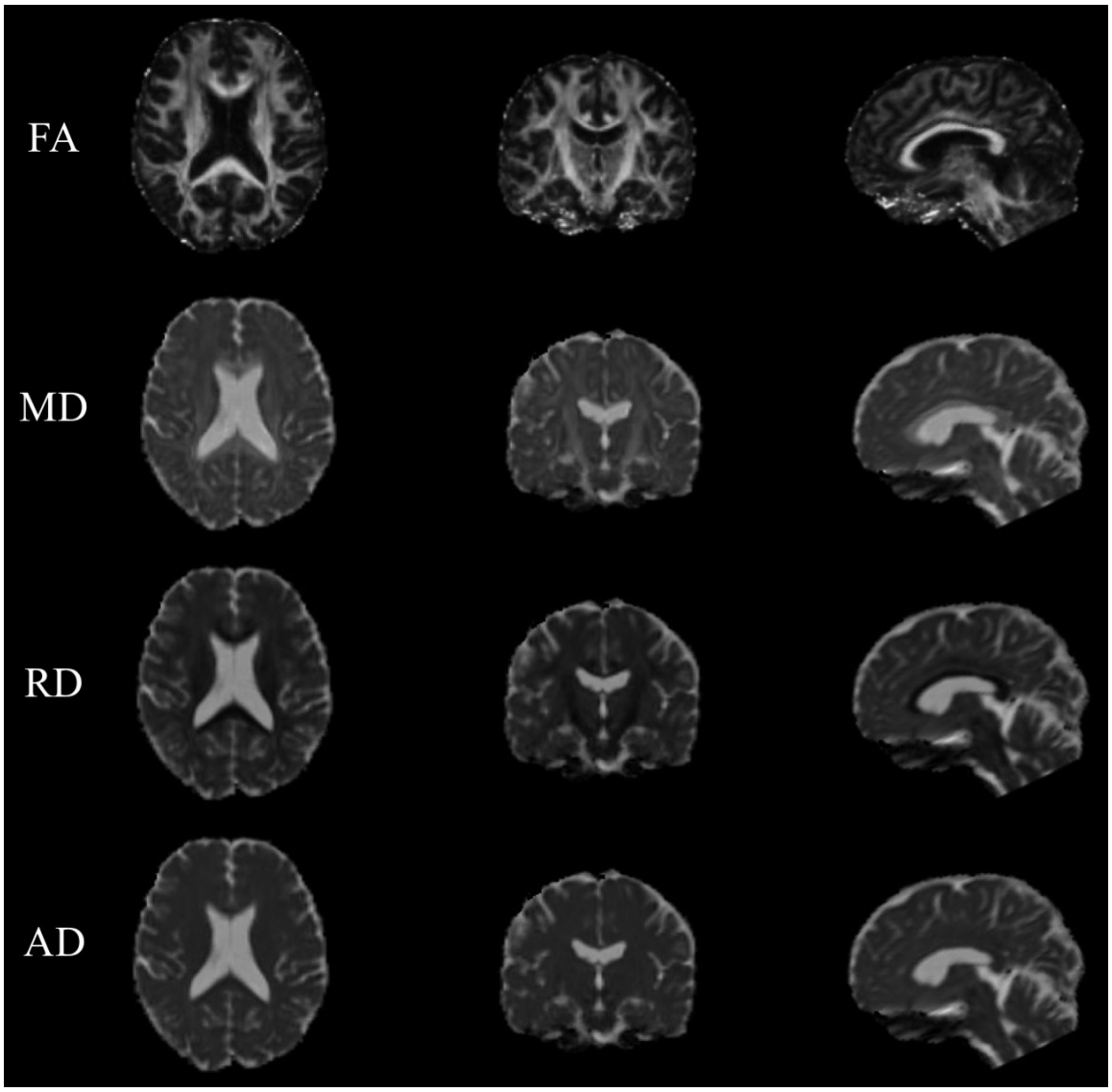

Figure 1.4: DTI metric maps. From up to down, FA, MD, RD and AD are presented.

1.2.2.2 Neurite orientation dispersion and density imaging

Beyond DTI, other models have been proposed in the community (Zhang et al., 2012; Pasternak et al., 2009; Eaton-Rosen et al., 2017). Neurite orientation dispersion and density imaging (NODDI) model was firstly proposed by Zhang et al (Zhang et al., 2012). They demonstrated that NODDI model, compared to DTI model, offered higher tissue-specificity. Note that NODDI, compared to conventional DTI model, requires a multi-shell diffusion MRI sequence which takes about 30 minutes to acquire in a clinical routine. The image preprocessing procedure, which will be detailed in the next section, is similar to that of single-shell data, including corrections for head motion, susceptibility and eddy-current distortion.

NODDI models the diffusion signal from three compartments: i) free water, S_{fwf} is the signal from the free water and V_{fwf} is the volume fraction of each voxel

representing free water, ii) intracellular space, S_{in} and V_{in} represent the signal and volume fraction from the intracellular compartment (e.g., intra-axonal in WM) and iii) extracellular space, S_{ex} and V_{ex} mean the signal and volume fraction from the extracellular compartment. Thus, the total signal at each voxel can be written with the following equation:

$$S_t = (S_{fwf} \times V_{fwf}) + (1 - V_{fwf})(S_{in} \times V_{in} + (1 - V_{in}) \times S_{ex})$$

where S_t is the measured diffusion signal in total.

The NODDI model derives three metrics: neurite density index (NDI) and orientation dispersion index (ODI) quantify the density and angular variation of neurites, respectively, while free water fraction (FWF) captures the contamination of tissues by free water at the microstructural level. NODDI metric maps are shown in Figure 1.5

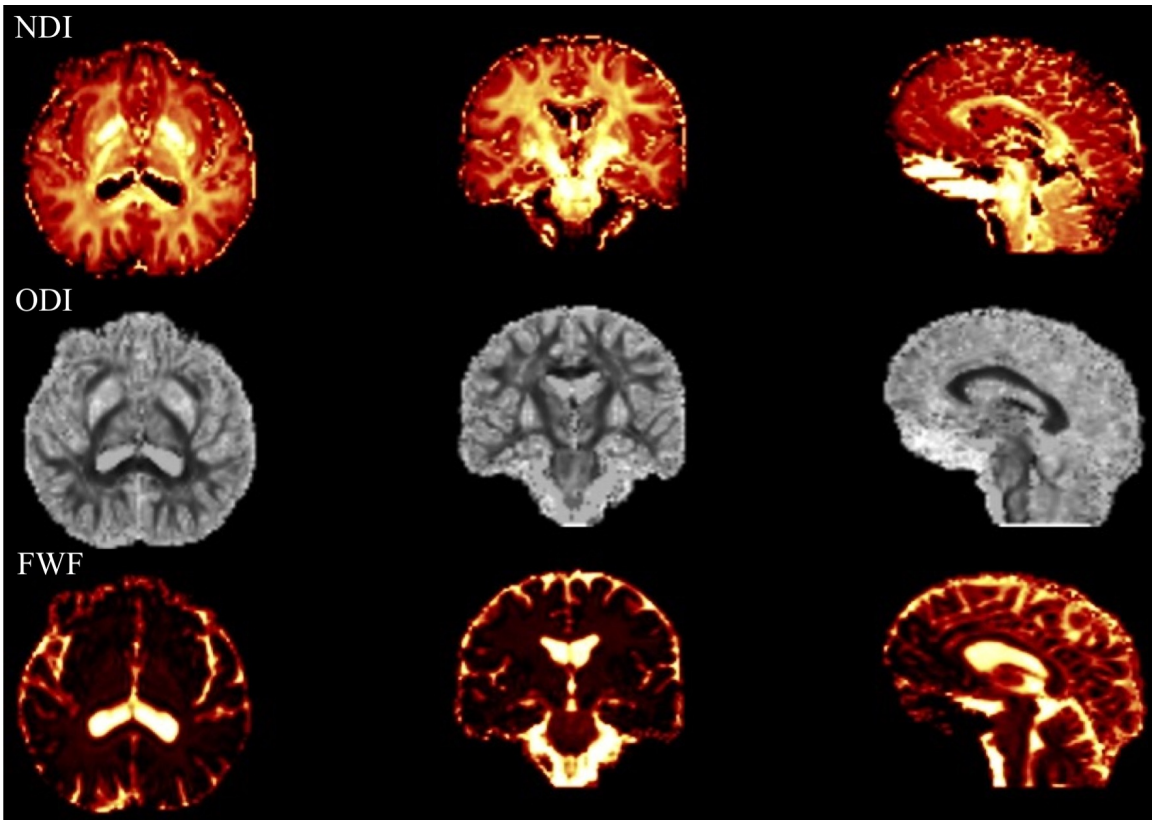

Figure 1.5: NODDI metric maps. From up to down, NDI, ODI and FWF are presented.

1.3 Image preprocessing

MR images may suffer from various artifacts. These may result from physiological sources (e.g., head motion, respiration and anxiety) or from the scanner itself

(e.g., geometric distortions and signal losses). A proper image preprocessing is necessary for a successful quantitative analysis. In the context of classification, researcher has proven that image processing procedures have a strong influence on classification results (Uchida, 2013; Lu and Weng, 2007; Cuingnet et al., 2011). Generally, the image preprocessing procedure includes the main following steps: bias field correction, intensity rescaling and standardization, skull stripping, eddy current-induced distortion correction, susceptibility-induced distortion correction and registration. According to the data modality (e.g., T1w MRI or diffusion) and the scientific question of interest (e.g., conventional ML or DL methods), different sources of artifacts may be present and different correction methods should be adapted.

In this section, we present the most essential preprocessing steps for T1w MRI and diffusion MRI. We then introduce the Clinica [6] open-source platform for reproducible neuroimaging studies implemented and maintained by the ARAMIS laboratory [7]. Lastly, we summarize the extracted features which are used in the following analyses in this dissertation. Note that we present here only the basic knowledge on MRI processing, readers can refer to (Bankman, 2008) for more details.

1.3.1 Bias field correction

MR images can be corrupted by a low frequency and smooth signal caused by magnetic field inhomogeneities. This bias field induces variations in the intensity of the same tissue in different locations of the image, which deteriorates the performance of image analysis algorithms such as registration (Vovk, Pernus, and Likar, 2007). Several methods exist to correct these intensity inhomogeneities, two popular ones being the nonparametric nonuniformity intensity normalization (N3) algorithm (Sled, Zijdenbos, and Evans, 1998), available for example in the Freesurfer software package [8], and the N4 algorithm (Tustison et al., 2010) implemented in ITK [9]. Moreover, MRtrix [10] also provided tools for B1 field inhomogeneity correction for diffusion MRI data (Zhang, Brady, and Smith, 2001).

1.3.2 Intensity rescaling and standardization

As MRI is usually not a quantitative imaging modality itself, MR images usually have different intensity ranges and the intensity distribution of the same tissue

[6] http://www.clinica.run/
[7] http://www.aramislab.fr
[8] http://surfer.nmr.mgh.harvard.edu/fswiki/recon-all
[9] http://hdl.handle.net/10380/3053
[10] http://www.mrtrix.org

type may be different between two images, which might affect the subsequent image preprocessing steps. The first point can be dealt with by globally rescaling the image, for example between 0 and 1 using the minimum and maximum intensity values (Juszczak, Tax, and Duin, 2002). Intensity standardization can be achieved using techniques such as histogram matching (Madabhushi and Udupa, 2005).

1.3.3 Skull stripping

Non-brain tissues can be an obstacle for image analysis algorithms (Kalavathi and Prasath, 2016). A large number of methods have been developed for brain extraction, also called skull stripping, and many are implemented in software tools, such as the Brain Extraction Tool (BET) (Smith, 2002) available in FSL [11], or the Brain Surface Extractor (BSE) (Shattuck et al., 2001) available in BrainSuite [12]. These methods are often sensitive to the presence of noise and artifacts, which can result in over or under segmentation of the brain.

1.3.4 Image registration

Medical image registration consists of spatially aligning two or more images, either globally (rigid and affine registration) or locally (non-rigid registration), so that voxels in corresponding positions contain comparable information. A large number of software tools have been developed for MRI-based registration (Oliveira and Tavares, 2014). FLIRT [13] (Greve and Fischl, 2009; Jenkinson et al., 2002; Jenkinson and Smith, 2001) and FNIRT [14] (Andersson, Jenkinson, and Smith, 2010) are FSL tools dedicated to linear and non-linear registration, respectively. The Statistical Parametric Mapping (SPM) software package [15] and Advanced Normalization Tools [16] (ANTs) also offer solutions for both linear and non-linear registration (Ashburner and Friston, 2000; Avants et al., 2014; Friston et al., 1995).

1.3.5 Head motion correction

MR images are sensitive to subject motion due to the sequential acquisition for multiple volumes, as in the case of diffusion MRI. Subject motion may induce artifacts and reduce image quality and diagnostic or scientific relevance (Godenschweger et al., 2016). Researchers has put a huge effort to prevent, suppress or

[11] https://fsl.fmrib.ox.ac.uk/fsl/fslwiki/BET/UserGuide
[12] http://brainsuite.org/processing/surfaceextraction/bse
[13] https://fsl.fmrib.ox.ac.uk/fsl/fslwiki/FLIRT
[14] https://fsl.fmrib.ox.ac.uk/fsl/fslwiki/FNIRT
[15] https://www.fil.ion.ucl.ac.uk/spm
[16] http://stnava.github.io/ANTs

correct motion artifacts. One typical case of head motion artifact can be referred as MRI-based motion (Godenschweger et al., 2016). It happens when there are at least two MR images/volumes at different time points within subject. The head motion caused during the interval time between images/volumes can be calculated by registration algorithms or by comparison to training data sets on the basis of 3D volumes. The type of motion can be divided into linear (e.g., rigid) or non-linear. The registration-based solution can be achieved by the registration tools mentioned above. Beyond the MRI-based motion, it exists other types of motions and the corresponding correction methods, including both prospective or retrospective head motion correction methods (see (Godenschweger et al., 2016) for more details).

1.3.6 Eddy current-induced distortion correction

Eddy current-induced off-resonance field, frequently present in diffusion weighted EPI images, is caused by the rapidly switched diffusion encoding gradients, which is an additional source of off-resonance. The rapidly changing magnetic field results in eddy currents (EC) in conductors within the bore, thus in turn inducing a magnetic field (Andersson and Sotiropoulos, 2016). Numerous studies focused on the correction of this artifact. The most common used technique is the eddy tool [17] from FSL. This tool integrates the corrections for eddy current-induced distortions and subject movements. It simultaneously models the effects of diffusion eddy currents and movements on the image, allowing it to work with higher b-value data (Andersson and Sotiropoulos, 2016).

1.3.7 Susceptibility-induced distortion correction

Another common artifact of diffusion MRI is the so-called susceptibility-induced distortion. The reason behind this artifact is as follows. Diffusion images are sensitive to off-resonance fields due to the low bandwidth in the phase-encode (PE) direction, which results in telltale unidirectional distortions (Schmitt, Stehling, and Turner, 1998). Various sources of off-resonance exit during image sequence. For instance, the object itself in the scanner will disrupt the existing homogeneous magnetic field, rendering the resulting field inhomogeneous. Also, air in the brain and the presence of metallic ions in tissues can cause similar susceptibility-induced distortions. In the field, FSL provides a robust tool, topup [18], for susceptibility-induced distortion correction. One prerequisite is that the data shoud be collected

[17] https://fsl.fmrib.ox.ac.uk/fsl/fslwiki/eddy
[18] https://fsl.fmrib.ox.ac.uk/fsl/fslwiki/topup

with reversed phase-encode blips, resulting in pairs of images with distortions going in opposite directions (Andersson, Skare, and Ashburner, 2003; Smith et al., 2004).

1.3.8 Other processing steps

Beyond these steps mentioned above, other procedures, such as image segmentation or cortical reconstruction, may also be necessary. For instance, image segmentation is the most critical step in region of interest (ROI) analyses. The regional features (e.g., regional volumetric measures based on an anatomical atlas) depend on the results of image segmentation. Different software, such as FreeSurfer and SPM, integrate image segmentation steps and one can refer to (Despotović, Goossens, and Philips, 2015) for more details on different segmentation techniques. Another example is that the cortical surface reconstruction (Fischl, 2012; Fischl et al., 1999) is critical to precisely extract the cortex-wise features (e.g., cortical thickness).

1.3.9 Implementation: Clinica open source platform

The complexity of neuroimaging analyses can make it difficult, especially for newcomers in this field, to perform or reproduce a study. Often, researchers performed their analysis by combining different software packages widely used in the community, such as FreeSurfer and SPM. However, such hand-craft strategy makes it difficult to reproduce their studies for the following reasons. i) Heterogeneous data organization. No existing automatic tools exist to convert the raw data from the extensively used databases (e.g., ADNI dataset) to a standard data format. ii) Inflexible software deployment, different software exist in the field but may not be mutually compatible. Steps have been made in the right direction. The Brain Imaging Data Structure (BIDS) data organization standard (Gorgolewski et al., 2016) and Nipype pipelining system (Gorgolewski et al., 2011) have been proposed in the community. To help further address the limitations mentioned above, we developed Clinica, a software that aims at making clinical neuroimaging studies easier and more reproducible.

An overview of Clinica is shown on Figure 1.6. Three main components can be summarized: i) data management tools, such as automatic tools to convert the raw data of public databases into BIDS format, or tools for participant selection; ii) feature extraction pipelines, different software or tools can be easily deployed and tested with the Nipype modular architecture; iii) Statistics and machine learning, such as generalized linear model (GLM), conventional ML and DL.

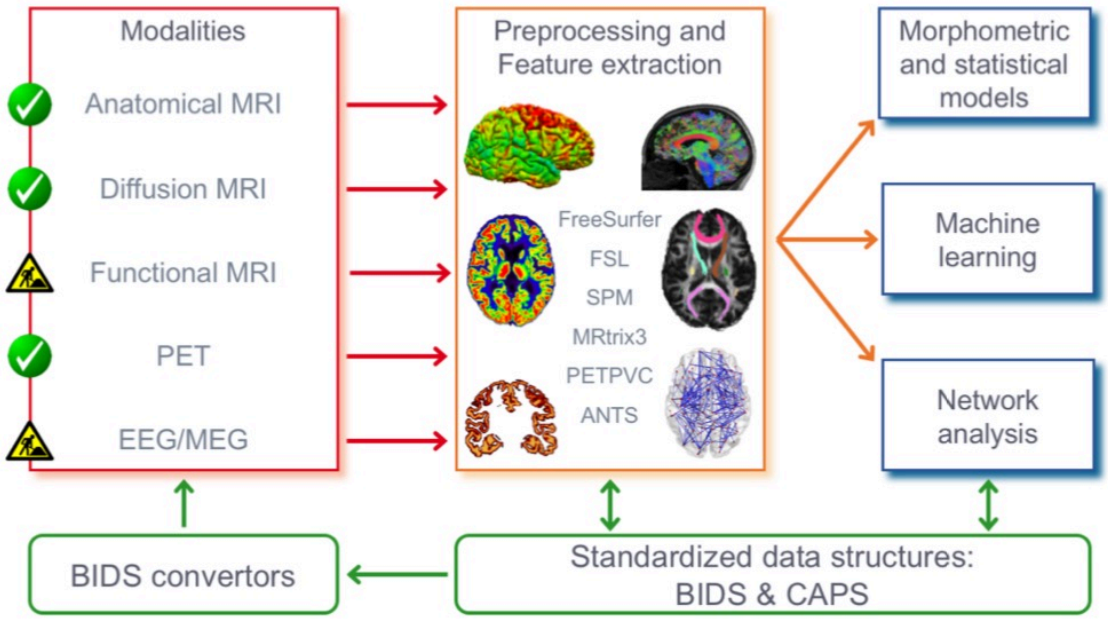

Figure 1.6: Clinica, an open source platform for reproducible neuroimaging studies.

Note that The Clinica software is publicly available and under active development. The current dissertation highly depends on the Clinica software. Conversely, I contributed to the development of Clinica, namely to the following components: T1w MRI surface-based extraction and statistics, DTI processing, NODDI processing, and machine learning.

1.3.10 Extracted features

According to the type of analysis (i.e., GLM or machine learning), features were extracted based on different preprocessing procedures. We summarize and present here all the features extracted based on the Clinica software and involved in our analyses (Figure 1.7).

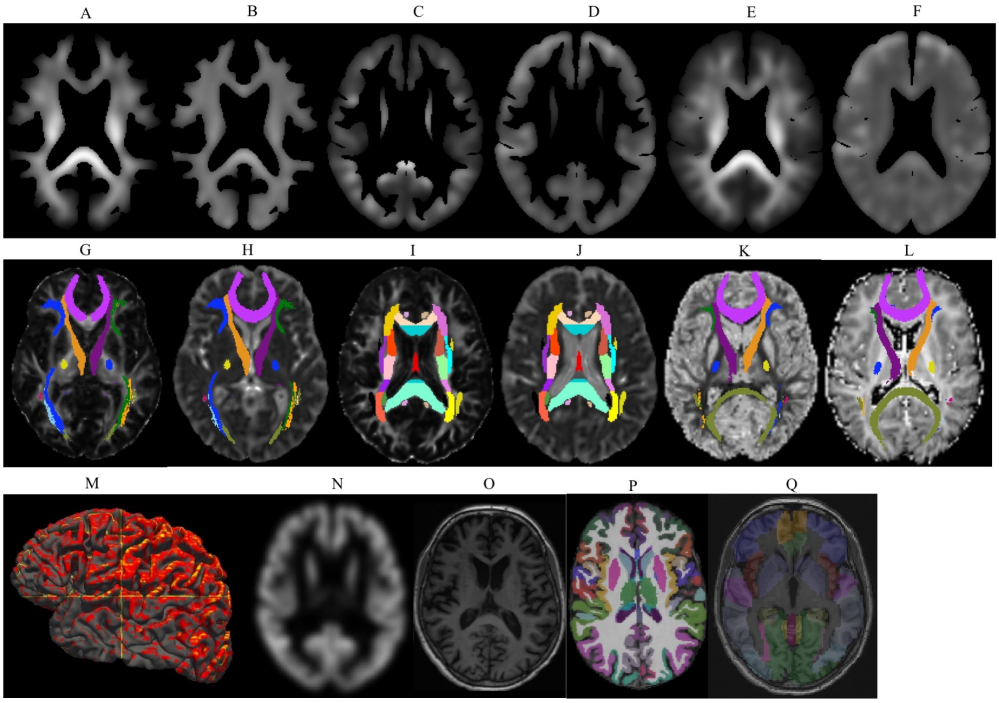

Figure 1.7: Extracted neuroimaging features from both diffusion MRI and T1w MRI used in the current dissertation.

- A) voxel WM+FA features: diffusion MRI was preprocessed for head motion correction, eddy current-induced distortion correction and susceptibility-induced distortion correction. Then DTI model was fit to generate FA map, which was masked by T1w MRI tissue (WM) probability map.
- B) voxel WM+MD features: MD map was masked by T1w MRI tissue (WM) probability map.
- C) voxel GM+FA features: FA map was masked by T1w MRI tissue (GM) probability map.
- D) voxel GM+MD features: MD map was masked by T1w MRI tissue (GM) probability map;
- E) voxel GM+WM+FA features: FA map was masked by T1w MRI tissue (WM+GM) probability map.
- F) voxel GM+WM+MD features: MD map was masked by T1w MRI tissue (WM+GM) probability map.
- G) regional FA features from JHU white-matter tractography atlas (denoted as JHUTract25): FA map was quantized by JHUTract25 atlas, including 20 white matter tracts.

- H) regional MD features from JHUTract25: MD map was quantized by JHUTract25 atlas.
- I) regional FA features from ICBM-DTI-81 white-matter labels atlas (denoted as JHULabel): FA map was quantized by JHULabel atlas, including 48 white matter tracts.
- J) regional MD features from JHULabel: MD map was quantized by JHULabel atlas.
- K) regional ODI features from JHUTract25: NODDI model was fit to the preprocessed diffusion data and generated ODI map. ODI maps was quantized by JHUTract25 atlas.
- L) regional NDI features from JHUTract25: NDI map was quantized by JHUTract25.
- M) regional Desikan FWF features: FWF map was projected at the middle cortex and quantized by Desikan atlas.
- N) voxel GM density map: voxel features from T1w MRI gray matter density map. T1w MRI was preprocessed with a complex procedure, including non-linear registration, intensity normalization, segmentation, etc.
- O) full brain density map from T1w MRI. T1w MRI was preprocessed only with intensity rescaling, bias field correction and a linear registration into MNI space.
- P) regional Desikan density map: regional feature from T1w MRI quantized by Desikan atlas. T1w MRI was preprocessed with a complex processing procedure, including segmentation, cortical construction.
- Q) regional AAL2 density map: regional features from T1w MRI quantized by AAL2 atlas. T1w MRI was preprocessed with a complex processing procedure, including segmentation, non-linear registration.

With the extracted features from both T1w MRI and diffusion MRI, further analysis can be performed depending on the scientific question of interest. In the current dissertation, we applied these features into two categories of analyses: i) classical statistics (see Section 1.4) for identifying neuroimaging biomarkers at the presymptomatic stage of C9orf72 carriers and ii) advanced ML techniques (see Section 1.5) for early and accurate diagnosis of AD.

1.4 Classical statistics

Classical statistical models have been used to identify biomarkers in dementia during the disease trajectory. Generally, this approach helps decide if significant difference exists between two groups within a disease population on the chosen features (e.g., regional volumetric measures). For instance, researchers collected one group of AD patients (denoted as AD) and another group of cognitively normal subjects (denoted as CN). Here, the chosen feature could be the volumetric measures of each ROI based on an pre-defined anatomical atlas. By leveraging the classical statistics, researchers may address the following scientific questions:

- i) Is there significant difference in brain atrophy between two groups (reflected by the p-value)?
- ii) How much is the magnitude of this difference (reflected by the effect size)?

The Generalized Linear Model (GLM), the most common type of regression model, could be used for this purpose. A p-value can be derived from a hypothesis test for each ROI, resulting in the so-called uncorrected p-values (one for each ROI). A correction (e.g., bonferroni correction) for these multiple comparisons can be then performed to reduce the false positive rate (also known as Type 1 error). GLM has been widely used in neuroimaging studies to identify neuroimaging-based biomarkers.

In this section, we present the basic knowledge of GLM. Readers should feel free to skip this section given their background and knowledge. Conversely, for more details, see (McCullagh, 2018) on this topic.

1.4.1 Generalized linear model

GLM is a flexible and generalized form of ordinary linear regression. One should not confuse the general linear model and the generalized linear model: the generalized linear model allows for the distribution of the error of the response variables to be non-normal (e.g., binomial distribution), whereas general linear model requires strictly a Gaussian distribution.

In a GLM, both systematic and random components can be encompassed. A GLM can be characterized by the following components:

- i) A dependent variable Y whose distribution with parameter θ is one of the exponential family of probability distributions.
- ii) A set of independent variables (X_i) and the linear predictor $Y = \sum \beta X_i$.

- iii) A linking function $\theta = f(Y)$ to connect the distribution parameter and the dependent variable Y of the model.

Thus a GLM could be written as follows:

$$Y = \beta_0 + \beta_1 X_{1i} + \beta_2 X_{2i} + ... + \beta_p X_{pi} + \epsilon_i$$

where ϵ_i is the errors part.

Fitting the formulated GLM can be achieved by maximum likelihood. The maximum likelihood estimates can be found using an iteratively reweighted least squares algorithm or a Newton's method with updates of the form. For more basis of mathematics, refer to (Nelder and Wedderburn, 1972).

1.4.2 P-value and effect size

Statistical significance, namely p-value, is the probability that the observed difference between two groups is due to chance (Sullivan and Feinn, 2012). The p-value is often used in a dichotomous way. For instance, if the p-value is larger than the chosen alpha level (e.g, 0.05), any observed difference is due to the sampling variability or by chance. Conversely, an opposite conclusion, the two groups are significantly different, is made if the p-value is smaller than 0.05. This interpretation may have limitations. First, the alpha level is more or less arbitrarily, subjectively and manually chosen. R. A. Fisher, in the 1920's, firstly proposed 0.05 as a standard (Fisher, 1992). This was driven partly by the fact that the five percent cutoff, in a normal distribution, falls nearby the second standard deviation away from the mean of the distribution. Currently, some researchers have advocated to shift the alpha level to be more strict (e.g., 0.005 or 0.001) (Benjamin et al., 2018). However, others argued that to boil all this down to a binary decision based on a p-value threshold of 0.05, 0.01, 0.005, or anything else, is not acceptable (Trafimow et al., 2018). Moreover, p-value is dependent on the sample size, which means that, with a sufficiently large sample, a statistical test will almost always demonstrate a significant difference. Thus, reporting only the p-value for a hypothesis test analysis is not adequate for readers to fully understand the results. Argues still exist about the correct use of p-value and researchers have become increasingly aware of its shortcomings and the potential for abuse (see the call on this issue on Nature for more details: `https://www.nature.com/articles/d41586-019-00857-9`).

Effect size, the magnitude of the differences between groups, was proposed to be reported along together with the p-value. Effect size can refer to the raw difference between group means, or absolute effect size, as well as standardized measures of effect, which are calculated to transform the effect to an easily understood scale (Sullivan and Feinn, 2012). One property of effect size is its independence

from the sample size, leading to the use to quantitatively compare results from different studies. Commonly used effect size indices are as follows:

- i) Cohen's d is based on differences between means and derived as the difference between two means divided by a standard deviation.
- ii) Cohen's $f2$ is one form of effect size measures to use in the context of an F-test for ANOVA.
- iii) Cohen's q is used with correlation differences between two Fisher transformed Pearson regression coefficients..

1.5 Machine learning

Another application focuses on using the advanced ML methods for automatic disease diagnosis and prognosis, due to their main virtue of modelling high-dimensional neuroimaging data. This approach can be categorized into two phases according to time and the computational hardware development (e.g., GPU). During the first phase, researchers leveraged conventional ML models, such as kernel machines (e.g., SVM) and graphical models (e.g., Bayesian network), for individualized disease diagnosis. It was widely applied to several neurodegenerative diseases and obtained promising performances for certain tasks, such as diagnosis of AD (Rathore et al., 2017). At that time, neural network was also in the field but did not attract so much attention as today. The turning point of neural network came until 2009, when researchers obtain impressive performance on the classification tasks based on the ImageNet dataset (Deng et al., 2009). This was the beginning of second phase for early dementia diagnosis. A large body of studies has looked at the potential of DL methods, most often the convolutional neural network (CNN), for instance, for AD classification in the very recent years.

Although no clear separation of the two phases, researchers usually refer the traditional algorithms, such as SVM and RF, as conventional ML methods. These methods are limited in their ability to process natural data in their raw form and demand hand-craft feature engineering. Whereas, DL has the ability to learn the data with intermediate feature representation, which automatically and autonomously extract low-to-high level features. With the huge algorithm advance and also hardware computational power improvement (e.g., GPU), nowadays is the gold rush era of DL. DL conversely demands a huge appetite of data and computational power (LeCun, Bengio, and Hinton, 2015).

In this section, we briefly introduce these techniques. Again, for the readers who seek for more details on the related topics, please refer to (Bishop, 2009) about conventional ML and (Goodfellow et al., 2016) about DL.

1.5.1 Conventional machine learning

A large number of conventional ML algorithms was firstly introduced in the context of dementia classification. Here, we present the main algorithms used in the field.

1.5.1.1 Support vector machine

Support vector machines (SVM) is a popular kernel machine algorithm because of its robustness to high dimensional data and to the overfitting problem. The mechanism of SVM is to find an optimal separating hyperplane that maximizes the margin between two classes. Apart from the linear classification task, SVMs can be used for a non-linear classification by means of the so-called kernel trick. The kernel functions are used to map the original data (linear/nonlinear) into a higher dimensional space with view to making it linearly separable. Different types of kernels can be applied in this case. When the dimensionality is high compared to the number of subjects, like in the case of neuroimaging studies, a linear kernel is a natural choice, as non-linear kernels would have the effect of transforming the data into an even higher dimensional space.

1.5.1.2 Logistic regression

Logistic regression (LR) is another widely used model in the context of classification. It models the relationship between the categorical dependent variable (e.g., group labels for AD and CN) and one or more independent variables (i.e., the extracted features). This approach can be seen as a special case of GLM, or of linear regression, but with the two major distinct properties. First, the conditional distribution of LR is a Bernoulli distribution rather than a Normal distribution. Secondly, it outputs the probabilities restricted to (0,1) through the logistic distribution function, rather than the outcomes themselves.

With its simple implementation, LR was adopted in the task of AD classification (Desikan et al., 2006). However, it exists evident drawbacks. First, the assumption of linearity between the dependent and independent variables is not always valid. Secondly, it is sensitive to multicollinearity and outliers. Lastly, LR does not provide accurate results with high dimensional data. In that case, it can be regularized with different types of penalties (e.g., the l_1 and l_2 norm) in order to prevent overfitting.

1.5.1.3 Random forest

Random forest (RF) is a typical representative of the ensemble learning method. It outputs the final decision by constructing a multitude of individual trees at training time (Ho, 1995). RFs have also been used, although not as frequently as other approaches, for AD classification (see (Rathore et al., 2017) for details). Most of the studies adopted the voxel-based approach, which would take decisions at the voxel level, resulting in a high computational cost.

More generally, ensemble learning approaches can also be adopted with different weak classifiers. For instance, in (Farhan, Fahiem, and Tauseef, 2014), a bunch of different classifiers (e.g., SVM, multilayer perceptron and decision trees) was used and a majority voting was followed to provide a classification accuracy of 94% for AD vs CN classification.

1.5.2 Deep learning

DL has become more and more popular in the very recent years and has been applied to various fields, including medical imaging. This section introduces the basic concepts regarding the key aspects of DL, including the main building layers of CNN, classical CNN architectures and methods to tackle the overfitting problem. Readers should feel free to skip this section given their background and knowledge. Conversely, for more details, see (Goodfellow et al., 2016).

1.5.2.1 Main building layers of CNN

CNNs are the most widely used type of network for computer vision and image analysis. A CNN is made of an input and an output layer, as well as different hidden layers. The hidden layers typically include convolutional layers, pooling layers, activation functions and fully connected (FC) layers.

The convolutional layer is the core building block of a CNN. It acts as an automatic feature extractor (on the contrary, conventional ML methods would typically use hand-craft feature extraction or selection). Convolutional layers apply learnable filters to all available receptive fields with a convolutional operation. A filter or kernel is a 2D (or 3D for MRI) matrix of weights. A receptive field is a local patch of the input image, of the same size as the filter. The filter is convolved with all the local receptive fields. The application of a given filter to the whole input image generates a feature map or activation map. All the feature maps are then stacked to constitute the output volume of a convolutional layer. Several hyperparameters (number of filters, stride size and padding size) control the size of the output volume (see (Dumoulin and Visin, 2016) for more details).

Another building block of CNNs is the pooling layer, which reduces the dimensionality of the feature maps. The pooling layer combines the outputs of a cluster of neurons of the current layer into a single neuron in the next layer (Ciresan et al., 2011; Krizhevsky, Sutskever, and Hinton, 2012). Pooling can be of different types, such as max, average and sum pooling (Scherer, Müller, and Behnke, 2010).

To learn a mapping between the adjacent convolutional layers, one applies activation functions to the output volume of each convolutional layer. The rectified linear unit (ReLU) is the most common activation function and ensures a sparse and non-linear representation (Glorot, Bordes, and Bengio, 2011; Krizhevsky, Sutskever, and Hinton, 2012; Nair and Hinton, 2010). However, ReLU can be fragile during backpropagation. Indeed, the fact that ReLU sets all negative values to be zero can cause the problem of gradient vanishing or dying ReLU. If this happens, the gradient flowing through the unit will be forever zero during backpropagation. One alternative, leaky ReLU, can overcome this drawback by introducing a small negative slope (e.g. 0.01), thus allowing a small positive gradient when the unit is not active (Maas, Hannun, and Ng, 2013).

FC layers learn the relationship between the features, extracted by previous convolutional and pooling layers, and the target (in our case the patient's diagnosis). In a FC layer, all the neurons in the current layer are connected to all the neurons in the previous layer. The output volumes (one for each feature map) from the previous convolutional layers are first flattened and then fed as input to the FC. For a n-class classification problem, the output of the last FC layer is composed of n neurons which values indicate membership to a given class. This can be transformed into n probabilities by using a softmax function on the outputs (Goodfellow et al., 2016).

The loss function is used to measure the difference between the predicted and true labels. Cross entropy loss, measuring the distance between the output distribution and the real distribution, is widely used in classification tasks (Boer et al., 2005). Other loss functions were also discussed in the literature, such as mean squared error (MSE) loss and hinge loss (see (Janocha and Czarnecki, 2017) for details).

The weights and biases of the network are learned using an optimization algorithm, such as the stochastic gradient descent (SGD). Most often, backpropagation is used to successively update the weights of the different layers.

1.5.2.2 Classical CNN architectures

Several CNN architectures have become classical, often due to their performance on the ImageNet Large Scale Visual Recognition Challenge (ILSVRC): a benchmark in object category classification and detection on hundreds of object categories and millions of images (Deng et al., 2009). These architectures were originally designed for 2D natural images. However, some of them have been adapted to the applications of MRIs.

Before the ILSVRC that began in 2010, Yann Lecun proposed LeNet-5 to recognize handwritten digits from the MNIST database (Lecun et al., 1998). This network includes seven layers: two convolutional layers associated with pooling layers, followed by three FC layers.

In 2012, AlexNet (Krizhevsky, Sutskever, and Hinton, 2012) significantly outperformed all the prior competitors of the ILSVRC, reducing the top-5 error from 26% to 15.3%. The network went deeper than LeNet-5, with more filters per layer. It consisted of five convolutional layers with decreasing filter size (11x11, 5x5 and 3x3) and three FC layers.

The runner-up at ILSVRC 2014 was VGGNet (Simonyan and Zisserman, 2014), which consists of 16 convolutional layers. It was appealing because of its uniform architecture, including only 3x3 convolutional filters cross the entire architecture. One of the main conclusion of this architecture is that using many small filters of size 3x3 is more efficient than using only a few filters of bigger size. The winner of that year was GoogleNet or Inception V1 (Szegedy et al., 2015). It went deeper (22 layers) and achieved a top-5 error rate of 6.67%. This architecture was inspired by LeNet-5 and implemented a novel element called the inception layer. The idea behind the inception layer is to convolve over larger receptive fields, but also keep a fine resolution based on smaller receptive fields. Thus, different filter sizes (from 1x1 to 5x5) were used in the same convolutional layer.

ILSVRC 2015 was won by the Residual Neural Network (ResNet) (He et al., 2016) with a top-5 error rate of 3,57%. ResNet includes over a hundred layers by introducing a novel architecture with shortcut connections that perform identity mapping and heavy batch normalization. Such shortcut connections make the deep residual nets easier to optimize than their counterpart “plain” nets.

DenseNet was presented at ILSVRC 2016 (Huang et al., 2017). It introduces the so-called dense block: each layer receives the outputs of all previous layers as input. The underlying assumption of dense connectivity is that each layer should have access to all the preceding feature maps and this “collective knowledge” therefore helps to improve the performance. In the same way than ResNet, dense connectivity allows the construction of very deep CNNs, such as DenseNet-264 which consists of 264 layers.

1.5.2.3 Methods to deal with overfitting

Neuroimaging datasets of AD patients are usually of relatively small size (typically a few hundreds of samples) compared, for instance, to those in computer vision (typically several million). DL models tend to easily overfit when trained on small samples due to the large number of learnt parameters (Goodfellow et al., 2016). Here, we summarize the main strategies to alleviate overfitting.

Data augmentation aims at generating new data samples from the available training data (Perez and Wang, 2017). It can be categorized into: i) transformation methods, which apply a combination of simple transformations (e.g. rotation, distortion, blurring and flipping) on the training data and ii) data synthesis methods, which aim to learn the training distribution to then generate new samples. Data synthesis often relies on autoencoders (AE) (Bourlard and Kamp, 1988; Hinton and Zemel, 1994; Yann, 1987) and Generative Adversarial Networks (GANs) (Goodfellow, 2016).

Dropout randomly and independently drops neurons, setting their output value to be zero along with their connections (Srivastava et al., 2014). This aims to make the network less complex and thus less prone to overfitting.

Another approach involves a regularization of the weights which makes the model less complex. This enhances the generalizability of the model. In DL, a common regularization is weight decay, where the updated weights are regularized by multiplying by a factor slightly smaller than 1 (Krogh and Hertz, 1992).

Batch normalization is a procedure which normalizes the input of a given set of layers (the normalization is done using the mean and standard-deviation of a batch, hence the name) (Ioffe and Szegedy, 2015). This procedure acts as a regularizer, in some cases eliminating the need for dropout (Ioffe and Szegedy, 2015). In addition, it helps battle against the gradient explosion phenomenon and allows using much higher learning rates and being less careful about initialization (Panigrahi, Chen, and C. Jay Kuo, 2018).

Transfer learning is a broadly defined terminology. In general, it consists in using a model trained on a given task, called the source task (e.g. ImageNet classification task or unsupervised learning task), in order to perform a target task (e.g. AD classification). Here, we introduce two transfer learning approaches that have been used in the context of AD classification. The first one is based on performing unsupervised learning before the supervised learning on the task of interest. It is supposed to be useful when one has limited labeled data but a larger set of unlabeled data. In that case, the most common approach is to use an AE (Yann, 1987). Strictly speaking, the AE is made of two parts: an encoder layer and a decoder layer. Generally, several AEs are stacked, the resulting being called stacked AE, but which we will refer to as AE for the sake of simplicity. The encoder learns to

compress the original data and produces a representation, the decoder then reconstructs the input using only this representation. An illustration of AE is shown in Figure 1.8. The weights and biases of the target network (e.g. CNNs) are then initialized with those of the encoder part of AE, which should provide a better initialization. The second approach involves transferring a model trained on ImageNet to the problem of classification of AD. As for the AE, the weights and biases of the target network are initialized with those of the source network. The idea behind is that random weight initialization of DL models may place parameters in a region of the parameter space where poor generalization occurs, while transfer learning may provide a better initialization (Erhan et al., 2010).

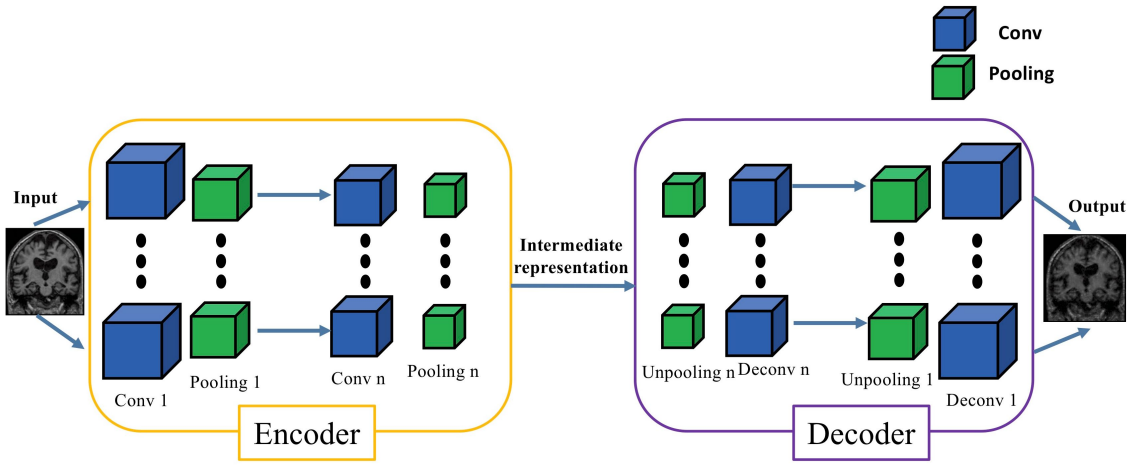

Figure 1.8: For the n-th AE, the encoder part is made of one convolutional layer (Conv n), one pooling layer (Pooling n) and one activation function, sequentially. Correspondingly, the decoder part consists of one activation function, one unpooling layer (Unpooling n) and one deconvolutional layer (Deconv n), sequentially. The n AEs's encoder and decoder parts are separated and then stacked to construct the final stacked AE. This layer-wise fashion ensures that the output of the former AE's encoder/decoder connects as input for the next AE's encoder/decoder. The intermediate representation provides a reduced representation of the data.

Early Stopping consists in stopping the learning process at an earlier point. It aims to determine the number of epochs (or iterations) at which the network should be stopped before being severely overfitted. For instance, one can select the model parameters corresponding to the lowest validation error rather than the last updated parameters. Various other stopping criterions have been proposed (Prechelt, 2012; Yao, Rosasco, and Caponnetto, 2007; Zhang and Yu, 2005).

1.5.3 Validation

1.5.3.1 Cross-validation

Cross-validation aims at assessing how the trained model will generalize to an independent data set. Alternatively stated, it consists of applying the model trained on a training data (from which the model learns) to the unseen dataset (test data, where the model is evaluated), while keeping the bias of this estimation as small as possible. In the application of neuroimaging and ML, it is critical to perform a proper cross-validation. However, data leakage (Rathore et al., 2017; Kriegeskorte et al., 2009), the use of information coming from the test set during the training phase, still occurred in a considerable proportion of peer-reviewed papers in the literature.

Different strategies may be adopted according to the algorithm you choose. In the case of conventional ML models, researchers have addressed the importance of the proper way for the optimization of model hyperparameters (e.g., the C parameter of SVM, controlling how much you want to avoid misclassifying each subject). Recent cross-validation guidelines, highly demanding an inner loop of cross-validation, or nested cross-validation, was proposed in (Varoquaux et al., 2017). Moreover, bad practices due to this can be witnessed in the literature, where this step has not been properly followed (Querbes et al., 2009; Wolz et al., 2011), leading to over-optimistic results, as presented in (Eskildsen et al., 2013; Maggipinto et al., 2017). On the other hand, the cross-validation in DL seems more tricky. First, unlike conventional ML models which have limited hyperparameter for optimizing, DL models have a huge number of hyperparameters for tuning, including both model architecture hyperparameters (e.g., number of layers) and training hyperparameters (e.g., learning rate). Due to the limitation of computational power and time, one can not try each combination of these hyperparameters in an exhaustive manner. Moreover, the need of an independent test dataset is more urgent in DL because the process of hyperparameter optimization could easily contaminate the so-called test dataset, which is actually the validation dataset in many studies. Accordingly, the data leakage problem flooded seriously in DL and cautions need to be advocated. See the State of the art section in Chapter 5 for details.

1.5.3.2 Performance metrics

Different metrics are used to quantify the performance of a trained model. In the context of a binary classification, accuracy, sensitivity and specificity are most often used. In this setting, we introduce the following definitions:

- True positive (TP): number of instances that are correctly identified;

- False positive (FP): number of instances that are incorrectly identified;
- True negative (TN): number of instances that are correctly rejected;
- False negative (FN): number of instances that are incorrectly rejected.

$$sensitivity = \frac{TP}{TP + FN}$$
$$specificity = \frac{TN}{TN + FP}$$
$$accuracy = \frac{TP + TN}{TN + FP + TP + FN}$$

Another metric commonly used is the area under the receiver operating characteristic curve (AUC), which quantify the performance measurement for classification problem at various thresholds. It tells how much the model is capable of distinguishing between classes.

Nevertheless, in the domain of neuroimaging, the collected datasets are often imbalanced, meaning that the majority group has much more subjects than the minority group. Data imbalance distorts the metric of accuracy. Alternatively, we encourage to use balanced accuracy, which is the average of the sensitivity and the specificity. It is less affected by unbalanced data. Unfortunately, through our literature review, which will be detailed in Chapter 4 and 5, we have found that, often, only a subset of these metrics is presented, most often the accuracy, leading to biased performances.

Another question is how to objectively compare the performances across studies. Many papers claim superiority of an approach with respect to another, based on either a slightly quantitative improvement of accuracy (e.g., 1 to 3 percentage) or a statistical test (e.g., t-test). However, such claims are often inadequate because: i) a few percentage point difference might be related to the specific sample of subjects at hand and not generalizable to the whole population, and ii) standard hypothesis tests are not valid in the context of cross-validation (Nadeau and Bengio, 2000). Instead, a good practice is to report the empirical variance for the performances. However, one should keep in mind that such approach underestimates the true variance, since, as exposed in (Nadeau and Bengio, 2000; Bengio and Grandvalet, 2004), there is no unbiased estimate of the variance for cross-validation.

1.6 Neuroimaging biomarkers of C9orf72 diseases at presymptomatic stage

FTLD and ALS are neurodegenerative diseases sharing common genetic causes, the most frequent being the C9orf72 gene (DeJesus-Hernandez et al., 2011; Renton et al., 2011), accounting for between 13% and 26% of genetic cases (Mahoney et al., 2012a). The clinical phenotype associated with C9orf72 repeat expansion could be bvFTD, ALS, FTD-ALS or less commonly PPA (Snowden et al., 2012). The presymptomatic stage can be defined as the stage during which pathological changes accumulate in the absence of any symptoms, but the underlying pathology may become active already. Thus, robust biomarkers are highly demanded in order to track and monitor the disease trajectory, especially at the presymptomatic stage. From a clinical trial perspective, presymptomatic carriers of genetic mutation represent the optimal target population for the development of new disease-modifying treatments against C9orf72 carriers. It is now well-known that neurodegenerative diseases cause biological and morphological changes decades before symptom onset (Bateman et al., 2012); the presymptomatic stage represents the best time for therapeutic interventions because it allows stopping the neurodegenerative process before irreversible brain damage occurs. Thus, establishing the chronology of structural and microstructural changes during the presymptomatic stage is crucial to identify markers of disease progression and monitor the effect of treatments.

Researchers have tried to establish the blueprint of neuroimaging-based biomarkers at the presymptomatic phase (Rohrer et al., 2015; Walhout et al., 2015; Lee et al., 2016; Cash et al., 2017; Papma et al., 2017; Popuri et al., 2018; Bertrand et al., 2017; Papma et al., 2017; Jiskoot, 2018). The modalities involved among these studies are T1w MRI (Rohrer et al., 2015; Walhout et al., 2015; Lee et al., 2016; Cash et al., 2017; Papma et al., 2017; Popuri et al., 2018), diffusion MRI (Lee et al., 2016; Bertrand et al., 2017; Papma et al., 2017) and functional MRI (Lee et al., 2016). Moreover, recent preclinical development of disease-modifying drugs, such as antisense oligonucleotides that target mutant RNA, offer promising therapeutic perspectives in C9orf72 disease. However, no robust biomarkers of genetic FTLD exist yet to i) stratify correctly into treatment groups based on the pathological subtypes, ii) assess the diseases severity and progression, iii) discriminate between the disease stages (e.g., presymptomatic stage or late symptomatic stage) and iv) finally to track and monitor disease progression and the therapeutic treatment response. Please refer to (Floeter and Gendron, 2018; Jiskoot, 2018) for more details on biomarkers of C9orf72 disease.

1.7 Classification of AD based on neuroimaging data

Early and accurate diagnosis of AD is difficult, partly because of the large number of measures involved, such as neuroimaging and fluid biomarkers or neuropsychological tests. The ability of ML algorithms to learn relevant patterns within the data is expected to enable accurate automatic classifications and predictions.

It has been suggested that the neuroimaging-based biomarkers can be valuable to track the characteristics of neurodegeneration, as measured with structural MRI (Frisoni et al., 2010). Further alterations quantified by other modalities were also discussed (Agosta et al., 2012). However, the subtle changes at the early stages of AD are difficult to distinguish. Thus early and accurate identification of patients with AD remains challenging. In recent years, a large body of papers has been published on neuroimaging and machine learning (ML) techniques for automatic classification of AD. Depending on the stages that are considered, different classification tasks can be formulated.

- i) AD vs CN: to classify patients with AD dementia (AD) from cognitively normal subjects (CN);
- ii) MCI vs CN: to classify subjects with mild cognitive impairment from cognitively normal subjects;
- iii) pMCI vs sMCI: to distinguish the progression of MCI subjects to AD, meaning to classify subjects that will progress to AD (denoted as pMCI) in the future (e.g. in 12, 18 or 36 months) from those who will remain stable (denoted as sMCI);
- iv) AD vs MCI: to classify patients with AD dementia from the MCI subjects;
- v) multiclass classification: to classify subjects into one of three or more classes.

A large majority of studies (see (Magnin et al., 2009; Vemuri et al., 2008; Klöppel et al., 2008) for example) examined the task of AD vs CN and achieved encouraging but varied performances, generally ranging from 76% to 95% of accuracy for conventional ML methods (see review paper (Rathore et al., 2017) for details), from 80% to 100% for DL methods. The distinguishable pattern between AD and CN is evident and easily detectable in MRI and cognitive tests, thus the translation to clinical practice from this task is limited, but it could be useful to reinforce the confidence in the diagnosis.

Other studies have then focused on discriminating MCI subjects from cognitively normal subjects (MCI vs CN). The difficulty of this task is the heterogeneity of the MCI state, which means that a MCI subject could possibly develop AD but also other neurodegenerative diseases, or remain stable as MCI or even revert back to the CN stage. Therefore, this task may not be very relevant to predict AD directly, but a large number of papers has performed this task. The obtained classification accuracy typically ranges from 65% to 85% for conventional ML, even though a few studies reach over 90% (Rathore et al., 2017), and from 62% to 98% for DL.

A more challenging task is to predict the progression of MCI subjects to AD: pMCI vs sMCI. In the literature, the classification perforances varied across studies, ranging from 62% to 83% for conventional ML (Rathore et al., 2017) and from 62% to 83% for DL. Indeed, a few studies achieved higher accuracies (e.g., Cabral et al., 2015). Nevertheless, such results must be taken with caution since some of these studies involved i) small samples (Misra, Fan, and Davatzikos, 2009; Cabral et al., 2015), ii) imbalanced groups and iii) inadequate details on the cross-validation procedure, which may lead to over-optimistic results.

The task of AD vs MCI was also presented in the literature (see (Wee et al., 2013; Lillemark et al., 2014) as example). The performances across papers differ, ranging from 70% to 90% for conventional ML (Rathore et al., 2017) and from 67% to 100% for DL. However, with similar limitations, these performances may be biased and over-optimistic.

Apart from the binary classification tasks mentioned above, researchers have also looked at multiclass classification. Generally, this is more challenging and several papers used DL, most often convolutional neural networks (CNN), for that purpose. The performances vary according to the specific tasks and the validity of their methodology (see (Islam and Zhang, 2018; Valliani and Soni, 2017) as example).

The review papers, such as in (Rathore et al., 2017) aid to get an overview of the state of the art. In the current PhD, we performed a systematic and exhaustive literature search regarding classification of AD using conventional ML with diffusion MRI (see Chapter 4) and CNNs with anatomical MRI (see Chapter 5). According to the high accuracies obtained in the literature, one may question how much confidence we can put on the reported accuracies? One step further, how far are we away from the translation to clinical practice? One will see in the results of our literature reviews that the reported accuracies in the literature are not directly comparable across studies. Moreover, the high accuracies, sometimes nearly a perfect accuracy, are not always reliable due to the existence of bad practices.

1.8 Datasets

In this section, we briefly present the datasets which were used in this dissertation.

1.8.1 PREVDEMALS dataset for C9orf72 carriers

PREVDEMALS is a national multicentric study cohort which enrolled patients and their first-degree relatives of C9orf72 mutation carriers from 48 families. This study was approved by the Comité de Prévention des Personnes Ile de France VI of the Hôpital Pitié-Salpêtrière, and written informed consent was obtained from all participants.

The aim of this study is to identify biomarkers of this disease at the presymptomatic stage. All the patients underwent an anatomical MRI (T1w MRI), diffusion MRI (both single-shell and multi-shell diffusion MRI), functional MRI, FLAIR MRI, arterial spin labeling (ASL) MRI, FDG PET scans and cognitive tests. We used only the T1w and diffusion MRI data in this dissertation.

1.8.2 Public databases for AD

Three publicly available datasets have been mainly used for the study of AD: the Alzheimer's Disease Neuroimaging Initiative (ADNI), the Australian Imaging, Biomarkers and Lifestyle (AIBL) and the Open Access Series of Imaging Studies (OASIS). In the following, we briefly describe these datasets and provide explanations on the diagnosis labels provided. Indeed, the diagnostic criteria of these studies differ, hence there is no strict equivalence between the labels of ADNI and AIBL, and those of OASIS.

The ADNI study is composed of 4 cohorts: ADNI-1, ADNI-GO, ADNI-2 and ADNI-3. These cohorts are dependent and longitudinal, meaning that a given patient may be examined at multiple points in time and that different cohorts may include the same patients. Many modalities are included in these datasets including clinical, genetic, imaging (MRI and PET) data, as well as biospecimen analyses such as blood, urine and cerebrospinal fluid (CSF). Diagnosis labels are given by a physician after a series of tests (Petersen et al., 2010). The existing labels are:

- AD (Alzheimer's disease): mildly demented patients;
- MCI (mild cognitive impairment): patients in the prodromal phase of AD;
- NC (normal controls): elderly control participants;

- SMC (significant memory concern): participants with cognitive complaints and no abnormal neuropsychological findings. The designations SMC and subjective cognitive decline (SCD) are equivalently found in the literature.

Since the ADNI-GO and ADNI-2 cohorts, new patients at the very beginning of the prodromal stage have been recruited (Aisen et al., 2010), hence the MCI label has been split into two labels:

- EMCI (early MCI): patients at the beginning of the prodromal phase;
- LMCI (late MCI): patients at the end of the prodromal phase (similar to the previous label MCI of ADNI-1).

The AIBL project includes a longitudinal cohort of patients. Several modalities are present in the dataset, such as clinical and imaging (MRI and PET) data, as well as the analysis of blood and CSF samples. As in ADNI, the diagnosis is given according to a series of clinical tests (Ellis et al., 2010; Ellis et al., 2009) and the existing labels are AD, MCI and NC.

The OASIS project includes three cohorts, OASIS-1, OASIS-2 and OASIS-3. The first cohort OASIS-1 is only cross-sectional, whereas the other two are longitudinal. Available data is far more limited than in ADNI with only few clinical tests and imaging data (MRI and PET only in OASIS-3). Diagnosis labels are given only based on the clinical dementia rating (CDR) scale (Marcus et al., 2007). Two labels can be found in the OASIS-1 dataset:

- AD, which corresponds to patients with a non-null CDR score. This class gathers patients who would be spread between the MCI and AD classes in ADNI. A subdivision of this class is done based on the CDR, the scores of 0.5, 1, 2 and 3 representing very mild, mild, moderate and severe dementia, respectively;
- Control, which corresponds to patients with a CDR of zero. Unlike in ADNI, some of the controls are younger than 55.

In many datasets, the label related to the stability of the diagnosis (i.e. sMCI and pMCI) is not given in the baseline data and must be deduced from the longitudinal data. The way these labels were defined in our study is described in the Materials section and its implementation is available at: `https://gitlab.icm-institute.org/aramislab/AD-ML`.

Note that some of the image preprocessing steps may have already been performed by the dataset provider. However, different preprocessing pipelines can be run on the same dataset, so the name of the dataset does not provide sufficient information to know which methods have been applied to the data. It is thus crucial to describe all the preprocessing steps applied to the subjects' images.

Chapter 2

Early Cognitive, Structural, and Microstructural Changes in Presymptomatic C9orf72 Carriers Younger Than 40 Years

This chapter has been published as a journal article on *JAMA Neurology* (Bertrand et al., 2017):

- Bertrand, A., **Wen, J. (Co-first author)**, Rinaldi, D., Houot, M., Sayah, S., Camuzat, A., Fournier, C., Fontanella, C., Routier, A., Couratier, P., Pasquier, F., Habert, M., Hannequin, D., Martinaud, O., Caroppo, P., Levy, R., Dubois, B., Brice, A., Durrleman, S., Colliot, O., Le Ber, I. Early Cognitive, Structural, and Microstructural Changes in Presymptomatic C9orf72 Carriers Younger Than 40 Years, **JAMA neurology**, 75(2), pp.236-245. https://hal.inria.fr/hal-01654000/document.

2.1 Abstract

IMPORTANCE Presymptomatic carriers of chromosome 9 open reading frame 72 (C9orf72) mutation, the most frequent genetic cause of frontotemporal lobar degeneration and amyotrophic lateral sclerosis, represent the optimal target population for the development of disease-modifying drugs. Preclinical biomarkers are needed to monitor the effect of therapeutic interventions in this population.

OBJECTIVES To assess the occurrence of cognitive, structural, and microstructural changes in presymptomatic C9orf72 carriers.

DESIGN,SETTING,AND PARTICIPANTS The PREVDEMALS study is a prospective, multicenter, observational study of first-degree relatives of individuals carrying the C9orf72 mutation. Eighty-four participants entered the study between October 2015 and April 2017; 80 (95%) were included in cross-sectional analyses

of baseline data. All participants underwent neuropsychological testing and magnetic resonance imaging; 63 (79%) underwent diffusion tensor magnetic resonance imaging. Gray matter volumes and diffusion tensor imaging metrics were calculated within regions of interest. Anatomical and microstructural differences between individuals who carried the C9orf72 mutation (C9+) and those who did not carry the C9orf72 mutation (C9-) were assessed using linear mixed-effects models. Data were analyzed from October 2015 to April 2017.

MAIN OUTCOMES AND MEASURES Differences in neuropsychological scores,gray matter volume, and white matter integrity between C9+ and C9- individuals.

RESULTS Of the 80 included participants, there were 41 C9+ individuals (24[59%] female; mean [SD] age, 39.8 [11.1] years) and 39 C9- individuals (24 [62%] female; mean [SD] age, 45.2 [13.9] years). Compared with C9- individuals, C9+ individuals had lower mean (SD) praxis scores (163.4 [6.1] vs 165.3 [5.9]; P = 0.01) and intransitive gesture scores (34.9 [1.6] vs 35.7 [1.5]; P = 0.004), atrophy in 8 cortical regions of interest and in the right thalamus, and white matter alterations in 8 tracts. When restricting the analyses to participants younger than 40 years, compared with C9- individuals, C9+ individuals had lower praxis scores and intransitive gesture scores, atrophy in 4 cortical regions of interest and in the right thalamus, and white matter alterations in 2 tracts.

CONCLUSIONS AND RELEVANCE Cognitive, structural, and microstructural alterations are detectable in young C9+ individuals. Early and subtle praxis alterations, underpinned by focal atrophy of the left supramarginal gyrus, may represent an early and non-evolving phenotype related to neurodevelopmental effects of C9orf72 mutation. White matter alterations reflect the future phenotype of frontotemporal lobar degeneration/amyotrophic lateral sclerosis, while atrophy appears more diffuse. Our results contribute to a better understanding of the preclinical phase of C9orf72 disease and of the respective contribution of magnetic resonance biomarkers.

2.2 Introduction

Frontotemporal lobar degeneration (FTLD) and amyotrophic lateral sclerosis (ALS) are neurodegenerative dis- eases with common genetic causes, the most frequent being a GGGGCC repeat expansion in the chromosome 9 open reading frame 72 (C9orf72) gene (DeJesus-Hernandez et al., 2011; Renton et al., 2011). This expansion may lead to a loss of C9orf72 function and causes abnormal neuronal aggregation of nuclear RNA foci, dipeptides repeats (DPR), and transactive response DNA-binding protein 43 (TDP-43) inclusions (Cruts et al., 2013). Recent preclinical development of disease-modifying drugs, such as antisense oligonucleotides that

tar-get mutant RNA, offer promising therapeutic perspectives in C9orf72 disease (Donnelly et al., 2013; Jiang et al., 2016).

Presymptomatic carriers of genetic mutation represent the optimal target population for the development of new disease-modifying treatments against FTLD and ALS. It is now established that neurodegenerative diseases cause biological and morphological changes decades before symptom onset (Bateman et al., 2012); the presymptomatic stage represents the best time-window for therapeutic interventions, by allowing the possibility to stop the neurodegenerative process before irreversible brain damage. Establishing the chronology of structural and microstructural changes during the presymptomatic stage is thus crucial, in order to identify markers of disease progression and monitor the effect of treatments. Three studies (Lee et al., 2016; Rohrer et al., 2015; Walhout et al., 2015) have suggested that atrophy, studied with anatomical MRI, could be detected years before symptom onset in C9orf72 presymptomatic carriers, but were limited by the small number of participants. One study also detected alterations of white matter integrity, using diffusion MRI (Lee et al., 2016), but another failed to identify such changes (Walhout et al., 2015). The present work aims at assessing cognitive, structural and microstructural changes in a large cohort of asymptomatic C9orf72 carriers, in order to characterize the presymptomatic course of the disease and identify potential neuroimaging biomarkers of preclinical disease progression.

2.3 Material and Methods

2.3.1 Participants

Eighty-four individuals out of 48 C9orf72 families, all first degree relatives of C9orf72 mutation carriers, were enrolled in a national multicentric study (PrevDemAls) between 2015 and 2017.

At inclusion, asymptomatic status of participants was ascertained based on relative's interview, neurological examination and the normality of behavioral scales and neuropsychological scores, taking into account age and educational level. Neuropsychological tests are detailed in Supplementary A eMethod1. Two participants were excluded from the analysis because mild cerebellar syndrome or cognitive impairment were detected during the visit; two other participants were excluded because of incomplete MRI protocol. Eighty neurologically healthy participants were finally included in the analyses. The C9orf72 genetic status was determined by repeat-primed-PCR on lymphocytes DNA. Forty-one participants (C9+) carried a pathogenic expansion (>23 GGGGCC repeats); 39 participants without expansion (C9-) constituted the control group. Expected ages at onset of C9orf72

carriers were estimated by averaging the ages at onset of affected relatives, similarly to previous studies (Rohrer et al., 2015).

2.3.2 MRI acquisition

All MRI acquisitions were performed on a 3T MR system (Siemens Prisma 3T n= 64; Philips Achieva 3T n= 9; GE 3T n=7), in 3 imaging centers belonging to the harmonized national network of CATI (Centre d'Acquisition et de Traitement d'Images, cati-neuroimaging.com/) (Operto et al., 2016). CATI performs on-site visits for the setup of imaging protocols and regular follow-up. 3DT1 sequence parameters were similar for the 3 centers, while DTI sequence was performed in only one center (see Supplementary A eMethod2 for detailed sequence parameter). Systematic quality check of MR images were performed by CATI, using a dedicated software programme with quantitative and qualitative indices, allowing the check for 1) protocol consistency (MRI scanner, software version, type of reception coil, acquisition slab position, sequence parameters and sequence order); 2) presence and localization of artifacts (motion artifacts, spike artifacts, other); 3) overall image quality based on signal-to-noise ratio, contrast-to-noise ratio and intensity non-uniformity (Operto et al., 2016). Among the 80 MR dataset, 75 (94%) were considered of good quality and 5 (6%) of acceptable quality.

2.3.3 Anatomical MRI processing

FreeSurfer image analysis software 5.3 (`http://surfer.nmr.mgh.harvard.edu`) was used to process the T1-weighted images. The processing pipeline included non-uniformity and intensity correction, skull stripping, grey/white matter segmentation, reconstruction of the cortical surface, extraction of cortical ROI volumes using the Desikan atlas, and subcortical ROI volumes and total intracranial volume (TIV) using the aseg atlas. We used for analyses the normalized volume of each ROI, defined as NVROI = (TIVm.VROI)/TIV, where TIVm is the average total intracranial volume computed across all participants, which is constant, and VROI is the volume of the ROI. The role of the constant multiplicative factor TIVm is simply to preserve the order of magnitude of NVROI similar to that of VROI.

2.3.4 Diffusion MRI processing

All raw DWI volumes were aligned to the average b0 image with first 6 degrees of freedom (dof), to correct for head motion, and diffusion directions were appropriately updated (Leemans and Jones, 2009). A registration with 12 dof was

used to correct for eddy current distortions. These registrations were done using the FSL flirt tool (www.fmrib.ox.ac.uk/fsl). Field map image was used to correct for echo-planar imaging (EPI) induced susceptibility artifacts (Jezzard and Balaban, 1995) with the FSL prelude/fugue tools. DWI volumes were corrected for nonuniform intensity using ANTs N4 bias correction algorithm (Tustison and Avants, 2013). A single multiplicative bias field from the averaged b0 image was estimated (Jeurissen et al., 2014). The DWI datasets were up-sampled at 1mm in order to improve the registration between the T1-weighted image and the DWI. A diffusion tensor model was fitted at each voxel to calculate Fractional Anisotropy (FA), Mean Diffusivity (MD), Radial Diffusivity (RD) and Axial Diffusivity (AD) maps. White matter tracts were defined using the JHU white-matter tractography atlas (Mori et al., 2005), with a 25% probabilistic threshold. For each subject, the FA map was registered onto the JHU atlas template with the ANTs SyN algorithm (Avants et al., 2008). Then, the estimated non-linear deformation was applied to the parametric maps and we extracted, in each patient, the average values of DTI metrics (FA, MD, RD and AD) within each tract of the JHU atlas.

2.3.5 Statistical analysis

Statistical analyses were performed using R 3.4.0 (The R Foundation for Statistical Computing, Vienna, Austria) and GraphPad Prism 7.0 (La Jolla, CA, USA). Demographic characteristics and clinical tests were compared between groups using chi-squared test (for dichotomous and categorical variables) or Mann-Whitney test (for numerical variables). Structural and microstructural differences between carriers and non-carriers of the C9orf72 mutation were assessed using linear mixed-effects models. We used real age and group (i.e., mutation status) as fixed effects, and family membership as random effect, with the following model:

$$y_{ik}^{j} = \mu + \beta \times gender_i + \lambda \times age_i + \eta \times group_i + U_k + \epsilon_{ik}^{j}$$

where y_{ik}^{j} is the response of the j^{th} ROI for the i^{th} subject and the k^{th} family; $gender_i$, age_i and $group_i$ are the fixed effects; μ, β, λ and η are their estimated parameters; U_k is the random effect measuring the difference between the average response in the family and in the whole population; ϵ_{ik}^{j} is the random error.

2.4 Results

2.4.1 Participants

There were no statistical differences between C9+ and C9- subjects regarding age at evaluation and demographic characteristics (Table 3.1). In C9+ subjects, real age and expected years to onset were strongly correlated (Supplementary A eFigure 1, $p < 0.001$; $r^2 = 0.802$, Pearson correlation coefficient), with a mean estimated age of onset of 58.9 $\pm$ 4.9 years. C9+ subjects had significantly lower praxis score; this difference remained statistically significant in subjects $\leq$ 40-year-old, who were 25.4 $\pm$ 8.1 years to onset (165.2 $\pm$ 3.4 in C9+ vs. 167.6 $\pm$ 0.6 in C9-, p=0.036). Praxis score was significantly correlated with age in both C9+ and C9- (Fig. 2.1 B). When analyzing the subscores of praxis test, all were lower for the C9+ group, but statistical significance was reached only for the subscore of non-transitive gestures (Fig. 2.1 C); this difference remained statistically significant in subjects $\leq$ 40-year-old (35.0 $\pm$ 1.7 in C9+ vs. 36 $\pm$ 0 in C9-, p = 0.036). Lastly, the total recall score of the FCRT test was significantly lower in C9+ as compared to C9- (Fig. 2.1E), but with a large overlap of scores between the 2 groups (Fig. 2.1 F), and no significant difference among subjects $\leq$ 40-year-old (47 $\pm$ 1.3 in C9+ vs. 47 $\pm$ 1.4 in C9-, p = 0.08).

Characteristic	Mean(SD)		P Value
	C9-(n = 39)	C9+(n = 41)	
Demographic characteristics			
Age, y	45.2 (13.9)	39.8 (11.1)	0.08
<40 y, No. (%)	16 (41)	22 (54)	NA
Female, No. (%)	24 (62)	24 (59)	0.78
Right laterality, No. (%)	33 (85)	35 (85)	0.92
Expected time to onset, y	NA	19.3 (11.2)	NA
Familial phenotype, No. (%)			
FTLD	15 (38)	18 (44)	0.77
ALS	2 (5)	3 (7)	
Mixed	21 (54)	20 (49)	
Unavailable	1 (3)	0	
MMSE score (maximum, 30)	28.8 (1.5)	28.6 (1.3)	0.34
MDRS score			
Total score (maximum, 144)	141.5 (3.2)	141.4 (2.6)	0.54
Initiation (maximum, 37)	36.5 (1.3)	36.6 (1.1)	0.72
Concept (maximum, 39)	38.3 (1.2)	38.3 (1.1)	0.75
Attention (maximum, 37)	36.7 (0.8)	36.7 (0.6)	0.95
Construction (maximum, 6)	5.9 (0.2)	6.0 (0.0)	0.23
Memory (maximum, 25)	24.0 (1.4)	23.8 (1.6)	0.81
FBI	0.8 (1.8)	1.3 (2.6)	0.54
FAB score (maximum, 18)	16.8 (1.4)	17.1 (0.9)	0.39
Mini-SEA			
Emotion recognition test (maximum, 35)	29.9 (2.7)	29.8 (2.5)	0.73
Faux pas test (maximum, 30)	26.2 (4.7)	25.6 (3.5)	0.13
Praxis score			
Total score (maximum, 168)	165.3 (5.9)	163.4 (6.1)	0.01
Finger dexterity (maximum, 36)	35.5 (1.2)	35.4 (1.2)	0.57
Melokinetic apraxia (maximum, 24)	23.2 (1.5)	22.8 (2.3)	0.37
Nonrepresentational gestures (maximum, 36)	35.7 (0.9)	35.4 (1.2)	0.16
Intransitive gestures (maximum, 36)	35.7 (1.5)	34.9 (1.6)	0.004
Transitive gestures (maximum, 36)	35.2 (2.0)	34.9 (2.9)	0.79
Benson figure			
Copy (maximum, 17)	16.5 (0.8)	16.6 (0.6)	0.92
Recall (maximum, 17)	12.8 (2.2)	13.0 (2.5)	0.52
Free and cued recall test			
Free recall (maximum, 48)	35.6 (4.8)	32.9 (5.5)	0.06
Total recall (maximum, 48)	47.1 (1.5)	46.4 (1.5)	0.005
Delayed free recall (maximum, 16)	13.2 (2.1)	13.0 (2.2)	0.88
Delayed total recall (maximum, 16)	15.5 (1.8)	15.6 (0.9)	0.70
Boston naming test (maximum, 30)	27.2 (2.0)	27.2 (2.2)	0.93
Fluency tasks			
Categories (animals)	36.1 (10.3)	36.3 (7.1)	0.82
Letter (P)	24.7 (8.0)	23.5 (6.5)	0.23

Table 2.1: Study Group Characteristics. Abbreviations: ALS, amyotrophic lateral sclerosis; C9-, individuals without the C9orf72 mutation; C9+, individuals with the C9orf72 mutation; FAB, frontal assessment battery; FBI, Frontal Behavioural Inventory; FTLD, frontotemporal lobar degeneration ; MMSE, Mini-Mental State Examination; MDRS, Mattis dementia rating scale; NA, not applicable; SEA, Social Cognition and Emotional Assessment.

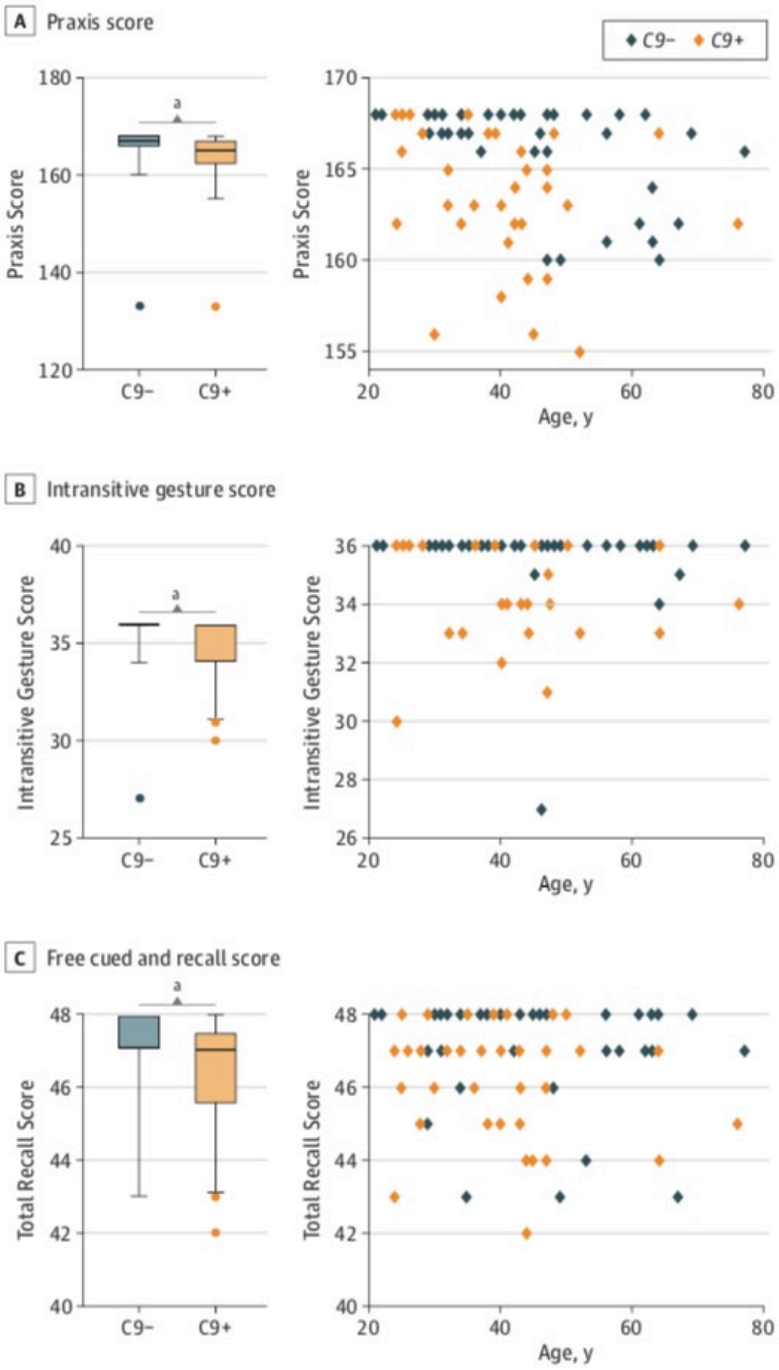

Figure 2.1: Early Cognitive Changes in C9orf72 Mutation Carriers. Outliers are presented as individual data points. The exact age of individuals is not provided to prevent individuals from identifying their mutation status.

2.4.2 Association of C9orf72 Mutation With Cortical Structures

C9+ participants showed diffuse cortical atrophy within the associative cortex, with a sparring of primary sensorimotor and visual cortex, frontobasal cortex, and superior temporal cortex (Figure 2.2A). After correction for multiple comparisons,

this association remained significant for 1 frontal, 3 inferior temporal, and 4 parietal ROIs (Figure 2.2B) (eTable 1 in the Supplementary A). In these 8 ROIs, we performed the same analyses restricted to participants younger than 40 years and found significant atrophy within the right caudal middle frontal cortex, left and right precuneus cortex, and left supramarginal cortex.

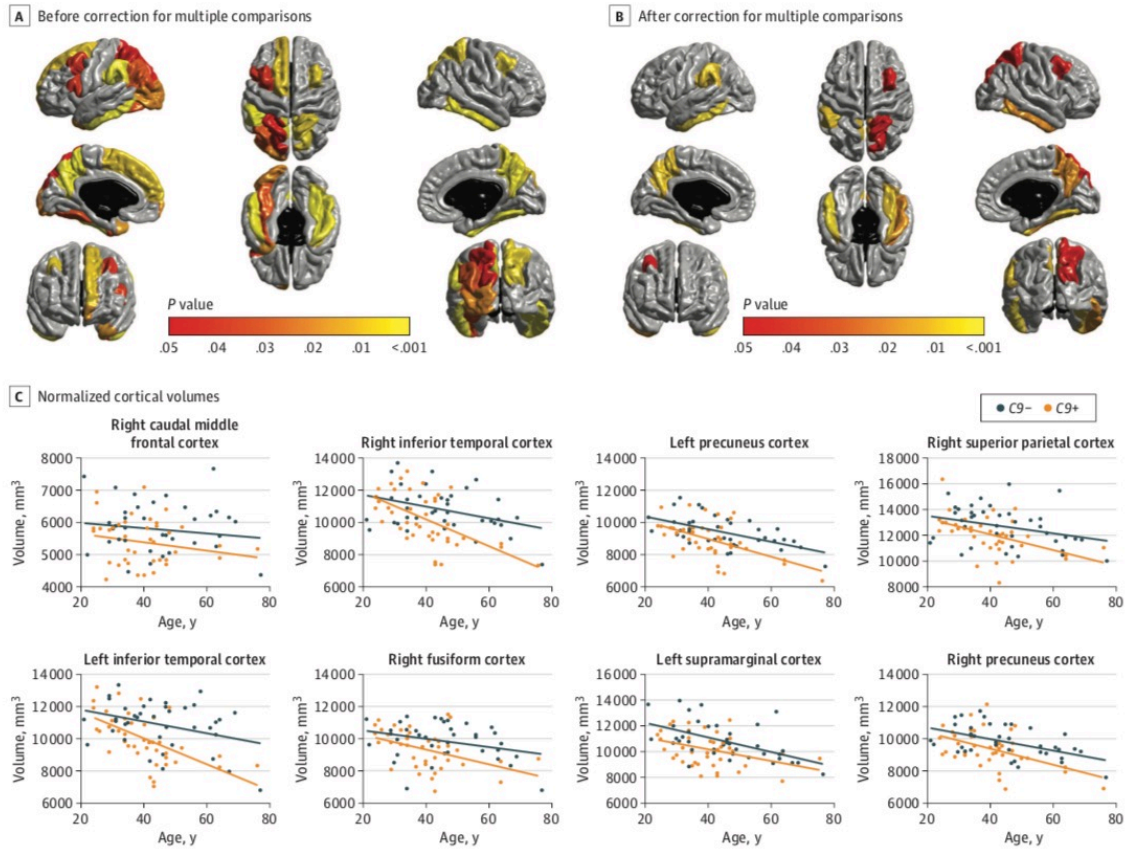

Figure 2.2: Cortical Atrophy in C9orf72 Mutation Carriers. Color-coded representation of P values corresponding to the association of C9orf72 mutation with the volume of cortical regions of interest before (A) and after (B) correction for multiple comparisons. C, Graphs of normalized cortical volumes as a function of age in individuals who carried the C9orf72 mutation (C9+) and individuals who did not carry the C9orf72 mutation (C9-). The exact age is not provided to prevent individuals from identifying their mutation status.

2.4.3 Association of C9orf72 Mutation With Subcortical Structures

C9+ participants showed significant atrophy in the left and right thalamus compared with C9- participants (Figure 2.3A). After correction for multiple comparisons, this association remained significant for the right thalamus (Figure 2.3B) (eTable 2 in the Supplementary A) and persisted when restricting the analysis to participants younger than 40 years.

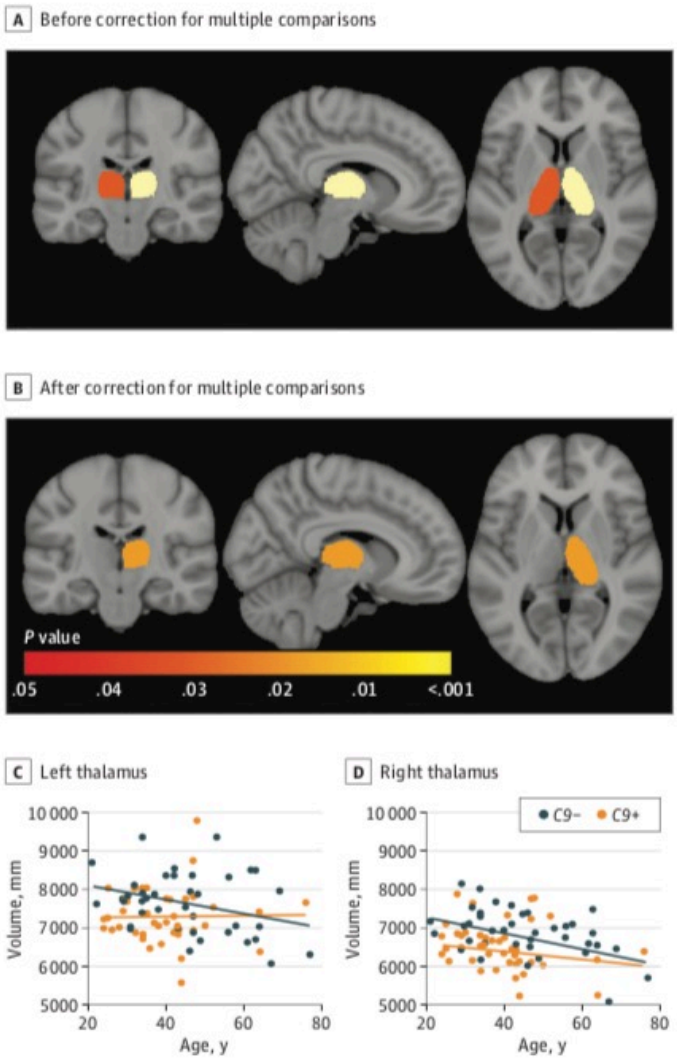

Figure 2.3: Subcortical Atrophy in C9orf72 Mutation Carriers. Color-coded representation of P values corresponding to the association of C9orf72 mutation with the volume of subcortical structures before (A) and after (B) correction for multiple comparisons. C, Graph of normalized thalamic volumes in the left thalamus as a function of age in individuals who carried the C9orf72 mutation (C9+) and individuals who did not carry the C9orf72 mutation (C9-). D, Graph of normalized thalamic volumes in the right thalamus as a function of age in C9+ and C9- individuals. The exact age is not provided to prevent individuals from identifying their mutation status.

2.4.4 Association of C9orf72 Mutation With White Matter Microstructure

C9+ participants showed diffuse alteration of white matter microstructure (i.e., decreased fractional anisotropy, increased mean diffusivity, axial diffusivity, and radial diffuivity), predominating in frontal regions and affecting corticospinal tracts bilaterally (Figure 2.4) (eTable 3 and eFigure 2 in the Supplementary A). Only for

this modality, we observed that the oldest C9+ participant was an outlier for some DTI metrics (eFigure 2 in the Supplementary A); to make sure that results were not driven by this outlier, we performed the same analyses without this participant and still found significant differences in 23 DTI metrics (instead of 27) within the same white matter tracts. After correction for multiple comparisons, 8 tracts remained significantly altered: the left corticospinal tract, the right anterior thalamic radiation, 4 tracts connected to the frontal lobes (i.e., forceps minor, bilateral inferior fronto-occipital fasciculus, and right superior longitudinal fasciculus), and 2 tracts connected to the temporal lobes (i.e., bilateral inferior longitudinal fasciculus). In these tracts, we performed the same analyses restricted to participants younger than 40 years and still found significantly increased radial diffusivity and decreased fractional anisotropy within the right anterior thalamic radiation and increased radial diffusivity within the right forceps minor.

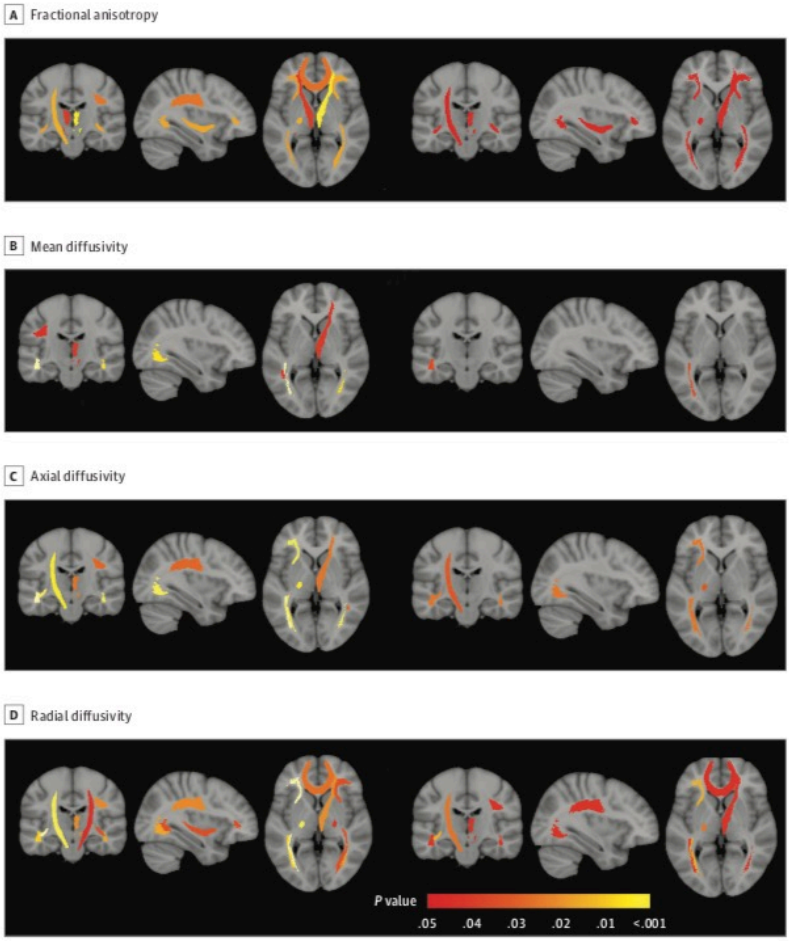

Figure 2.4: Alterations of White Matter in C9orf72 Mutation Carriers. Color-coded representation of P values corresponding to the association of C9orf72 mutation with the diffusion tensor magnetic resonance imaging scalars of white matter regions of interest, both before (left 3) and after (right 3) correction for multiple comparisons.

2.4.5 Correlation Between Structural Changes and Clinical Scores

We looked for possible correlations between the neuropsychological scores altered in C9+ participants (i.e., praxis, intransitive gestures, and free cued and recall test scores) and the markers of structural and microstructural alterations in C9+ participants (i.e., volume of cortical and subcortical regions and DTI metrics significantly altered in C9+ individuals after correction for multiple comparisons). No correlation was found between the 3 scores and structural or microstructural changes.

2.5 Discussion

Using a large cohort of presymptomatic C9orf72 carriers, this study reveals unexpected results. We show that cognitive, structural, and microstructural changes can be detected very early in C9+ individuals aged 20 to 40 years, corresponding to a mean (SD) time to expected onset of 25.4 (8.1) years. We also show that praxis score appears as the first cognitive do- main to be altered in young C9+ individuals. Lastly, we show that presymptomatic C9+ individuals display distinct patterns of atrophy and white matter alterations; cortico- subcortical atrophy appears as a diffuse process, while white matter microstructural changes predominate in the areas specifically affected during FTLD and ALS.

In this study, we choose to model the effect of C9orf72 mutation on atrophy and white matter microstructure using the real age of subjects. Instead of real age, some authors (Rohrer et al., 2015) have used the distance to mean age of onset in affected relatives, as an estimation of expected years to onset in presymptomatic carriers of C9orf72. However, age of onset is highly variable even within individuals of the same family, one of the possible reasons being a possible anticipation phenomenon (Van Mossevelde et al., 2017). Thus, it must be highlighted that quantification of the effects of C9orf72 mutation on brain structure remains currently limited by the difficulty to accurately estimate expected age at onset in presymptomatic carriers.

2.5.1 Cognitive, Structural and Microstructural Changes are Detected in Young C9+ Subjects

During the preclinical course of neurodegenerative diseases, structural changes are expected 10-15 years and clinical changes 5 years before expected symptom onset, according to the largest presymptomatic FTLD (Rohrer et al., 2015) and Alzheimer's disease cohorts (Bateman et al., 2012; Benzinger et al., 2013). However, the pace of progression varies depending on the underlying mutation. In

C9orf72-FTLD patients, disease duration can be remarkably long (Gómez-Tortosa et al., 2013; Khan et al., 2012; Suhonen et al., 2015) and atrophy progresses at a slow rate (Whitwell et al., 2015), as compared to other genetic or sporadic forms. Thus, it is conceivable that the preclinical phase of C9orf72 disease would last particularly long. Our study evidences that subtle cognitive, structural and microstructural alterations can be detected in young C9orf72 carriers before 40 years of age. This finding suggests that young subjects may represent the optimal target population for future disease-modifying interventions. Previous studies have suggested that atrophy emerge in young C9orf72 carriers (Lee et al., 2016; Rohrer et al., 2015), either based on group differences obtained on extrapolated measures (Rohrer et al., 2015), or because no acceleration of atrophy was detected during aging in C9orf72 carriers (Lee et al., 2016). Our results confirm this hypothesis, by showing significant differences of metrics directly measured in young C9+ and C9- subjects.

2.5.2 Praxis Impairment Is an Early Feature of C9orf72 Disease

The evidence of subtle praxis alterations in young C9+ subjects is a surprising result. One study has suggested that cognitive and behavioral changes could occur 10 to 15 years from symptom onset in presymptomatic C9orf72 carriers, based on extrapolated data (Rohrer et al., 2015); however, praxis evaluation was not reported. Our result is particularly striking, as a clear separation was visible between the praxis scores of C9+ and C9- young individuals (Figure 2.1B). Praxis score has been reported to decrease during normal aging (Peigneux and Linden, 1999; Rodrigues Cavalcante and Caramelli, 2009); similarly, it was inversely correlated with age in both C9- and C9+ subjects in our study (Figure 2.1B). The difficulty of this task may explain its sensitivity to detect subtle preclinical changes in C9+ subjects. The observed impairment in non-transitive gestures (symbolic gestures without the use of an object) is a feature of ideomotor apraxia, which involves the posterior part of the left parietal lobe, mainly the left supramarginal gyrus (Króliczak, Piper, and Frey, 2016). Consistently, the impairment in non-transitive gestures in young C9+ subjects was associated with a focal atrophy of this region (i.e., left supramarginal cortex). No correlation was detected between volume of left supramarginal cortex and non-transitive gesture score in C9+ subjects; this lack of correlation was likely related to the relatively low variance of the score, which was only slightly altered in C9+ (1 to 6 points below the normal score of 36, see Figure 2.1D). Praxis alteration was unexpected, as it is not a salient feature of C9orf72 FTLD; although it has been occasionally reported (Floris et al., 2015; Mahoney et al., 2012b; Mahoney et al., 2012a; Van Langenhove et al., 2013), it is usually less

marked than executive and behavioral dysfunction (Devenney et al., 2014; Floeter et al., 2017; Sha et al., 2012; Suhonen et al., 2017). Thus, praxis impairment may represent an early-expressed and non-evolving phenotype of C9orf72 mutation. These intriguing findings stress the need to characterize C9orf72 mutation alterations on the scale of the entire lifespan of mutation carriers, including childhood, in order to disentangle possible developmental alterations (Lee et al., 2016; Walhout et al., 2015), from potential preclinical prognostic markers of C9orf72 disease. It also emphasizes the fact that neuropsychological features of C9orf72 mutation may extend well beyond the classical spectrum of FTLD, and require extensive neuropsychological characterization.

Additionally, we also observed a slight decrease in recall performance in C9+ carriers. Interestingly, C9orf72 mutation is associated with abnormal deposition of TDP-43, DPR and RNA foci in the hippocampus (Mackenzie, Frick, and Neumann, 2014). However, the slight memory impairment we observed appeared less striking than praxis impairment: there was a large overlap of values between C9+ and C9- subjects, and the difference did not persist when restricting the analysis to subjects ≤ 40 years of age. Moreover, we did not detect any significant atrophy in the hippocampus of C9+ subjects.

2.5.3 C9orf72 Mutation Is Associated With Early Thalamic Atrophy

Thalamic atrophy appears as a reliable effect of C9orf72 mutation. Thalamic atrophy has been previously reported in smaller cohorts of presymptomatic C9orf72 carriers (Lee et al., 2016; Rohrer et al., 2015; Walhout et al., 2015), and also in symptomatic C9orf72 carriers with FTLD (Floeter et al., 2016; Mahoney et al., 2012a) or ALS (Agosta et al., 2017). Thalamic atrophy may be related to the presence of pathological deposits, i.e. TDP-43 and/or DPR, but it can also be caused by deafferentation processes secondary to the diffuse cortical atrophy, due to the high number of connections between the hemispheric cortex and the thalamus. These mechanisms are not exclusive and may be associated, which would explain the high sensitivity of previous studies for detecting early thalamic atrophy in C9+ subjects.

2.5.4 White Matter Microstructural Changes, but not Cortical Atrophy Reflects the Expected Topography of FTLD-ALS in C9+ Subjects

Our study demonstrates a major difference of pattern between atrophy and white matter alterations in C9+ subjects. Atrophy appears as a widespread phenomenon, with a relative sparing of primary motor cortex and frontobasal cortex, areas that are preferentially involved during ALS and FTLD, respectively (Figure 2.2). Conversely, white matter alterations seem to preferentially target corticospinal tracts and frontal white matter (Figure 2.4). These suggest that in C9+ subjects, white matter changes may be more predictive of future cognitive and motor deficits than cortical atrophy. These different patterns are reminiscent of the topography of the two histopathological hallmarks of C9orf72 mutation, DPR and TDP-43. Even if this is still debated, DPR deposits have a diffuse distribution unrelated to the clinical phenotype of patients (Davidson et al., 2016; Davidson et al., 2014; Gomez-Deza et al., 2015; Mackenzie et al., 2015), and seem to precede TDP-43 deposition (Vatsavayai et al., 2016). Conversely, TDP-43 deposits may represent a downstream process more correlated to clinical symptoms. Furthermore, TDP-43 deposits are present both in cortical neurons and white matter glial cells (Neumann et al., 2007); thus, white matter changes, possibly more reflective of future clinical deficits, may relate more to TDP-43 pathology than to DPR in presymptomatic C9orf72 disease.

2.6 Conclusion

The present work demonstrates that pathological processes emerge during early adulthood in C9orf72 mutation carriers. Early and subtle praxis alterations in young C9+ subjects, underpinned by a focal atrophy of the left supramarginal gyrus, may represent a non-evolving phenotype, which highlights the possible overlaps and intricacy between neurodevelopmental and neurodegenerative processes. The distinct patterns of atrophy and white matter changes observed in C9+ subjects suggest that white matter integrity might be more reflective of the future FTLD/ALS phenotype than atrophy. Our results contribute to a better understanding of the spectrum of C9orf72 disease, and of the respective contribution of MR biomarkers in assessing disease-related changes.

Chapter 3

Neurite density is reduced in the presymptomatic phase of C9orf72 disease

This chapter has been published as a journal article on *Journal of Neurology, Neurosurgery, and Psychiatry* (Wen et al., 2019):

- **Wen, J.**, Zhang, H., Alexander, D., Durrleman, S., Routier, A., Rinaldi, D., Houot, M., Couratier, P., Hannequin, D., Pasquier, F., Zhang, J., Colliot, O., Le Ber, I. and Bertrand, A. Neurite density is reduced in the presymptomatic phase of C9orf72 disease, **J Neurol Neurosurg Psychiatry**, pp.jnnp-2018. https://hal.inria.fr/hal-01907482/document.

3.1 Abstract

OBJECTIVE. To assess the added value of neurite orientation dispersion and density imaging (NODDI) compared to conventional DTI and anatomical MRI to detect changes in presymptomatic carriers of chromosome 9 open reading frame 72 (C9orf72) mutation.

METHODS. The PREVDEMALS study is a prospective, multicenter, observational study of first-degree relatives of individuals carrying the C9orf72 mutation. Sixty-seven participants (38 presymptomatic C9orf72 mutation carriers [C9+], 29 non carriers [C9-]) were included in the present cross-sectional study. Each participant underwent one single-shell, multi-shell diffusion MRI and 3DT1 MRI. Volumetric measures, DTI and NODDI metrics were calculated within regions of interest. Differences in white matter integrity, gray matter volume and free water fraction between C9+ and C9- individuals were assessed using linear mixed-effects models.

RESULTS. Compared with C9-, C9+ demonstrated white matter abnormalities in 10 tracts with neurite density index, and only 5 tracts with DTI metrics. Effect

size was significantly higher for the neurite density index than for DTI metrics in two tracts. No tract had a significantly higher effect size for DTI than for NODDI. For gray matter cortical analysis, free water fraction was increased in 13 regions in C9+, whereas 11 regions displayed volumetric atrophy.

CONCLUSIONS. NODDI provides higher sensitivity and greater tissue-specificity compared to conventional DTI for identifying white matter abnormalities in the presymptomatic C9orf72 carriers. Our results encourage the use of neurite density as biomarker of the preclinical phase.

3.2 Introduction

Frontotemporal lobar degeneration (FTLD) and amyotrophic lateral sclerosis (ALS) are two degenerative diseases that share common genetic causes, the most frequent being a GGGGCC repeat expansion in the chromosome 9 open reading frame 72 (C9orf72) gene. DeJesus-Hernandez et al., 2011; Renton et al., 2011. Early stages of C9orf72 carriers have received much interest, because presymptomatic carriers represent the optimal target population for the development of new disease-modifying treatments against FTLD and ALS. Anatomical magnetic resonance imaging (MRI) derived metrics, such as volumetry, have revealed brain atrophy in presymptomatic individuals who carry the C9orf72 mutation (C9+). (Rohrer et al., 2015; Walhout et al., 2015; Lee et al., 2016; Bertrand et al., 2017; Cash et al., 2017; Papma et al., 2017; Popuri et al., 2018). Three studies (Lee et al., 2016; Bertrand et al., 2017; Papma et al., 2017) also detected disruptions of white matter integrity using diffusion tensor imaging (DTI) technique, whereas another study failed to identify such abnormalities (Walhout et al., 2015). The DTI results are promising but with limitations. First, DTI metrics, such as fractional anisotropy (FA), are non-specific biomarker of microstructural architecture. (Alexander et al., 2007; O'Donnell and Westin, 2011). For instance, FA changes could be underpinned by combinations of neurite density reduction and orientation dispersion changes Zhang et al., 2012. Besides, DTI is limited when an image voxel suffers from partial volume effect. Neurite orientation dispersion and density imaging (NODDI) was proposed to characterize alterations of microstructural integrity with higher tissue-specificity (Zhang et al., 2012). NODDI derives a neurite density index (NDI) and orientation dispersion index (ODI) to quantify the density and angular variation of neurites, respectively. In addition, NODDI includes a free water fraction (FWF) parameter designed to capture the contamination of tissues by free water at the microstructural level.

In the present work, we assess the added value of NODDI compared to conventional DTI and anatomical MRI to detect changes at the presymptomatic phase of

C9orf72 disease. We hypothesize that NDI and ODI offer higher sensitivity than FA, mean diffusivity (MD), axial diffusivity (AD) and radial diffusivity (RD) for detecting white matter abnormalities. Additionally, FWF is compared with volumetry and may provide complementary information for identifying gray matter changes.

3.3 Material and Methods

3.3.1 Participants

Eighty-six first-degree relatives of C9orf72 mutation carriers from 48 families were enrolled in an ongoing national multicentric study (PREVDEMALS) between October 2015 and October 2017. This study was approved by the Comité de Prévention des Personnes Ile de France VI of the Hôpital Pitié-Salpêtrière, and written informed consent was obtained from all participants. At inclusion, asymptomatic status of participants was ascertained based on relative's interview, neurological examination, and the normality of behavioral scales and neuropsychological scores, taking into account age and educational level. In the present study, sixty-seven neurologically healthy participants, who underwent a single-shell diffusion weighted image (DWI) sequence, a multi-shell DWI sequence and a 3DT1 sequence, were included in the analyses. C9orf72 genetic status was determined by repeat-primed polymerase chain reaction on lymphocytes DNA. Thirty-eight C9+ participants carried a pathogenic expansion (>23 GGGGCC repeats); twenty-nine control participants did not carry this expansion (C9-). The study population characteristics are shown in Table 3.1. Demographic characteristics and clinical tests were compared between groups using the χ^2 test for dichotomous and categorical variables or Mann-Whitney test for numerical variables. There was no statistical difference between C9+ and C9- regarding age at inclusion (P = 0.18), gender (P = 0.65) and clinical scores (Mini-Mental State Examination, P = 0.83; Mattis dementia rating scale, P = 0.37; Frontal assessment battery, P = 0.40).

Characteristic	Mean(SD)		P Value
	C9- (n=29))	C9+(n = 38)	
Demographic characteristics			
Age, y	44.8 (13.5)	40.7 (11.5)	0.18
Female, No. (%)	17 (59)	19 (50)	0.65
Right laterality, No. (%)	24 (83)	33 (87)	0.91
Expected time to onset, y	NA	18.6 (11.4)	NA
Familial phenotype, No. (%)			
FTLD	12 (42)	18 (47)	0.91
ALS	2 (7)	3 (8)	
Mixed	14 (48)	17 (45)	
Unavailable	1 (3)	0	
Neuropsychological scores			
MMSE score (maximum, 30)	28.7 (1.2)	28.5 (1.5)	0.83
FAB (maximum, 18)	16.9 (1.3)	17.1 (1.2)	0.40
MDRS score (maximum, 144)	141.9 (2.2)	141.3 (2.7)	0.37

Table 3.1: Study Group Characteristics. Abbreviations: ALS, amyotrophic lateral sclerosis; FAB, Frontal Assessment Battery; FTLD, frontotemporal lobar degeneration; MDRS, Mattis Dementia Rating Scale; MMSE, Mini-Mental State Examination; NA, not applicable.

3.3.2 MRI acquisition

All MRI acquisitions were performed on a 3-T MRI system (Siemens Prisma Syngo 3T) in a single center (Paris) belonging to the harmonized national network of the Centre d'Acquisition et de Traitement d'Images (http://cati-neuroimaging.com/) (Operto et al., 2016). The Centre d'Acquisition et de Traitement d'Images performed onsite visits for the setup of imaging protocols and regular follow-up. Each participant underwent a 3DT1 sequence with the following parameters: voxel size 1.1x1.1x1.1 mm^3; TE/TR = 2.93/2200 ms; Bandwidth = 240 Hz. One single-shell DWI sequence with two repeats was acquired for DTI with the following parameters: voxel size 2.5x2.5x2.5 mm^3; TE/TR = 90/7300 ms; Bandwidth = 1580 Hz; 64 diffusion-weighted directions, b-value = 1000 s/mm^2, 9 T2-weighted images (b-value = 0 s/mm^2, referred to as b0 image). One field map image was acquired to estimate the susceptibility-induced off-resonance field. One three-shell DWI sequence with two repeats was acquired with reversed phase encoding directions for NODDI model: voxel size 2x2x2 mm^3; TE/TR = 70/3000 ms; Bandwidth = 2090 Hz; 60, 32 and 9 diffusion-weighted directions at b-value = 2200, 700 and 300 s/mm^2 respectively; 13 b0 images. Of note, the DTI analysis was based on the single-shell data (b=1000 s/mm^2). Indeed, DTI model is known to be a poor representation of the DWI signals at the high b-value (> 2000). On the other hand, the low b-values (300 and 700) are acquired at prolonged TE designed to accommodate the high b-value. So these low b-values data are not representative of

standard DTI data. Systematic quality checks of MRI results were performed by the Centre d'Acquisition et de Traitement d'Images as in previous work (Bertrand et al., 2017). All images were of satisfactory quality except for one T1 acquisition and one single-shell DWI acquisition from different individuals. These two images were excluded respectively from gray matter and white matter analyses.

3.3.3 Anatomical MRI processing

T1-weighted images were processed with the FreeSurfer image analysis suite (Version 5.3; https://surfer.nmr.mgh.harvard.edu/), including skull stripping, intensity normalization, cortical and subcortical segmentation, cortical surface reconstruction and parcellation of the cortex using the Desikan-Killiany atlas (Desikan et al., 2006). We studied gray matter volumes of 68 cortical regions of interest (ROIs) and 18 subcortical ROIs. The list of regions is provided in Supplementary B (supplementary-appendix e-1). All ROI volumes were normalized by total intracranial volume (TIV).

3.3.4 DTI processing

The single-shell DWI data were processed with the same approach as in previous work (Bertrand et al., 2017). To summarize, head motion was corrected by rigidly registering the raw DWI volumes to the average b0 image, and an affine registration was used to correct for eddy current-induced distortions. The field map image was used to estimate the susceptibility-induced off-resonance field (Jenkinson and Smith, 2001). A single multiplicative bias field from the averaged b0 image was estimated and applied to the single-shell DWI data (Jeurissen et al., 2014). FA, MD, RD and AD were estimated using an iteratively reweighted linear least squares estimator (Tournier, Calamante, and Connelly, 2012). Each individual FA map was aligned onto the JHU white-matter tractography atlas template (Hua et al., 2008) with a rigid plus deformable registration (Avants et al., 2008). MD, AD and RD maps were subsequently registered into the JHU atlas using the transformation field from the previous step. The regional mean values of FA, MD, AD and RD maps were extracted. The list of regions is provided in Supplementary B (supplementary-appendix e-2).

3.3.5 NODDI processing

From the pairs of images with reversed phase encoding directions, the susceptibility-induced off-resonance field was estimated using *topup* tool (Andersson, Skare, and

Ashburner, 2003). Besides, eddy current-induced distortions and subject movements were corrected by simultaneously modelling the effects of diffusion eddy currents and movements on the image using *eddy* tool (Andersson and Sotiropoulos, 2016). The b-vector was subsequently corrected. The NODDI model was then fitted to the artifact-corrected data, generating NDI, ODI and FWF maps using NODDI Matlab toolbox (https://www.nitrc.org/projects/noddi_toolbox). For white matter analysis, DTI model was applied to the middle-shell data (b-value = 700 s/mm^2) to generate the FA map, in order to estimate the transformation field from the native diffusion space to the JHU space. Then NDI and ODI maps were registered into the JHU space using the transformation field obtained from the previous step. Finally, the regional mean values of NDI and ODI were calculated.

For gray matter analysis, the normalized skull-stripped T1 image in FreeSurfer conformed space was rigidly registered onto the first b0 image of the artifact-corrected multi-shell DWIs. Then the inverse transformation field was applied to register FWF map in the FreeSurfer conformed space with a linear interpolation. For subcortical ROI analysis, a 2-voxel morphological erosion operator was performed on each segmented subcortical ROI (Pfefferbaum et al., 2010). For cortical ROI analysis, FWF signal was projected onto cortical middle surface. The projected FWF value was calculated with a weighted average of signals from the seven intermediate surfaces, which were expanded at different fraction of cortical thickness (35%, 40%, 45%, 50%, 55%, 60% and 65%) from the white surface. Subsequently, the averaged middle surface was registered onto the FsAverage template in FreeSurfer conformed space using a surface-based registration method (Fischl et al., 1999). The aim of the erosion and middle surface projection approach was to avoid the partial volume effect (i.e., elimination of free water contamination at the edges of ventricle and the borders of the brain parenchyma). Finally, the regional mean values of FWF were extracted for further cortical and subcortical analyses.

3.3.6 Statistical analysis

All statistical analyses were performed with R Version 3.4.0 (The R Foundation). Structural and microstructural differences between C9+ and C9- participants were assessed using linear mixed-effects models. We used real age, gender and group (i.e., mutation status) as fixed effects and family membership as random effect measuring the difference between the average response in the family and in the whole population (supplementary B supplementary-appendix e-3). Likelihood ratio test was used to test each effect and P values were corrected by the Benjamini-Hochberg method with a significance level of $P < 0.05$. Besides, the effect size of

each ROI between C9+ and C9- was also reported using Cohen's *f2*. Effect sizes obtained for different models or metrics (e.g., NODDI vs DTI) were compared using permutation tests with 10000 iterations for significant ROIs.

3.4 Results

3.4.1 White matter analysis

Figure 3.1 displays altered white matter tracks after correction for multiple comparisons. Compared with C9-, C9+ showed extensive alterations in white matter integrity (i.e., reduced NDI, elevated MD, AD and RD), involving several fronto-temporal related tracts (i.e., bilateral inferior fronto-occipital fasciculus, bilateral inferior longitudinal fasciculus, right uncinate fasciculus, right anterior thalamic radiation, forceps minor) and both cortico-spinal tracts. 10 tracts were significantly altered in C9+ with NDI, and only 5 tracts with DTI metrics (MD, AD or RD). Results before correction for multiple comparisons are shown in supplementary B (supplementary-figure e-1). Effect size results confirmed that NDI was more sensitive than DTI metrics: among the 11 tracts in which significant differences were detected in either NDI or DTI metrics (MD, AD or RD), 7 tracts had higher effect size with NDI than with DTI metrics (Figure 3.2). The effect size was significantly higher with NDI than with DTI for two of these tracts: left inferior fronto-occipital fasciculus (P = 0.009) and right uncinate fasciculus (P = 0.008). None of the tracts had a significantly higher effect size with DTI than with NDI. Effect size results are shown in supplementary B (supplementary-table e-1).

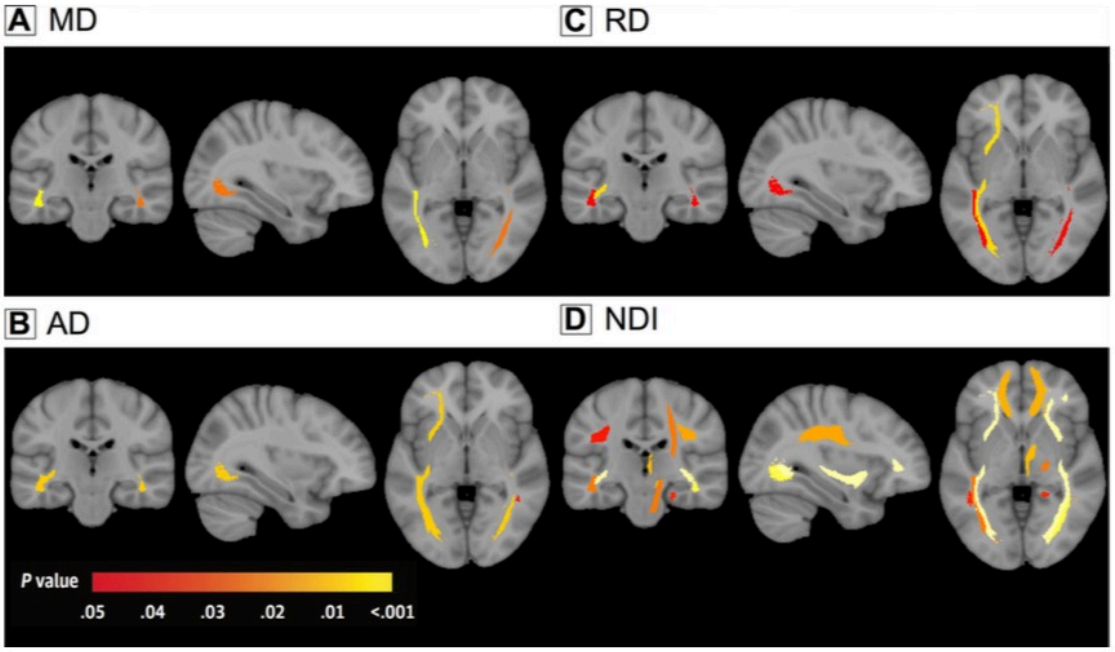

Figure 3.1: White matter alterations in C9orf72 mutation carriers. Colour-coded representation of p values corresponding to the associations of C9orf72 mutation with white matter integrity after correction for multiple comparisons. (a) Mean diffusivity (MD), (B) axial diffusivity (AD), (c) radial diffusivity (RD) and (D) NDI, neurite density index (NDI).

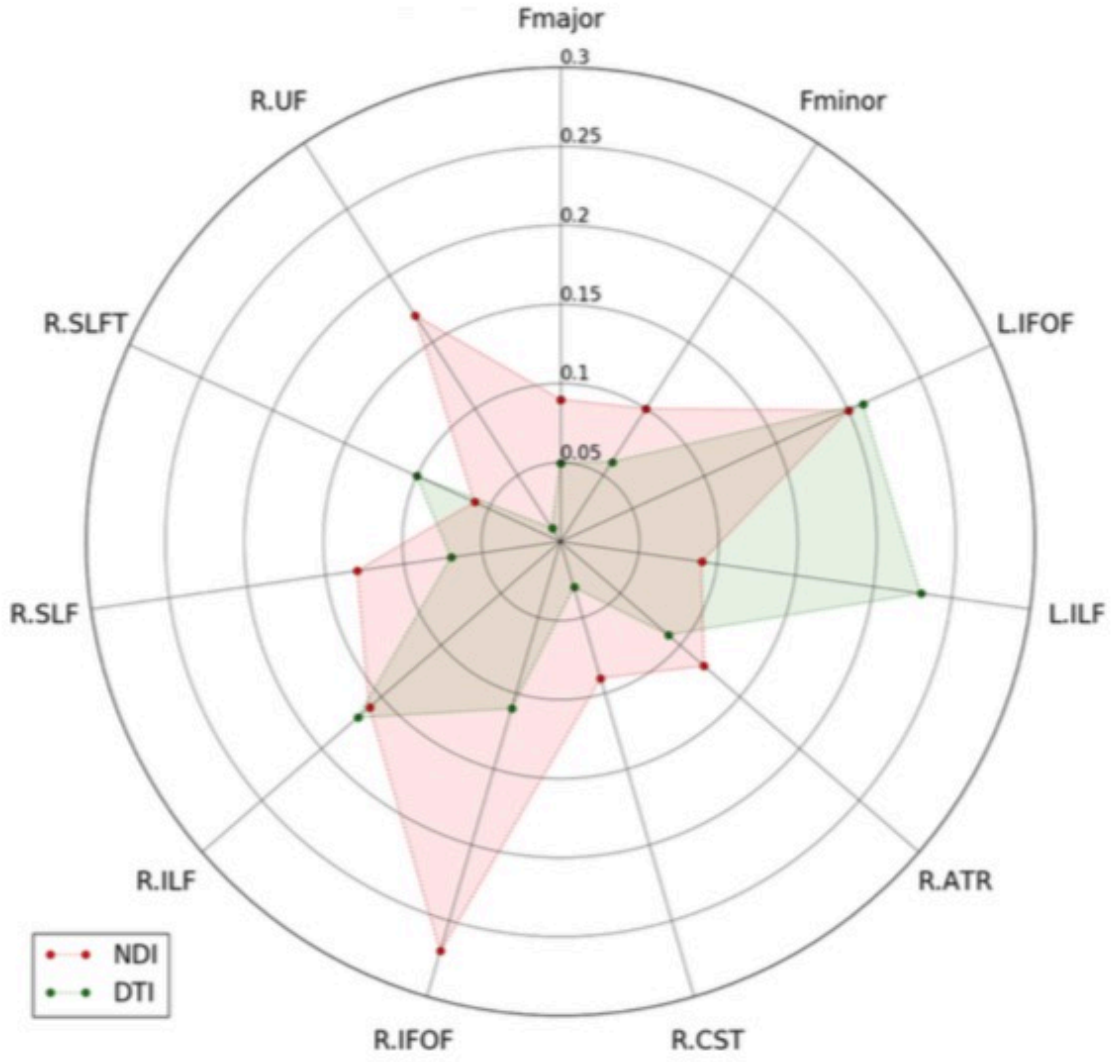

Figure 3.2: Effect size of white matter alterations in C9orf72 mutation carriers. Effect size (cohen's f2) corresponding to the associations of C9orf72 mutation with white matter integrity. Only ROIs in which significance, after correction for multiple comparisons, was detected in either NDI or DTI metrics are displayed. aTR, anterior thalamus radiation tract; csT, corticospinal tract; DTI, diffusion tensor imaging; Fmajor, forceps major tract; Fminor, forceps minor tract; IFOF, inferior fronto-occipital fasciculus; ILF, inferior longitudinal fasciculus; L, left; NDI, neurite density index; R, right; ROI, region of interest; sLF, superior longitudinal fasciculus; sLFT, superior longitudinal fasciculus (temporal part); UF, uncinate fasciculus.

3.4.2 Cortical gray matter analysis

Figure 3.3 displays altered cortical regions after correction for multiple comparisons. Compared with C9-, C9+ showed reduced cortical gray matter volume and elevated FWF. 13 ROIs were significantly altered with FWF (4 frontal, 1 temporal, 4 parietal, 3 occipital and the left insula), and 11 ROIs with volumetry (2 frontal, 5 temporal and 4 parietal ROIs). Results before correction for multiple comparisons

are shown in supplementary B (supplementary-figure e-2). Figure 3.4 displays effect sizes for the 21 regions that were significantly altered according to either FWF or volumetry. Among the 21 regions, the left insula (P = 0.002), the lateral occipital cortex (P = 0.001) and the left pericalcarine cortex (P = 0.008) had a significantly higher effect size with FWF than with volumetry. Only the left temporal pole cortex showed significantly higher effect size with volumetry than with FWF (P = 0.02). Effect size results are shown in supplementary B (supplementary-table e-2).

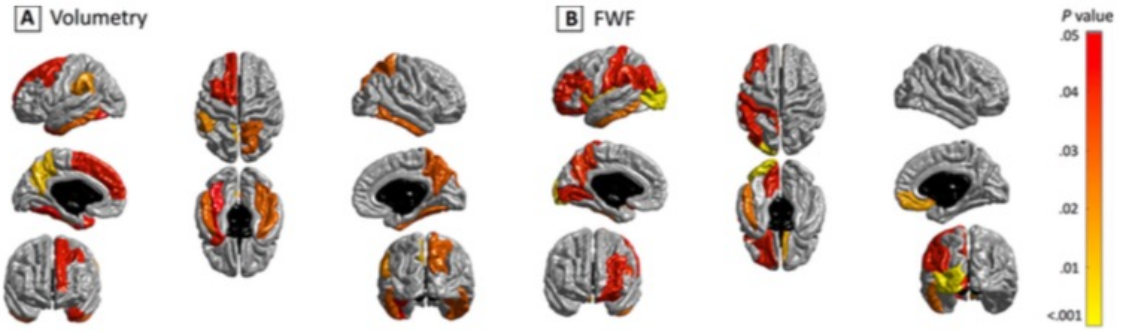

Figure 3.3: Cortical alterations in C9orf72 mutation carriers. Colour-coded representation of p values corresponding to the associations of C9orf72 mutation with the cortical ROI measures ((a), ROI volume and (B) FWF, respectively) after correction for multiple comparisons. FWF, free water fraction; ROI, region of interest.

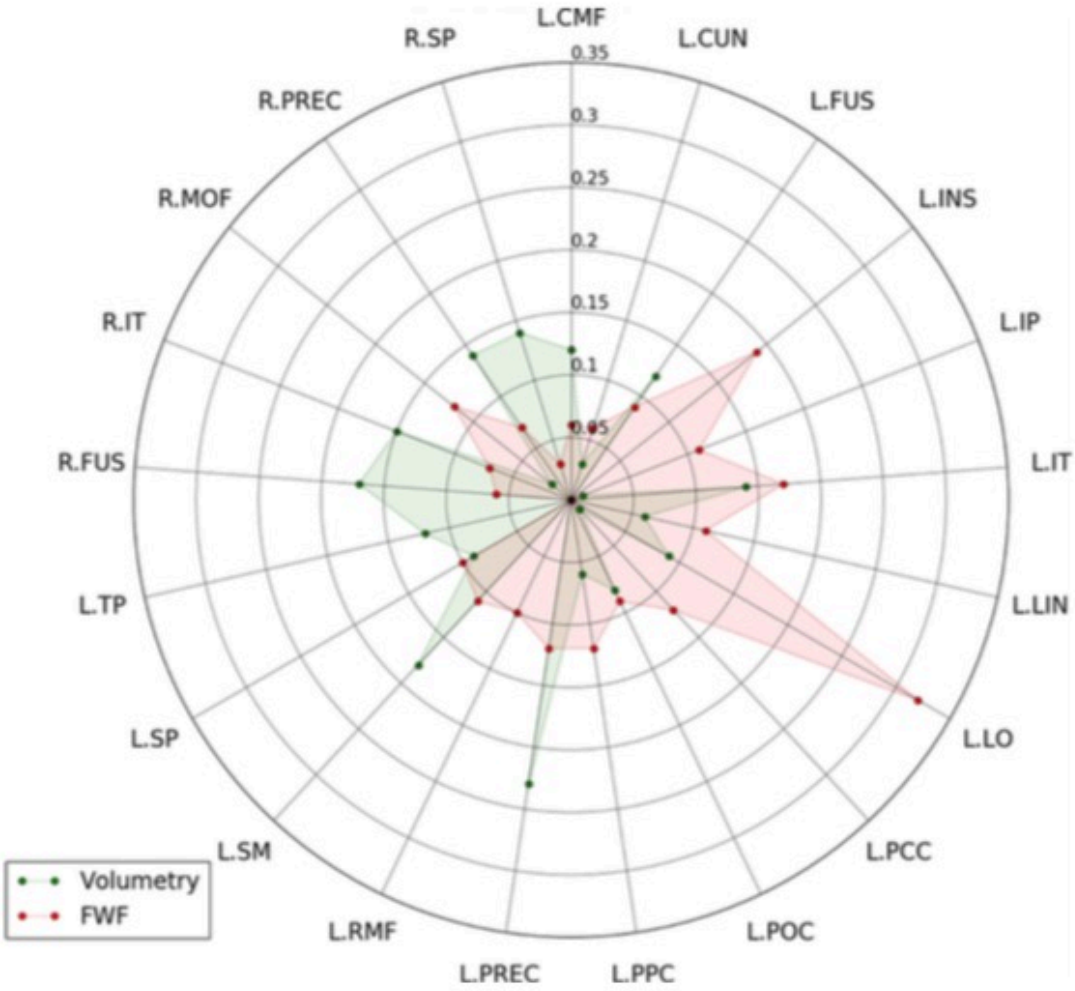

Figure 3.4: Effect size of cortical alterations in C9orf72 mutation carriers. Effect size (cohen's f2) corresponding to the associations of C9orf72 mutation with the cortical ROI measures (ROI volume and FWF, respectively). Only ROIs in which significance, after correction for multiple comparisons, was detected in either volumetry or FWF are displayed. CMF, caudal middle frontal cortex; CUN, cuneus cortex; FUS, fusiform; FWF, free water fraction; INS, insula; IP, inferior parietal cortex; IT, inferior temporal cortex; L, left; LIN, lingual; LO, lateral occipital cortex; MOF, medial orbitofrontal cortex; PCC, pericalcarine; POC, postcentral cortex; PPC, pars opercularis cortex; PREC, precuneus; R, right; RMF, rostral middle frontal cortex; ROI, region of interest; SM, supramarginal cortex; SP, superior parietal cortex; TP, temporal pole cortex.

3.4.3 Subcortical gray matter analysis

Compared with C9-, C9+ showed subcortical volume reduction of the right thalamus after correction for multiple comparisons. FWF failed to detect any significant alterations (Figure 3.5). Results before correction for multiple comparisons are presented in supplementary B (supplementary-figure e-3). The right thalamus did not

show statistically higher effect size with volumetry than with FWF (P = 0.062). Effect size results are shown in supplementary B (supplementary-table e-3).

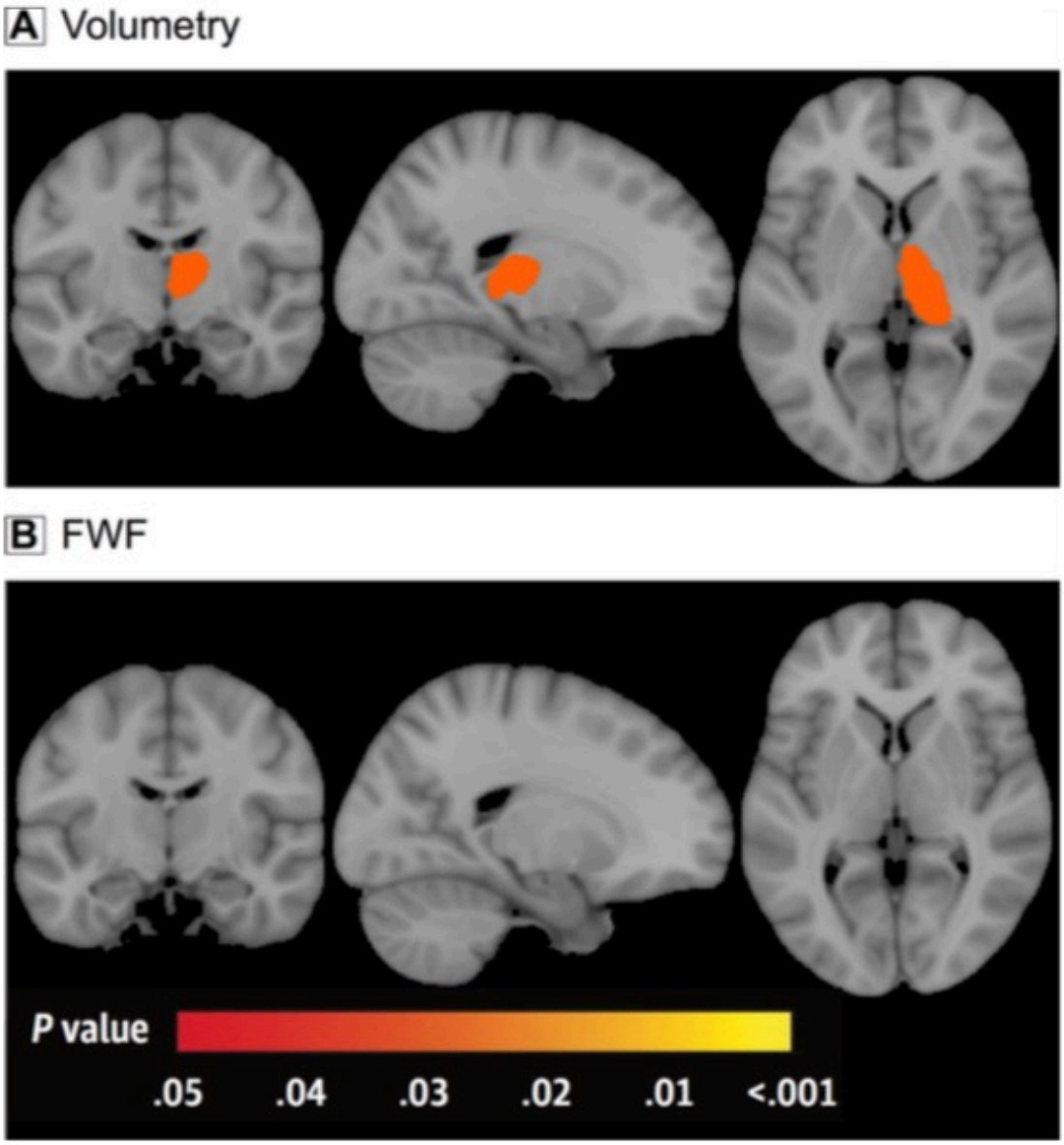

Figure 3.5: Subcortical alterations in C9orf72 mutation carriers. Colour-coded representation of p values corresponding to the associations of C9orf72 mutation with the subcortical ROI measures ((a) ROI volume and (B) FWF) after correction for multiple comparisons. FWF, free water fraction; ROI, region of interest.

3.5 Discussion

The current study, for the first time, compared NODDI to conventional DTI and anatomical MRI in a large cohort of presymptomatic C9orf72 carriers. There are three key findings. First, we demonstrate that NODDI provides higher sensitivity

than DTI for detecting white matter microstructural changes. Second, the greater tissue-specificity of NODDI suggests that the reduction of neurite density is a more likely cause of signal changes than the alterations of neurite orientation dispersion during the presymptomatic stage. Third, the pattern of FWF alterations slightly differs from that of gray matter volumetric atrophy, suggesting that both FWF and volumetry provide complimentary information on the integrity of cortical and subcortical structures.

When comparing the multi-shell DWI sequence with the standard single-shell DWI sequence, we hypothesized that NODDI could be more sensitive than conventional DTI for detecting white matter abnormalities during the presymptomatic stage. Previous works have shown that NODDI could be more sensitive than DTI for detecting white matter changes related to aging (Kodiweera et al., 2016) or young onset Alzheimer's disease (Slattery et al., 2017). Here, for the first time, we show that NODDI outperformed DTI for identifying white matter abnormalities during the presymptomatic stage of a neurodegenerative disease. The spatial pattern of white matter changes is consistent with previous findings with conventional DTI (Lee et al., 2016; Bertrand et al., 2017; Papma et al., 2017). Specifically, reduced NDI was mainly found in the cortico-spinal tract and frontal-temporal related tracts during the presymptomatic stage for C9orf72 carriers, which were preferentially involved in symptomatic mutation carriers who develop FTLD, ALS or both. On the other hand, to the best of our knowledge, there has been no prior study using NODDI in C9orf72 disease, neither at the presymptomatic nor at the symptomatic stage. The interpretation of specificity for DTI metrics has been discussed (Song et al., 2002; DeBoy et al., 2007), suggesting that RD and AD reflect respectively demyelination and axonal damage and both provide more specific information than FA. However, these interpretations were also argued in the literature (Wheeler-Kingshott and Cercignani, 2009). Compared with DTI, the more biophysically motivated NODDI model allows more direct analysis of independent microstructural effects: the loss of neurite density and the alteration of neurite orientation dispersion. This potential for greater tissue-specificity has motivated application of NODDI in a few neurodegenerative disease studies (Song et al., 2018; Schneider et al., 2017; Kamagata et al., 2016; Slattery et al., 2017; Grussu et al., 2017). In young onset Alzheimer's disease, one study showed widespread NDI reduction and regional ODI reduction in the corpus callosum and internal capsule of patients (Slattery et al., 2017). In Parkinson disease, another study observed reduced NDI in the substantia nigra and putamen of patients (Kamagata et al., 2016). In the present study, we detected widespread NDI decrease in the white matter, but no alteration of ODI (Figure 3.1). This suggests that the reduction of neurite density, not the alterations of neurite orientation dispersion, is

the predominant pathological process in white matter during the presymptomatic stage of C9orf72 carriers. Interestingly, similar reduction of neurite density within cortico-spinal tract have been found in ALS patients (Broad et al., 2017). Our observation suggests that the neurite loss is the main pathological process, but this needs further histological confirmation. We note however that Grussu et al have demonstrated, in the tissue specimen of multiple sclerosis, that ODI correlated well with histological measures of neurite orientation dispersion, and NDI with histological measures of neurite density (Grussu et al., 2017).

Mapping the free water in tissues is important in order to estimate the variations in extracellular volume (related to free water fraction) due to pathological processes (Pasternak et al., 2009). FWF has been applied in several neurodegenerative diseases. Using a bi-tensor model, FWF has been demonstrated as an imaging biomarker of progression of Parkinson's disease in the posterior substantia nigra (Planetta et al., 2016; Burciu et al., 2017). Interestingly, a chronic treatment effect of rasagiline, an irreversible inhibitor of monoamine oxidase-B as a medical monotherapy, has been verified with FWF in basal ganglia in Parkinson's disease (Burciu et al., 2016). These findings support the use of FWF as a promising biomarker in neurodegenerative diseases to evaluate the free water related alterations. In the present study, FWF detected free water alterations mainly in frontal and temporal lobes. This finding is consistent with previous studies using volumetric measure (Rohrer et al., 2015; Walhout et al., 2015; Lee et al., 2016; Bertrand et al., 2017; Cash et al., 2017; Papma et al., 2017; Popuri et al., 2018). The unique differences detected with FWF in left insula and left lateral occipital lobe were also reported in literatures using volumetric measure (Rohrer et al., 2015; Walhout et al., 2015; Lee et al., 2016; Cash et al., 2017). These suggest that macroscopic brain atrophy may accompany free water alterations inside the cortex. Surprisingly, FWF failed to show changes in subcortical structures, such as the thalamic atrophy where a significant effect of C9orf72 mutation was evidenced by volumetry. These findings suggest that distinct degenerative processes could occur in cortical and subcortical structures at the same time during the presymptomatic stage.

Reliability of an imaging technique is an important issue for its use in clinical trials. We do not have test-retest scans in our participants. However, the reliability of NODDI has been assessed in previous studies (Tariq et al., 2012; Chang et al., 2015). NODDI metrics were shown to have excellent reproducibility with coefficients of variation below 5% in all measured regions of interest and even below 3% in the vast majority of regions (Chang et al., 2015). Furthermore, the reproducibility of NODDI metrics was shown to be comparable to that of conventional DTI (Tariq et al., 2012). This, together with its higher sensitivity to detect white matter alterations, supports the use of NODDI in clinical trials.

3.6 Limitations

Our study has the following limitations. First, the cross-model comparison between NODDI and DTI used two different DWI acquisitions, which were performed within one week sequentially for each participant. However, the single-shell and multi-shell DWI sequences were optimized for DTI and NODDI model, respectively. Thus, this systematic comparison helps clarify the added value of a longer but clinically feasible multi-shell diffusion sequence. Second, caution should be exercised in diffusion MRI-based cortical analysis. NODDI, by construction, accounts for partial volume effects from CSF contamination, thus minimizing the influence of atrophy on the NODDI metrics. Moreover, a recent paper (Parker et al., 2018) has explicitly looked at the influence of cortical thickness on NODDI metrics, showing that the majority of changes in NODDI metrics persisted following adjustment for cortical thickness. Nevertheless, the cortex is a thin structure compared to the resolution of diffusion MRI and partial volume effect may impact on the computation of regional FWF measures. Although we implemented specific image processing procedures to mitigate partial volume effects, it is still possible that some partial volume effect remains, impacting on FWF estimates.

Chapter 4

Reproducible evaluation of diffusion MRI features for automatic classification of patients with Alzheimer's disease

This chapter has been submitted as a journal article to *Neuroinformatics* (Wen et al., 2018b):

- **Wen, J.**, Samper-González, J., Bottani, S., Routier, A., Burgos, N., Jacquemont, T., Fontanella, S., Durrleman, S., Epelbaum, S., Bertrand, A., and Colliot, O. Reproducible evaluation of diffusion MRI features for automatic classification of patients with Alzheimer's disease., Submitted to **Neuroinformatics**. https://arxiv.org/pdf/1812.11183.pdf.

4.1 Abstract

Diffusion MRI is the modality of choice to study alterations of white matter. In the past years, various works have used diffusion MRI for automatic classification of Alzheimer's disease. However, the performances obtained with different approaches are difficult to compare because of variations in components such as input data, participant selection, image preprocessing, feature extraction, feature selection (FS) and cross-validation (CV) procedure. Moreover, these studies are also difficult to reproduce because these different components are not readily available. In a previous work (Samper-González et al., 2018), we proposed an open- source framework for the reproducible evaluation of AD classification from T1-weighted (T1w) MRI and PET data. In the present paper, we extend this framework to diffusion MRI data. The framework comprises: tools to automatically convert ADNI data into the BIDS standard, pipelines for image preprocessing and feature extraction, baseline classifiers and a rigorous CV procedure. We demonstrate the use of

the framework through assessing the influence of diffusion tensor imaging (DTI) metrics (fractional anisotropy - FA, mean diffusivity - MD), feature types, imaging modalities (diffusion MRI or T1w MRI), data imbalance and FS bias. First, voxel-wise features generally gave better performances than regional features. Secondly, FA and MD provided comparable results for voxel-wise features. Thirdly, T1w MRI performed better than diffusion MRI. Fourthly, we demonstrated that using non-nested validation of FS leads to unreliable and over-optimistic results. All the code is publicly available: general-purpose tools have been integrated into the Clinica software (`www.clinica.run`) and the paper-specific code is available at: `https://gitlab.icm-institute.org/aramislab/AD-ML`.

4.2 Introduction

Alzheimer's disease (AD), the most prevalent form of dementia, is expected to affect 1 out of 85 people in the world by the year 2050 (Brookmeyer et al., 2007). Neuroimaging offers the possibility to study pathological brain changes associated with AD in vivo (Ewers et al., 2011). The most common neuroimaging modalities used to study AD are T1-weighted (T1w) magnetic resonance imaging (MRI) and positron emission tomography (PET) with various tracers (Frisoni et al., 2010; Vemuri and Jack, 2010). These techniques allow studying different types of alterations in the gray matter (GM). However, while AD is often considered primarily a gray matter disease, white matter (WM) is also extensively altered. There has thus been an increased interest in using diffusion MRI to study alterations in WM as the disease progresses (Fellgiebel et al., 2006; Kantarci et al., 2001; Müller et al., 2007; Müller et al., 2005).

In the past decades, there has been a strong interest in developing machine learning methods to assist diagnosis and prognosis of AD based on neuroimaging data (Rathore et al., 2017; Falahati, Westman, and Simmons, 2014; Haller, Lovblad, and Giannakopoulos, 2011). In particular, a large number of studies using machine learning have looked at the potential of diffusion MRI for AD classification Maggipinto et al., 2017; Dyrba et al., 2015b; Lella et al., 2017; Cui et al., 2012; Xie et al., 2015; Li et al., 2014. Several of these studies make use of the same publicly available dataset: the Alzheimer's Disease Neuroimaging Initiative (ADNI) (adni.loni.usc.edu). However, classification performances are not directly comparable across these studies because of differences in participant selection, feature extraction and selection, and performance metrics. It is thus difficult to know which approach performs best and which components of the method have the greatest influence on classification performances. We recently proposed a framework for the reproducible evaluation of machine learning algorithms in AD and

demonstrated its use on PET and T1w MRI data (Samper-González et al., 2018). The framework is composed of tools for management of public datasets and in particular their conversion into the Brain Imaging Data Structure (BIDS) format (Gorgolewski et al., 2016), standardized preprocessing pipelines, feature extraction tools and classification algorithms as well as procedures for evaluation. This framework was devoted to T1w MRI and PET data.

In the present work, we extend this framework to diffusion MRI data. We first perform a systematic review of the previous works devoted to automatic classification of AD using diffusion MRI data. We then present the different components of the framework, namely tools to convert ADNI diffusion MRI data into BIDS, preprocessing pipelines, feature extraction and selection methods and evaluation framework. We finally apply the framework to study the influence of various components on the classification performance: feature type (voxel-wise or regional features), imaging modality (T1w or diffusion MRI), data imbalance and feature selection (FS) strategy.

All the code (both of the framework and of the experiments) is publicly available: the general-purpose tools have been incorporated into Clinica (Routier et al., 2018), an open-source software platform that we developed for brain image analysis, and the paper-specific code is available at: `https://gitlab.icm-institute.org/aramislab/AD-ML`.

4.3 State of the art

AD is associated with altered integrity of WM, in particular the loss of cellular barriers that constrain free water motion (Xie et al., 2006). The fact that DTI was designed to study WM microstructure has led to the hypothesis that DTI-based features can be used for AD classification (Selnes et al., 2013). In recent years, a large body of research has been published for classification of AD using diffusion MRI. Here, we provide a review of these works.

We performed an online search of publications concerning classification of AD using diffusion MRI. We included only publications in English language, only original research publications (excluding review papers) and only peer-reviewed papers (either in journals or in conference proceedings), thereby excluding abstracts and preprints. We first searched on PubMed with the following search criteria: i) keywords: "(((classification diffusion MRI alzheimer's disease[Title/Abstract]) OR classification DTI alzheimer's disease[Title/Abstract]) OR diagnosis DTI alzheimer's disease[Title/Abstract]) OR diagnosis diffusion MRI alzheimer's disease[Title/Abstract]", ii) publication date: before the 31st October 2018, and iii) study species: humans.

We identified 616 studies based on these criteria. Among these studies, 105 review papers were excluded. Based on the abstract, we then selected only papers devoted to AD classification and using at least diffusion MRI. This resulted in 18 studies. Secondly, another query was performed on Scopus with the following criteria: i) keywords: "(TITLE- ABS-KEY(classification OR diagnosis) AND TITLE-ABS-KEY((diffusion AND mri) OR dti) AND TITLE-ABS-KEY((alzheimer's OR alzheimer) AND disease))", and ii) publication date before the search day (the 31st October 2018). This resulted in 425 studies. We then excluded 104 review papers. Moreover, limiting to only peer-reviewed journals or conference proceedings resulted in 298 studies. Based on the abstract, we selected only papers devoted to AD classification and using at least diffusion MRI, resulting in 27 studies. After merging the studies found by both PubMed and Scopus, we obtained 32 studies. To complete this search, we also did a search on Google Scholar with keywords: "classification diffusion MRI alzheimer's disease" or "classification DTI alzheimer's disease" or "diagnosis DTI alzheimer's disease" or "diagnosis diffusion MRI alzheimer's disease". Two additional studies were included, resulting in a total of 34 studies which are presented in the current state-of-the-art section.

These 34 studies can be categorized according to the following criteria. i) Studied modality. While the majority used only diffusion MRI, some used multimodal data (combining diffusion MRI with T1w MRI or functional MRI for instance). ii) Type of features. We subdivided between papers using DTI metric features, such as fractional anisotropy (FA) and mean diffusivity (MD), and those using more advanced features, such as tract-based or network-based features. iii) Classifiers. The most commonly used are SVM but RF, LR, NN or NB were also used in some studies. iv) Dataset. The most commonly used dataset is the ADNI although it does not constitute an overwhelming majority, unlike for T1w-MRI or PET studies. This is probably because diffusion MRI was not present in ADNI1. v) Classification tasks. Some studies focused on the discrimination between AD patients and CN subjects while other tackled classification of patients with MCI or prediction of progression to AD among MCI patients. A summary of these characteristics for the different studies is presented in Table 4.1 (for those using DTI metric features) and Table 4.2 (for connectivity or tractography features). Besides, if multimodal imaging or different type of features (i.e., DTI metric and more advanced features) were used in a study, we reported the accuracy of the best performance.

Study	Subject			Modality	dMRI Feature	Classifier	Database	Performance			
	AD	MCI	CN					CN/ AD	CN/ MCI	sMCI/ pMCI	AD/ MCI
(Ahmed et al., 2017)	45	58	52	dMRI T1w	Hippocampal voxel MD	SVM	ADNI	0.90[1]	0.79[1]	–	0.77[1]
(Cui et al., 2012)	–	0.79[b]	204	dMRI T1w	Regional FA	SVM	MAS	–	0.71[1]	–	–
(Dyrba et al., 2013)	137	–	143	dMRI	Voxel FA, MD	SVM	EDSD	0.83[1]	–	–	–
(Dyrba et al., 2015b)	–	0.35[c]	25	dMRI T1w	Voxel FA, MD, MO	SVM	EDSD	–	0.77[1,d]	0.68[1]	–
(Dyrba et al., 2015a)	28	–	25	dMRI, T1w, fMRI	Voxel FA, MD, MO	SVM	DZNE	0.89[2]	–	–	–
(Demirhan et al., 2015)	43	–	70	dMRI	Voxel and Regional FA	SVM	ADNI	0.88[1]	0.78[1]	–	0.86[1]
(Friese et al., 2010)	21	–	20	dMRI, T1w	Voxel FA, MD	LR	Local	0.88[2]	–	–	–
(Graña et al., 2011)	20	–	25	dMRI	Voxel FA, MD	SVM	HSA	1.00[1]	–	–	–
(Gao et al., 2015)	–	41	63	dMRI, T1w, fMRI	Regional FA	–	UHG	–	0.85[1]	–	–
(Jung et al., 2015)	27	18	–	dMRI, T1w	Regional FA, MD	SVM	MICPNU	–	–	–	0.87[1]
(Lee, Park, and Han, 2015)	35	73	33	dMRI	Voxel FA, MO	SVM	MICPNU	0.88[1]	–	–	0.90[1]
(Lella et al., 2017)	40	–	40	dMRI	Voxel FA, MD	SVM, RF, NB	ADNI	0.78[1]	–	–	–
(Mesrob et al., 2012)	15	–	16	dMRI T1w	Voxel and regional FA, MD	SVM	RRMC	1.00[1]	–	–	–
(Li et al., 2014)	21	–	15	dMRI, T1w	Regional FA	SVM	TJH	0.94[1]	–	–	–
(Maggipinto et al., 2017)	90	90	89	dMRI	Voxel FA, MD	RF	ADNI	0.76[1]	0.60[1]	–	–
(O'Dwyer et al., 2012)	–	19[a],14[b]	40	dMRI	Voxel FA, MD, RD, AD	SVM	EDSD	–	0.93[1]	–	–
(Haller et al., 2013)	–	18[e], 13[f], 35[g]	–	dMRI	Voxel FA	SVM	Local	–	–	0.99[1,e,f]	–
(Schouten et al., 2016)	77	–	173	dMRI, T1w, fMRI	Regional FA, MD	LR	PRODEM	0.95[2]	–	–	–
(Termenon et al., 2011)	15	–	20	dMRI	Voxel FA, MD	SVM, RVM, NN	HSA	0.99[1]	–	–	–
(Xie et al., 2015)	–	64[b]	64	dMRI, T1w	Voxel FA, MD	SVM	MCXWH	–	0.84[1]	–	–
(Zhang and Liu, 2018)	48	39[h], 75[i]	51	dMRI	Regional FA, MD, RD, AD	SVM, LR	ADNI	0.90[1]	–	0.93[1]	–

Table 4.1: Summary of the studies using DTI metric features for AD classification. Abbreviations: dMRI: diffusion MRI; T1w: T1-weighted MRI; fMRI: functional MRI; SVM: support vector machine; RVM: relevance vector machine; RF: random forest; NB: naive bayes; LR: logistic regression; NN: nearest neighbor; 1: accuracy; 2: area under the curve; EDSD: European DTI Study on Dementia; MAS: Sydney Memory and Aging; RRMC: Research and Resource Memory; HSA: Hospital de Santiago Apostol; PRODEM: Prospective Registry on Dementia study; ADNI: Alzheimer's Disease Neuroimaging Initiative; IDC: Ilsan Dementia Cohort; MCXWH: Memory Clinical at Xuan Wu Hospital; TJH: Tong Ji Hospital; MICPNU: Memory Impairment Clinic of Pusan National University Hospital; UHG: University Hospital of Geneva; DZNE: German Center for Neurodegenerative Diseases Rostock database; Local: private database; RD: radial diffusivity; AD: axial diffusivity; MO: mode of anisotropy; a: non-amnestic Mild Cognitive Impairment; b: amnestic Mild Cognitive Impairment; c: MCI-Aβ 42-; d: MCI-Aβ 42+; e: sd-aMCI, single domain amnestic MCI; f: sd-fMCI, single domain frontal MCI; g: md-aMCI, multiple domains amnestic MCI; h: late MCI; i: early MCI; –, not applicable.

Study	Subject			Modality	dMRI Feature	Classifier	Database	Performance			
	AD	MCI	CN					CN/ AD	CN/ MCI	sMCI/ pMCI	AD/ MCI
(Amoroso et al., 2017)	47	–	52	dMRI	Network measures	–	ADNI	0.95[3]	–	–	–
(Cai et al., 2018)	165	–	165	dMRI T1w	Network measures	LDA	ADNI	0.85[2]	–	–	–
(Doan et al., 2017)	79	55 30[a]	–	dMRI	Tract measures, regional FA, MD, RD, AD	LR	NorCog	–	–	–	0.71[3]
(Ebadi et al., 2017)	15	15	15	dMRI	Network measures	LR, RF, NB, SVM, NN	–	0.80[2]	0.70[2]	–	0.80[2]
(Lee, Park, and Han, 2013)	–	39	39	dMRI	Network measures, voxel and regional FA	SVM	ADNI	–	1.00[2]	–	–
(Lella et al., 2018)	40	30	52	dMRI	Network measures	SVM	ADNI	0.77[3]	–	–	–
(Nir et al., 2015)	37	113	50	dMRI	Tract measures, FA, MD	SVM	ADNI	0.85[2]	0.79[2]	–	–
(Prasad et al., 2015)	38	38[b] 74[c]	50	dMRI	Network measures	SVM	ADNI	0.78[2]	–	0.63[2]	–
(Schouten et al., 2017)	77	–	173	dMRI	Network measures, voxel FA, MD, RD, AD	LR	PRODEM	0.92[2]	–	–	–
(Wee et al., 2012)	–	10	17	dMRI fMRI	Network measures	SVM	DUBIAC	– –	0.96[2]	–	–
(Wang et al., 2018a)	–	169	379	dMRI T1w	Network measures	SVM, RF	ADNI NACC	– –	0.75[3]	–	–
(Zhu et al., 2014)	–	22	22	dMRI fMRI	Network measures	SVM	NACC	– –	0.95[2]	–	–
(Zhan et al., 2015)	39	112	51	dMRI	Network measures	LR	ADNI	0.71[1]	0.57[1]	–	0.69[1]

Table 4.2: Summary of the studies using tract-based or network-based features for AD classification. Abbreviations: dMRI: diffusion MRI; T1w: T1-weighted MRI; fMRI: functional MRI; SVM: support vector machine; LDA: linear discriminant analysis; RF: random forest; NB: naive bayes; LR: logistic regression; NN: nearest neighbor; 1: balanced accuracy; 2: accuracy; 3: area under the curve; DUBIAC: Duke-UNC Brain Imaging and Analysis Center; RRMC: Research and Resource Memory; PRODEM: Prospective Registry on Dementia study; ADNI: Alzheimer's Disease Neuroimaging Initiative; NACC: National Alzheimer's Coordinating Center; NorCog: Norwegian registry for persons being evaluated for cognitive symptoms in specialized health care. a: subjective decline MCI; b: late MCI; c: early MCI; –, not applicable.

Twenty-one studies used DTI metrics as features (see details in Table 4.1). Among the DTI derived metrics, FA and MD were most frequently used (O'Dwyer et al., 2012; Maggipinto et al., 2017; Dyrba et al., 2013; Dyrba et al., 2015b; Lella et al., 2017; Mesrob et al., 2012; Zhang and Liu, 2018; Xie et al., 2015; Friese et al., 2010; Schouten et al., 2016; Jung et al., 2015; Dyrba et al., 2015a). Besides, RD, AD and MO were also examined in some papers (O'Dwyer et al., 2012; Dyrba et al., 2015b; Lee, Park, and Han, 2015; Zhang and Liu, 2018; Dyrba et al., 2015a). Voxel- and region-wise features were both used. For voxel-wise classification, all voxels from the segmented GM or WM were used. For region-wise classification, the mean value within each ROI of DTI metric maps were extracted using an anatomical atlas. The most commonly used atlases were the JHU atlases (Hua et al., 2008). Ten studies adopted only diffusion MRI for AD classification (O'Dwyer et al., 2012; Maggipinto et al., 2017; Dyrba et al., 2013; Lella et al., 2017; Zhang and Liu, 2018; Termenon et al., 2011; Demirhan et al., 2015; Haller et al., 2013; Graña et al., 2011; Lee, Park, and Han, 2015). The other eleven studies looked at the potential of multimodal MRI, for instance T1w MRI and diffusion MRI, for AD diagnosis and compared the performances cross modalities. For the DTI metric-based studies, SVM was most frequently used (O'Dwyer et al., 2012; Dyrba et al., 2013; Dyrba et al., 2015b; Lella et al., 2017; Cui et al., 2012; Mesrob et al., 2012; Zhang and Liu, 2018; Termenon et al., 2011; Xie et al., 2015; Jung et al., 2015; Demirhan et al., 2015; Ahmed et al., 2017; Li et al., 2014; Lee, Park, and Han, 2015; Graña et al., 2011; Haller et al., 2013; Dyrba et al., 2015a).

Thirteen works demonstrated the usage of more complex features, such as tract-based or network-based features (see details in Table 4.2). In such approaches, tractography is used to extract WM tracts from diffusion MRI data. To be reliable, such a procedure requires to have high angular resolution diffusion imaging data. Then, tract-based approaches compute indices that characterize the tract, including tract volume, average FA/MD across the tract or more advanced features (Doan et al., 2017; Nir et al., 2015; Lee, Park, and Han, 2013). Such indices are used as input of the classifier. In network-based features, the result of the tractography (also called the tractogram) is used to build a graph of anatomical connections. Usually, the GM is parcellated into a set of anatomical regions and the connectivity between two given regions is computed based on the tractogram. To that purpose, different measures have been used, including the number of fibers or the average FA along the connection. This results in a connectivity network which can be described through network-based measures. Such features characterize the local and global topology of the network and are fed to a classifier. Ten studies used network-based features derived from diffusion MRI for AD classification (Schouten et al., 2017; Ebadi et al., 2017; Prasad et al., 2015; Wee et al., 2012; Cai

et al., 2018; Lella et al., 2018; Wang et al., 2018b; Zhan et al., 2015; Amoroso et al., 2017; Zhu et al., 2014).

There is a high variability in terms of classification performances across studies. For DTI metric features, the classification accuracy ranges from 0.71 to 1 for task CN vs AD. With regard to the accuracies across types of features, no consistency existed across studies. For instance, Nir et al observed that, in their study, the performances of MD outperformed FA (Nir et al., 2015). However, O'Dwyer et al reported higher accuracy for FA than MD in their experiments (O'Dwyer et al., 2012) and another study obtained comparable accuracies for both metrics (Dyrba et al., 2013). Conflicting results were also reported for the comparison of different modalities. Mesrob et al obtained higher accuracy with T1w MRI than with diffusion MRI (Mesrob et al., 2012) while Dyrba et al came to the opposite conclusion (Dyrba et al., 2015b). For network- or tract-based features, the classification accuracy ranges from 0.71 to 0.95 for task CN vs AD, a range which is comparable to that obtained with DTI metrics.

In this work, we choose to focus on DTI metrics because: i) they are more simple than connectivity or tractography features; ii) they can be easily computed and can make use of standard diffusion MRI sequences, thus are more adapted to translation to clinical practice, iii) to date, there is no clear evidence that connectivity/tractography features lead to higher accuracies for AD classification and iv) conflicting results exist regarding the respective performance of different DTI metrics in this context.

4.4 Materials

The data used in the preparation of this article were obtained from the Alzheimer's Disease Neuroimaging Initiative database (ADNI) (adni.loni.usc.edu). The ADNI was launched in 2003 as a public-private partnership, led by Principal Investigator Michael W. Weiner, MD. The primary goal of ADNI has been to test whether serial MRI, PET, other biological markers, and clinical and neuropsychological assessment can be combined to measure the progression of MCI and early AD. Over 1,650 participants were recruited across North America during the first three phases of the study (ADNI1, ADNI GO and ADNI2). Around 400 participants were diagnosed with AD, 900 with MCI and 350 were control subjects. Three main criteria were used to classify the subjects (Petersen et al., 2010). The normal subjects had no memory complaints, while the subjects with MCI and AD both had to have complaints. CN and MCI subjects had a MMSE score between 24 and 30 (inclusive), and AD subjects between 20 and 26 (inclusive). The CN subjects had a CDR score of 0, the MCI subjects of 0.5 with a mandatory requirement of the

memory box score being 0.5 or greater, and the AD subjects of 0.5 or 1. The other criteria can be found in (Petersen et al., 2010).

Five diagnosis groups were considered:

- CN: subjects who were diagnosed as CN at baseline;
- AD: subjects who were diagnosed as AD at baseline;
- MCI: subjects who were diagnosed as MCI, EMCI or LMCI at baseline;
- pMCI: subjects who were diagnosed as MCI, EMCI or LMCI at baseline, were followed during at least 36 months and progressed to AD between their first visit and the visit at 36 months;
- sMCI: subjects who were diagnosed as MCI, EMCI or LMCI at baseline, were followed during at least 36 months and did not progress to AD between their first visit and the visit at 36 months.

Naturally, all participants in the pMCI and sMCI groups are also in the MCI group. Note that the reverse is false, as some MCI subjects did not convert to AD but were not followed long enough to state whether they were sMCI or pMCI.

The DWIs of ADNI were downloaded in October 2016. They all came from ADNI GO and ADNI2 phases. Two different acquisition protocols are described for DWIs: Axial DTI (images with "Sequence" field starting by "AX_DTI" and "Axial_DTI" in the file of "IDA_MR_Metadata_Listing.csv") and Enhanced Axial DTI (images with "Sequence" field equal to "Enhanced_Axial_DTI" in the file of "IDA_MR_Metadata_Listing.csv"). In total, Axial DTI were available for 1019 visits and Enhanced Axial DTI for 102 visits. Only Axial DTI images were available for the baseline visit (222). In the current study, we included the participants whose diffusion and T1w MRI scans were both available at baseline. These DWIs were acquired with the following parameters: 35 cm field of view, 128×128 acquired matrix, reconstructed to a 256×256 matrix; voxel size: 1.35×1.35×2.7mm ; scan time = 9 min; 41 diffusion-weighted directions at b-value = 1000 s/mm^2 and 5 T2-weighted images (b-value = 0 s/mm^2, referred to as b0 image). Besides, each participant underwent a T1w MRI sequence with following parameters: 256×256 matrix; voxel size = 1.2×1.0×1.0 mm ; TI = 400 ms; TR = 6.98 ms; TE = 2.85 ms; flip angle = 11°. We used QC information provided by ADNI to select participants (see below Section 4.1). Moreover, QC was conducted on the results of the preprocessing pipeline (see below Section 4.2). Four participants were excluded because of the lower image resolution (4.5×4.5×4.5mm). Finally, 46 CN, 97 MCI, 54 sMCI, 24 pMCI and 46 AD were included.

Table 4.3 summarizes the demographics, and the MMSE and global CDR scores of the participants in this study.

	N	Age	Gender	MMSE	CDR
CN	46	72.7 ± 6.0[59.8,89.0]	21M/25F	28.9 ± 1.4[24,30]	0:46
MCI	97	72.9 ± 7.3[55.0,87.8]	62M/35F	27.7 ± 1.7[24,30]	0.5:97
sMCI	54	72.6 ± 7.7[55.0,87.8]	21M/25F	28.0 ± 1.7[24,30]	0.5:54
pMCI	24	74.2 ± 6.1[56.5,85.3]	16M/8F	26.8 ± 1.4[24,30]	0.5:24
AD	46	74.4 ± 8.4[55.6,90.3]	28M/18F	23.4 ± 1.9[20,26]	0.5:17;1:29

Table 4.3: Summary of participant demographics, mini-mental state examination (MMSE) and global clinical dementia rating (CDR) scores. Values are presented as mean ± SD [range]. M: male, F: female

4.5 Methods

The classification framework is illustrated in Figure 4.1. It includes: tools for data management, image processing, feature extraction and selection, classification, and evaluation. Conversion tools allow an easy update of ADNI as new subjects become available. To facilitate future development and testing, the different components were designed in a modular-based architecture: processing pipelines using Nipype (Gorgolewski et al., 2011), and classification and evaluation tools using the scikit-learn [19] library (Pedregosa et al., 2011). Thus the objective measurement of the impact of each component on the results could be clarified. A simple command line interface is provided and the code can also be used as a Python library.

[19] http://scikit-learn.org

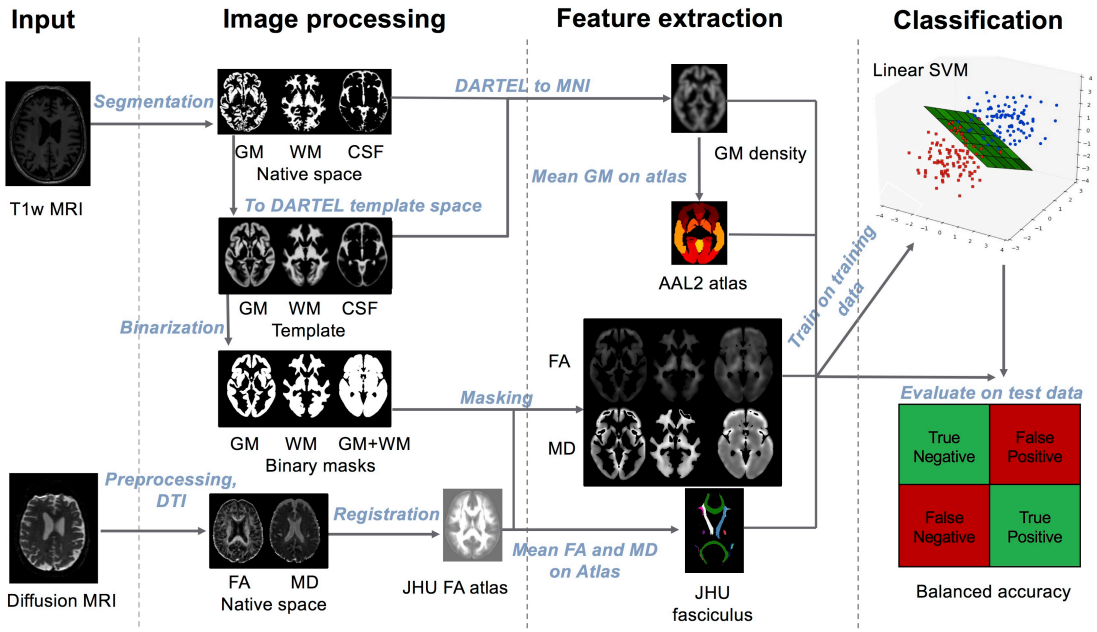

Figure 4.1: Overview of the framework.

4.5.1 Converting datasets to a standardized data structure

Public datasets, such as ADNI, are extremely useful to the research community. However, using the ADNI can be difficult because the downloaded raw data does not possess a clear and uniform organization. We thus proposed to convert ADNI data into the BIDS format (Gorgolewski et al., 2016), a community standard which allows storing multiple neuroimaging modalities as well as clinical and sociodemographic data. BIDS is based on a file hierarchy rather than on a database management system. It can thus be easily deployed in any research laboratory.

The ADNI to BIDS converter that we developed allows to automatically convert the raw dataset downloaded from the ADNI website to BIDS. The converter requires that the user has downloaded all the ADNI study data (tabular data in csv format) and the imaging data of interest. Importantly, the downloaded files must be kept exactly as they were downloaded. All conversion steps are then performed by the automatic converter, requiring no user intervention.

Details regarding conversion of clinical, sociodemographic and T1w MRI data can be found in (Samper-González et al., 2018). For the DWIs, first, we selected from the file "IDA_MR_Metadata_Listing.csv", all entries containing "DTI" in the "Sequence" field. Images with a sequence name containing "Enhanced" were discarded. Then, "IMAGEUID" field was matched to corresponding "loni_image"

field of 'MAYOADIRL_MRI_IMAGEQC_12_08_15.csv' file, to find QC information for each image. In cases where there existed several scans for a visit, we kept the one marked as selected (1 in 'series_selected' field of QC csv file). If there was no image marked as selected, then we chose the image with the best quality, (as specified in "series_quality" field, ranging from 1 to 4, 1 being excellent and 4 being unusable), excluding the images that failed QC (series_quality = 4). If there were several images for the same visit and QC information was not present, we chose the scan that was acquired the first. Once paths for each of the selected images were gathered, the images in dicom format were converted to nifti format using the *dcm2niix*[20] tool, or in case of error the *dcm2nii*[21] tool (Li et al., 2016). Images failing the conversion using both tools were manually discarded. Finally, the converted images in nifti format were organized in the corresponding BIDS folder. Note that all these steps are automatically performed by the converter.

We also provide tools for subject selection according to the duration of follow up and the diagnose. In the present study, all the participants whose T1w MRI and diffusion MRI scans were available at baseline were included. Finally, we organized all the outputs of the experiments into a BIDS-inspired standardized structure.

4.5.2 Preprocessing pipelines

4.5.2.1 Preprocessing of T1w MRI

The image processing pipeline for T1w MRI was previously described in (Samper-González et al., 2018). In brief, the Unified Segmentation procedure (Ashburner and Friston, 2005) is first used to simultaneously perform tissue segmentation, bias correction and spatial normalization of the input image. Next, a group template is created using DARTEL (Ashburner, 2007), from the subjects' tissue probability maps in native space obtained at the previous step. Lastly, the DARTEL to MNI method (Ashburner, 2007) is applied, providing a registration of the native space images into the MNI space. Besides, the GM and WM tissue maps from DARTEL template were binarized (with a threshold of 0.3) to obtain the corresponding tissue masks that are subsequently used in diffusion MRI pipeline.

[20] https://github.com/rordenlab/dcm2niix
[21] https://www.nitrc.org/plugins/mwiki/index.php/dcm2nii:MainPage

4.5.2.2 Preprocessing of diffusion MRI

For each subject, all b0 images were rigidly registered to the first b0 image and then averaged as the b0 reference. The raw DWIs were corrected for eddy current-induced distortions and subject movements by simultaneously modelling the effects of diffusion eddy currents and movements on the image using eddy tool (Andersson and Sotiropoulos, 2016) from FMRIB Software Library (FSL) software (Jenkinson et al., 2012). To correct for susceptibility-induced distortions, as fieldmap data were not available in ADNI GO or ADNI2, the T1w MRI was used instead in this context. The skull-stripped b0 image was registered to the T1w MRI with two sequential steps: first a rigid registration using FSL flirt tool and then a non-linear registration using SyN registration algorithm from ANTs (Avants et al., 2008). SyN is an inverse-consistent registration algorithm allowing EPI induced susceptibility artifacts correction (Leow et al., 2007). Finally, the DWI volumes were corrected for nonuniform intensity using the ANTs N4 bias correction algorithm (Tustison and Avants, 2013) and the diffusion weighting directions were appropriately updated (Leemans and Jones, 2009). The implementation of these different steps is available in the dwi-preprocessing-using-t1 pipeline of Clinica.

We performed QC on the results of the preprocessing pipeline. Specifically, we inspected the results for the presence of head motion artifacts and eddy current artifacts. Registration quality was also visually checked by overlapping the source image onto the target image. All preprocessed data were considered of acceptable quality.

The DTI model was then fitted to generate FA and MD maps using MRtrix (Tournier, Calamante, and Connelly, 2012). FA maps were nonlinearly registered onto the JHU atlas FA template in MNI space with the ANTs SyN algorithm (Avants et al., 2008). The estimated nonlinear deformation was finally applied to the MD maps to have all the FA and MD maps in the same space. These procedures were implemented in the dwi-processing-dti pipeline of Clinica.

4.5.3 Feature extraction

We extracted two types of features: voxel-wise and regional features. After image preprocessing, all T1w MRI and diffusion MRI are in MNI space and we have a voxel-wise correspondence across subjects. Voxel-wise features simply correspond to all the voxels in GM for T1w MRI. In order to extract the DTI-based voxel-wise features, FA and MD maps were masked using the tissue masks (i.e., WM, GM and GM+WM tissue binarized masks) obtained from T1w MRI pipeline. Then a Gaussian smoothing kernel with FWHM at 8 mm was applied to the masked FA and MD maps. The resulting maps were masked again by the tissue masks.

Thus voxels in GM, WM or GM+WM tissue maps were used as voxel-wise features for diffusion MRI. Regional features correspond to the average value (GM density for T1w MRI; FA or MD for diffusion MRI) computed in a set of ROIs obtained from different atlases. AAL2 atlas containing 120 ROIs (Rolls, Joliot, and Tzourio-Mazoyer, 2015) was used for T1w MRI. Two JHU atlases, ICBM-DTI-81 white-matter labels atlas (referred as JHULabel with 48 ROIs) and JHU white-matter tractography atlas with a 25% threshold (referred as JHUTract25 with 20 ROIs), were used for diffusion MRI. The different features are shown in Table 4.4.

Modality	Feature Type	Feature
Diffusion MRI	Voxel-wise	WM-FA
		WM-MD
		GM-FA
		GM-MD
		WM+GM-FA
		WM+GM-MD
	Region-wise	JHULabel-FA/MD
		JHUTract25-FA/MD
T1w MRI	Voxel-wise	GM-Density
	Region-wise	AAL2

Table 4.4: Summary of the different types of features.

4.5.4 Classification

Classification was performed using a linear SVM for both voxel-wise and regional features. As output of the classification, we reported the balanced accuracy, AUC, accuracy, sensitivity, specificity. Additionally, the optimal margin hyperplane (OMH) coefficient maps were reported. The OMH coefficient map represents the influence of each voxel or region on the classification performance. Thus, the OMH coefficient map characterizes the potential anatomical patterns associated to a given classifier (Cuingnet et al., 2013).

4.5.5 Cross-validation

As emphasized in the recent literature (Varoquaux et al., 2017), it is important to properly perform the cross-validation (CV) procedures. In the present work, the CV procedure included two nested loops: an outer loop evaluating the classification performances and an inner loop used to optimize the hyperparameters of the model (C for SVM). More precisely, repeated random splits (all of them stratified) with 250 repetitions was used for outer CV. For hyperparameter optimization, we

used an inner loop with 10-fold CV. For each split, the model with the highest balanced accuracy is selected, and then these selected models are averaged across splits to profit of model averaging.

When FS is performed, it is crucial that FS is adequately incorporated into the CV procedure. FS is a process to identify relevant features and thereby reduce the dimensionality. It has the potential to reduce overfitting (Bermingham et al., 2015). In the present work, we aim to explore the impact of FS bias. The FS bias, also known as non-nested FS strategy, arises when FS is performed on the entire dataset and not within the CV procedure, thus introducing data leakage. On the contrary, a nested FS is a procedure blind to the test data and embedded into the nested CV (Maggipinto et al., 2017).

Two different FS algorithms were applied: an ANOVA univariate test and an embedding SVM recursive feature elimination (SVM-RFE) (Guyon et al., 2002; Chandrashekar and Sahin, 2014). Specifically, the ANOVA test can been seen as a filter without taking the classifier into account and was performed for each feature independently. SVM-RFE uses the coefficients from the SVM models to assess feature importance. Then the least important features, which have the least effect on classification, are iteratively pruned from the current set of features. The remaining features are kept for the next iteration until the desired number of features has been obtained. For both methods, we tested varying numbers of selected features (1% of the total number of features and then from 10% to 100%, increasing by 10% at each step).

4.5.6 Classification experiments

Four different classification tasks were considered: CN vs AD, CN vs pMCI, sMCI vs pMCI and CN vs MCI.

For all classification tasks, we assessed the influence of different components on the performance. First of all, we compared the performance obtained with different DTI metrics (FA, MD), different feature types (voxel, regional) and different atlases. Secondly, we compared the classification performance between diffusion MRI and T1w MRI. To note, the nested CV procedure, in each iteration, guaranteed the same subjects for data split (i.e., training and testing data) between modalities. Thirdly, we studied the impact of imbalanced data. Three tasks (i.e., CN vs pMCI, CN vs MCI and sMCI vs pMCI) have imbalanced data: the number of subjects of the majority group is nearly twice as many as that of the minority group. To assess the impact of data imbalance, a random down-sampling technique was used for each imbalanced task. In each iteration of the outer CV, this technique randomly

excluded certain subjects from the majority group to ensure the subject balance between groups. Lastly, we evaluated the effect of FS bias.

4.6 Results

Here, we present the results of classification tasks using original data or balanced data in Tables 4.5 and 4.6. Balanced accuracy was used as performance metric. All the results with other performance metrics are available at https://gitlab.icm-institute.org/aramislab/AD-ML.

Modality	Feature	CN/AD	CN/pMCI	sMCI/pMCI	CN/MCI
Diffusion MRI	WM-FA	0.73 ± 0.099	0.52 ± 0.108	0.43 ± 0.088	0.57 ± 0.090
	WM-MD	0.71 ± 0.098	0.53 ± 0.087	0.49 ± 0.048	0.59 ± 0.068
	GM-FA	0.71 ± 0.097	0.59 ± 0.107	0.48 ± 0.089	0.57 ± 0.088
	GM-MD	0.76 ± 0.095	0.61 ± 0.115	0.51 ± 0.098	0.60 ± 0.084
	WM+GM-FA	0.71 ± 0.099	0.59 ± 0.112	0.47 ± 0.094	0.58 ± 0.086
	WM+GM-MD	0.76 ± 0.098	0.60 ± 0.118	0.51 ± 0.106	0.60 ± 0.088
	JHULabel-FA	0.70 ± 0.107	0.51 ± 0.112	0.47 ± 0.088	0.57 ± 0.081
	JHULabel-MD	0.50 ± 0	0.50 ± 0	0.50 ± 0	0.50 ± 0
	JHUTract25-FA	0.66 ± 0.102	0.54 ± 0.118	0.47 ± 0.078	0.55 ± 0.077
	JHUTract25-MD	0.47 ± 0	0.50 ± 0	0.50 ± 0	0.50 ± 0
T1w MRI	GM-Density	0.88 ± 0.066	0.73 ± 0.112	0.64 ± 0.113	0.58 ± 0.086
	AAL2	0.86 ± 0.073	0.69 ± 0.120	0.64 ± 0.118	0.59 ± 0.090

Table 4.5: Results of all the classification experiments using original (imbalanced) data. Balanced accuracy was used as performance metric. Values are presented as mean ± standard deviation (SD).

Modality	Feature	CN/pMCI	sMCI/pMCI	CN/MCI
Diffusion MRI	WM-FA	0.55 ± 0.151	0.44 ± 0.150	0.56 ± 0.113
	WM-MD	0.61 ± 0.140	0.48 ± 0.138	0.55 ± 0.090
	GM-FA	0.60 ± 0.137	0.47 ± 0.151	0.59 ± 0.107
	GM-MD	0.62 ± 0.144	0.51 ± 0.146	0.57 ± 0.101
	WM+GM-FA	0.61 ± 0.146	0.44 ± 0.156	0.57 ± 0.110
	WM+GM-MD	0.62 ± 0.139	0.51 ± 0.150	0.57 ± 0.105
	JHULabel-FA	0.53 ± 0.138	0.47 ± 0.138	0.57 ± 0.101
	JHULabel-MD	0.55 ± 0.088	0.48 ± 0.142	0.58 ± 0.078
	JHUTract25-FA	0.57 ± 0.135	0.48 ± 0.142	0.54 ± 0.118
	JHUTract25-MD	0.64 ± 0.148	0.53 ± 0.144	0.59 ± 0.103

Table 4.6: Results of all the classification experiments using balanced data. Balanced accuracy was used as performance metric. Values are presented as mean ± standard deviation (SD).

4.6.1 Influence of the type of features

Generally, voxel-wise features provided higher accuracies than regional features. While the difference was moderate for FA, it was particularly striking for MD: MD region-wise classifications did not perform better than chance for all tasks. In general, for voxel-wise features, the performances obtained with FA and MD were of the same order of magnitude. However, one can note that accuracies were (moderately but systematically) higher for MD than for FA. Finally, for MD, the inclusion of GM (either in isolation or when combined with WM) considerably increased the performance over the use of WM alone (see Table 4.5).

4.6.2 Influence of the imaging modality

Compared to diffusion MRI, T1w MRI lead to higher accuracies for tasks CN vs AD, CN vs pMCI and sMCI vs pMCI (Figure 4.2). On the other hand, both modalities led to low performance for the task CN vs MCI.

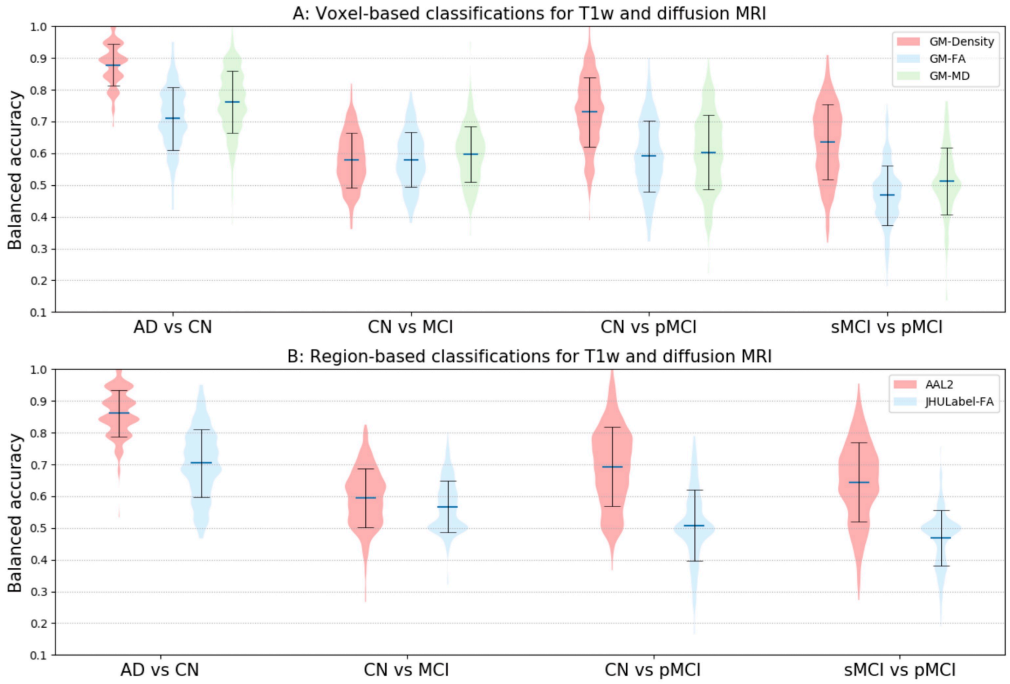

Figure 4.2: Distribution of the balanced accuracy obtained from both T1w and diffusion MRI for tasks CN vs AD, CN vs pMCI and sMCI vs pMCI. Both the results for voxel (top) and regional (bottom) feature with reference atlases are shown.

4.6.3 Influence of the imbalanced data

For voxel-wise classification, compared to the results of classification using imbalanced data, balanced data showed comparable accuracies for all three tasks, as shown in Figure 4.3. For MD region-wise approach, switching from imbalanced data to balanced data, accuracy considerably increased from 0.5 to 0.64 for task CN vs pMCI and from 0.5 to 0.59 for task CN vs MCI.

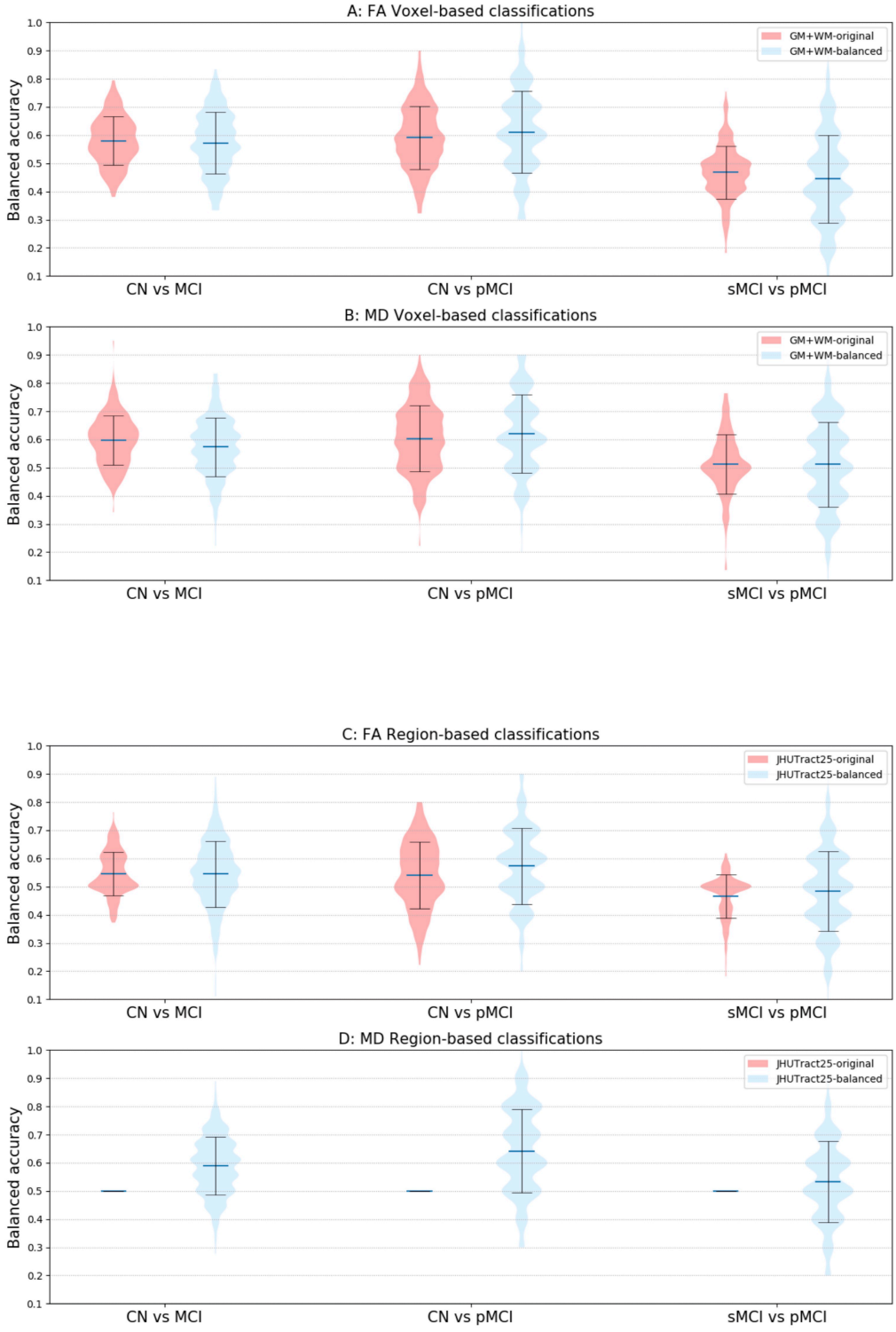

Figure 4.3: Distribution of the balanced accuracy obtained from the randomly balanced classifications for tasks CN vs MCI, CN vs pMCI and sMCI vs pMCI. For comparison, the original data classification results are also displayed. Both the results for voxel (top 2) and regional (bottom 2) feature are shown.

4.6.4 Influence of the feature selection bias

To assess the influence of FS bias, the experiments were restricted to GM+WM-FA and GM+WM-MD features for task CN vs AD, which are the cases with the highest number of features and for which the performance is higher. Results are presented in Figure 4.4.

For both FS algorithms, the non-nested approach resulted in vastly over-optimistic evaluations of performances, from 5% up to 40% increase in balanced accuracy. Specifically, for ANOVA, the highest balanced accuracy was obtained with the first 1% most informative voxels for non-nested approach (0.78 for FA and 0.83 for MD), and with all available voxels for nested approach (0.71 for FA and 0.76 for MD). For SVM-RFE, the highest balanced accuracy was achieved with the first 10% most informative voxels for non-nested approach (0.99 for FA and 0.83 for MD), and with the first 70% most informative voxels with FA (0.75) and the first 1% most informative voxels with MD (0.77) for nested approach. Compared to non-FS (no FS was performed), the nested ANOVA FS did not give better performance. Whilst while the nested SVM-RFE obtained slightly higher accuracies than non-FS: balanced accuracy increases from 0.71 (non-FS) to 0.75 (nested FS) for FA and 0.76 (non-FS) to 0.77 (nested FS) for MD.

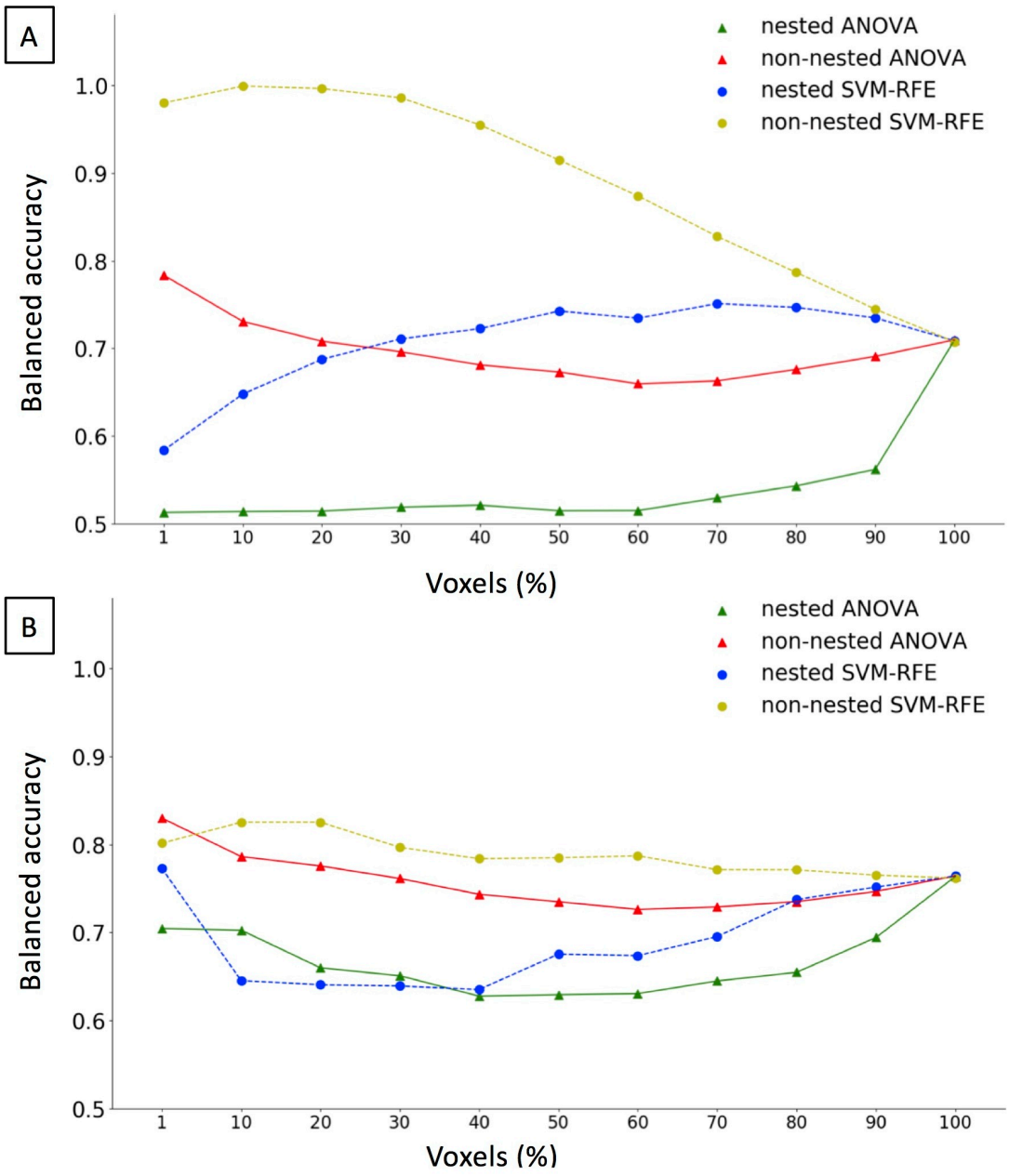

Figure 4.4: Balanced accuracy of CN vs AD obtained varying the number of voxels for ANOVA and SVM-RFE approaches. (A) GM+WM-FA feature; (B) GM+WM-MD feature.

4.6.5 Potential anatomical pattern

Figure 4.5 displays the OMH coefficient maps for the most successful task CN vs AD. For MD features, discriminative voxels were mainly within the GM (hippocampus and medial temporal cortex) (Figure 4.5B). When restricting the analysis to WM, only small regions were discriminative and these regions where outside those of the JHUTract25 atlas (Figure 4.5D), which is consistent with the poor

performances obtained with MD regional features. For GM- density features (Figure 4.5C), the discriminative voxels also included these regions but were more extended (including some regions in the lateral temporal cortex and in the parietal and frontal lobes). For FA, discriminative voxels included both GM and WM regions (Figure 4.5A). In the GM, discriminative voxels were mainly located within the medial temporal lobe. In the WM, they were more diffuse and absent of the deep WM. These regions were close to the forceps minor and major tracts and inferior fronto-occipital fasciculus.

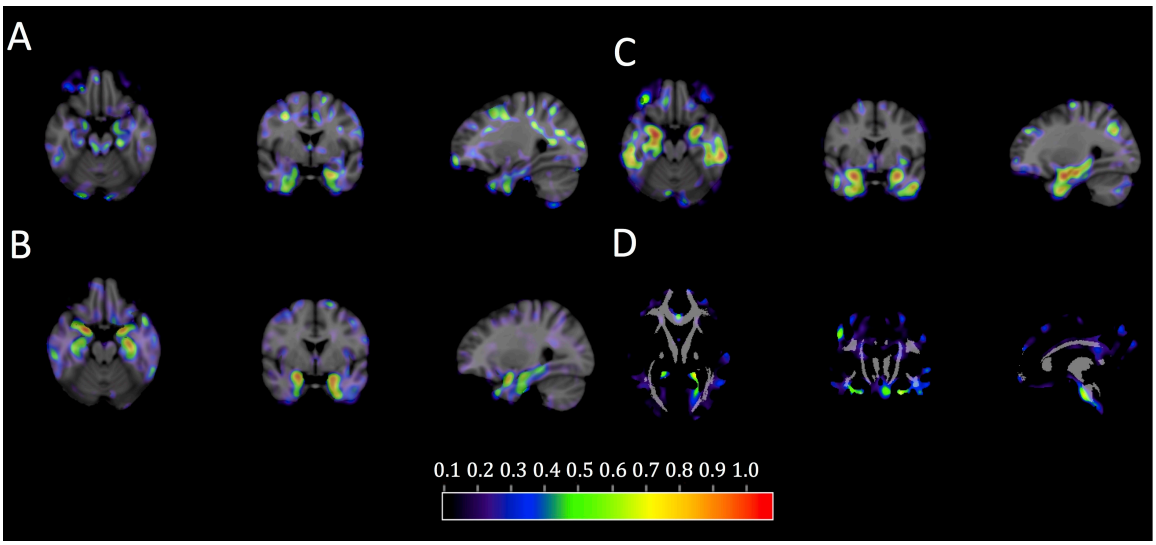

Figure 4.5: Normalized coefficient maps in MNI space. Task CN vs AD with A) GM+WM-FA features; B) GM+WM-MD features; C) GM-Density features; D) WM-MD features superimposed onto the JHUTract25 atlas (in gray). Warm colors, it means higher likelihood of classification into AD.

4.7 Discussion

In the present work, we proposed an open-source framework for the reproducible evaluation of AD classification from diffusion MRI, which extends our previous framework devoted to T1w MRI and PET. We demonstrated its use to assess the influence of different components on classification performances, specifically i) feature types, ii) imaging modalities (T1w MRI and diffusion MRI), iii) data imbalance and iv) FS strategies.

Generally, we hopefully contribute to make evaluation of machine learning approaches in AD more reproducible and more objective. Firstly, providing the tools to fully automatically convert original ADNI diffusion MRI into the community standard BIDS, we hope to facilitate the future work of researchers. Secondly, the literature (Uchida, 2013; Cuingnet et al., 2011; Lu and Weng, 2007) suggested that

image processing procedures, including steps such as preprocessing, parcellation, registration and intensity normalization, have a strong influence on classification results. Hence, a standard diffusion MRI processing pipeline was proposed in the present work. Lastly, we proposed rigorous CV procedures following recent best practices (Varoquaux et al., 2017). The key components are publicly available in Clinica, a freely available software platform for clinical neuroscience research studies. We hope this framework will allow researchers to easily and rigorously evaluate their own classification algorithms, FS algorithms or image processing pipelines.

We then aimed to provide a baseline performance for future work. The results obtained in our framework were in line with the state-of-the-art. In our experiments, we obtained the balanced accuracy with 0.76 for task CN vs AD, 0.60 for task CN vs MCI and 0.61 for task CN vs pMCI. In general, the performances are low and support the idea that DTI metrics, alone, are not highly discriminant for AD classification. However, one can note that, in the literature, several studies using DTI-based features reported superior performances over our work (O'Dwyer et al., 2012; Nir et al., 2015; Demirhan et al., 2015; Mesrob et al., 2012; Termenon et al., 2011; Graña et al., 2011). However, these discrepancies may come from i) the differences in image quality due to different dataset, ii) different sample size and iii) the FS bias, which we will specifically discuss below.

Different types of DTI-based features were assessed. Generally, voxel-wise features provided higher accuracies than region-wise features. This was consistent with a previous study (Demirhan et al., 2015), which reported accuracies of 0.75 for region-wise classification and of 0.88 for voxel-wise classification. Of note, the most discriminative voxels for WM-MD classification are outside the regions of the JHUTract25 atlas. This finding explains the poor performances obtained using MD regional features. Thus, the atlas used for region-wise approaches should be chosen with care. Moreover, FA and MD gave comparable performances for voxel-wise classification. This finding was supported by previous studies (Dyrba et al., 2013; Maggipinto et al., 2017; Lella et al., 2017). One study, which adopted a non-nested FS, reported that MD (accuray of 0.81) outperformed FA (accuracy of 0.75) to discriminate CN from AD (Nir et al., 2015).

We also systematically compared the classification performance between T1w and diffusion MRI. The results showed that T1w MRI outperformed diffusion MRI. Several previous studies have compared the performances of these two modalities. Mesrob et al found that T1w MRI outperformed diffusion MRI (accuracy of O.77 for T1w MRI vs 0.69 for FA from DTI) for task CN vs AD (Mesrob et al., 2012). However, their results were biased due to the adoption of a non-nested FS. Cui et al founded superior performance of T1w MRI over diffusion MRI (accuracy

of 0.61 for T1w MRI vs 0.54 for FA from DTI) when classifying CN from MCI for both modalities (Cui et al., 2012). Using a predefined hippocampus ROI approach, Ahmed et al obtained comparable accuracies for both modalities for tasks CN vs AD (accuracy of O.71 for T1w MRI vs 0.72 for MD from DTI) and CN vs MCI (accuracy of O.65 for T1w MRI vs 0.68 for MD from DTI) (Ahmed et al., 2017). Given the larger sample size and proper FS procedure in our work, we believe that the superior performances of T1w MRI over diffusion MRI is reliable and robust. Several factors could explain the better performances of T1w MRI. First, it is controversial but possible that WM degeneration is a secondary degenerative process compared to brain atrophy (Xie et al., 2006; Agosta et al., 2011). Another possibility is that ADNI diffusion MRI acquisitions used within our study do not make use of the state-of-the-art methods that impact on image quality. In particular, no fieldmap data is acquired which leads to suboptimal correction of magnetic susceptibility artifacts (Wu et al., 2008).

We evaluated the impact of data imbalance on the classification performance. It is commonly agreed that imbalanced data may adversely impact the classification performance as the learned model will be biased towards the majority class to minimize the overall error rate (Estabrooks, 2000; Japkowicz and Others, 2000; Dubey et al., 2014). Efforts have been made to deal with imbalanced data, which could be generally classified as algorithmic level (Akbani, Kwek, and Japkowicz, 2004) and data level (Dubey et al., 2014). In the current study, for voxel-wise classification, we found that the low accuracies obtained in discriminating pMCI from sMCI or CN are potentially caused by the small sample size, rather than by the imbalanced data. Interestingly, Dubey et al showed that a balanced data obtained by several data resampling techniques gave better results than the imbalanced data using T1w MRI from ADNI (Dubey et al., 2014). Thus our hypothesis for the limited sample size needs to be further confirmed as more subjects are becoming available.

In the literature, researchers have emphasized that "double-dipping", referring to the use of test subjects in any part of the training process, such as non-nested FS in this context, is bad practice and may lead to over-fitted classification (Kriegeskorte et al., 2009; Rathore et al., 2017). Similarly, in a recent study, Maggipinto et al showed that the adoption of FS strategies should be taken with care (Maggipinto et al., 2017). They proved that a biased FS, usually a non-nested FS, leads to over-optimistic results. Unfortunately, many previous studies using diffusion MRI for AD classification adopted the non-nested FS and reported nearly perfect classification (O'Dwyer et al., 2012; Mesrob et al., 2012; Graña et al., 2011). In the current study, our finding reinforced the message that non-nested FS could result in over-optimistic results. With the adoption of the non-nested SVM-RFE FS, a

nearly perfect performance was achieved. Besides, FA outperformed MD for classification accuracies for this non-nested FS approach. Similar patterns were also witnessed in the study of Maggipinto et al (Maggipinto et al., 2017). Replacing the non-nested FS with the nested one, we obtained considerably inferior performances. On the other hand, we found that, with SVM-RFE not with ANOVA, the nested FS could potentially (slightly) improve the performance compared to the case no FS was performed. The difference between ANOVA and SVM-RFE may stem from the fact that ANOVA is performed for each feature (voxel) independently while GM and WM in contiguous voxels are highly correlated (Mechelli et al., 2005). Interestingly, another study found that, with the adoption of ReliefF algorithm, FS improved the classification accuracy up to 8% compared to the non-FS for task CN vs AD (Demirhan et al., 2015). However, they did not give enough details concerning their validation scheme. In particular, it is not clear if they used a nested FS (Demirhan et al., 2015).

Visualization of optimal margin hyperplane coefficient maps allowed to study which voxels contribute the most to the discrimination. FA, MD and GM-Density features shared a typical AD anatomical pattern: voxels in hippocampus and temporal lobe showed more discriminative ability in the classification. These findings were consistent with the literature. DTI-based group comparison analyses demonstrated altered FA or MD in the hippocampus (Fellgiebel et al., 2006; Kantarci et al., 2001; Müller et al., 2005; Müller et al., 2007; Hanyu et al., 1998) and in the temporal lobe (Hanyu et al., 1998; Fellgiebel et al., 2005; Head et al., 2005; Stahl et al., 2007). Moreover, the OMH coefficient map displayed a diffuse pattern for WM voxels in our work. Similar patterns of WM voxels were also witnessed in the FS procedure using diffusion MRI (Demirhan et al., 2015; Dyrba et al., 2013).

Our study has the following limitations. First, ADNI diffusion MRI data was not acquired using the state-of-the-art methods which leads to suboptimal image quality. Related works have proven the negative impact of low image quality on MRI analyses (Yendiki et al., 2014; Alexander-Bloch et al., 2016; Reuter et al., 2015). It is thus possible that diffusion MRI acquired using more recent protocols would provide higher classification accuracies. Second, our experiments were performed with a limited data sample size. The limitation came from the data currently available in ADNI. In a previous study (Samper-González et al., 2018), we have demonstrated that increased training set size led to increased classification performances. Thus, both limitations can result in inferior classification performances. Lastly, our study only explored DTI-based features. With a proper CV and FS, more sophisticated features, such as brain tractography- or network-based features, could also be studied.

Chapter 5

Convolutional Neural Networks for Classification of Alzheimer's Disease: Overview and Reproducible Evaluation

This chapter has been submitted as a journal article to *Medical Image Analysis*:

- **Wen, J.**, Thibeau–Sutre, E., Samper-González., J, Routier, A., Bottani, S., Durrleman, S., Burgos, N., Colliot, O. Convolutional Neural Networks for Classification of Alzheimer's Disease: Overview and Reproducible Evaluation, Submitted to **Medical Image Analysis**. https://arxiv.org/pdf/1904.07773.pdf.

5.1 Abstract

Early and accurate diagnosis of Alzheimer's disease (AD) is an important and challenging task. Numerous studies have proposed to address this challenge using machine learning (ML) from brain imaging data. In particular, in the past two years, over 30 papers have proposed to use convolutional neural network (CNN) for AD classification. However, the classification performances across studies are difficult to compare due to variations in components such as participant selection, image preprocessing or validation procedure. Moreover, these studies are hardly reproducible because their frameworks are not publicly accessible and because implementation details are lacking. Lastly, some of these papers may reported biased performances due to inadequate or unclear validation procedure and also it is unclear how the model architecture and parameters were chosen. In the present work, we aim to address these limitations through three main contributions. First, we performed a systematic literature review of studies using CNN for AD classification from anatomical MRI. We identified four main

types of approaches:i) 2D slice-level, ii) 3D patch-level, iii) ROI-based and iv) 3D subject-level CNN. Moreover, we found that more than half of the surveyed papers may have suffered from data leakage and thus reported biased performances. Our second contribution is an open-source framework for classification of AD using CNN and T1-weighted MRI. The framework comprises: tools to automatically convert ADNI, AIBL and OASIS data into the BIDS standard, a modular set of image preprocessing procedures, classification architectures and an evaluation framework. Thirdly, we used this framework to rigorously compare different CNN architectures, which are representative of the existing literature, and to study the influence of key components on classification performances. Importantly, the data was split into training/validation/test sets at the very beginning. Training/validation sets were used in a CV procedure for model selection. To avoid any overfitting of the test sets by testing different architectures, hyperparameters or preprocessing, the test sets were left untouched until the end of the peer-review procedure. We included three test sets: one from ADNI to assess generalization to different patients from the same study, one from AIBL for generalization to a different study but with similar imaging protocols and inclusion criteria, one from OASIS to assess generalization to different protocols and inclusion criteria. [Results will be modified after peer-review]. On the validation set, the ROI-based (hippocampus) CNN achieved highest balanced accuracy (0.86 for AD vs CN and 0.80 for sMCI vs pMCI) compared to other approaches. Transfer learning with autoencoder pre-training did not improve the average accuracy but reduced the variance. Training using longitudinal data resulted in similar or higher performance, depending on the approach, compared to training with only baseline data. Sophisticated image preprocessing did not improve the results. Lastly, CNN performed similarly to standard SVM for task AD vs CN but outperformed SVM for task sMCI vs pMCI, demonstrating the potential of deep learning for challenging diagnostic tasks. All the code of the framework and the experiments is publicly available: general-purpose tools have been integrated into the Clinica software (`www.clinica.run`) and the paper-specific code is available at: `https://gitlab.icm-institute.org/aramislab/AD-ML`.

5.2 Introduction

Alzheimer's disease (AD), a chronic neurodegenerative disease causing the death of nerve cells and tissue loss throughout the brain, usually starts slowly and worsens over time (McKhann et al., 1984). AD is expected to affect 1 out of 85 people in the world by the year 2050 (Brookmeyer et al., 2007). The cost of caring

for AD patients is also expected to raise dramatically, thus the need of individual computer-aided systems for early and accurate AD diagnosis.

Magnetic resonance imaging (MRI) offers the possibility to study pathological brain changes associated with AD in vivo (Ewers et al., 2011). Over the past decades, neuroimaging data have been increasingly used to characterize AD by means of machine learning (ML) methods, offering promising tools for individualized diagnosis and prognosis (Falahati, Westman, and Simmons, 2014; Haller, Lovblad, and Giannakopoulos, 2011; Rathore et al., 2017). A large number of studies have proposed to use predefined features (including regional and voxel-based measurements) from image preprocessing pipelines followed by different types of classifiers, such as support vector machines (SVM) or random forests. Such approach is often referred to as conventional ML (LeCun, Bengio, and Hinton, 2015). More recently, deep learning (DL), as a newly emerging ML methodology, has made a big leap in the domain of medical imaging (Bernal et al., 2018; Liu et al., 2018a; Selvikvåg Lundervold and Lundervold, 2018; Razzak, Naz, and Zaib, 2018; Wen et al., 2018a). As the most widely used architecture of DL, convolutional neural network (CNN) has attracted huge attention due to its great success in image classification (Krizhevsky, Sutskever, and Hinton, 2012). Contrary to conventional ML, DL allows the automatic abstraction of low-to-high level latent feature representations (e.g. lines, dots, or edges for low level features, and objects or larger shapes for high level features). Thus, one can hypothesize that DL depends less on image preprocessing and requires less prior on other complex procedures, such as feature selection, resulting in a more objective and less bias-prone process (LeCun, Bengio, and Hinton, 2015).

Very recently, numerous studies have proposed to assist diagnosis of AD by means of CNNs (Aderghal et al., 2018; Aderghal, Benois-Pineau, and Afdel, 2017; Aderghal et al., 2017; Bäckström et al., 2018; Basaia et al., 2018; Cheng and Liu, 2017; Cheng et al., 2017; Farooq et al., 2017; Gunawardena, Rajapakse, and Kodikara, 2017; Hon and Khan, 2017; Hosseini Asl et al., 2018; Islam and Zhang, 2018; Islam and Zhang, 2017; Korolev et al., 2017; Lian et al., 2018; Li, Liu, and Alzheimer's Disease Neuroimaging Initiative, 2018; Li, Cheng, and Liu, 2017; Lin et al., 2018; Liu et al., 2018c; Liu et al., 2018b; Liu et al., 2018e; Qiu et al., 2018; Senanayake, Sowmya, and Dawes, 2018; Shmulev, Belyaev, and The Alzheimer's Disease Neuroimaging Initiative, 2018; Taqi et al., 2018; Valliani and Soni, 2017; Vu et al., 2018; Vu et al., 2017; Wang et al., 2019; Wang et al., 2017; Wang et al., 2018b; Wu et al., 2018). However, classification performances among these studies are not directly comparable because they differ in terms of: i) sets of participants; ii) image preprocessing procedures, iii) cross-validation (CV) procedure and iv) reported evaluation metrics. It is thus impossible to determine which approach performs best.

The generalization ability of these approaches also remains unclear. In DL, the use of fully independent test sets is even more critical than in conventional ML, because of the very high flexibility with numerous possible model architecture and training hyperparameter choices. Assessing generalization to other studies is also critical to ensure that the characteristics of the considered study have not been overfitted. In previous works, the generalization may be questionable due to: i) inadequate validation procedures, ii) absence of independent test set, or iii) test set chosen from the same study.

In our previous studies (Samper-González et al., 2018; Wen et al., 2018b), we have proposed an open source framework for reproducible evaluation of AD classification using conventional ML methods. The framework comprises: i) tools to automatically convert three publicly available datasets into the Brain Imaging Data Structure (BIDS) format (Gorgolewski et al., 2016) and ii) a modular set of preprocessing pipelines, feature extraction and classification methods, together with an evaluation framework, that provide a baseline for benchmarking the different components. We demonstrated the use of this framework on positron emission tomography (PET), T1-weighted (T1w) MRI (Samper-González et al., 2018) and diffusion MRI data (Wen et al., 2018b).

In the present work, we extended the framework to DL approaches using CNNs. We first reviewed and summarized the different studies using CNNs and anatomical MRI for AD classification. In particular, we reviewed their validation procedures and the possible presence of data leakage. Then, different CNN architectures were implemented in our open source framework. We compared the performance of these approaches and studied the influence of key components on the classification performance. The proposed CNNs were also compared to a conventional ML approach based on a linear SVM. Lastly, we assessed the generalization ability of the CNN models within (training and testing on ADNI) and across datasets (training on ADNI and testing on AIBL or OASIS).

All the code of the framework and the experiments is publicly available: general-purpose tools have been integrated into Clinica (Routier et al., 2018), an open-source software platform that we developed to process data from neuroimaging studies, and the paper-specific code is available at: `https://gitlab.icm-institute.org/aramislab/AD-ML`.

5.3 State of the art

We performed an online search of publications concerning classification of AD using neural networks based on anatomical MRI in PubMed and Scopus, from January 1990 to the 15th of January 2019. This resulted in 406 records which were

screened according to their abstract, type and content (more details are provided in online supplementary C eMethod 1) to retain only those focused on the classification of AD stages using at least anatomical MRI as input of a neural network. This resulted in 71 studies. Out of these 71, 32 studies used CNN on image data in an end-to-end framework, which is the focus of our work. We found that a substantial proportion of these studies performed a biased evaluation of results, due to the presence of data leakage, hence we first discuss the data leakage issues that we encountered in our bibliography (Section 3.1). We then review the 32 studies that used end-to-end CNNs on image data, the main focus of this work (Section 3.2). Finally, we briefly describe other studies that were kept in our bibliography but that are out of our scope (Section 3.3).

5.3.1 Main causes of data leakage

Unbiased evaluation of classification algorithms is critical to assess their potential clinical value. A major source of bias is data leakage, which refers to the use of test data in any part of the training process (Kriegeskorte et al., 2009; Rathore et al., 2017). Data leakage can be difficult to detect for DL approaches as they can be complex and very flexible. We assessed the prevalence of data leakage among the papers described in section 3.2 and analyzed its causes. The articles were labeled into three categories: i) *Clear* when data leakage was explicitly witnessed; ii) *Unclear* when no sufficient explanation was offered and iii) *None detected*. The results are summarized in the last of column of Table 5.1. They were further categorized according to the cause of data leakage. Four main causes were identified:

- **Bad data split**. Not splitting the dataset at the subject-level when defining the training, validation and test sets can result in data from the same subject to appear in several sets. This problem can occur when patches or slices are extracted from a 3D image, or when images of the same subject are available at multiple time points. (Bäckström et al., 2018) showed that, using a longitudinal dataset, a biased dataset split (at the image level) can result in an accuracy increase of 8 percent points compared to an unbiased split (at the subject-level).

- **Late split**. Procedures such as data augmentation, feature selection or AE pre-training must never use the test set and thus be performed after the training/validation/test split to avoid biasing the results. For example, if data augmentation is performed before isolating the test data from the training/validation data, then images generated from the same original image may be found in both sets, leading to a problem similar to the wrong data split.

- **Biased transfer learning**. Transfer learning can result in data leakage when the source and target domains overlap, for example when a network pre-trained on the AD vs CN task is used to initialize a network for the MCI vs CN task and that the CN subjects in the training or validation sets of the source task (AD vs CN) are also in the test set of the target task (MCI vs CN).
- **Absence of an independent test set**. The test set should only be used to evaluate the final performance of the classifier, not to chose the training hyperparameters (e.g. learning rate) of the model. A separate validation set must be used beforehand for hyperparameter optimization.

Note that we did not consider data leakage occurring when designing the network architecture, possibly chosen thanks to successive evaluations on the test set, as the large majority of the studies does not explicit this step.

All these data leakage causes may not have the same impact on data performance. For instance, it is likely that a wrong data split in a longitudinal dataset or at the slice-level is more damaging than a late split for AE pre-training.

5.3.2 Classification of AD with end-to-end CNNs

This section focuses on CNNs applied to an Euclidean space (here a 2D or 3D image) in an end-to-end framework (from the input to the classification). A summary of these studies can be found in Table 5.1. The table indicates whether data leakage was potentially present, which can have biased the performance upwards. Below, we categorized studies according to the type of input of the network: i) 2D slice-level, ii) 3D patch-level, iii) ROI-based and iv) 3D subject-level.

Study	Performance				Approach	Data leakage	
	AD/CN	sMCI/pMCI	MCI/CN	AD/MCI	Multi-class		
(Aderghal, Benois-Pineau, and Afdel, 2017)	0.84[1]	–	0.65[1]	0.67[1]	–	ROI-based	None detected
(Aderghal et al., 2018)	0.90[2]	–	0.73[2]	0.83[2]	–	ROI-based	None detected
(Bäckström et al., 2018)	0.90[1]	–	–	–	–	3D subject-level	None detected
(Cheng et al., 2017)	0.87[1]	–	–	–	–	3D patch-level	None detected
(Cheng and Liu, 2017)	0.85[1]	–	–	–	–	3D subject-level	None detected
(Islam and Zhang, 2018)	–	–	–	–	0.93[1]	2D slice-level	None detected
(Korolev et al., 2017)	0.80[1]	–	–	–	–	3D subject-level	None detected
(Li, Cheng, and Liu, 2017)	0.88[1]	–	–	–	–	3D subject-level	None detected
(Li, Liu, and Alzheimer's Disease Neuroimaging Initiative, 2018)	0.90[1]	–	0.74[1]	–	–	3D patch-level	None detected
(Lian et al., 2018)	0.90[1]	0.80[1]	–	–	–	3D patch-level	None detected
(Liu et al., 2018e)	0.91[1]	0.78[1]	–	–	–	3D patch-level	None detected
(Liu et al., 2018b)	0.91[1]	–	–	–	–	3D patch-level	None detected
(Qiu et al., 2018)	–	0.83[1]	–	–	–	2D slice-level	None detected
(Senanayake, Sowmya, and Dawes, 2018)	0.76[1]	–	0.75[1]	0.76[1]	–	3D subject-level	None detected
(Shmulev, Belyaev, and The Alzheimer's Disease Neuroimaging Initiative, 2018)	–	0.62[1]	–	–	–	3D subject-level	None detected
(Valliani and Soni, 2017)	0.81[1]	–	–	–	0.57[1]	2D slice-level	None detected
(Aderghal et al., 2017)	0.91[1]	–	0.66[1]	0.70[1]	–	ROI-based	Unclear (b,c)
(Basaia et al., 2018)	0.99[2]	0.75[2]	–	–	–	3D subject-level	Unclear (b)
(Hon and Khan, 2017)	0.96[1]	–	–	–	–	2D slice-level	Unclear (a,c)
(Hosseini Asl et al., 2018)	0.99[1]	–	0.94[1]	1.00[1]	0.95[1]	3D subject-level	Unclear (a)
(Islam and Zhang, 2017)	–	–	–	–	0.74[1]	2D slice-level	Unclear (b,c)
(Lin et al., 2018)	0.89[1]	0.73[1]	–	–	–	ROI-based	Unclear (b)
(Liu et al., 2018c)	0.85[1]	0.74[1]	–	–	–	3D patch-level	Unclear (d)
(Taqi et al., 2018)	1.00[1]	0.74[1]	–	–	–	2D slice-level	Unclear (b)
(Vu et al., 2017)	0.85[1]	–	–	–	–	3D subject-level	Unclear (a)
(Wang et al., 2018b)	0.98[1]	–	–	–	–	2D slice-level	Unclear (b)
(Bäckström et al., 2018)	0.99[1]	–	–	–	–	3D subject-level	Clear (a)
(Farooq et al., 2017)	–	–	–	–	0.99[1]	2D slice-level	Clear (a,c)
(Gunawardena, Rajapakse, and Kodikara, 2017)	–	–	–	–	0.96[1]	3D subject-level	Clear (a,b)
(Vu et al., 2018)	0.86[1]	–	0.86[1]	0.77[1]	0.80[1]	3D subject-level	Clear (a,c)
(Wang et al., 2017)	–	–	0.91[1]	–	–	2D slice-level	Clear (a,c)
(Wang et al., 2019)	0.99[1]	–	0.98[1]	0.94[1]	0.97[1]	3D subject-level	Clear (b)
(Wu et al., 2018)	–	–	–	–	0.95[1]	2D slice-level	Clear (a,b)

Table 5.1: Summary of the studies performing classification of AD using CNNs on anatomical MRI. Summary of the studies performing classification of AD using CNNs on anatomical MRI. Studies are categorized according to the potential presence of data leakage: (A) studies without data leakage; (B) studies with potential data leakage. Types of data leakage if presented: a, Wrong dataset split; b, Absence of independent test set; c, Late split; d, Biased transfer learning. 1: accuracy; 2: balanced accuracy. * In (Bäckström et al., 2018), data leakage was introduced on purpose in order to study its influence. Thus, this study is present in both categories. † Use of imbalanced accuracy on a severely imbalanced dataset (one class is less than half of the other), leading to an over-optimistic estimation of performance.

5.3.2.1 2D slice-level CNN

Several studies used 2D CNNs with input composed of the set of 2D slices extracted from the MRI 3D volume (Farooq et al., 2017; Gunawardena, Rajapakse, and Kodikara, 2017; Hon and Khan, 2017; Islam and Zhang, 2018; Islam and Zhang, 2017; Qiu et al., 2018; Taqi et al., 2018; Valliani and Soni, 2017; Wang et al., 2017; Wang et al., 2018b; Wu et al., 2018). The main advantages of this approach are: i) existing CNNs which had huge successes for natural image classification tasks (e.g. ResNet and VGGNet) can be easily borrowed and used in a transfer learning fashion; ii) the number of training samples is the number of slices, thus potentially much larger than the number of subjects.

In this subsection of the bibliography, we found only one study in which neither data leakage was detected neither biased metrics were used (Valliani and Soni, 2017). They used a single axial slice per subject (taken in the middle of the 3D volume) to compare the ResNet to an original CNN with only one convolutional layer and two FC layers. They studied the impact of both transfer learning by initializing their networks with models trained on ImageNet, and data augmentation with affine transformations. They conclude that the ResNet architecture is more efficient than their baseline CNN and that pre-training and data augmentation improve the accuracy of the ResNet architecture.

In all other studies, we detected a problem in the evaluation: either data leakage was present (or at least suspected) (Farooq et al., 2017; Gunawardena, Rajapakse, and Kodikara, 2017; Hon and Khan, 2017; Islam and Zhang, 2017; Taqi et al., 2018; Wang et al., 2017; Wang et al., 2018b; Wu et al., 2018) or they used an imbalanced metric on a severely imbalanced dataset (one class is less than half of the other) (Islam and Zhang, 2018; Qiu et al., 2018). Causes of data leakage are described in 3.1 section. Theses studies differ in terms of slice selection: i) one study used all slices of a given plane (except the very first and last ones that are not informative) (Farooq et al., 2017); ii) other studies selected several slices using an automatic (Hon and Khan, 2017; Wu et al., 2018) or manual criterion (Qiu et al., 2018); iii) one study used only one slice (Wang et al., 2018b). Working with several slices implies to fuse the classifications obtained at the slice-level to obtain a classification at the subject-level. Only one study (Qiu et al., 2018) explained how they performed this fusion. Other studies didn't implement fusion and reported the slice-level accuracy (Farooq et al., 2017; Gunawardena, Rajapakse, and Kodikara, 2017; Hon and Khan, 2017; Wang et al., 2017; Wu et al., 2018) or it is unclear if the accuracy was computed at the slice- or subject-level (Islam and Zhang, 2018; Islam and Zhang, 2017; Taqi et al., 2018).

The main limitation of the 2D slice-level approach is that MRI is 3-dimensional, whereas the 2D convolutional filters analyze all slices of a subject independently.

Moreover, there are many different ways to select slices that are used as input (as all of them may not be informative) and slice-level accuracy and subject-level accuracy are often confused.

5.3.2.2 3D patch-level CNN

To compensate for the absence of 3D information in the 2D slice-level approach, more studies focused on the 3D patch-level classification (see Table 5.1). In these frameworks, the input is composed of a set of 3D patches extracted from an image. In principle, this could results, as in the 2D slice-level approach, in a larger sample size, since the number of samples would be the number of patches (and not the number of subjects). However, this potential advantage is not used in the surveyed papers because they trained independent CNNs for each patch. Additional advantages of patches are the lower memory usage which may be useful when one has limited resources and the lower number of learnt parameters. However, this last advantage is present only when one uses the same network for all patches.

Two studies (Cheng et al., 2017; Liu et al., 2018c) used very large patches. Specifically, they extracted 27 overlapping 3D patches of size 50x41x40 voxels covering the whole volume of the MRI data (100x81x80 voxels). They individually trained 27 convolutional networks (one per patch) comprising four convolutional layers and two FC layers. Then, an ensemble CNN was trained to provide a decision at the subject level. This ensemble CNN is partly initialized with the weights of the previously trained CNNs. (Liu et al., 2018c) reused exactly the same architecture than (Cheng et al., 2017) and enriched it with a fusion of PET and MRI inputs. They also gave the results obtained using the MRI modality only, which is the result reported in Table 5.1.

(Li, Liu, and Alzheimer's Disease Neuroimaging Initiative, 2018) used smaller patches (32x32x32). By decreasing the size of the patches, they had to take into account a possible discrepancy between patches taken at the same coordinates for different subjects. To avoid this dissimilarity between subjects without performing a non-linear registration, they clustered their patches using k-means. Then they trained one CNN per cluster, and assembled the features obtained at the cluster-level in a similar way than (Cheng et al., 2017; Liu et al., 2018c).

The following three studies (Lian et al., 2018; Liu et al., 2018e; Liu et al., 2018b) decided to use even smaller patches (19x19x19). Nevertheless, they did not use all possible patches from the MRI data but chose only some of them based on anatomical landmarks. These anatomical landmarks are found in a supervised manner via a group comparison between AD and CN subjects. However, this method requires a non-linear registration in order to build the correspondence between voxels of different subjects. Similarly to other studies, in (Liu et al., 2018b), one CNN is

pre-trained for each patch and the outputs are fused to obtain the diagnosis of a subject. The approach of (Liu et al., 2018e) is slightly different as they consider that one patch cannot be labelled with a diagnosis, hence they do not train one CNN per patch individually before ensemble learning but train the ensemble network from scratch. Finally (Lian et al., 2018) proposed a weakly-supervised guidance: the loss of the network is based on the final classification scores at the subject-level as well as the intermediate classification done on the patch- and region-level.

There are far less data leakage problems in this section, with only one doubt on the validity of the transfer learning between the AD vs CN task and the MCI vs CN task in (Liu et al., 2018c) because of a lack of explanations. Nevertheless this has no impact on the result of the AD vs CN task for which we didn't detect any problem of data leakage.

As for 2D-slice level in which a selection of slices must be made, one must choose the size and stride of patches. The choice of these hyperparameters will depend on the MRI preprocessing (e.g. a non-linear registration is likely needed for smaller patches). Nevertheless, note that the impact of these hyperparameters has been studied in the pre-cited studies (which has not been done for the 2D slice-level approaches). The main drawback of these approaches is the complexity of the framework: one network is trained for each patch position and these networks are successively fused and retrained at different levels of representation (region-level, subject-level).

5.3.2.3 ROI-based CNN

3D patch-level methods use the whole MRI by slicing it in smaller inputs. However, most of these patches are not informative as they contain parts of the brain that are not affected by the disease. Methods based on regions of interest (ROI) overcome this issue by focusing on regions which are known to be informative. In this way, the complexity of the framework can be decreased as fewer inputs are used to train the networks. In all the following studies, the ROI chosen was the hippocampus, which is well-known to be affected early in AD (Dickerson et al., 2001; Salvatore et al., 2015; Schuff et al., 2009). Studies differ by the definition of the hippocampal ROI.

(Aderghal, Benois-Pineau, and Afdel, 2017; Aderghal et al., 2017; Aderghal et al., 2018) performed a linear registration and defined a 3D bounding box comprising all the voxels of the hippocampus according to a segmentation with the AAL atlas. As they use only one or three patches (based on hippocampus) per patient, they do not cover the entire region. The first study (Aderghal, Benois-Pineau, and Afdel, 2017) only uses the sagittal view and classifies one patch per patient. The architecture of the CNN is made of two convolutional layers associated with max

pooling, and one FC layer. In the second study (Aderghal et al., 2017), all the views (sagittal, coronal and axial) are used to generate patches. Then, three patches are generated per subject and accordingly three networks are trained for each view and then fused. The last study of the same author (Aderghal et al., 2018) focuses on the transfer learning from anatomical MRI to diffusion MRI, which is out of our scope.

In (Lin et al., 2018) a non-linear registration was performed to obtain a voxel correspondence between the subjects, and the voxels belonging to the hippocampus were identified after a segmentation implemented with MALP-EM (Ledig et al., 2015). 151 patches were extracted per image with sampling positions fixed during experiments. Each of them was made of the concatenation of three 2D slices along the three possible planes (sagittal, coronal and axial) originated at one voxel belonging to the hippocampus.

The main drawback of this methodology is that it studies only one (or a few) regions while AD alterations span over multiple brain areas. However, it may allow to avoid overfitting because the inputs are smaller (3000 voxels in our bibliography) and fewer than in methods allowing patch combinations.

5.3.2.4 3D subject-level CNN

Recently, with the boost of high-performance computing resources, more studies used a 3D subject-level approach (see Table 5.1). In this approach, the whole MRI is used at once and the classification is performed at the subject level. The advantage is that the spatial information is fully integrated.

Some studies readapted two classical architectures to fit the whole MRI: the ResNet and VGGNet (Korolev et al., 2017; Shmulev, Belyaev, and The Alzheimer's Disease Neuroimaging Initiative, 2018). In both cases, results obtained on VGG and ResNet are equivalent, and their best results are below those of other studies of the same section. Another study (Senanayake, Sowmya, and Dawes, 2018) proposed to use a set of complex modules from classical architectures such as ResNet and DenseNet (dilated convolutions, dense blocks and residual blocks), also without success.

Other studies defined original architectures (Bäckström et al., 2018; Basaia et al., 2018; Cheng and Liu, 2017; Hosseini Asl et al., 2018; Li, Cheng, and Liu, 2017; Vu et al., 2018; Wang et al., 2019). Among these, we did not detect data leakage in only three of them (Bäckström et al., 2018; Cheng and Liu, 2017; Li, Cheng, and Liu, 2017). (Bäckström et al., 2018; Cheng and Liu, 2017) had a similar approach by training one network from scratch on augmented data. One crucial difference between these two studies is the preprocessing step: (Bäckström et al., 2018) used a non-linear registration whereas (Cheng and Liu, 2017) performed no registration.

(Li, Cheng, and Liu, 2017) proposed a more complex framework fusing the results of a CNN and three networks pre-trained with an AE.

For the other studies using original architectures, we suspect data leakage (Bäckström et al., 2018; Basaia et al., 2018; Hosseini Asl et al., 2018; Vu et al., 2017; Vu et al., 2018; Wang et al., 2019), hence their performance cannot be fairly compared to the previous ones. However we noted that (Hosseini Asl et al., 2018; Vu et al., 2017; Vu et al., 2018) studied the impact of pre-training with an AE, and concluded that it improved their results (accuracy increased from 5 to 10 percent points).

In 3D-subject level approach the number of samples is small compared to the number of parameters to optimize. Indeed, there is one sample per subject, typically a few hundreds to thousands subjects in a dataset, thus increasing the risk of overfitting.

5.3.2.5 Conclusion

A high number of these 32 studies presented biased performance because of data leakage: 10 were labeled as *Unclear* because of lack of explanations, and 6 as *Clear* in which we assert the presence of data leakage (we do not count here the study of Backstrom et al (Bäckström et al., 2018) as data leakage was done deliberately to study its impact). This means that about 50% of the surveyed studies could report biased performances (see Table 1 and Section 3.1 for more details).

In addition to that problem, most studies are not comparable because the datasets used, subjects selected among them and preprocessing performed are different. Furthermore, these studies often do not motivate the choice of their architecture or hyperparameters. It might be that many of them have been tried (but not reported) thereby resulting in biased performances on the test set. Finally, the code is often not available, neither are key implementation details (such as hyperparameters values) making them difficult if not impossible to reproduce.

5.3.3 Other deep learning approaches for AD classification

Several studies found in our literature search are out of our scope: either CNNs were not used in an end-to-end manner or not applied to images, or other network architectures were implemented, or the approach required longitudinal or multimodal data.

In several studies, the CNN is used as a feature extractor only and the classification is performed using either a random forest (Chaddad, Desrosiers, and Niazi, 2018), SVM with linear or polynomial kernels and logistic regression (ÇitakER, Goularas, and Ormeci, 2017), extreme ML (Lin et al., 2018), SVM with different kernels (Shen et al., 2018), or logistic regression and XGBoost (decision trees)

(Shmulev, Belyaev, and The Alzheimer's Disease Neuroimaging Initiative, 2018). Only Shmulev et al compared the results obtained with the CNN classification and those obtained with other classifiers based on features extracted by the CNN and concluded that the latter is more efficient. Instead of being directly applied to the image, CNNs can be applied to pre-extracted features. This is the case of (Suk et al., 2017) where the CNN is applied to the outputs of several regression models performed between MRI-based features and clinical scores with different hyper-parameters. CNNs can also be applied to non-Euclidean spaces, such as graphs of patients (Parisot et al., 2018) or the cortical surface (Mostapha et al., 2018).

Other architectures have been applied to anatomical MRI. Many studies used a variant of the multilayer perceptron composed of stacked FC layers (Amoroso et al., 2018; Baskar, Jayanthi, and Jayanthi, 2018; Cárdenas-Peña, Collazos-Huertas, and Castellanos-Dominguez, 2017; Cárdenas-Peña, Collazos-Huertas, and Castellanos-Dominguez, 2016; Dolph et al., 2017; Gorji and Haddadnia, 2015; Gutiérrez-Becker and Wachinger, 2018; Jha, Kim, and Kwon, 2017; Lu et al., 2018; Mahanand et al., 2012; Maitra and Chatterjee, 2006; Ning et al., 2018; Raut and Dalal, 2017; Shams-Baboli and Ezoji, 2017; Zhang et al., 2018; Zhou et al., 2019) or of a probabilistic neural network (Duraisamy, Shanmugam, and Annamalai, 2019; Mathew, Vivek, and Anurenjan, 2018). In other studies, high-level representations of the features are extracted using both unsupervised (deep Boltzmann machine (Suk, Lee, and Shen, 2014) and AE (Suk, Lee, and Shen, 2015)) and supervised structures (deep polynomial networks (Shi et al., 2018)), and an SVM is used for classification. Non-CNNs architectures require extensive preprocessing as they have to be applied to imaging features such as cortical thickness, shapes, or texture and regional features. Moreover, feature selection or embedding is also often required (Amoroso et al., 2018; Dolph et al., 2017; Jha, Kim, and Kwon, 2017; Lu et al., 2018; Mahanand et al., 2012; Mathew, Vivek, and Anurenjan, 2018; Suk, Lee, and Shen, 2015; Suk, Lee, and Shen, 2014) to further reduce dimensionality.

DL-based classification approaches are not limited to cross-sectional anatomical MRI. Longitudinal studies exploit information extracted from several time points of the same subject. A specific structure, the recurrent neural network, has been used to study the temporal correlation between the images (Bhagwat et al., 2018; Cui, Liu, and Li, 2018; Wang et al., 2018c). Several studies exploit multimodal data (Aderghal et al., 2018; Cheng and Liu, 2017; Esmaeilzadeh et al., 2018; Li et al., 2015; Liu et al., 2016; Liu et al., 2015; Liu et al., 2018c; Liu et al., 2018d; Lu et al., 2018; Ning et al., 2018; Ortiz et al., 2016; Qiu et al., 2018; Raut and Dalal, 2017; Senanayake, Sowmya, and Dawes, 2018; Shi et al., 2018; Shmulev, Belyaev, and The Alzheimer's Disease Neuroimaging Initiative, 2018; Spasov et al., 2018; Suk, Lee, and Shen, 2014; Thung, Yap, and Shen, 2017; Vu et al., 2017; Vu et al., 2018;

Zhou et al., 2019; Zhou et al., 2017), such as multiple imaging modalities (positron emission tomography and diffusion tensor imaging), demographic data, genetics, clinical scores, or cerebrospinal fluid biomarkers. Note that multimodal studies that also reported results with MRI only (Aderghal et al., 2018; Cheng and Liu, 2017; Liu et al., 2018c; Qiu et al., 2018; Senanayake, Sowmya, and Dawes, 2018; Shmulev, Belyaev, and The Alzheimer's Disease Neuroimaging Initiative, 2018; Vu et al., 2017; Vu et al., 2018) are displayed in Table 5.1. Exploiting multiple time-points and/or modalities is expected to improve the classification performance. However, these studies can be limited by the small number subjects having all the required time points and modalities.

5.4 Materials

The data used in our study are from three public datasets: ADNI AIBL and OASIS. Information about these datasets is presented in supplementary C eMethod 2. We used the T1w MRI available in each of these studies. For the detailed MRI protocols, one can see (Samper-González et al., 2018). This also describes which T1 MRI was chosen in case where multiple images for a given visit exist.

The ADNI dataset used in our experiments comprises 1455 participants for whom a T1w MR image was available at at least one visit. For each ADNI subset, five diagnosis groups were considered:

- CN: sessions of subjects who were diagnosed as CN at baseline and stayed stable during the follow-up;
- AD: sessions of subjects who were diagnosed as AD at baseline and stayed stable during the follow-up;
- MCI: sessions of subjects who were diagnosed as MCI, EMCI or LMCI at baseline, who did not encounter multiple reversions and conversions and who did not regress to CN diagnosis;
- pMCI: sessions of subjects who were diagnosed as MCI, EMCI or LMCI at baseline, and progressed to AD between the current visit and the visit at 36 months;
- sMCI: sessions of subjects who were diagnosed as MCI, EMCI or LMCI at baseline, never progressed to AD months and were followed at least 36 months after the current visit.

Naturally, all sessions of the pMCI and sMCI groups are included in the MCI group. Note that the reverse is false, as some MCI subjects did not convert to

AD but were not followed long enough to state whether they were sMCI. Moreover, for 30 sessions, the preprocessing did not pass the quality check (QC) (see the Method section) and these data were removed from our dataset. 2 subjects were entirely removed because the preprocessing failed for all their sessions. Table **??** summarizes the demographics, and the MMSE and global CDR scores of the ADNI participants.

Table 5.2 summarizes the demographics, and the MMSE and global CDR scores of the participants in this study.

	Subjects	Sessions	Age	Gender	MMSE	CDR
CN	330	1830	74.4 ± 5.8[59.8,89.6]	160M/170F	29.1 ± 1.1[24,30]	0:330
MCI	787	3458	73.3 ± 7.5[54.4,91.4]	464M/323F	27.5 ± 1.8[23,30]	0:2;0.5:785
sMCI	298	1046	72.3 ± 7.4[55.0,88.4]	175M/123F	28.0 ± 1.7[23,30]	0.5:298
pMCI	295	865	73.8 ± 6.9[55.1,88.3]	176M/119F	26.9 ± 1.7[23,30]	0.5:293;1:2
AD	336	1106	75.0 ± 7.8[55.1,90.9]	185M/151F	23.2 ± 2.1[18,27]	0.5:160;1:175; 2:1

Table 5.2: Summary of participant demographics, mini-mental state examination (MMSE) and global clinical dementia rating (CDR) scores for ADNI. Values are presented as mean ± SD [range]. M: male, F: female

The AIBL dataset considered in this work is composed of 598 participants for whom a T1w MR image and an age value was available at at least one visit. The criteria used to create the diagnosis groups are identical to the ones used for ADNI. Table 5.3 summarizes the demographics, and the MMSE and global CDR scores of the AIBL participants. After the preprocessing pipeline, 7 sessions were removed without changing the number of subjects.

	N	Age	Gender	MMSE	CDR
CN	429	72.5 ± 6.2[60,92]	183M/246F	28.8 ± 1.2[25,30]	0:406;0.5:22;1:1
MCI	93	75.4 ± 6.9[60,96]	50M/43F	27.0 ± 2.1[20,30]	0:6;0.5:86;1:1
sMCI	13	76.7 ± 6.5[64,87]	8M/5F	28.2 ± 1.5[26,30]	0.5:13
pMCI	20	78.1 ± 6.6[63,79]	10M/10F	26.7 ± 2.1[22,30]	0.5:20
AD	76	73.9 ± 8.0[55,93]	33M/43F	20.6 ± 5.5[6,29]	0.5:31;1:36;2:7;3:2

Table 5.3: Summary of participant demographics, mini-mental state examination (MMSE) and global clinical dementia rating (CDR) scores for AIBL. Values are presented as mean ± SD [range]. M: male, F: female

The OASIS dataset considered in this work is composed of 193 participants aged 62 years or more (minimum age of the participants diagnosed with AD). Table 5.4 summarizes the demographics, and the MMSE and global CDR scores of the OASIS participants. After the preprocessing pipeline, 39 sessions were excluded leading to the loss of the same amount of subjects.

	N	Age	Gender	MMSE	CDR
CN	76	76.5 $\pm$ 8.4[62,94]	14M/62F	29.0 $\pm$ 1.2[25,30]	0:76
AD	78	75.6 $\pm$ 7.0[62,96]	35M/43F	24.4 $\pm$ 4.3[14,30]	0.5:56;1:20;2:2

Table 5.4: Summary of participant demographics, mini-mental state examination (MMSE) and global clinical dementia rating (CDR) scores for OASIS. Values are presented as mean $\pm$ SD [range]. M: male, F: female

5.5 Methods

In this section, we present the main components of our framework: automatic converters of public datasets for reproducible data management (Section 5.1), preprocessing of MRI data (5.2), classification models (5.3), transfer learning approaches (5.4), classification tasks (5.5), evaluation strategy (5.6) and framework implementation details (5.7).

5.5.1 Converting datasets to a standardized data structure

ADNI, AIBL and OASIS, as public datasets, are extremely useful to the research community. However, they may be difficult to use because the downloaded raw data do not possess a clear and uniform organization. We thus used our previously developed converters (Samper-González et al., 2018) (available in the open source software platform Clinica) to convert the raw data into the BIDS format (Gorgolewski et al., 2016). Finally, we organized all the outputs of the experiments into a standardized structure, inspired from BIDS.

5.5.2 Preprocessing of T1w MRI

In principle, CNN require only minimal preprocessing because of their ability to automatically extract low-to-high level features. However, in AD classification where datasets are relatively small and thus where deep networks may be difficult to train, it remains unclear whether they can benefit from more extensive

preprocessing. Moreover, previous studies have used varied amounts of preprocessing procedures but without systematically assessing their impact. Thus, in the current study, we compared two different image preprocessing procedures: one "Minimal" and one more "Extensive" procedure. Both procedures included bias correction, and (optional) intensity rescaling. In addition, the "Minimal" processing included a linear registration while the "Extensive" included non-linear registration and skull-stripping.

In brief, the "Minimal" preprocessing procedure performs the following operations. The N4ITK method (Tustison et al., 2010) was firstly used to correct the bias field. Next, a linear (affine) registration was performed using SyN algorithm from ANTs (Avants et al., 2008) to register each image from the native space to the MNI space (ICBM 2009c nonlinear symmetric template) (Fonov et al., 2011; Fonov et al., 2009). To improve the computational efficiency, the registered images were further cropped to remove the border background. The final image size is $169 \times 208 \times 179$ with 1 mm3 isotropic voxels. Intensity rescaling, which was performed based on the min and max values, denoted as MinMax, was set to be optional to study its influence on classification results.

In the "Extensive" preprocessing procedure, bias correction and non-linear registration are performed using the Unified Segmentation approach (Ashburner and Friston, 2005) available in SPM12. Note that we do not use the tissue segmentation but only the nonlinearly registered, bias corrected, MR images. Subsequently, we perform skull-stripping based on a brain mask drawn in MNI space. We chose this mask-based approach over direct image-based skull-stripping procedures because the later did not prove robust on our data. This mask-based approach is less accurate but more robust. In addition, we performed intensity rescaling as in the "Minimal" pipeline.

We performed QC on the outputs of the preprocessing procedures. For the "Minimal" procedure, we used DL-based QC framework [22] (Fonov et al., 2018) to automatically check the quality of the linearly registered data. This software outputs a probability indicating how accurate the registration is. We visually checked the scans whose probability was lower than a threshold of 0.70. Out of these, 30 ADNI scans, 7 AIBL scans, and 39 OASIS scans had a bad linear registration and were excluded.

5.5.3 Classification models

We considered four different approaches for classification: i) 3D subject-level CNN, ii) 3D ROI-based CNN, iii) 3D patch-level CNN and iv) 2D slice-level CNN.

[22] https://github.com/vfonov/deep-qc

In the case of DL, one challenge is to find the "optimal" model (i.e. global minima), including the architecture hyperparameters (e.g. number of layers, dropout, batch normalization) and the training hyperparameters (e.g. learning rate, weight decay).

We first reviewed the architectures used in the literature among the studies in which no data leakage problem was witnessed (Table 1A). There was no consensus in the litterature, thus we used the following heuristic strategy for the each of the four approaches.

For the 3D subject-level approach, we began with an overfitting model that was very heavy because of the high number of FC layers (4 convolutional blocks + 5 FC layers). Then, we iteratively repeated the following operations:

- the number of FC layers was decreased until accuracy on the validation set decreased substantially;
- we added one more convolutional block.

In this way, we explored the architecture space from 4 convolutional blocks + 5 FC layers to 7 convolutional blocks + 2 FC layers. Among the best performing architectures, we chose the shallowest one: 5 convolutional blocks + 3 FC layers.

As the performance was very similar for the different architectures tested with the 3D subject-level approach and as this search method is time costly, it was not used for the 3D patch-level approach for which only four different architectures were tested:

- 4 convolutional blocks + 2 FC layers;
- 4 convolutional blocks + 1 FC layer;
- 7 convolutional blocks + 2 FC layers;
- 7 convolutional blocks + 1 FC layer.

The best architecture (4 convolutional blocks + 2 FC layers) was kept and used both in 3D patch-level and ROI-based approaches. Note that the other architectures were only slightly worse.

For these 3 approaches, other architecture hyperparameters were explored: with or without batch normalization, with or without dropout.

For the 2D slice-level approach, we chose to use a classical architecture, the ResNet-18 with FC layers added at the end of the network. We explored from 1 to 3 added FC layers and the best results were obtained with one. We then explored the number of layers to fine-tune (2 FC layers or the last residual block + 2 FC

layers) and chose to fine-tune the last block and the 2 FC layers. We always used dropout and tried different dropout rates.

For all four approaches, training hyperparameters (learning rate, weight decay) were adapted for each model depending on the evolution of the training accuracy.

The list of the chosen architecture hyperparameters is given in online supplementary C eTables 1, 2 and 3. The list of the chosen training hyperparameters is given in online supplementary C eTables 4 and 5.

5.5.3.1 3D subject-level CNN

For the 3D-subject-level approach, the proposed CNN architecture is shown in Figure5.1. The CNN consisted of 5 convolutional blocks, 3 FC layers and one softmax layer. Each convolutional block was sequentially made of one convolutional layer, one batch normalization layer, one ReLU and one max pooling layer (more architecture details are provided in online supplementary C eTable 1).

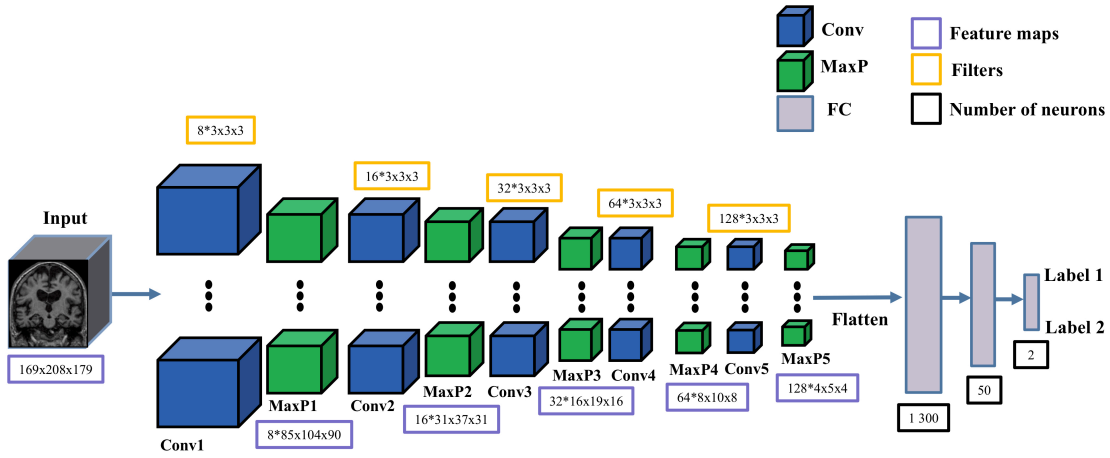

Figure 5.1: Architecture of the 3D subject-level CNNs. For each convolutional block, we only presented the convolutional layer and max pooling layer. Filters for each convolutional layer represent the number of filters × filter size. Feature maps of each convolutional block represent the number of feature maps × size of each feature map. Conv: convolutional layer; MaxP: max pooling layer; FC: fully connected layer.

5.5.3.2 3D ROI-based and 3D patch-level CNN

For the 3D ROI-based and 3D patch-level approaches, the chosen CNN architecture, shown in Figure 5.2, consisted of 4 convolutional blocks (with the same structure as in the 3D subject-level), 3 FC layers and one softmax layer (more architecture details are provided in online supplementary C eTable 2).

To extract the 3D patches, a sliding window (50×50×50 mm3) without overlap was used to convolve over the entire image, generating 36 patches for each image.

For the 3D ROI-based approach, we chose the hippocampus as a ROI, as done in previous studies. We used a cubic patch (50×50×50 mm3) enclosing the left (resp. right) hippocampus. The center of this cubic patch was manually chosen based on the MNI template image (ICBM 2009c nonlinear symmetric template). We ensured visually that this cubic patch included all the hippocampus.

For the 3D patch-level approach, two different training strategies were considered. First, all extracted patches were fitted into a single CNN (denoting this approach as 3D patch-level single-CNN). Secondly, we used one CNN for each patch, resulting in finally 36 (number of patches) CNNs (denoting this approach as 3D patch-level multi-CNN).

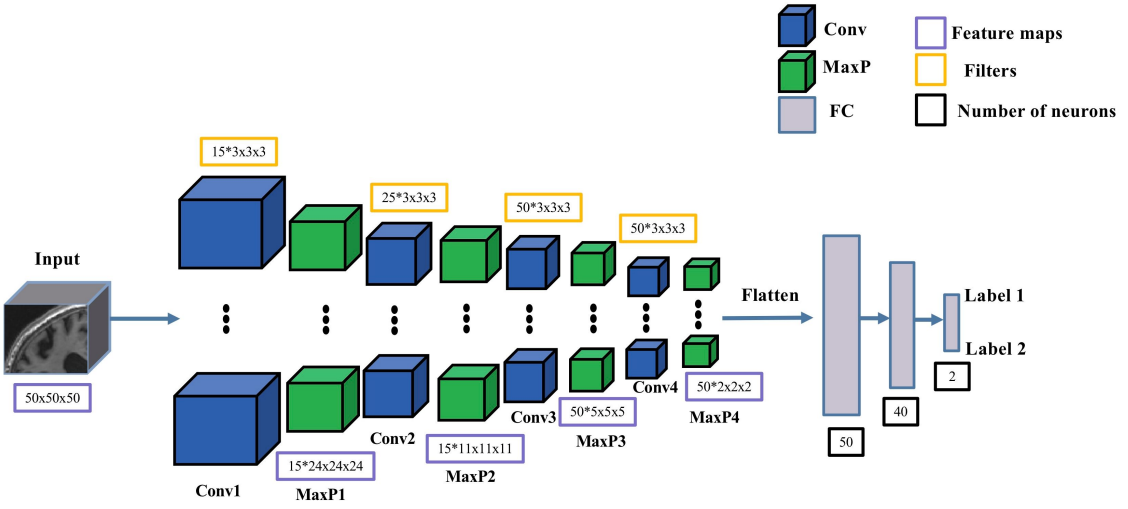

Figure 5.2: Architecture of the 3D ROI-based and 3D patch-level CNNs. For each convolutional block, we only presented the convolutional layer and max pooling layer. Filters for each convolutional layer represent the number of filters × filter size. Feature maps of each convolutional block represent the number of feature maps × size of each feature map. Conv: convolutional layer; MaxP: max pooling layer; FC: fully connected layer.

5.5.3.3 2D slice-level CNN

For 2D slice-level, the ResNet pre-trained on ImageNet was adopted and fine-tuned. The architecture is shown in Figure 5.3. The architecture details of ResNet can be found in He et al (He et al., 2016). We added one FC layer and one softmax layer on top of the ResNet (more architecture details are provided in online supplementary C eTable 3). Fine-tuning was performed only on the last convolutional

layers and last FC layer and the added FC layer. The weight and bias of the other layers of the CNN were frozen during fine-tuning to avoid overfitting.

For each subject, each sagittal slice was extracted and replicated into R, G and B channels respectively, in order to generate a RGB image. The first and last twenty slices were excluded due to the lack of information, which resulted in 129 RGB slices for each image.

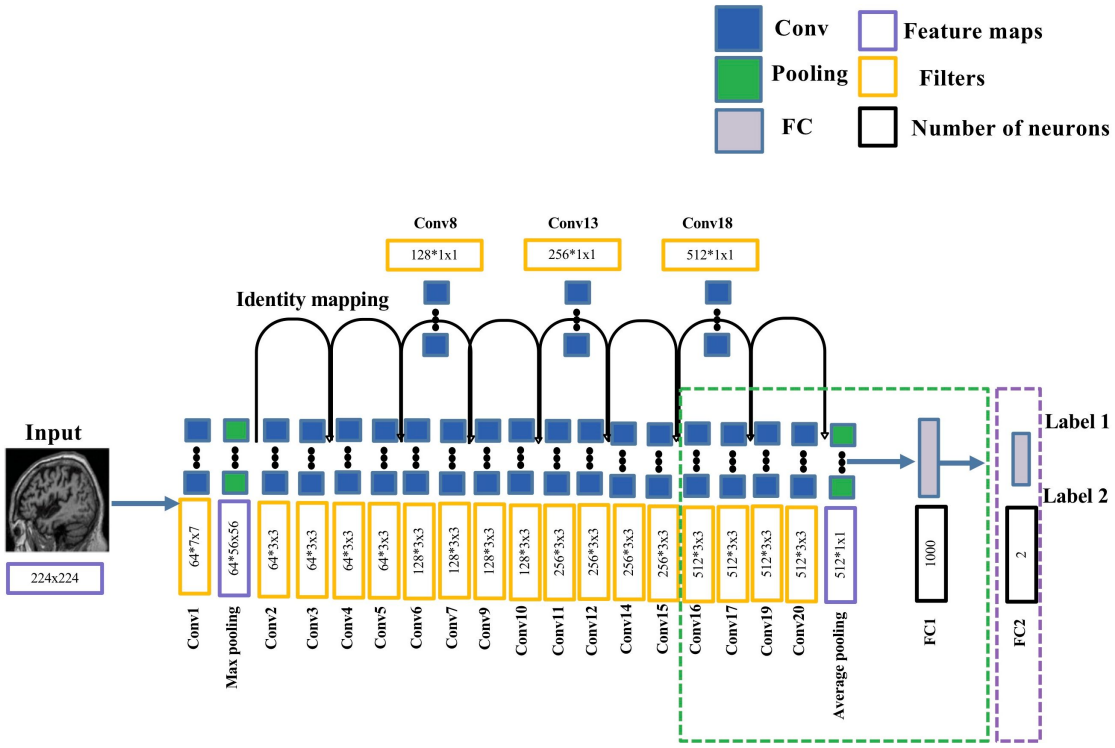

Figure 5.3: Architecture of the 2D slice-level CNN. An FC layer (FC2) was added on top of the ResNet. The last five convolutional layers and the last FC of ResNet (green dotted box) and the added FC layer (purple dotted box) were fine-tuned and the other layers were frozen during training. Filters for each convolutional layer represent the number of filters × filter size. Feature maps of each convolutional block represent the number of feature maps × size of each feature map. Conv: convolutional layer; FC: fully connected layer.

5.5.3.4 Majority voting system

For 3D patch-level, 3D ROI-based and 2D slice-level CNNs, we adopted a soft voting system (Raschka, 2015) to generate the subject-level decision. The subject-level decision is generated based on the decision for each slice (resp. for each patch / for the left and right hippocampus ROI).

The subject-level decision was calculated based on the predicted probabilities p of all the slices/patches/ROIs/CNNs from the same patient:

$$\hat{y} = \arg\max_{x} \sum_{j}^{m} w_j p_{ij}$$

where w_j is the weight assigned to the j-th patch/slice/ROI/CNN. w_j reflects the importance of each slice/patch/ROI/CNN and is weighted by the normalized accuracy of the j-th slice/patch/ROI/CNN.

For 3D patch-level multi-CNN approach, the 36 CNNs were trained independently. In this case, the weaker classifiers' weight (accuracy < 0.7) was set to be 0 with the consideration that the labels' probabilities of these classifiers could harm the majority voting system (e.g. AD and CN has both probabilities near to 0.5).

5.5.3.5 Comparison to a linear SVM on voxel-based features

For comparison purpose, classification was also performed with a linear SVM classifier. The SVM took as input the modulated GM density maps non-linearly registered using the DARTEL method (Ashburner, 2007) as in our previous study (Samper-González et al., 2018).

5.5.4 Transfer learning

Two different approaches were used for transfer learning: i) AE pre-training for 3D CNNs; and ii) ResNet pre-trained on ImageNet for 2D CNNs.

5.5.4.1 AE pre-training

The AE was constructed based on the corresponding architecture of CNN. Specifically, the encoder part of the AE shared the same architecture with the CNN: the encoder is composed of a sequence of convolutional blocks, each block having one convolutional layer, one batch normalization layer, one ReLU and one max pooling layer. The architecture of the decoder mirrored that of the encoder, except that the order of the convolution layer and the ReLU was swapped. Of note, the pre-training with AE and classification with CNNs in our experiments used the same training and validation data splits in order to avoid potential data leakage problems. Also, each AE was trained on all available data in the training sets. For instance, all MCI, AD and CN subjects in training dataset were used to pre-train the AE for the AD vs CN classification task.

5.5.4.2 ImageNet pre-training

For the 2D-slice experiments, we investigated the possibility to transfer a ResNet pre-trained on ImageNet (He et al., 2016) to our specific tasks. Next, the fine-tuning procedure was performed on the chosen layers (see Figure 5.3).

5.5.5 Classification tasks

We performed two tasks in our application: first, the AD vs CN classification, a baseline task to easily compare the results of our different framework. Then the best frameworks obtained on this task were selected to perform the prediction task sMCI vs pMCI: the weights and biases of the model learnt on the source task (AD vs CN) were transferred to a new model fine-tuned on the target task (sMCI vs pMCI). For SVM, the sMCI vs pMCI was done either training directly on sMCI vs pMCI or using training on AD vs CN and applying the trained model to sMCI vs pMCI.

5.5.6 Evaluation strategy

5.5.6.1 Validation procedure

Rigorous validation is essential to objectively assess the performance. This is particularly critical in the case of DL as one may easily overfit the validation dataset when manually performing model selection and hyperparameter fine-tuning. An independent test set should be, at the very beginning, partitioned and concealed. It should not be touched until the CV, based on the training and validation dataset, is finished and the final model is chosen. This test dataset should be used only to assess the performance (i.e. generalization) of a fully specified and trained classifier (Kriegeskorte et al., 2009; Ripley, 1996; Sarle, 1997). Considering this, we chose a classical split into training/validation/test sets. Training/validation sets were used in a CV procedure for model selection while the test set was left untouched. Of note, as mentioned in the beginning, we have not yet used the test set and will do so only after the review process of the paper has been finished. Only the best performing model for each approach (3D subject-level, 3D patch-level, 3D ROI-based, 2D slice-level) as defined by the CV on training/validation sets, will be tested on the test set.

First, the test set was built as follows. ADNI data was split into training/validation and test sets. The ADNI test dataset consisted of 100 randomly chosen age- and sex-matched subjects for each diagnostic class (i.e. 100 CN subjects, 100 AD patients). The rest of ADNI data was used as training/validation set. We ensured that age and sex distributions between training/validation and test sets were not

significantly different. Two other test sets were composed of all subjects of OASIS and AIBL. Thus, as a result, we have three test sets: i) an ADNI test set which will be used to assess model generalization within the same dataset (thereby assessing that model choice has not overfitted the training/validation set); ii) an AIBL test set which will be used to assess generalization to another dataset but with similar inclusion criteria and image acquisition parameters to those of ADNI; iii) an OASIS test which will be used to assess generalization to other inclusion criteria and image acquisition parameters.

Secondly, the model selection procedure, including model architecture selection and training hyperparameters fine-tuning, was performed using only the training/validation dataset. For that purpose, a 5-fold CV was performed, which resulted in one fold (20%) of the data for validation and the rest for training. Note that the 5-fold data split was performed only once for all experiments with a fixed seed number (*random_state* = 2), thus guaranteeing that all the experiments used exactly the same subjects during CV. Also, no overlapping exists between the MCI subjects used for AE pre-training (using all available AD, CN and MCI) and the test dataset of sMCI vs pMCI. Thus, the evaluation of the cross-task transfer learning (from AD vs CN to sMCI vs pMCI) is unbiased. Finally, for the linear SVM, the hyperparameter C controlling the amount of regularization was chosen using an inner loop of 10-fold CV (thereby performing a nested CV).

5.5.6.2 Metrics

We computed the following performance metrics: balanced accuracy, AUC, accuracy, sensitivity and specificity. In the manuscript, for the sake of concision, we report only the balanced accuracy but all other metrics are available at https://gitlab.icm-institute.org/aramislab/AD-ML.

5.5.7 Implementation details

The image preprocessing procedures were implemented with Nipype (Gorgolewski et al., 2011). The DL models were built using the Pytorch library [23] (Paszke et al., 2017). The linear SVM was built using scikit-learn (Pedregosa et al., 2011). TensorboardX [24] was embedded into the current framework to dynamically monitor the training process. Specifically, we evaluated and reported the training and validation accuracy/loss after each epoch or certain iterations. Of note, instead of using

[23] https://pytorch.org/
[24] https://github.com/lanpa/tensorboardX

only the current batch of data, the accuracy was evaluated based on all the training/validation data. Moreover, we organized the classification outputs in a hierarchical way inspired from BIDS, including the TSV files containing the classification results, the outputs of TensorboardX for dynamic monitoring of the training and the best performing models selected based on the validation accuracy.

We applied the following early stopping strategy for all the classification experiments: the training procedure does not stop until the validation loss is continuously higher than the lowest validation loss for N epochs. Otherwise, the training continues to the end of the pre-defined number of epochs. The selected model was the one which obtained the highest validation accuracy during training. For the AE pre-training, the AE was trained to the end of the pre-defined number of epochs. We then visually check the validation loss and the quality of the reconstructed images.

All experiments were performed on the cluster of the Brain and Spine Institute [25] in Paris, which is equipped with 4 NVIDIA P100 GPU cards (64 GB shared memory) and 24 CPUs (120 GB shared memory).

5.6 Experiments and results

5.6.1 Results on training/validation set

The different classification experiments and results (validation accuracy during 5-fold CV) are detailed in Table 5.5. For each experiment, the training process of the best fold (with highest validation accuracy) is presented as illustration (see supplementary C eFigures 1-4 for details). Lastly, the training hyperparameters (e.g. learning rate and batch size) for each experiments are presented in supplementary C eTable 4.

[25] https://icm-institute.org/

Classification architectures	Training data	Image preprocessing	Intensity rescaling	Data split	Training approach	Transfer learning	Task	Validation accuracy
3D subject-level CNN	Baseline	Minimal	None	subject-level	single-CNN	None	AD vs CN	0.50 ± 0.00[0.50,0.50,0.50,0.50,0.50]
			MinMax					0.77 ± 0.08[0.78,0.87,0.83,0.75,0.63]
						AE pre-train		0.78 ± 0.05[0.79,0.83,0.82,0.79,0.68]
	Longitudinal	Minimal	MinMax	subject-level	single-CNN	AE pre-train		0.85 ± 0.03[0.89,0.87,0.86,0.82,0.82]
		Extensive						0.85 ± 0.05[0.88,0.91,0.85,0.85,0.78]
		Minimal					sMCI vs pMCI	0.74 ± 0.03[0.75,0.77,0.70,0.76,0.72]
	Baseline							0.74 ± 0.03[0.72,0.76,0.72,0.78,0.71]
3D ROI-based CNN	Baseline	Minimal	MinMax	subject-level	single-CNN	AE pre-train	AD vs CN	0.86 ± 0.03[0.84,0.89,0.86,0.88,0.82]
							sMCI vs pMCI	0.80 ± 0.03[0.84,0.79,0.75,0.79,0.82]
	Longitudinal						AD vs CN	0.85 ± 0.02[0.84,0.87,0.86,0.88,0.82]
							sMCI vs pMCI	0.79 ± 0.03[0.82,0.78,0.73,0.79,0.81]
3D patch-level CNN	Baseline	Minimal	MinMax	subject-level	single-CNN	AE pre-train	AD vs CN	0.72 ± 0.09[0.75,0.83,0.75,0.73,0.56]
	Longitudinal							0.72 ± 0.06[0.77,0.74,0.77,0.69,0.61]
	Baseline				multi-CNN		AD vs CN	0.81 ± 0.03[0.85,0.81,0.75,0.79,0.83]
							sMCI vs pMCI	0.76 ± 0.04[0.80,0.75,0.68,0.79,0.78]
	Longitudinal						AD vs CN	0.79 ± 0.02[0.81,0.75,0.80,0.80,0.80]
							sMCI vs pMCI	0.76 ± 0.03[0.78,0.77,0.71,0.78,0.76]
2D slice-level CNN	Baseline	Minimal	MinMax	subject-level	single-CNN	ImageNet pre-train	AD vs CN	0.79 ± 0.04[0.82,0.83,0.72,0.82,0.76]
	Longitudinal							0.79 ± 0.05[0.79,0.85,0.80,0.82,0.70]
	Baseline			slice-level				1.00 ± 0[1.00,1.00,1.00,1.00,1.00]
SVM	Baseline	DartelGM	SPM-based	subject-level	None	None	AD vs CN	0.85 ± 0.02[0.85,0.88,0.83,0.86,0.84]
							$sMCIvspMCI^1$	0.69 ± 0.02[0.71,0.70,0.66,0.67,0.72]
							$sMCIvspMCI^2$	0.72 ± 0.04[0.67,0.78,0.70,0.76,0.68]
	Longitudinal						AD vs CN	0.85 ± 0.01[0.87,0.85,0.84,0.86,0.85]
							$sMCIvspMCI^1$	0.68 ± 0.07[0.76,0.76,0.59,0.63,0.65]
							$sMCIvspMCI^2$	0.69 ± 0.03[0.66,0.73,0.70,0.73,0.65]

Table 5.5: Summary of all the classification experiments and validation results in our analyses. MinMax: for CNNs, intensity rescaling was done based on min and max values, resulting all values to be in the range of [0, 1]; SPM-based: the intensity rescaling was performed with SPM; AE: autoencoder. For DL models, sMCI vs pMCI tasks were done with as follows: the weights and biases of the model learnt on the source task (AD vs CN) were transferred to a new model fine-tuned on the target task (sMCI vs pMCI). For SVM, the sMCI vs pMCI was done either training directly on sMCI vs pMCI or using training on AD vs CN and applying the trained model to sMCI vs pMCI.

5.6.1.1 3D subject-level

Influence of intensity rescaling. We first assessed the influence of intensity rescaling. Without rescaling, the CNN did not perform better than chance (balanced accuracy = 0.50 $\pm$ 0.00) and there was an obvious generalization gap (high training but low validation accuracy). With intensity rescaling, the balanced accuracy improved to 0.77 $\pm$ 0.08. Based on these results, intensity rescaling was used in all subsequent experiments.

Influence of transfer learning (AE pre-training). The performance was slightly higher with AE pre-training (0.78 $\pm$ 0.05) than without (0.77 $\pm$ 0.08) and the standard deviation was lower. Based on this, we decided to always use AE pre-training, even though the difference is small.

Influence of the training dataset size. We then assessed the influence of the amount of training data, comparing training using only baseline data to those with longitudinal data. The performance was substantially higher with longitudinal data (0.85 $\pm$ 0.03) compared to baseline data only (0.78 $\pm$ 0.05). We choose to continue exploring the influence of this choice because the four different approaches have a very different number of learnt parameters and the sample size is intrinsically augmented in 2D slice-level and 3D single-CNN patch-level approaches.

Influence of preprocessing. We then assessed the influence of the preprocessing comparing the "Extensive" and "Minimal" preprocessing procedures. The performance was equivalent with the "Minimal" preprocessing (0.85 $\pm$ 0.03) and with the "Extensive" preprocessing (0.85 $\pm$ 0.05). Hence in the following experiments we kept the "Minimal" preprocessing.

Classification of sMCI vs pMCI. The balanced accuracy was the same for baseline data and for longitudinal data (0.74 $\pm$ 0.03).

5.6.1.2 3D ROI-based

For AD vs CN, the balanced accuracy was 0.86 $\pm$ 0.03 for baseline data and 0.85 $\pm$ 0.02 for longitudinal data. This is comparable to the results obtained with the subject-level approach. For sMCI vs pMCI, the balanced accuracy was 0.80 $\pm$ 0.03 for baseline data and 0.79 $\pm$ 0.03 for longitudinal data. This is substantially higher than with the 3D-subject level approach.

5.6.1.3 3D patch-level

Single CNN. The accuracy was 0.72 $\pm$ 0.09 for baseline data and 0.72 $\pm$ 0.06 for longitudinal data.

Multi CNN. For AD vs CN, the accuracy was 0.81 $\pm$ 0.03 for baseline data and 0.79 $\pm$ 0.02 for longitudinal data, thereby outperforming the single CNN approach.

For sMCI vs pMCI, the accuracy was 0.76 $\pm$ 0.04 for baseline data and 0.76 $\pm$ 0.03 for longitudinal data. The performance for both tasks is lower than that of the 3D ROI-based approach. Compared to the 3D subject-level approach, this method works better for sMCI vs pMCI.

5.6.1.4 2D slice-level

In general, the performance of the 2D-slice level approach was lower to that of the 3D ROI-based, 3D patch-level multi CNN and 3D subject-level (when trained with longitudinal data) approaches but higher than that of the 3D patch-level single CNN approach. For 2D slice-level, the use of longitudinal data for training did not improve the performance (0.79 $\pm$ 0.04 for baseline data; 0.79 $\pm$ 0.05 for longitudinal data). Finally, we studied the influence of data leakage using a slice-level data split strategy. As expected, the accuracy was 1.00 $\pm$ 0.00.

5.6.1.5 Linear SVM

For task AD vs CN, the accuracies were 0.85 $\pm$ 0.02 when trained with baseline data and 0.85 $\pm$ 0.01 when trained with longitudinal data. For task sMCI vs pMCI, when training from scratch, the accuracies were 0.690.02 when trained with baseline data and 0.680.07 when trained with longitudinal data. When using transfer learning from the task AD vs CN to the task sMCI vs pMCI, the accuracies were 0.720.04 (when trained with baseline data) and0.690. 03 (when trained with longitudinal data). The performance of the SVM on AD vs CN is thus higher than that of most DL models and comparable to the best ones. Whereas for task sMCI vs pMCI, the accuracy of the SVM is lower than that of DL models.

5.6.2 Results on the test sets

Results on the three test sets (ADNI, OASIS and AIBL) are presented in Table **??**. For each category of approach, we only applied the best models for both baseline and longitudinal data. The results will be computed and presented after the end of the peer-review process.

Classification architectures	Training data	Image preprocessing	Intensity rescaling	Data split	Training approach	Transfer learning	Task	Validation accuracy	ADNI test accuracy	AIBL test accuracy	OASIS test accuracy
3D subject-level CNN	Baseline	Minimal	MinMax	subject-level	single-CNN	AE pre-train	AD vs CN	0.78 ± 0.05			
	Longitudinal							0.85 ± 0.03			
	Baseline						sMCI vs pMCI	0.75 ± 0.02			
	Longitudinal							0.74 ± 0.03			
3D ROI-based CNN	Baseline	Minimal	MinMax	subject-level	single-CNN	AE pre-train	AD vs CN	0.86 ± 0.03			
							sMCI vs pMCI	0.80 ± 0.03			
	Longitudinal						AD vs CN	0.85 ± 0.02			
							sMCI vs pMCI	0.79 ± 0.03			
3D patch-level CNN	Baseline	Minimal	MinMax	subject-level	single-CNN	AE pre-train	AD vs CN	0.81 ± 0.03			
							sMCI vs pMCI	0.76 ± 0.04			
	Longitudinal						AD vs CN	0.79 ± 0.02			
							sMCI vs pMCI	0.76 ± 0.03			
2D slice-level CNN	Baseline	Minimal	MinMax	subject-level	single-CNN	ImageNet pre-train	AD vs CN	0.79 ± 0.04			
	Longitudinal							0.79 ± 0.05			
	Baseline			slice-level				1.00 ± 0			
SVM	Baseline	DartelGM	SPM-based	subject-level	None	None	AD vs CN	0.85 ± 0.02			
							$sMCIvspMCI^1$	0.72 ± 0.04			
	Longitudinal						AD vs CN	0.85 ± 0.01			
							$sMCIvspMCI^2$	0.69 ± 0.03			

Table 5.6: Summary of all the classification experiments and validation results in our analyses. MinMax: for CNNs, intensity rescaling was done based on min and max values, resulting all values to be in the range of [0, 1]; SPM-based: the intensity rescaling was performed with SPM; AE: autoencoder.

5.7 Discussion

The present studies contains three main contributions. First, we performed a systematic and critical literature review, which highlighted several important problems. Then, we proposed an open-source framework for the reproducible evaluation of AD classification using CNNs and T1w MRI. Finally, we applied the framework to rigorously compare different CNN approaches and to study the impact of key components on the performances. We hope that the present paper will provide a more objective assessment of the performance of CNN for AD classification and constitute a solid baseline for future research.

This paper first proposes a survey of existing CNN methods for AD classification. We hope to provide a useful overview of the different strategies. However, the survey highlighted several serious problems with the existing literature. First, we found that data leakage was potentially present in half of the 32 surveyed studies. This problem was evident in six of them and possible (due to inadequate description of the validation procedure) in ten others. This is a very serious issue, in particular considering that all these studies have undergone peer-review. This was likely to bias the performance upwards. In addition, in our experiments, we simulated one type of data leakage and found, as expected, that it led to a biased evaluation of the accuracy (1.00 instead of 0.79). Similar findings were observed in (Bäckström et al., 2018). Moreover, the survey highlighted that many studies did not motivate the choice of their architecture or training hyperparameters. Only two of them (Wang et al., 2019; Wang et al., 2018b) explored and gave results obtained with different architecture hyperparameters. However, it is possible that these performances were computed on the test set to help choosing their final model, hence they may be contaminated by data leakage. For other studies, it is also likely that they tried multiple number of choices leading to biased performances on the test set.We believe that these issues may potentially be caused by the lack of expertise in medical imaging or DL. For instance, splitting at the slice-level comes from a lack of knowledge of the nature of medical imaging data. We hope that the present paper will help to spread knowledge and good practices in the field.

Then, we proposed an open-source framework for reproducible experiments on AD classification using CNN. Some studies in our bibliography also provided their code on open source platforms (Hon and Khan, 2017; Hosseini-Asl, Gimel'farb, and El-Baz, 2016; Korolev et al., 2017; Liu et al., 2018c). Of note, two studies (Cheng and Liu, 2017; Liu et al., 2018c) used the online code of (Hosseini-Asl, Gimel'farb, and El-Baz, 2016) to compare to their framework and neither of them succeeded

in reproducing the results of the original study (for the AD vs CN task they report both an accuracy of 0.82 while the original study reports an accuracy of 0.99). Our framework comprises unified tools for data management using the community standard BIDS (Gorgolewski et al., 2016), modular preprocessing pipelines, a set of CNN models which are representative of the literature and rigorous validation procedures. It builds upon our previously proposed framework but extends it to DL techniques (Samper-González et al., 2018; Wen et al., 2018b). We hope to contribute in improving the reproducibility and objectivity in application of AD classification using DL methods. Our open-source framework facilitates the reproducible and objective evaluation of performances. It also allows to rigorously study the impact of the different components. Calls and emphasises have been made on reproducibility in both neuroimaging (Gorgolewski and Poldrack, 2016; Poldrack et al., 2017) and ML (Sonnenburg et al., 2007; Stodden, Leisch, and Peng, 2014; Vanschoren et al., 2014). We hope that our framework will be useful to future research in the field. Indeed, researchers can easily embed new CNN architectures or image preprocessing pipelines and study their added value.

We then demonstrated the use of our framework on three public datasets. Through this, we aim to provide a trustworthy baseline performance for the community. On the validation dataset, the diagnostic accuracy of CNNs ranged from 0.72 to 0.86 for task AD vs CN and from 0.74 to 0.80 for task sMCI vs pMCI, respectively. These baseline performances are in line with the state-of-the-art results (studies without data leakage in Table 1A), where classification accuracy typically ranged from 0.76 to 0.91 for the task AD vs CN and 0.62 to 0.83 for the task sMCI vs pMCI.

Different approaches, namely 3D subject-level, 3D ROI-based, 3D patch-level and 2D slice-level CNNs, were compared. Our study is the first one to systematically compare the performances of the four approaches. In the literature, three studies (Cheng et al., 2017; Li, Liu, and Alzheimer's Disease Neuroimaging Initiative, 2018; Liu et al., 2018c) using a 3D patch-level approach compared their results with a 3D subject-level approach. In all studies, the 3D patch-level multi-CNN gave better results than the 3D-subject CNN (3 or 4 percent points of difference between the two approaches). However, except for Liu et al (Liu et al., 2018c) who reused the code provided by (Hosseini-Asl, Gimel'farb, and El-Baz, 2016), the methods used for the comparison are poorly described and the studies would thus be difficult, if not impossible, to reproduce. In general, in our comparative study, the 3D ROI-based approach provided the best performances. The 3D subject-level CNN was competitive with 3D ROI-based for AD vs CN classification but not for sMCI vs pMCI. The superior performance of the ROI-based approach may appear surprising since it uses only a specific portion of the brain

(the hippocampus) while 3D subject-level approach uses all information available. Indeed, even though the hippocampus is affected early and severely by AD (Braak and Braak, 1998), alterations in AD are not confined to the hippocampus and extend to other regions in the temporal, parietal and frontal lobes. A previous comparative study, using different types of ML techniques but not CNN, has shown that whole-brain approaches are more effective than methods using only the hippocampus (Cuingnet et al., 2011). In the case of DL, it is possible that the ROI-based CNNs work better because they are less complex (fewer learnt parameters) than the 3D subject-level CNNs, thus leading to less overfitting. It may thus be that whole brain approaches would result in higher performance when trained on larger samples. Two papers in the literature using hippocampal ROI reported high accuracies for task AD vs CN (0.84 and 0.90), comparable to ours, even though their definition of the ROI was different (Aderghal et al., 2018; Aderghal, Benois-Pineau, and Afdel, 2017). As for the 3D subjects (Bäckström et al., 2018; Cheng and Liu, 2017; Korolev et al., 2017; Li, Cheng, and Liu, 2017; Senanayake, Sowmya, and Dawes, 2018; Shmulev, Belyaev, and The Alzheimer's Disease Neuroimaging Initiative, 2018) results of the literature varied across papers, from 0.76 to 0.90. Although we cannot prove it directly, we believe that this variability stems from the high risk of overfitting. Moreover, 3D patch-level and 2D slice-level approaches led to lower accuracies compared to 3D ROI-based or 3D subject-level CNNs. One can hypothesize that this is because the spatial information is not adequately modeled by these approaches (no 3D consistency between slices, no consistency at the border of patches). Other studies with 3D patch-level approaches in the literature (Cheng et al., 2017; Lian et al., 2018; Li, Liu, and Alzheimer's Disease Neuroimaging Initiative, 2018; Liu et al., 2018b; Liu et al., 2018e) reported higher accuracies (from 0.87 to 0.91) than ours (0.81). We hypothesize that it may come from the increased complexity of their approach, including patch selection and fusion. Only one paper (without data leakage) has explored 2D slice-level using ImageNet pre-trained ResNet (Valliani and Soni, 2017). Their accuracy is very similar to ours (0.81 for task AD vs CN). Here, we provided a direct comparison with other approaches and demonstrated that a 2D slice-level approach leads to lower performances compared to 3D ROI-based or 3D subject-level CNNs.

For the 3D patch-level, we showed that the multi-CNN approach (0.81) was superior to the single-CNN approach (0.72). This is probably because fitting all patches/slices into one single CNN could lead to losing the voxel correspondence across patches/slices. However, the multi-CNN approach (0.81) obtained lower accuracies compared to the 3D subject-level approach (0.85).

After the peer-review process, when the results on the three test datasets have been obtained, we will include a paragraph discussing the results on the test dataset

and the implications for the generalizability of the models. We will discuss both generalizability to unseen data of the same study (ADNI) and to other studies with similar (AIBL) or different (OASIS) inclusion criteria and imaging parameters.

We studied the influence of several key choices on the performance. First, we studied the influence of AE pre-training and showed that it did not improve the average accuracy over training from scratch. However, AE pre-training resulted in a lower variance over the 5-folds of the CV. Three previous papers studied the impact of AE pre-training (Hosseini-Asl, Gimel'farb, and El-Baz, 2016; Vu et al., 2017; Vu et al., 2018) and found that it improved the results. However, they are all at least suspected of data leakage. We thus conclude that, to date, it is not proven that AE pre-training leads to increased average accuracy. A difficulty in AD classification using DL is the limited data sample for training. We demonstrated that training with longitudinal data gave superior (3D subject-level) or comparable (other approaches) performances compared to baseline data. This discrepancy across approaches may come from the fact that 3D subject-level CNNs were more complex (more learnt parameters) than other approaches, and thus that more training data has more impact on this approach. The absence of improvement for the majority of cases may be due to several factors. First, training with longitudinal data implies training with data from more advanced disease stages, since patients are seen at a later point in the disease course. This may have an adverse effect on the performance of the model when tested on baseline data, at which the patients are less advanced. Also, since the additional data come from the same patient, this does not provide a better coverage of inter-individual variability. We studied the impact of image preprocessing. First, as expected, we found that CNNs cannot be successfully trained without intensity rescaling. We then studied the influence of two different procedures ("Minimal" and "Extensive"). Of note, "Extensive" procedure requires redundantly a non-linear registration, instead of a linear one, and skull stripping compared to "Minimal" procedure. They led to comparable results. In principle, this is not surprising as DL methods do not require extensive preprocessing. In the litterature, varied types of preprocessing have been used. . Some studies used non-linear registration (Bäckström et al., 2018; Basaia et al., 2018; Lian et al., 2018; Liu et al., 2018b; Liu et al., 2018e; Lin et al., 2018; Wang et al., 2019; Wang et al., 2018b) while others used only linear (Aderghal, Benois-Pineau, and Afdel, 2017; Aderghal et al., 2017; Aderghal et al., 2018; Hosseini Asl et al., 2018; Li, Liu, and Alzheimer's Disease Neuroimaging Initiative, 2018; Liu et al., 2018c; Shmulev, Belyaev, and The Alzheimer's Disease Neuroimaging Initiative, 2018) or no registration (Cheng and Liu, 2017). None of them compared these different preprocessings with the exception of (Bäckström et al., 2018) which compared preprocessed data using FreeSurfer to no preprocessing. They found that training the

network with the raw data obtained inferior classification performance (38% drop for accuracy) compared to the preprocessed data using FreeSurfer (Bäckström et al., 2018). However, FreeSurfer comprises a complex pipeline with many preprocessing steps so it is unclear, from their results, which part drives the superior performance.

One interesting question is whether DL could perform better than conventional ML methods for AD classification. Here, we chose to compare CNN to a linear SVM. SVM has been used in many AD classification studies and obtained competitive performances (Falahati, Westman, and Simmons, 2014; Haller, Lovblad, and Giannakopoulos, 2011; Rathore et al., 2017). In the current study, compared to SVM, CNN gave comparable performances for task AD vs CN and superior performances for task sMCI vs pMCI. Note that we used a standard linear SVM with standard voxel-based features. For task AD vs CN, we do not claim that possibly more sophisticated DL architectures would not outperform the SVM. However, this is not the case with the architectures that we tested which are representative of the existing literature on AD classification. Besides, it is possible that CNN will outperform SVM when larger public dataset are available in the future. On the other hand, the CNN outperformed the SVM for the most difficult (and more interesting) sMCI vs pMCI classification task (0.80 vs 0.72). This is an interesting result which demonstrates the potential of DL for challenging diagnostic tasks.

Unbiased evaluation of the performances is an essential task in ML. This is particularly critical for deep learning because of the extreme flexibility of the models and the numerous possible choices that can be made regarding architecture and hyperparameter choices. In particular, it is crucial that such choices are not made using the test set. We chose a very strict validation strategy in that respect: the test sets were left untouched until the end of the peer-review process. This guarantees that only the final models, after all possible adjustments, are carried to the test set. Moreover, it is important to assess generalization not only to unseen subjects but also to other studies in which image acquisitions or patient inclusion criteria can vary. In the present paper, we used three test sets from ADNI, AIBL and OASIS to assess generalization to these different conditions.

Our study has the following limitations. First, a very large number of different choices can be made regarding the model architecture and training hyperparameters. Even though we did our best efforts to make meaningful choices and for testing a relatively large number of possibilities, we cannot exclude that other choices could have led to better results. [Note to reviewers: suggestions for other choices are welcome, as long as they are within a reasonable number]. To overcome this limitation, our framework is freely available to the community. We will

thus hope that other researchers will use it to propose and validate potentially better performing models. In particular, with our proposed framework, researchers can easily try their own models without touching the concealed test dataset. Secondly, the CV procedures were performed only once. Of course, the training is not deterministic and one would ideally want to repeat the CV to get a more robust estimate of the performance. However, we did not perform this due to limited computational resources. Finally, overfitting always exist in our experiments, albeit different techniques have been tried (e.g. transfer learning, dropout or weight decay). This phenomenon occurs mainly due to our small data sample in AD classification. It is likely that training with much larger datasets would result in higher performance models. However, in the field of AD, such very large datasets are not yet publicly available.

Conclusion & Perspectives

The objectives of this dissertation are to advance: i) the discovery of biomarkers of the presymptomatic phase of genetic forms of FTLD due to C9orf72 disease, and ii) the computer-aided diagnosis and prognosis of AD based on machine learning techniques. Specifically, for C9orf72 carriers, with promising disease-modifying therapies tested in clinical trials, we currently lack robust biomarkers for monitoring the therapeutic effect. These biomarkers are also essential for improving staging, prognosis and onset prediction. We have therefore investigated and completed the clinical spectrum for potential markers based on neuroimaging data and neuropsychological tests in presymptomatic C9orf72 carriers. For AD classification, we critically and objectively reviewed the state-of-the-art in the field, pointing out the bad practices and tricky traps regarding both neuroimaging and ML aspects. We then proposed our open source framework, demonstrated its use on three public datasets, and studied the influences of key components in the framework on the classification performances. With all these, we hope to provide a baseline performance and facilitate future researchers with the improvement of transparency, reproducibility and objectivity.

Early cognitive, structural, and microstructural markers in presymptomatic C9orf72 carriers younger than 40 years

We evidenced that subtle cognitive, structural, and microstructural alterations can be detected in C9orf72 carriers younger than 40 years. This finding indicate that the young C9orf72 carriers may represent the best target population for future disease-modifying clinical trials. First, praxis impairment is an early and intriguing feature of C9orf72 disease. This finding is surprising and indicates an early-expressed and non-evolving phenotype of C9orf72 mutation and encourages to examine extensive neuropsychological tests during the entire lifespan of C9orf72 carriers. Secondly, early thalamic atrophy seems to be a reliable hallmark at early

stage of C9orf72 mutation carriers. Two mechanisms may exist and are not exclusive with each other for this phenomenon: i) thalamic atrophy may be related to the presence of pathological deposits, ie, TDP-43 and/or DPR or ii) it can also be caused by deafferentation processes secondary to the diffuse cortical atrophy owing to the high number of connections between the hemispheric cortex and the thalamus. Lastly, microstructural WM integrity corruption but not cortical atrophy reflects the expected topography of C9orf72 disease. Our study demonstrated two distinct patterns between WM and GM. Atrophy demonstrates a widespread pattern and WM conversely targets corticospinal tracts and frontal WM, suggesting that WM changes may be more predictive of future cognitive and motor deficits than cortical atrophy. Our results contribute to a better understanding of the preclinical phase of C9orf72 disease and of the respective contribution of magnetic resonance biomarkers. However, the main limitation of our study is its cross-sectional design. Our findings need to be confirmed on longitudinal study design.

NODDI offers promising biomarkers with higher specificity and sensitivity at presymptomatic stage

In a second study, we hope to find more sensitive and more specific biomarkers in presymptomatic C9orf72 carriers. More specifically, this study evaluated the added value of NODDI in the detection of brain microstructural changes in presymptomatic C9orf72 carriers compared to conventional techniques, namely DTI and volumetric analysis based on T1w MRI. In conclusion, NODDI offers higher sensitivity compared with conventional DTI for detecting white matter integrity abnormalities. Moreover, it offers the potential to reveal a more specific substrate of white matter damage, suggesting here that it consists mainly of reduced neurite density during the presymptomatic stage. These findings encourage the use of NODDI, a multishell DWI sequence taking nearly 30 minutes, in clinical studies. Our work highlights the potential use of NODDI for biomarker tracking, disease staging and diagnosis, and therapeutic treatment monitoring in neurodegenerative diseases.

The currents study has the following limitations. First, the cross-model comparison between NODDI and DTI used two different DWI acquisitions. However, the single-shell and multishell DWI sequences were optimized for DTI and NODDI model, respectively. Thus, this systematic comparison helps clarify the

added value of a longer but clinically feasible multishell diffusion sequence. Second, caution should be exercised in diffusion MRI-based cortical analysis. NODDI, by construction, accounts for partial volume effects from cerebrospinal fluid (CSF) contamination, thus minimizing the influence of atrophy on the NODDI metrics. Nevertheless, the cortex is a thin structure compared with the resolution of diffusion MRI, and partial volume effect may impact on the computation of regional FWF measures. Although we implemented specific image processing procedures to mitigate partial volume effects, it is still possible that some partial volume effect remains, impacting on FWF estimates.

Challenges and cautions in classification of AD: a long but promising pathway to clinical translation with deep learning

Another important contribution of this dissertation is to clarify where we currently are and how far we are away from the translation to clinical practice regarding classification of AD using neuroimaging and ML techniques. The last two studies extended the previous work of a colleague (Samper-González et al., 2018), which proposed a reproducible framework based on conventional ML methods for AD classification and demonstrated its use on T1w MRI and PET data. In this dissertation, we expanded this framework to diffusion MRI with conventional ML, and T1w MRI with DL methods.

The main contributions are summarized as follows. First, our exhaustive literature overview of the state-of-the-art revealed bad practices in the field. These include various traps for data leakage and the biased metrics for classification performance quantification (e.g., imbalanced dataset), resulting in often over-optimistic results. In the current dissertation, we demonstrated two sources of data leakage with our experiments. The first scenario is the adoption of a non-nested feature selection using SVM. The second example is the adoption of a bad data split strategy in DL methods. Other types of data leakage also exist in the filed and lead to unreliable and over-optimistic results. This is a serious obstacle for future clinical translation as these models may have poor generalization power for unseen data. Secondly, we proposed our open source framework for reproducible evaluation of these classification methods. It consist of a set of tools for automatic conversion of the three public databases, standard image preprocessing pipelines and ML tools following current best practices. Thirdly, we demonstrated the use of

the framework on two applications: i) conventional ML methods with DTI-based features and ii) CNNs with T1w MRI from the three public datasets. These baseline performances are in line with the state-of-the-art results. We systematically studied the impacts of key components, such as type of features and image prepocessing procedure, on the classification performance. Moreover, in conjunction with our previous work (Samper-González et al., 2018), the last two studies in this dissertation clarify that PET, T1w MRI and diffusion MRI obtained inferior performance one after another by using conventional ML methods. DL methods did not boost the classification performance compared to conventional ML models, such as SVM, possibly due to the fact that very large neuroimaging datasets, comparable to ImageNet dataset, are not available yet. Lastly, we stressed our opinions and suggestions regarding the existing issues and challenges in the field. Specifically, the data leakage problem is not trivial and should be strictly avoided during experiment design. Another open question regards the architecture and hyperparameter optimization in DL. In this dissertation, we explicitly explained how this optimization was performed. Moreover, one is encouraged to split an independent test dataset at the very beginning in order to avoid the data leakage and quantify the generalizability power of the trained model to unseen data.

Compared to conventional ML methods, DL seems to be more promising in clinical translation. The first prerequisite is the robustness and reliability of the classification performance. This means that the experimental design should strictly follow the good practices and avoid the potential biased results. As emphasized in the current dissertation, we hope to attract the attention of the whole community to follow those good practices. Moreover, another advantage of DL is the feasibility of real-time (or near real-time) application in clinical practice. In the application of conventional ML techniques, data preprocessing is dedicated and time-consuming (usually hours for one MRI). Alternatively, DL methods has minimum dependency on image preprocessing, which requires nearly 10 to 30 minutes for one MRI. Also, once trained, the model can be simultaneously applied to new patients, thus generating interpretable outputs from imaging data for immediate use in clinical decision making. One obstacle for this pathway is the poor performance precision, such as for task sMCI vs pMCI. This poor performance could be boosted when big data of medical image are available. Researchers are advancing this in the right direction. First, databases, such as ADNI, OASIS, AIBL, have been made publicly accessible in recent decades. Moreover, research hot topic has been focused on few-shot learning, which requires only a small sample of training data.

Limitations also exist in our last two studies. For conventional ML methods with diffusion MRI data, first, the diffusion MRI from ADNI has a limited sample size and was not acquired using the state-of-the-art methods. Better performance

could be possibly obtained with more recent protocols or larger samples. Secondly, we only explored the potential of DTI-based features, while more advanced features, such as brain tractography- or network-based features, could also be studied. Regarding DL methods with T1w MRI, first, we experimented with a set of reasonable set of model architecture and training hyperparameters, but did not perform an extensive search due to the limited time and computational power. To overcome this limitation, our framework is freely available to the community. Thus we call for researchers to assist the search of the optimal model by using our framework. Moreover, overfitting always exist in our experiments, albeit different techniques have been tried (e.g. transfer learning, dropout or weight decay).

Release of open source software packages for scientific reproducibility

In this dissertation, another important contribution is the development and release of open source software packages to the community. This thesis highly depends on these open source software packages and conversely contributes to their development. First, Clinica software platform (http://www.clinica.run) offers the tools for automatic conversion of three public databases, standardized image preprocessing pipelines, and general implementation of statistical and ML models. The four studies highly relies on Clinica for data conversion, image preprocessing for feature extraction and data analysis. Secondly, the implementation of classical statistical models, which was used for the statistical analysis in the first two studies (Chapter 2 and Chapter 3), is publicly accessible on GitHub (https://github.com/anbai106/NeuroStatisticR). Lastly, another software package (https://gitlab.icm-institute.org/aramislab/AD-ML), for reproducible evaluation of ML methods for AD classification, was made publicly accessible. This not only includes the general implementation of ML models (both conventional ML and DL models), but also the experiments results and pre-trained models, which are specific to the last two studies in the dissertation (Chapter 4 and Chapter 5). We hope that our framework, the experimental results and the saved pre-trained models will be useful to researchers working in the field, allowing them to objectively evaluate and compare their new approaches.

* *
*

There are multiple perspectives to our work.

First, we hope to advance our work on presymptomatic C9orf72 carriers with the design of longitudinal studies. A previous study (Rohrer et al., 2015) proposed a hypothetical pattern of biomarker changes in family FTLD: from early presymptomatic phase to symptom onset, CSF biomarkers are firstly visible, followed by markers from PET tracer binding. Later at the presymptomatic stage, neuroimaging changes, including lower functional and structural connectivity and GM volume, appear. Shortly before or around symptom onset, behavioural symptoms and deficits in social cognition can be objectified. Functional changes and deficits in other cognitive domains are often only quantifiable after symptom onset (Rohrer et al., 2015; Jiskoot, 2018). However, this was obtained using extrapolated measures. Longitudinal studies would not only shed light on the temporal and spatial cascade of pathological changes in a larger lifespan, but also allow the validation of biomarkers robustness and disease-modifiying therapies response.

Secondly, we are interested in advancing computer-aided diagnosis of dementias. As mentioned above, one of the limitations using conventional ML methods and diffusion MRI is the use of only DTI-based feature, we hope to explore more advanced features, such as tractography- and network-based features, under strict evaluation conditions. Moreover, in our framework, we only considered a unimodal approach and a single type of classifier. Another prospective is to extend our work to the multimodal or ensemble learning approach, as such approaches were also present in the literature and obtained competitive performances.

Another perspective is to advance the work on reproducible evaluation of CNNs for AD classification. First of all, we will quantify the generalization power of our trained models on the unseen independent datasets after the peer-review process (Chapter 5 is submitted to Medical Image Analysis and under review). This process ensures no contamination for the test dataset and thus avoids the potential data leakage during the revision stage. Moreover, we currently implemented only binary classifiers, distinguishing between two types of conditions. This is not the natural use case in clinical practice where multiple diagnostic situations exist. As the huge success of ImageNet classification which is a multiclass classification task, we naturally thought to extend our current work to multiclass scenarios. Instead of using one-vs-one or one-vs-all strategy, for instance, in the case of SVM, DL models were designed to solve the multiclass classification with a more direct fashion: softmax function offers the probability of being classified into each category for each subject. Lastly, we hope that the saved pre-trained models could be useful for transfer learning and application transplantation. For instance, our models pre-trained on AD classification (source task) may be transferred to another target task, such as classification of different phenotypes of FTLD (target task).

Another interesting proposal, such as Kaggle online competition [26], could be established to the whole community for the search of optimal models. We need the efforts of the whole community for the search of the optimal model for AD classification due to the above-mentioned limitations. Following the rigorous evaluation procedures, such as adoption of subject-level data split, concealing independent test dataset and use of balanced accuracy, participants can easily use our open-source framework for automatic data downloading and converting, image preprocessing, and network architecture construction. Different approaches and models thus could be objectively compared.

One further step may be decided. One can notice that our DL models always suffer from overfitting although strategies, such as drop out, batch normalization and weight decay, have been adopted. Two possible solutions could be considered. First, the community works together to build the medical "ImageNet" dataset. Similar proposition has been made (http://langlotzlab.stanford.edu/projects/medical-image-net/. Notwithstanding that the community is advancing in the right direction, such as the availability of open access dataset ADNI, OASIS and AIBL, this may be difficult since medical data is sensitive. Alternatively, data augmentation could be taken into account. Recent huge advances in deep unsupervised learning, especially GANs, enable neural networks to duplicate the true data under similar data distribution. Hopefully, these approaches could satisfy the huge appetite of DL models.

[26] https://www.kaggle.com

Appendix A

Early Cognitive, Structural, and Microstructural Changes in Presymptomatic C9orf72 Carriers Younger Than 40 Years

This appendix is the supplementary material of the Chapter 2, which has been published as a journal article on *JAMA Neurology* (Bertrand et al., 2017):

- Bertrand, A., **Wen, J. (Co-first author)**, Rinaldi, D., Houot, M., Sayah, S., Camuzat, A., Fournier, C., Fontanella, C., Routier, A., Couratier, P., Pasquier, F., Habert, M., Hannequin, D., Martinaud, O., Caroppo, P., Levy, R., Dubois, B., Brice, A., Durrleman, S., Colliot, O., Le Ber, I. Early Cognitive, Structural, and Microstructural Changes in Presymptomatic *c9orf72* Carriers Younger Than 40 Years, **JAMA neurology**, 75(2), pp.236-245. https://hal.inria.fr/hal-01654000/document.

Supplementary Online Content

Bertrand A, Wen J, Rinaldi D, et al; the Predict to Prevent Frontotemporal Lobar Degeneration and Amyotrophic Lateral Sclerosis (PREV-DEMALS) Study Group. Early cognitive, structural, and microstructural changes in *C9orf72* presymptomatic carriers younger than 40 years. *JAMA Neurol*. Published online December 2, 2017. doi:10.1001/jamaneurol.2017.4266

This supplementary material has been provided by the authors to give readers additional information about their work.

eMethods 1. Neuropsychological and behavioral tests

All the participants underwent a comprehensive neuropsychological and behavioral evaluation, based on internationally validated scales. Behavioral disorders were assessed using the Frontal Behavioural Inventory (FBI), the Neuropsychiatric Inventory (NPI), the Frontal Behavioural scale, the Frontotemporal dementia Rating Scale (FRS), the CBI-R and Starskein apathy scale. Functional disability was assessed using the Frontal CDR and DAD scale (Disability Assessment for Dementia). Depression and anxiety were assessed using the STAI and BDI-II scale. All the participants also underwent a detailed neuropsychological battery evaluating global cognitive efficiency (Mini Mental State Examination (MMSE)[1], MATTIS dementia rating scale (MDRS[2]); executive functions (Frontal Assessment battery[3]); social cognition and theory of mind (Social Emotion Assessment [4]); episodic memory (Free and cued recall test); language (verbal fluencies, Boston Naming test) visuospatial processing (Benson figure copy) and gestural praxis. Gestural praxis were assessed with a shortened version of the Batterie d'Evaluation des Praxies[5] with 5 testing conditions: (a) manual dexterity, using imitation of finger configuration, (b) melokinetic apraxia, using motor programming and alternate gestures, (c) imitation of non-representational gestures, (d) pantomime of intransitive gestures, (e) pantomime of transitive gestures.

eMethods 2. Magnetic resonance imaging sequence parameters

Parameters of 3DT1 sequence were as follow: spatial resolution = (1.1x1.1x1.1) mm3; TE/TR = 2.8-3ms/minimum; Bandwidth: 240-255 Hz. The 64 subjects imaged on a Siemens MR also underwent DTI with the following parameters: spatial resolution = (2x2x2.5) mm3; TE/TR = 90/7300ms; Bandwidth = 1580 Hz. Each DTI scan comprised 64 directions diffusion-weighted images (b value = 1000 s/mm2), 9 T2-weighted images (b value = 0 s/mm2) and a B0 field map.

eFigure 1. Correlation between age and expected years to onset

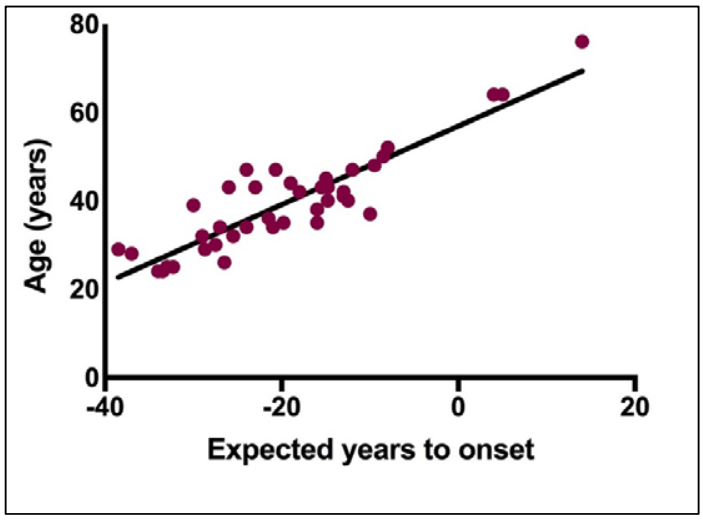

In c9+ subjects, real age and expected years to onset (based on the mean familial age at onset) showed strong correlation with high shared variance (Pearson correlation coefficient, $p < 0.0001$; $r^2 = 0.802$).

eFigure 2. Diffusion tensor magnetic resonance imaging metrics

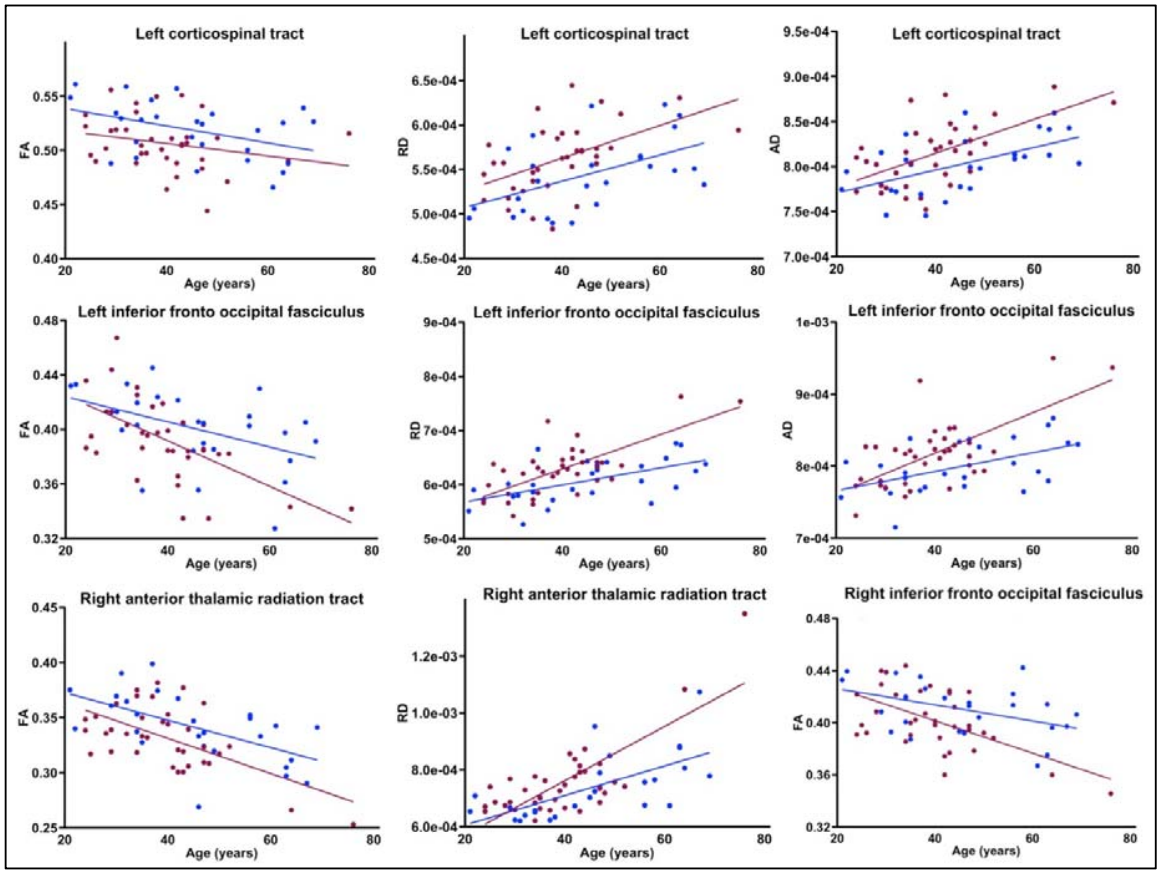

Graphs of DTI metrics as a function of age in c9+ and c9- subjects. The exact position of x-values (age) is not provided, in order to prevent individual subjects from identifying their mutation status.

eTable 1. Effect of *C9orf72* mutation on volume of cortical regions of interest

	c9orf72 mutation		
	Coefficient	Uncorr. p value	Corr. p value
Frontal lobe			
Left frontal pole	-76.8	0.016*	0.100
Left medial orbitofrontal	-199.8	0.096	0.211
Left lateral orbitofrontal	-185.1	0.113	0.240
Left pars orbitalis	-20.7	0.771	0.832
Left pars triangularis	-178.5	0.141	0.254
Left pars opercularis	-339.6	0.038*	0.155
Left rostral middle frontal	-208.3	0.536	0.675
Left caudal middle frontal	-381.2	0.039*	0.155
Left superior frontal	-1062.6	0.007*	0.053
Left precentral	-578.0	0.073	0.178
Right frontal pole	-28.1	0.502	0.649
Right medial orbitofrontal	-0.1	1.000	1.000
Right lateral orbitofrontal	-182.2	0.190	0.308
Right pars orbitalis	-138.5	0.058	0.155
Right pars triangularis	-109.8	0.394	0.558
Right pars opercularis	-278.4	0.066	0.166
Right rostral middle frontal	-635.8	0.053	0.155
Right caudal middle frontal	-490.1	0.005*	0.046*
Right superior frontal	-736.1	0.054	0.155
Right precentral	-476.9	0.086	0.201
Temporal lobe			
Left temporal pole	-212.6	0.015*	0.100
Left banks sts	-54.6	0.572	0.695
Left transverse temporal	-74.3	0.116	0.240
Left superior temporal	-372.3	0.177	0.294
Left middle temporal	-78.1	0.771	0.832
Left inferior temporal	-1155.7	<0.001*	0.005*
Left fusiform	-502.2	0.033*	0.155
Left entorhinal	-107.0	0.135	0.254
Left parahippocampal	-51.1	0.485	0.649
Right temporal pole	-111.4	0.157	0.274
Right banks sts	-2.0	0.980	0.994
Right transverse temporal	-15.3	0.694	0.800
Right superior temporal	-376.5	0.142	0.254
Right middle temporal	-178.0	0.547	0.676
Right inferior temporal	-924.3	0.002*	0.018*
Right fusiform	-833.8	<0.001*	0.008*
Right entorhinal	-48.6	0.506	0.649
Right parahippocampal	-115.9	0.059	0.155
Parietal lobe			
Left postcentral	-377.6	0.094	0.211
Left superior parietal	-692.9	0.045*	0.155
Left inferior parietal	-674.2	0.030*	0.155
Left precuneus	-711.3	<0.001*	0.008*
Left supramarginal	-972.2	<0.001*	0.008*
Left paracentral	-17.3	0.855	0.899
Right postcentral	-344.6	0.126	0.245
Right superior parietal	-854.9	0.005*	0.046*
Right inferior parietal	-649.2	0.058	0.155
Right precuneus	-677.8	0.002*	0.018*
Right supramarginal	-308.8	0.232	0.358
Right paracentral	-37.5	0.717	0.812
Occipital lobe			
Left lingual	-380.1	0.051	0.155
Left lateral occipital	-695.0	0.019*	0.107
Left cuneus	-137.2	0.051	0.155

Left pericalcarine	76.2	0.213	0.336
Right lingual	-132.0	0.501	0.649
Right lateral occipital	-590.6	0.051	0.155
Right cuneus	-117.5	0.163	0.277
Right pericalcarine	111.1	0.122	0.245
Cingulate gyrus			
Left rostral anterior cingulate	-74.8	0.349	0.505
Left caudal anterior cingulate	-38.2	0.728	0.812
Left isthmus cingulate	-142.3	0.059	0.155
Left posterior cingulate	-13.7	0.890	0.917
Right rostral anterior cingulate	-93.2	0.265	0.400
Right caudal anterior cingulate	18.5	0.859	0.899
Right isthmus cingulate	-32.6	0.670	0.785
Right posterior cingulate	42.8	0.589	0.702
Insula			
Left insula	-111.3	0.320	0.473
Right insula	-96.1	0.441	0.613

Effect of c9orf72 mutation on volume of cortical ROI, with age and sex as covariates. Uncorr.: uncorrected for multiple comparison; Corr.: corrected for multiple comparisons. Cortical ROI showing significant p-value after correction are shown in bold.

eTable 2. Effect of *C9orf72* mutation on volume of subcortical structures

	c9orf72 mutation		
	Coefficient	Uncorr. p value	Corr. p value
Left cerebellum cortex	-1043.4	0.385	0.629
Right cerebellum cortex	-687.2	0.570	0.790
Left ventral diencephalon	-31.3	0.704	0.810
Right ventral diencephalon	-7.8	0.915	0.935
Left putamen	-141.9	0.302	0.556
Right putamen	-176.0	0.176	0.420
Left pallidum	-84.6	0.065	0.342
Right pallidum	-57.1	0.186	0.420
Left caudate	-25.8	0.720	0.810
Right caudate	-6.6	0.935	0.935
Left accumbens area	-18.5	0.480	0.720
Right accumbens area	-24.5	0.309	0.556
Left amygdala	-20.2	0.659	0.810
Right amygdala	-71.1	0.151	0.420
Left thalamus proper	-383.0	0.022*	0.202
Right thalamus proper	-444.1	0.001*	0.010*
Left hippocampus	-161.6	0.100	0.360
Right hippocampus	-175.6	0.076	0.342

Effect of c9orf72 mutation on volume of subcortical structures, with age and sex as covariates. Uncorr.: uncorrected for multiple comparison; Corr.: corrected for multiple comparisons. Subcortical ROI showing significant p-value after correction is shown in bold.

eTable 3. Effect of *C9orf72* mutation on diffusion tensor magnetic resonance imaging metrics

	FA			MD			RD			AD		
	Coeff. (x10)	Uncorr. p value	Corr. p value	Coeff. ($x10^3$)	Uncorr. p value	Corr. p value	Coeff. ($x10^4$)	Uncorr. p value	Corr. p value	Coeff. ($x10^4$)	Uncorr. p value	Corr. p value
L. anterior thalamic radiation	-0.120	0.035*	0.099	0.026	0.163	0.326	0.358	0.062	0.113	0.326	0.083	0.122
R. anterior thalamic radiation	-0.180	0.004*	0.049*	0.044	0.037*	0.229	0.596	0.011*	0.041*	0.546	0.015*	0.055
L. corticospinal tract	-0.165	0.008*	0.049*	0.006	0.531	0.758	0.279	0.002*	0.015*	0.209	0.004*	0.022*
R. corticospinal tract	-0.098	0.120	0.239	0.002	0.865	0.911	0.178	0.045*	0.099	0.124	0.086	0.122
L. cingulum cingulate gyrus	-0.230	0.105	0.239	0.022	0.334	0.542	0.506	0.053	0.105	0.410	0.065	0.119
R. cingulum cingulate gyrus	-0.171	0.246	0.378	-0.010	0.722	0.861	0.220	0.418	0.517	0.121	0.616	0.648
L. cingulum hippocampus	0.018	0.867	0.867	0.057	0.103	0.229	0.244	0.439	0.517	0.360	0.249	0.312
R. cingulum hippocampus	0.096	0.435	0.622	0.012	0.732	0.861	-0.024	0.970	0.970	0.024	0.924	0.924
Forceps major	-0.146	0.109	0.239	0.008	0.790	0.877	0.300	0.158	0.226	0.226	0.302	0.355
Forceps minor	-0.169	0.016*	0.052	0.001	0.958	0.958	0.277	0.016*	0.045*	0.187	0.067	0.119
L. inferior fronto occipital fasciculus	-0.163	0.010*	0.049*	0.023	0.077	0.229	0.334	<0.001 *	0.008*	0.290	0.002*	0.015*
R. inferior fronto occipital fasciculus	-0.129	0.009*	0.049*	0.012	0.352	0.542	0.225	0.025*	0.062	0.189	0.058	0.119
L. inferior longitudinal fasciculus	-0.038	0.582	0.670	0.037	0.001*	0.027*	0.285	0.006*	0.040*	0.311	0.001*	0.015*
R. inferior longitudinal fasciculus	-0.081	0.235	0.378	0.041	0.005*	0.055	0.267	0.009*	0.041*	0.314	0.002*	0.015*
L. superior longitudinal fasciculus	-0.064	0.146	0.265	0.018	0.046*	0.229	0.159	0.080	0.133	0.167	0.053	0.119
R. superior longitudinal fasciculus	-0.136	0.015*	0.052	0.018	0.103	0.229	0.279	0.012*	0.041*	0.244	0.018*	0.055
L. uncinate fasciculus	-0.065	0.489	0.652	0.011	0.591	0.788	0.190	0.302	0.402	0.165	0.348	0.386
R. uncinate fasciculus	-0.030	0.800	0.842	-0.032	0.082	0.229	-0.116	0.503	0.559	-0.182	0.195	0.260
L. superior longitudinal fasciculus temporal	0.072	0.593	0.670	0.025	0.193	0.350	0.047	0.743	0.782	0.155	0.072	0.119
R. superior longitudinal fasciculus temporal	-0.062	0.603	0.670	0.034	0.088	0.229	0.174	0.109	0.168	0.232	0.019*	0.055

Effect of c9orf72 mutation on DTI metrics, with age and sex as covariates. Uncorr.: uncorrected for multiple comparison; Corr.: corrected for multiple comparisons. L.: left; R.: right. Tract with at least one DTI metric showing significant p-value after correction are shown in bold.

eReferences.

1. Folstein MF, Folstein SE, McHugh PR. “Mini-mental state”. A practical method for grading the cognitive state of patients for the clinician. *J Psychiatr Res*. 1975;12(3):189-198.
2. Mattis S. Mental status examination for organic mental syndrome in the elderly patients. In: *Geriatrics Psychiatry: A Handbook for Psychiatrists and Primary Care Physicians*. New York: Grune & Stratton; 1976:77-121.
3. Dubois B, Slachevsky A, Litvan I, Pillon B. The FAB: a Frontal Assessment Battery at bedside. *Neurology*. 2000;55(11):1621-1626.
4. Funkiewiez A, Bertoux M, de Souza LC, Lévy R, Dubois B. The SEA (Social cognition and Emotional Assessment): a clinical neuropsychological tool for early diagnosis of frontal variant of frontotemporal lobar degeneration. *Neuropsychology*. 2012;26(1):81-90. doi:10.1037/a0025318.
5. Peigneux P, Van Der Linden M. Présentation d’une batterie neuropsychologique et cognitive pour l’évaluation de l’apraxie gestuelle. *Rev Neuropsychol*. 2000;10(2):311-362.

Appendix B

Neurite density is reduced in the presymptomatic phase of C9orf72 disease

This appendix is the supplementary material of the Chapter 3, which has been published as a journal article on *Journal of Neurology, Neurosurgery, and Psychiatry* (**wen_neurite_nodate**):

- **Wen, J.**, Zhang, H., Alexander, D., Durrleman, S., Routier, A., Rinaldi, D., Houot, M., Couratier, P., Hannequin, D., Pasquier, F., Zhang, J., Colliot, O., Le Ber, I. and Bertrand, A. Neurite density is reduced in the presymptomatic phase of C9orf72 disease, **J Neurol Neurosurg Psychiatry**, pp.jnnp-2018. https://hal.inria.fr/hal-01907482/document.

Supplementary material

Appendix e-1: Regions for gray matter analyses.
Appendix e-2: Regions for white matter analyses.
Appendix e-3: Mixed effects model.
Figure e-1: Color-coded representation of *P* values corresponding to the associations of *C9orf72* mutation with white matter integrity before correction for multiple comparisons.
Figure e-2: Color-coded representation of *P* values corresponding to the associations of *C9orf72* mutation with the cortical ROI measures before correction for multiple comparisons.
Figure e-3: Color-coded representation of *P* values corresponding to the associations of *C9orf72* mutation with the subcortical ROI measures before correction for multiple comparisons.
Table e-1: Effect sizes for DTI metrics and for NDI in white matter tracts.
Table e-2: Effect sizes for FWF and gray matter volume in cortical regions.
Table e-3: Effect sizes for FWF and gray matter volume in subcortical regions.

Appendix e-1. Regions for gray matter analyses.

We studied the following 68 cortical regions obtained from the Desikan-Killiany atlas:
Frontal lobe: left frontal pole, left medial orbitofrontal, left lateral orbitofrontal, left pars orbitalis, left pars triangularis, left pars opercularis, left rostral middle frontal, left caudal, middle frontal, left superior frontal, left precentral, right frontal pole, right medial orbitofrontal, right lateral orbitofrontal, right pars orbitalis, right pars triangularis, right pars opercularis, right rostral middle frontal, right caudal middle frontal, right superior frontal, right precentral.
Temporal lobe: left temporal pole, left banks sts, left transverse temporal, left superior temporal, left middle temporal, left inferior temporal, left fusiform, left entorhinal, left parahippocampal, right temporal pole, right banks sts , right transverse temporal, right superior temporal, right middle temporal, right inferior temporal, right fusiform, right entorhinal, right parahippocampal.
Parietal lobe: left postcentral, left superior parietal, left inferior parietal, left precuneus, left supramarginal, left paracentral, right postcentral, right superior parietal, right inferior parietal, right precuneus, right supramarginal, right paracentral.
Occipital lobe: left lingual, left lateral occipital, left cuneus, left pericalcarine, right lingual, right lateral occipital, right cuneus, right pericalcarine.
Cingulate gyrus: left rostral anterior cingulate, left caudal anterior cingulate, left isthmus cingulate, left posterior cingulate, right rostral anterior cingulate, right caudal anterior cingulate, right isthmus cingulate, right posterior cingulate.
Insula: left insula, right insula.

The following 18 subcortical regions were included for gray matter volume analyses:
left cerebellum cortex, right cerebellum cortex, left ventral diencephalon, right ventral diencephalon, left putamen, right putamen, left pallidum, right pallidum, left caudate, right caudate, left accumbens area, right accumbens area, left amygdala, right amygdala, left thalamus proper, right thalamus proper, left hippocampus, right hippocampus.

The following 12 subcortical regions were included for gray matter FWF analyses. The other 6 ROIs were excluded because, after the 2-voxel erosion procedure, they were too small to produce reliable regional estimates.
left putamen, right putamen, left pallidum, right pallidum, left caudate, right caudate, left amygdala, right amygdala, left thalamus proper, right thalamus proper, left hippocampus, right hippocampus.

Appendix e-2: Regions for white matter analyses.

We studied the following 20 tracts based on JHU atlas for white matter analyses:
left anterior thalamic radiation, right anterior thalamic radiation, left corticospinal tract, right corticospinal tract, left cingulum cingulate gyrus, right cingulum cingulate gyrus, left cingulum hippocampus, right cingulum hippocampus, forceps major, forceps major, left inferior fronto-occipital fasciculus, right inferior fronto-occipital fasciculus, left inferior longitudinal fasciculus, right inferior longitudinal fasciculus, left superior longitudinal fasciculus, right superior longitudinal fasciculus, right uncinate fasciculus, left uncinate fasciculus, left superior longitudinal fasciculus temporal, right superior longitudinal fasciculus temporal.

Appendix e-3. Mixed effects model.

Group differences between carriers and non-carriers of the *C9orf72* mutation were assessed using linear mixed-effects models. We used age, gender and group (i.e., mutation status) as fixed effects, and family membership as random effect, with the following model:

$$Y_{ik}{}^{(j)} = \mu + \beta \times Gender_i + \lambda \times Age_i + \eta \times Group_i + U_k + E_{ik}{}^{(j)}$$

where $Y_{ik}{}^{(j)}$ is the response of the j^{th} region of interest (ROI) for the i^{th} subject and the k^{th} family; $Gender_i$, Age_i and $Group_i$ are the fixed effects; μ, β, λ and η are their estimated parameters; U_k is the random effect measuring the difference between the average response in the family and in the whole population; $E_{ik}{}^{(j)}$ is the random error.

Figure e-1. Color-coded representation of *P* values corresponding to the associations of *C9orf72* mutation with white matter integrity before correction for multiple comparisons.

Abbreviations: FA, fractional anisotropy; MD, mean diffusivity; AD, axial diffusivity; RD, radial diffusivity; NDI, neurite density index; ODI, orientation dispersion index.

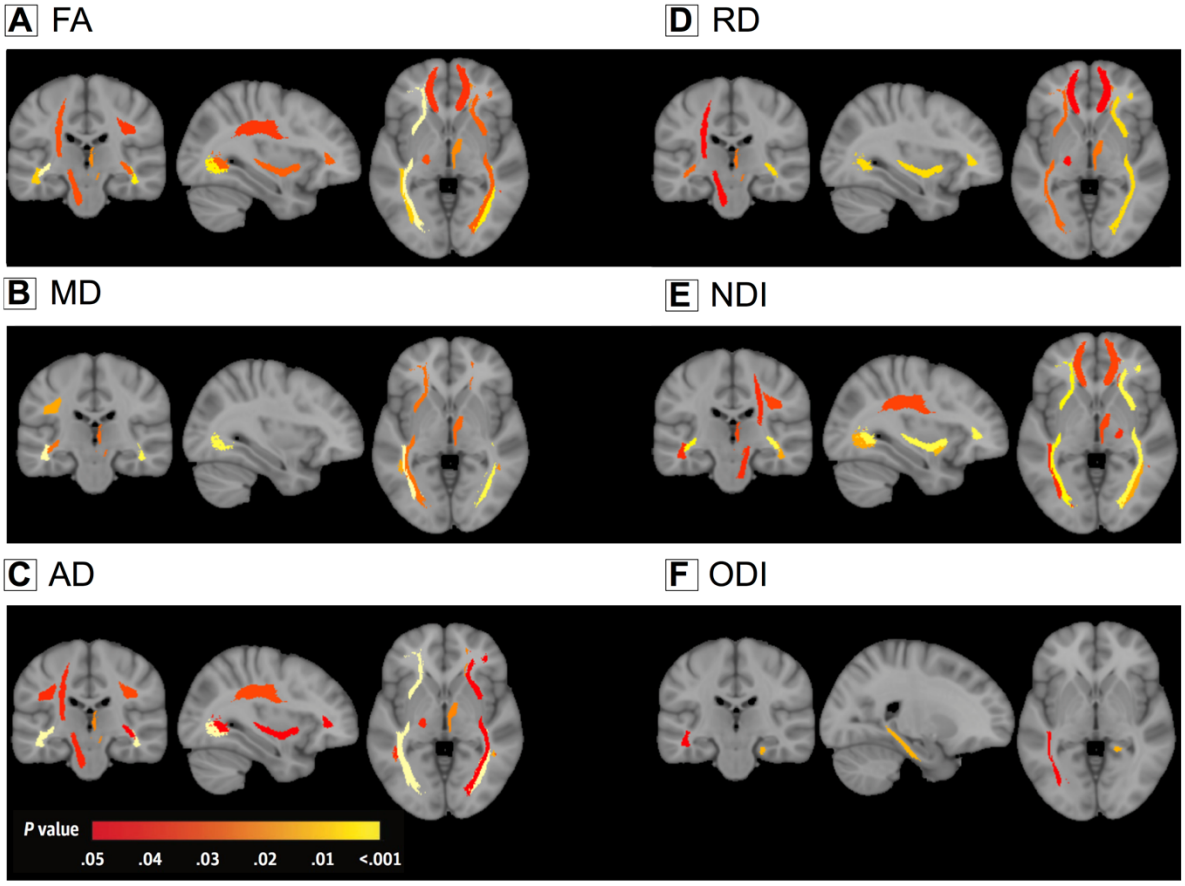

Table e-1. Effect sizes for DTI metrics and for NDI in white matter tracts.
The effect sizes for both NDI and DTI are shown below. For DTI, only the largest effect size among the different DTI metrics is shown. For regions for which a significant difference between C9+ and C9- was detected for any of the metrics, we compared the effect size of NODDI to that of DTI using a permutation test procedures with 10000 iterations. The table presents the *P* values corresponding to these permutation tests (with a significance level of $P < 0.05$).
Abbreviations: ART, anterior thalamus radiation tract; CST, cortico-spinal tract; CCG, Cingulum (cingulate gyrus) tract; CH, Cingulum (hippocampus) tract; Fmajor, forceps major tract; Fminor, forceps minor tract; IFOF, inferior fronto-occipital fasciculus; ILF, inferior longitudinal fasciculus; SLF, superior longitudinal fasciculus; UF, uncinate fasciculus; SLFT, superior longitudinal fasciculus (temporal part); R., right; L., left; NDI, neurite density index; DTI, diffusion tensor imaging; NA, not applicable.

ROI	Effect size (NDI/DTI)	*P* value	ROI	Effect size (NDI/DTI)	*P* value
L.ART	0.06/0.04	NA	L.IFOF	0.2/0.21	0.773
R.ATR	0.12/0.09	0.365	R.IFOF	0.27/0.11	0.009*
L.CST	0.05/0.07	NA	L.ILF	0.09/0.23	0.051
R.CST	0.09/0.03	0.154	R.ILF	0.16/0.17	0.719
L.CCG	0.03/0.04	NA	L.SLF	0.08/0.06	NA
R.CCG	0.02/0.02	NA	R.SLF	0.13/0.07	0.139
L.CH	0.01/0.05	NA	L.UF	0.03/0.02	NA
R.CH	0.07/0.01	NA	R.UF	0.17/0.01	0.008*
Fmajor	0.09/0.05	0.207	L.SLFT	0.06/0.05	NA
Fminor	0.1/0.06	0.307	R.SLFT	0.06/0.1	0.258

Figure e-2. Color-coded representation of *P* values corresponding to the associations of *C9orf72* mutation with the cortical ROI measures before correction for multiple comparisons.
Abbreviations: FWF, free water fraction.

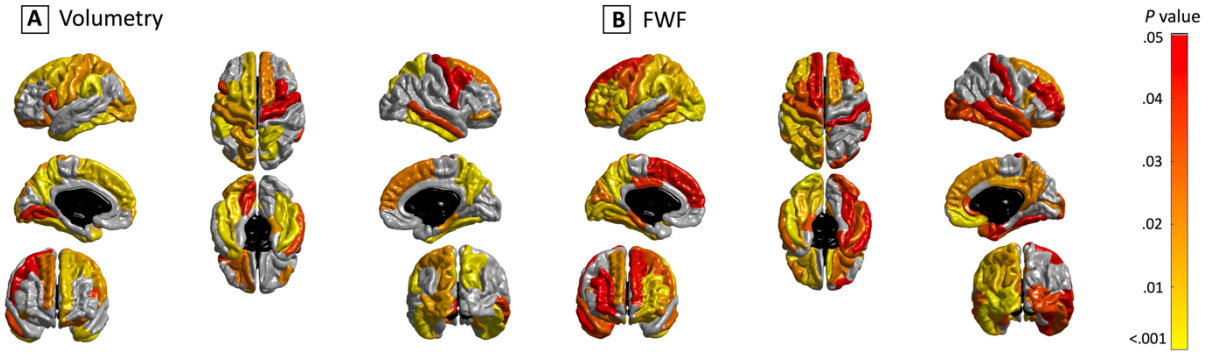

Table e-2: Effect sizes for FWF metrics and gray matter volume in cortical regions.

The effect sizes for both FWF and gray matter volume in cortical regions are shown below. For regions for which a significant difference between C9+ and C9- was detected for any of the metrics, we compared the effect size of FWF to that of volumetry using a permutation test procedures with 10000 iterations. The table presents the *P* values corresponding to these permutation tests (with a significance level of $P < 0.05$).

Abbreviations: CMF, caudal middle frontal cortex; CUN, cuneus cortex; FUS, fusiform; IP, inferior parietal cortex; IT, inferior temporal cortex; INS, insula; LO, lateral occipital cortex; LIN, lingual; PPC, pars opercularis cortex; PCC, pericalcarine; POC, postcentral cortex; PREC, precuneus; RMF, rostral middle frontal cortex; SP, superior parietal cortex; SM, supramarginal cortex; TP, temporal pole cortex; MOF, medial orbitofrontal cortex; BK, bankssts cortex; CAC, caudal anterior cingulate cortex; ENT, entorhinal cortex; FP, frontal pole cortex; IC, isthmus cingulate cortex; LOF, lateral orbitofrontal cortex; MT, middle temporal cortex; PAC, paracentral cortex; PHC, para hippocampal cortex; PB, pars orbitalis cortex; PTR, pars triangularis cortex; PCG, posterior cingulate cortex; PRC, precentral cortex; RAC, rostral anterior cingulate cortex; SF, superior frontal cortex; ST, superior temporal cortex; TT, transverse temporal cortex; R., right; L., left; FWF, free water fraction; NA, not applicable.

ROI	**Effect size** (FWF/Volumetry)	***P* value**	**ROI**	**Effect size** (FWF/Volumetry)	***P* value**
L.CMF	0.06/0.12	0.734	L.PREC	0.12/0.23	0.466
L.CUN	0.06/0.03	0.653	L.RMF	0.1/0	0.052
L.FUS	0.09/0.12	0.305	L.SP	0.1/0.09	0.712
L.IP	0.11/0.01	0.072	L.SM	0.11/0.18	0.639
L.IT	0.17/0.14	0.259	L.TP	0/0.12	0.025*
L.INS	0.19/0	0.002*	R.FUS	0.06/0.17	0.096
L.LO	0.32/0.09	0.001*	R.IT	0.07/0.15	0.406
L.LIN	0.11/0.06	0.092	R.MOF	0.12/0.02	0.051
L.PPC	0.12/0.06	0.201	R.PREC	0.07/0.14	0.483
L.PCC	0.12/0.01	0.008*	R.SP	0.03/0.14	0.140
L.POC	0.09/0.08	0.558	L.PB	0.08/0	NA
R.CMF	0.04/0.06	NA	L.PTR	0.08/0.01	NA
L.BK	0.08/0.01	NA	L.PCG	0.06/0	NA
L.CAC	0.04/0.01	NA	L.PRC	0.07/0.09	NA
L.ENT	0.02/0.01	NA	L.RAC	0/0.01	NA
L.FP	0.02/0.1	NA	L.SF	0.06/0.11	NA
L.IC	0.01/0.02	NA	L.ST	0.01/0.04	NA
L.LOF	0.11/0.06	NA	L.TT	0.01/0.04	NA
L.MOF	0.01/0.01	NA	R.BK	0.05/0.01	NA
L.MT	0.08/0.01	NA	R.CAC	0.04/0.03	NA
L.PAC	0.02/0.02	NA	R.CUN	0/0.04	NA
L.PHC	0.07/0	NA	R.ENT	0.06/0	NA
R.FP	0.04/0	NA	R.IP	0.01/0.01	NA
R.INS	0.05/0.02	NA	R.IC	0.04/0	NA
R.LOF	0.08/0.01	NA	R.LO	0.06/0.04	NA
R.LIN	0.04/0.02	NA	R.MT	0.06/0.07	NA
R.PAC	0.05/0.03	NA	R.PRC	0.03/0.06	NA
R.PHC	0.03/0.09	NA	R.RAC	0.08/0.02	NA
R.PPC	0.09/0.03	NA	R.RMF	0.06/0.02	NA

R.PB	0.04/0.08	NA	R.SF	0.09/0.08	NA
R.PTR	0.04/0.03	NA	R.ST	0.07/0.04	NA
R.PCC	0.09/0.01	NA	R.SM	0.03/0.05	NA
R.POC	0.05/0.05	NA	R.TP	0.04/0.06	NA
R.PCG	0.09/0	NA	R.TT	0/0.01	NA

Figure e-3. Color-coded representation of *P* values corresponding to the associations of *C9orf72* mutation with the subcortical ROI measures before correction for multiple comparisons.
Abbreviations: FWF, free water fraction.

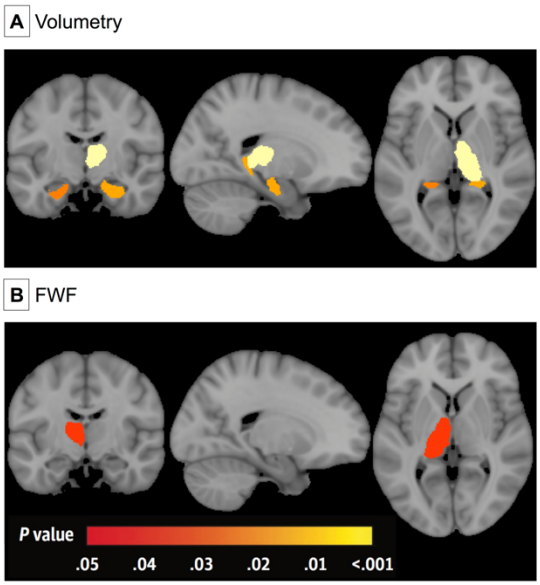

Table e-3. Effect sizes for FWF metrics and gray matter volume in subcortical regions.
The effect sizes for both FWF and gray matter volume in subcortical regions are shown below. For regions for which a significant difference between C9+ and C9- was detected for any of the metrics, we compared the effect size of FWF to that of volumetry using a permutation test procedures with 10000 iterations. The table presents the *P* values corresponding to these permutation tests (with a significance level of $P < 0.05$). For FWF effect size analysis, 6 ROIs were excluded because, after the 2-voxel erosion procedure, they were too small to produce reliable regional estimates.

Abbreviations: CB, cerebellum cortex; VD, ventral diencephalon; PUT, putamen; PAL, pallidum; CAU, caudate; ACC, accumbens area; THA, thalamus; HIP, hippocampus; FWF, free water fraction; NA, not applicable.

ROI	**Effect size** (FWF/Volumetry)	***P* value**	**ROI**	**Effect size** (FWF/Volumetry)	***P* value**
L. CB	NA/0	NA	R.CAU	0.01/0	NA
R.CB	NA/0	NA	L.ACC	NA/0	NA

L.VD	NA/0	NA	R.ACC	NA/0	NA
R.VD	NA/0	NA	L.AMY	0/0.03	NA
L.PUT	0.05/0.03	NA	R.AMY	0/0.04	NA
R.PUT	0.03/0.05	NA	L.THA	0.06/0.05	NA
L.PAL	0/0.02	NA	R.THA	0.03/0.16	0.062
R.PAL	0.09/0.02	NA	L.HIP	0/0.10	NA
L.CAU	0.02/0.00	NA	R.HIP	0/0.11	NA

Appendix C

Convolutional Neural Networks for Classification of Alzheimer's Disease: Overview and Reproducible Evaluation

This appendix is the supplementary material of the Chapter 5, which has been submitted to a journal article on to *Medical Image Analysis*:

- **Wen, J.**, Thibeau–Sutre, E., Samper-González., J, Routier, A., Bottani, S., Durrleman, S., Burgos, N., Colliot, O. Convolutional Neural Networks for Classification of Alzheimer's Disease: Overview and Reproducible Evaluation, Submitted to **Medical Image Analysis**. https://arxiv.org/pdf/1904.07773.pdf.

Convolutional Neural Networks for Classification of Alzheimer's Disease: Overview and Reproducible Evaluation

Supplementary Material

Junhao Wen[a,b,c,d,e], Elina Thibeau--Sutre[a,b,c,d,e], Jorge Samper-González[e,a,b,c,d], Alexandre Routier[e,a,b,c,d], Simona Bottani[e,a,b,c,d], Stanley Durrleman[e,a,b,c,d], Ninon Burgos[a,b,c,d,e], Olivier Colliot[a,b,c,d,e,f] , for the Alzheimer's Disease Neuroimaging Initiative and the Australian Imaging Biomarkers and Lifestyle flagship study of ageing

[a]*Institut du Cerveau et de la Moelle épinière, ICM, F-75013, Paris, France*

[b]*Sorbonne Université, F-75013, Paris, France*

[c]*Inserm, U 1127, F-75013, Paris, France*

[d]*CNRS, UMR 7225, F-75013, Paris, France*

[e]*Inria, Aramis project-team, F-75013, Paris, France*

[f]*AP-HP, Hôpital de la Pitié Salpêtrière, Department of Neurology and Neuroradiology, F-75013, Paris, France*

We present additional methodological explanations, tables and figures in this supplementary material. More specifically, we first present in detail the methodology of our literature review (eMethod 1). We then describe the datasets used in our study in eMethod 2. From eTable1 to eTable3, we present the architecture hyperparameters for the chosen models. The training hyperparameters for autoencoder pre-training and classification are shown in eTable 4 and eTable 5, respectively. Lastly, the monitoring of training process, including the display of the training/validation loss and accuracy, is presented from eFigure 1 to eFigure 4.

eMethod 1. Literature search methodology

We searched PubMed and Scopus for articles published up to the time of the search (15th of January 2019). Our request contains words linked to four different concepts: Alzheimer's disease, classification, deep learning and neuroimaging. The words matching these concepts were identified in the abstracts and titles of the articles of a first bibliography done on Google Scholar. In Scopus a restriction was added to remove the articles linked to electroencephalography that appeared with our query and were out of our scope. This restriction was not applied in PubMed as it concerns only a few articles (less than 10). The line of the query linked to the neuroimaging concept was extended to all fields, as some authors do not mention at all in the title, abstract or keywords the modalities that they employed.

Scopus query:
TITLE-ABS-KEY (alzheimer's OR alzheimer OR "Mild Cognitive Impairment")
AND
TITLE-ABS-KEY (classification OR diagnosis OR identification OR detection OR recognition)
AND
TITLE-ABS-KEY (cnn OR "Convolutional Network" OR "Deep Learning" OR "Neural Network" OR autoencoder OR gan)
AND
ALL (mri OR "Magnetic Resonance Imaging" OR "Structural Magnetic Resonance Imaging" OR neuroimaging OR brain-imaging)
AND NOT
TITLE-ABS-KEY (eeg OR eegs OR electroencephalogram OR electroencephalographic)

PubMed query:
(alzheimer's [Title/Abstract] OR alzheimer [Title/Abstract] OR "Mild Cognitive Impairment" [Title/Abstract])
AND
(cnn OR "Convolutional Network" [Title/Abstract] OR "Deep Learning" [Title/Abstract] OR "Neural Network" [Title/Abstract] OR autoencoder [Title/Abstract] OR gan [Title/Abstract])
AND
(classification [Title/Abstract] OR diagnosis [Title/Abstract] OR identification [Title/Abstract] OR detection [Title/Abstract] OR recognition [Title/Abstract])
AND
(mri OR "Magnetic Resonance Imaging" OR "Structural Magnetic Resonance Imaging" OR neuroimaging OR brain-imaging)

391 records were found with Scopus and 80 records were found with PubMed. After merging the two sets and removing duplicates, 406 records were identified. Before filtering the result, we removed from this list 10 conference proceedings books and 1 non-english article. We finally ended with 395 records to filter.

Once identified, all records were filtered in a 3-step process. We selected the records based on the abstract, the type and the content.

1.1. Record screening based on abstract

During this step, the abstracts of the articles were read to keep only the methods corresponding to the following criteria:

- use of anatomical MRI (when the modality was specified),
- classification of AD stages, then we excluded papers using deep learning to preprocess, segment or complete data, as well as the classification of different diseases or classification of different symptoms in AD population (depression, ICD…),
- exclusion of animal models,
- exclusion of reviews.

We chose to exclude the 31 reviews of our set as none of them focused on our topic. We did not detail the reasons of the exclusion of the papers in the diagram as many papers cumulate several criteria of exclusion. After this screening phase, we were left with 124 records.

1.2. Record screening based on type

Our search on PubMed and Scopus comprises only peer-reviewed items. However, there is a different level of peer-review between conference papers and journal articles, hence we kept all journal articles and recent conference papers (published since 2017). We decided to not only restrict to journal articles because it would have reduced the number of items to 48. We decided to keep recent conference papers because we considered that if the older ones were not transformed into journal articles it may mean that their contributions were not sufficient. After this step, the set contained 93 items.

1.3. Record screening based on content

This step was mainly used to sort the papers between the different sections of our state-of-the art. We detected in this way papers that were out of the scope of our review (longitudinal and multimodal studies, deep learning techniques other than CNN). We excluded only 22 papers because of i) use of another modality (1 paper); ii) duplicate content (2 papers); iii) lack of explanation on the method employed (7 papers); iv) no access to the content (12 papers). This step was reviewed by another member of the team to confirm the exclusions. In the end, our search resulted in 71 conference and journal articles, including 32 that are centered on our topic.

Diagram summarizing the bibliographic methodology

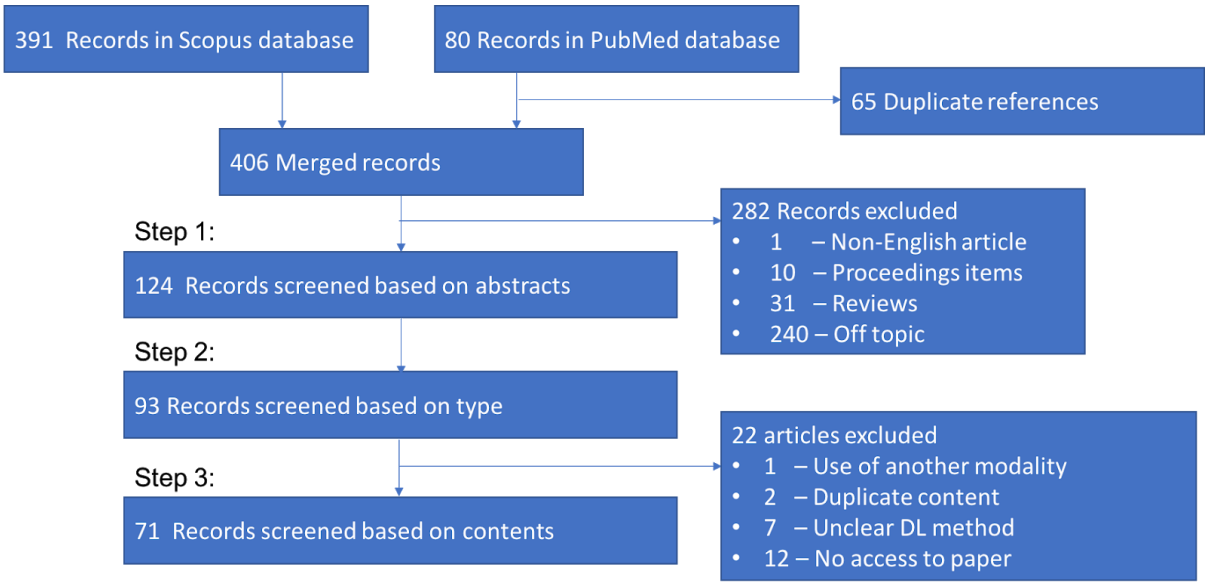

eMethod 2. Datasets used in our study

Part of the data used in the preparation of this article were obtained from the Alzheimer's Disease Neuroimaging Initiative database (adni.loni.usc.edu). The ADNI was launched in 2003 as a public-private partnership, led by Principal Investigator Michael W. Weiner, MD. The primary goal of ADNI has been to test whether serial MRI, PET, other biological markers, and clinical and neuropsychological assessment can be combined to measure the progression of mild cognitive impairment (MCI) and early AD. Over 1,650 participants were recruited across North America during the three phases of the study (ADNI1, ADNI GO and ADNI2). Around 400 participants were diagnosed with AD, 900 with MCI and 350 were control subjects. Three main criteria were used to classify the subjects (Petersen et al. 2010). The normal subjects had no memory complaints, while the subjects with MCI and AD both had to have complaints. CN and MCI subjects had a mini-mental state examination (MMSE) score between 24 and 30 (inclusive), and AD subjects between 20 and 26 (inclusive). The CN subjects had a clinical dementia rating (CDR) score of 0, the MCI subjects of 0.5 with a mandatory requirement of the memory box score being 0.5 or greater, and the AD subjects of 0.5 or 1. The other criteria can be found in (Petersen et al. 2010).

We also used data collected by the AIBL study group. Similarly to ADNI, the Australian Imaging, Biomarker & Lifestyle Flagship Study of Ageing seeks to discover which biomarkers, cognitive characteristics, and health and lifestyle factors determine the development of AD. AIBL has enrolled 1100 participants and collected over 4.5 years worth of longitudinal data: 211 AD patients, 133 MCI patients and 768 comparable healthy controls. AIBL study methodology has been reported previously (Ellis et al. 2009; Ellis et al. 2010). Briefly, the MCI diagnoses were made according to a protocol based on the criteria of, (Winblad et al. 2004) and the AD diagnoses on the NINCDS-ADRDA criteria (McKhann et al. 1984). Note that about half of the subjects diagnosed as healthy controls reported memory complaints (Ellis et al. 2009; Ellis et al. 2010).

Finally, we used data from the Open Access Series of Imaging Studies project whose aim is to make MRI datasets of the brain freely available to the scientific community. We focused on the "Cross-sectional MRI Data in Young, Middle Aged, Nondemented and Demented Older Adults" set (Marcus et al. 2007), which consists of a cross-sectional collection of 416 subjects aged 18 to 96. 100 of the included subjects over the age of 60 have been clinically diagnosed with very mild to moderate AD. The criteria used to evaluate the diagnosis was the CDR score. All participants with a CDR greater than 0 were diagnosed with probable AD. Note that there are no MCI subjects in OASIS.

eTable 1. Architecture hyperparameters for 3D subject-level CNN.

As the architecture depends on the size of the input, it slightly differs between the two types of preprocessing (i.e. “Minimal” or “Extensive”). This difference only affects the size of the input of the first FC layer (FC1). The output size of each layer is reported depending on the preprocessing used in the last two columns.

The padding size in convolutional layers has been set to 1 not to decrease the size of the convolutional layer outputs. Without any padding, the number of nodes at the end of the last convolutional layer is too small to reconstruct the image correctly using an autoencoder for the Extensive preprocessing.

The padding size in pooling layers depends on the input: columns of zeros are added along a dimension until the size along this dimension is a multiple of the stride size.

Layer	Filter size	Number of filters / neurons	Stride size	Padding size	Dropout rate	Output size (Minimal)	Output size (Extensive)
Conv1+BN+ReLU	3x3x3	8	1	1	--	8x169x208x179	8x121x145x121
MaxPool1	2x2x2	--	2	adaptive	--	8x85x104x90	8x61x73x61
Conv2+BN+ReLU	3x3x3	16	1	1	--	16x85x104x90	16x61x73x61
MaxPool2	2x2x2	--	2	adaptive	--	16x43x52x45	16x31x37x31
Conv3+BN+ReLU	3x3x3	32	1	1	--	32x43x52x45	32x31x37x31
MaxPool3	2x2x2	--	2	adaptive	--	32x22x26x23	32x16x19x16
Conv4+BN+ReLU	3x3x3	64	1	1	--	64x22x26x23	64x16x19x16
MaxPool4	2x2x2	--	2	adaptive	--	64x11x13x12	64x8x10x8
Conv5+BN+ReLU	3x3x3	128	1	1	--	128x11x13x12	128x8x10x8
MaxPool5	2x2x2	--	2	adaptive	--	128x6x7x6	128x4x5x4
Dropout	--	--	--	--	0.5	128x6x7x6	128x4x5x4
FC1	--	1300	--	--	--	1300	1300
FC2	--	50	--	--	--	50	50
FC3	--	2	--	--	--	2	2
Softmax	--	--	--	--	--	--	2

BN: batch normalization; Conv: convolutional layer; FC: fully connected; MaxPool: max pooling.

eTable 2. Architecture hyperparameters for 3D ROI-based and patch-level CNN.

The padding size in pooling layers depends on the input: columns of zeros are added along a dimension until the size along this dimension is a multiple of the stride size.

Layer	Filter size	Number of filters / neurons	Stride size	Padding size	Dropout rate	Output size
Conv1+BN+ReLU	3x3x3	15	1	0	--	15x48x48x48
MaxPool1	2x2x2	--	2	adaptive	--	15x24x24x24
Conv2+BN+ReLU	3x3x3	25	1	0	--	25x22x22x22
MaxPool2	2x2x2	--	2	adaptive	--	25x11x11x11
Conv3+BN+ReLU	3x3x3	50	1	0	--	50x9x9x9
MaxPool3	2x2x2	--	2	adaptive	--	50x5x5x5
Conv4+BN+ReLU	3x3x3	50	1	0	--	50x3x3x3
MaxPool4	2x2x2	--	2	adaptive	--	50x2x2x2
Dropout1	--	--	--	--	0.5	50x2x2x2
FC1	--	50	--	--	--	50
Dropout2	--	--	--	--	0.5	50
FC2	--	40	--	--	--	40
FC3	--	2	--	--	--	2
Softmax	--	--	--	--	--	2

BN: batch normalization; Conv: convolutional layer; FC: fully connected; MaxPool: max pooling.

eTable 3. Architecture hyperparameters for 2D slice-level CNN.

Table B explicits the architecture of our 2D slice-level CNN. Shortcuts are displayed with arrows and are adding the two feature maps linked together and applying ReLU to form a new feature map given to the following layer.
When shortcuts are linking feature maps of different sizes, the arrow is associated with a downsampling layer (see table A) applied to the largest feature map.

A. Characteristics of the downsampling layers

Layer	Filter size	Number of filters / neurons	Stride size	Padding size	Dropout rate
Conv8	1x1	128	2	0	--
Conv13	1x1	256	2	0	--
Conv18	1x1	512	2	0	--

B. Architecture of the 2D slice-level CNN (adaptation of the ResNet-18)

Layer	Filter size	Number of filters / neurons	Stride size	Padding size	Dropout rate	Output size
Conv1+BN+ReLU	7x7	64	2	3	--	64x112x112
MaxPool1	3x3	--	2	1	--	64x56x56
Conv2+BN+ReLU	3x3	64	1	1	--	64x56x56
Conv3+BN	3x3	64	1	1	--	64x56x56
Conv4+BN+ReLU	3x3	64	1	1	--	64x56x56
Conv5+BN	3x3	64	1	1	--	64x56x56
Conv6+BN+ReLU	3x3	128	2	1	--	128x28x28
Conv7+BN	3x3	128	1	1	--	128x28x28
Conv9+BN+ReLU	3x3	128	1	1	--	128x28x28
Conv10+BN	3x3	128	1	1	--	128x28x28
Conv11+BN+ReLU	3x3	256	2	1	--	256x14x14
Conv12+BN	3x3	256	1	1	--	256x14x14
Conv14+BN+ReLU	3x3	256	1	1	--	256x14x14
Conv15+BN	3x3	256	1	1	--	256x14x14
Conv16+BN+ReLU	3x3	512	2	1	--	512x7x7
Conv17+BN	3x3	512	1	1	--	512x7x7
Conv19+BN+ReLU	3x3	512	1	1	--	512x7x7
Conv20+BN	3x3	512	1	1	--	512x7x7
AveragePool1	7x7	--	1	0	--	512x1x1
FC1	--	1000	--	--	--	1000
Dropout	--	--	--	--	0.8	1000
FC2	--	2	--	--	--	2
Softmax	--	--	--	--	--	2

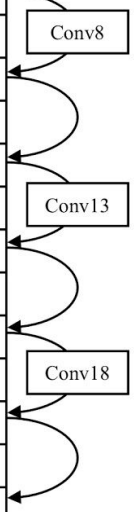

eTable 4. Training hyperparameters for classification experiments.

A summary of the experiments can be found in Table A. The corresponding hyperparameters are listed in Table B indicated by the experiments numbers.

Common hyperparameters for all experiments: optimizer: Adam; Adam parameters: betas=(0.9, 0.999), epsilon=1e-8; loss: cross entropy.

When transfer learning is applied, the corresponding experiment number is given between brackets and can be found in eTable 5 for AE pretraining (AE) and eTable 4 for cross-task transfer learning (CTT).

A. Summary of experiments performed

Experiment number	Classification architectures	Training data	Image preprocessing	Intensity rescaling	Data split	Training approach	Transfer learning	Task
1	3D subject-level CNN	Baseline	Minimal	None	subject-level	single-CNN	None	AD vs CN
2				MinMax				
3							AE (1)	
4		Longitudinal	Minimal	MinMax	subject-level	single-CNN	AE (1)	
5			Extensive				AE (2)	
6			Minimal				CTT (4)	sMCI vs pMCI
7		Baseline					CTT (3)	
8	3D ROI-based CNN	Baseline	Minimal	MinMax	subject-level	single-CNN	AE (3)	AD vs CN
9							CTT (8)	sMCI vs pMCI
10		Longitudinal					AE (4)	AD vs CN
11							CTT (10)	sMCI vs pMCI
12	3D patch-level CNN	Baseline	Minimal	MinMax	subject-level	single-CNN	AE (5)	AD vs CN
13		Longitudinal					AE (6)	
14		Baseline	Minimal	MinMax	subject-level	multi-CNN	AE (7)	AD vs CN
15							CTT (14)	sMCI vs pMCI
16		Longitudinal					AE (8)	AD vs CN
17							CTT (16)	sMCI vs pMCI
18	2D slice-level CNN	Baseline	Minimal	MinMax	subject-level	single-CNN	ImageNet pre-train	AD vs CN
19		Longitudinal						
20		Baseline	Minimal	MinMax	slice-level **(data leakage)**	single-CNN	ImageNet pre-train	AD vs CN

B. Hyperparameters corresponding to experiments described in Table A.

Approach	Experiment	Number of epochs	Learning rate	Batch size	Dropout rate	Weight decay	Patience
3D subject-level CNN	1	50	1e-4	12	0.5	1e-4	10
	2	50	1e-4	12	0.5	1e-4	10
	3	50	1e-4	12	0.5	1e-4	10
	4	50	1e-4	12	0.5	1e-4	5
	5	50	1e-4	12	0.5	1e-4	5
	6	50	1e-5	12	0.5	1e-4	10
	7	50	1e-5	12	0.5	1e-4	20
3D ROI-based CNN	8	200	1e-5	32	0.5	1e-4	10
	9	200	1e-5	32	0.5	1e-3	20
	10	200	1e-5	32	0.5	1e-4	10
	11	200	1e-5	32	0.5	1e-3	20
3D patch-level CNN	12	200	1e-5	32	0.5	1e-3	20
	13	200	1e-5	32	0.5	1e-3	20
	14	200	1e-5	32	0.5	1e-4	15
	15	200	1e-5	32	0.5	1e-3	20
	16	200	1e-5	32	0.5	1e-4	15
	17	200	1e-5	32	0.5	1e-3	20
2D slice-level CNN	18	50	1e-6	32	0.8	1e-4	15
	19	100	1e-6	32	0.8	1e-4	15
	20	50	1e-6	32	0.8	1e-4	15

eTable 5. Training hyperparameters for autoencoder pretraining experiments.

A summary of the experiments can be found in table A. The corresponding hyperparameters are listed in Table B using the same experiments numbers.

Common hyperparameters for all experiments: optimizer: Adam; Adam parameters: betas=(0.9, 0.999), epsilon=1e-8; loss: mean squared entropy loss; training data: AD + MCI + CN; data split: subject-level. The stopping criterion is the maximal number of epochs.

A. Summary of autoencoder pretraining experiments performed.

Experiment number	Classification architectures	Training data	Image preprocessing	Intensity rescaling	Training approach
1	3D subject-level CNN	Baseline	Minimal	MinMax	single-CNN
2			Extensive		
3	3D ROI-based CNN	Baseline	Minimal	MinMax	single-CNN
4		Longitudinal			
5	3D patch-level CNN	Baseline	Minimal	MinMax	single-CNN
6		Longitudinal			
7		Baseline			multi-CNN
8		Longitudinal			

B. Hyperparameters corresponding to autoencoder pretraining experiments described in Table A.

Approach	Experiment	Number of epochs	Learning rate	Batch size	Weight decay
3D subject-level CNN	1	50	1e-4	12	1e-4
	2	30	1e-4	12	1e-4
3D ROI-based CNN	3	200	1e-5	32	0
	4	100	1e-5	32	0
3D patch-level CNN	5	20	1e-5	32	0
	6	15	1e-5	32	0
	7	15	1e-5	32	0
	8	15	1e-5	32	0

eFigure 1. Training process monitoring for 3D subject-level CNN

Training and validation accuracy/loss during the training process were evaluated after the forward pass of 20 batches. The accuracy and loss curves were smoothed with a threshold (0.6).

For each plot a subfigure letter is used and the corresponding information on the experiment may be found in the table below or in eTable 4 according to the "Experiment number".

Subfigure	Experiment number	Fold displayed	Epoch where training stopped	Epoch of the highest validation accuracy	Highest validation accuracy
A	1	2	32	22	0.50
B	2	2	37	27	0.87
C	3	2	28	28	0.83
D	4	2	11	10	0.87
E	5	2	10	9	0.91
F	6	2	23	1	0.77
G	7	2	42	37	0.77

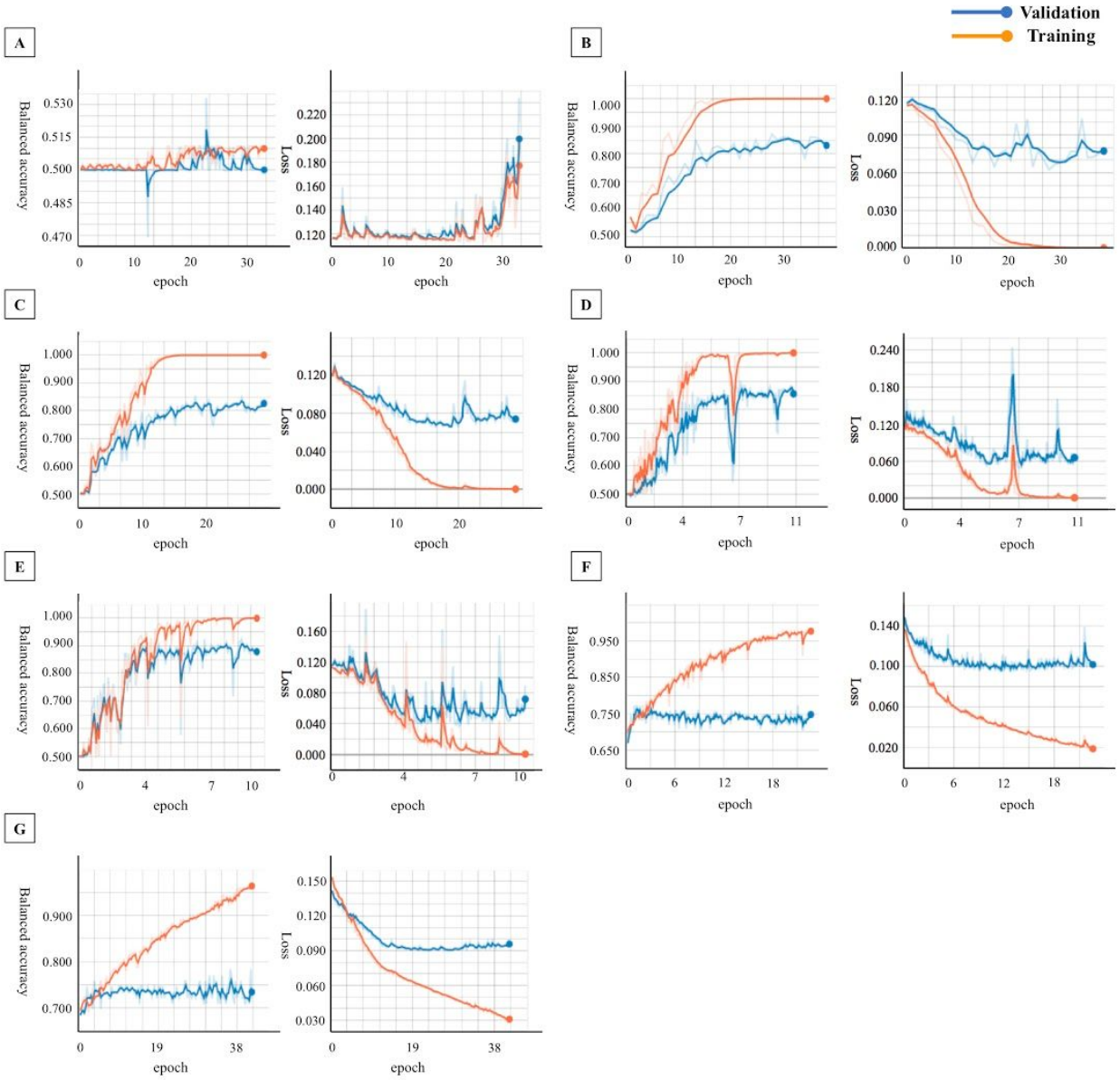

eFigure 2. Training process monitoring for 3D ROI-based CNN.

Training and validation accuracy/loss during the training process were evaluated after each epoch. The accuracy and loss curves were smoothed with a threshold (0.6).

For each plot a subfigure letter is used and the corresponding information on the experiment may be found in the table below or in eTable 4 according to the "Experiment number".

Subfigure	Experiment number	Fold displayed	Epoch where training stopped	Epoch of the highest validation accuracy	Highest validation accuracy
A	8	2	141	125	0.89
B	9	1	60	60	0.84
C	10	3	89	51	0.88
D	11	3	55	48	0.82

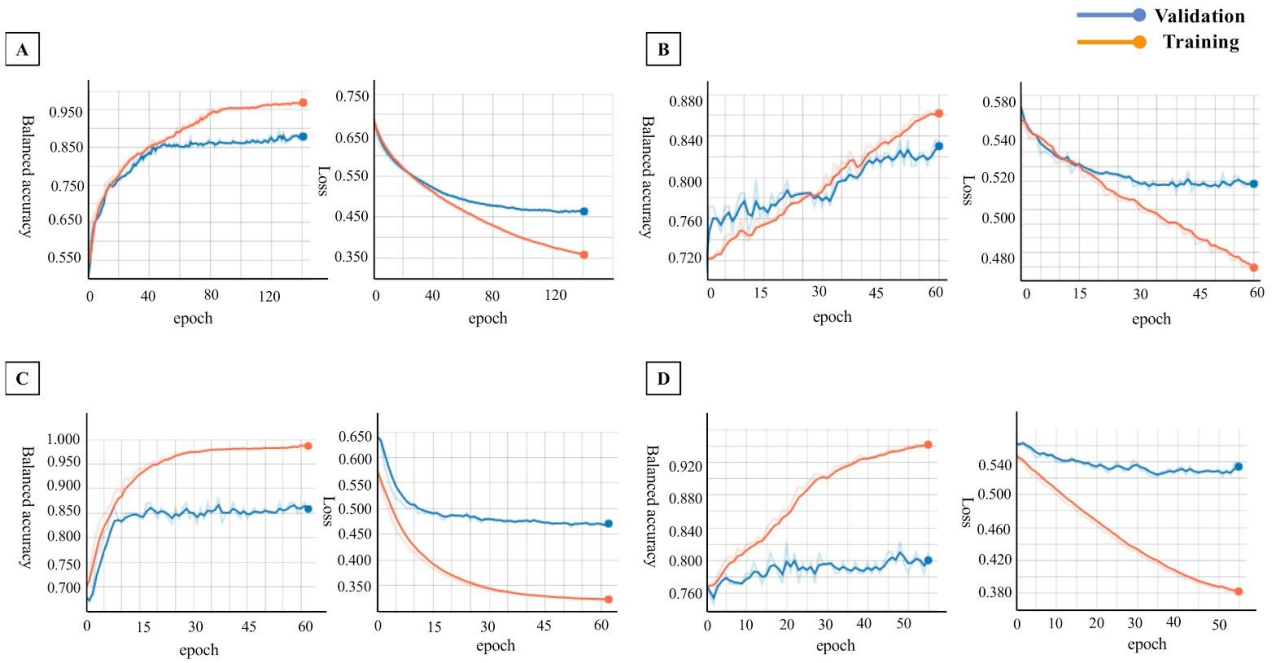

eFigure 3. Training process monitoring for 3D patch-level CNN

Training and validation accuracy/loss during the training process were evaluated after each epoch. The accuracy and loss curves were smoothed with a threshold (0.6).

For each plot a subfigure letter is used and the corresponding information on the experiment may be found in the table below or in eTable 4 according to the "Experiment number". For multi-CNN experiments the CNN number is provided.

Subfigure	Experiment number	Fold displayed	CNN number	Epoch where training stopped	Epoch of the highest validation accuracy	Highest validation accuracy
A	12	2	--	51	31	0.83
B	13	2	--	51	31	0.83
C	14	1	5	110	110	0.85
D	15	1	19	148	46	0.80
E	16	1	29	96	86	0.81
F	17	1	19	58	30	0.78

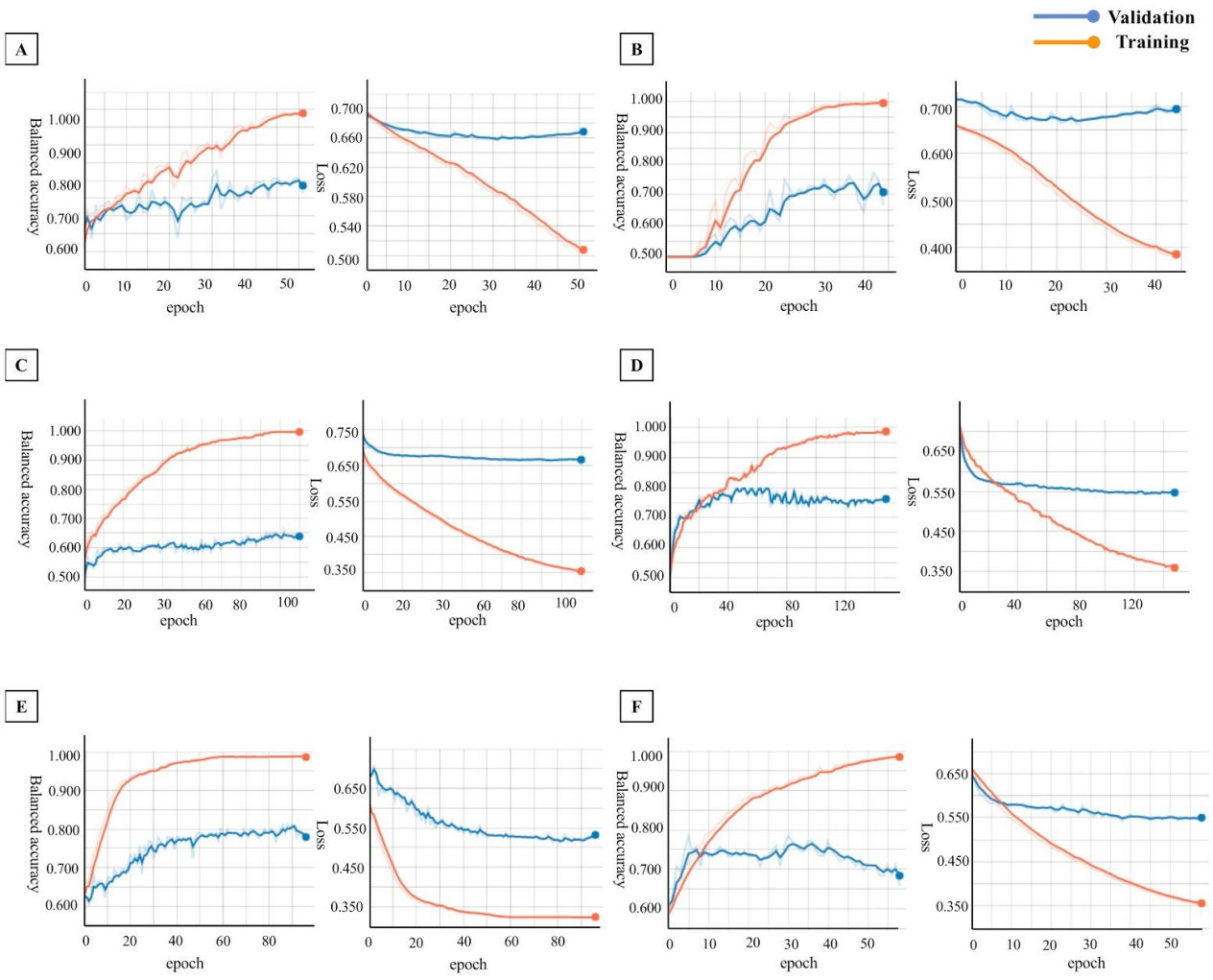

eFigure 4. Training process monitoring for 2D slice-level CNN

Training and validation accuracy/loss during the training process were evaluated after each epoch. The accuracy and loss curves were smoothed with a threshold (0.6).

For each plot a subfigure letter is used and the corresponding information on the experiment may be found in the table below or in eTable 4 according to the "Experiment number".

Subfigure	Experiment number	Fold displayed	Epoch where training stopped	Epoch of the highest validation accuracy	Highest validation accuracy
A	18	2	21	11	0.85
B	19	2	15	15	0.84
C	20	2	49	49	1.00

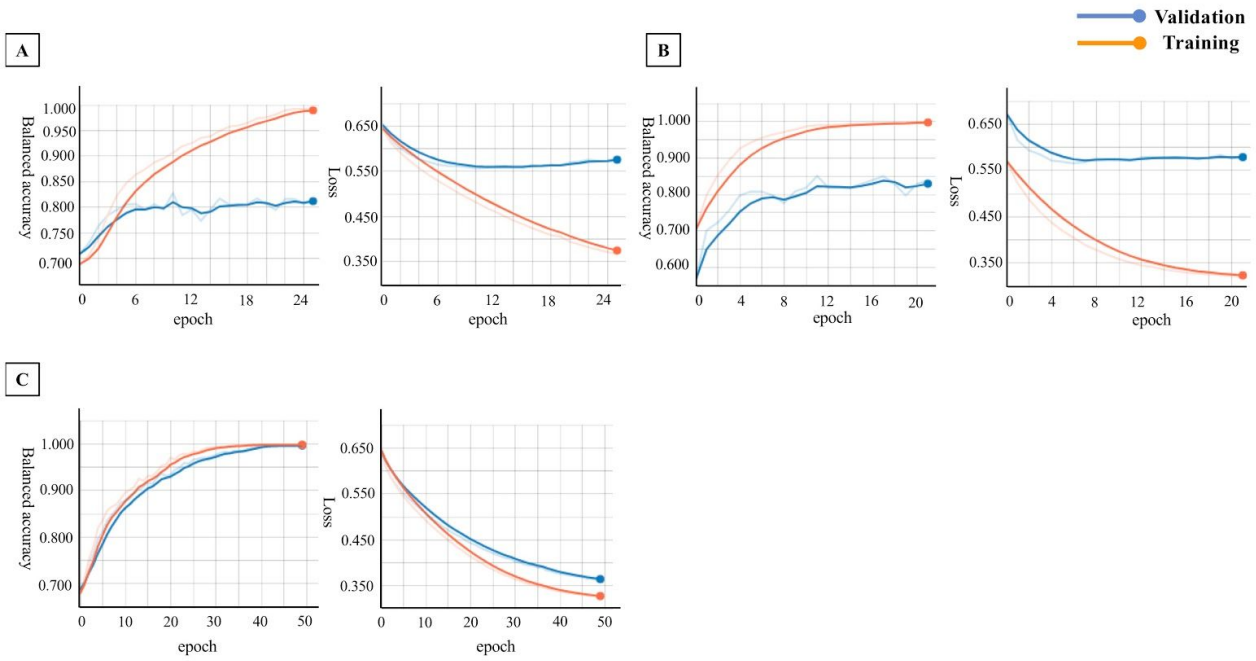

References

Ellis, K.A. et al., 2010. Addressing population aging and Alzheimer's disease through the Australian Imaging Biomarkers and Lifestyle study: Collaboration with the Alzheimer's Disease Neuroimaging Initiative. *Alzheimer's & Dementia*, 6(3), pp.291–296. Available at: http://dx.doi.org/10.1016/j.jalz.2010.03.009.

Ellis, K.A. et al., 2009. The Australian Imaging, Biomarkers and Lifestyle (AIBL) study of aging: methodology and baseline characteristics of 1112 individuals recruited for a longitudinal study of Alzheimer's disease. *International Psychogeriatrics*, 21(04), p.672. Available at: http://dx.doi.org/10.1017/s1041610209009405.

Marcus, D.S. et al., 2007. Open Access Series of Imaging Studies (OASIS): cross-sectional MRI data in young, middle aged, nondemented, and demented older adults. *Journal of cognitive neuroscience*, 19(9), pp.1498–1507.

McKhann, G. et al., 1984. Clinical diagnosis of Alzheimer's disease Report of the NINCDS-ADRDA Work Group* under the auspices of Department of Health and Human Services Task Force on Alzheimer's Disease. *Neurology*, 34(7), pp.939–939.

Petersen, R.C. et al., 2010. Alzheimer's Disease Neuroimaging Initiative (ADNI): clinical characterization. *Neurology*, 74(3), pp.201–209.

Winblad, B. et al., 2004. Mild cognitive impairment–beyond controversies, towards a consensus: report of the International Working Group on Mild Cognitive Impairment. *Journal of internal medicine*. Available at: https://onlinelibrary.wiley.com/doi/abs/10.1111/j.1365-2796.2004.01380.x.

Bibliography

Aderghal, K et al. (2018). "Classification of Alzheimer Disease on Imaging Modalities with Deep CNNs Using Cross-Modal Transfer Learning". In: *2018 IEEE 31st International Symposium on Computer-Based Medical Systems (CBMS)*, pp. 345–350.

Aderghal, K., J. Benois-Pineau, and K. Afdel (2017). "Classification of sMRI for Alzheimer's Disease Diagnosis with CNN: Single Siamese Networks with 2D+? Approach and Fusion on ADNI". In: *Proceedings of the 2017 ACM on International Conference on Multimedia Retrieval*. ICMR '17. New York, NY, USA: ACM, pp. 494–498.

Aderghal, K. et al. (2017). "FuseMe: Classification of sMRI images by fusion of Deep CNNs in 2D+ϵ projections". In: *Proceedings of the 15th International Workshop on Content-Based Multimedia Indexing*. ACM, p. 34.

Agosta, F. et al. (2011). "White Matter Damage in Alzheimer Disease and Its Relationship to Gray Matter Atrophy". In: *Radiology* 258.3, pp. 853–863. DOI: 10.1148/radiol.10101284.

Agosta, F. et al. (2012). "Resting state fMRI in Alzheimer's disease: beyond the default mode network". In: *Neurobiology of Aging* 33.8, pp. 1564–1578. DOI: 10.1016/j.neurobiolaging.2011.06.007.

Agosta, F. et al. (2017). "Structural and functional brain signatures of C9orf72 in motor neuron disease". In: *Neurobiology of Aging*. DOI: 10.1016/j.neurobiolaging.2017.05.024.

Ahmed, O. B. et al. (2017). "Recognition of Alzheimer's disease and Mild Cognitive Impairment with multimodal image-derived biomarkers and Multiple Kernel Learning". In: *Neurocomputing* 220, pp. 98–110.

Aisen, P. S. et al. (2010). "Clinical Core of the Alzheimer's Disease Neuroimaging Initiative: progress and plans". In: *Alzheimers. Dement.* 6.3, pp. 239–246.

Akbani, R., S. Kwek, and N. Japkowicz (2004). "Applying Support Vector Machines to Imbalanced Datasets". In: *Machine Learning: ECML 2004*. Springer Berlin Heidelberg, pp. 39–50.

Albert, M. S. et al. (2011). "The diagnosis of mild cognitive impairment due to Alzheimer's disease: recommendations from the National Institute on Aging-Alzheimer's Association workgroups on diagnostic guidelines for Alzheimer's

disease". In: *Alzheimer's & Dementia: The Journal of the Alzheimer's Association* 7.3, pp. 270–279. DOI: 10.1016/j.jalz.2011.03.008.

Alexander, A. L. et al. (2007). "Diffusion Tensor Imaging of the Brain". In: *Neurotherapeutics : the journal of the American Society for Experimental NeuroTherapeutics* 4.3, pp. 316–329. DOI: 10.1016/j.nurt.2007.05.011.

Alexander-Bloch, A. et al. (2016). "Subtle in-scanner motion biases automated measurement of brain anatomy from in vivo MRI". In: *Hum. Brain Mapp.* 37.7, pp. 2385–2397.

Amoroso, N. et al. (2017). "Topological Measurements of DWI Tractography for Alzheimer's Disease Detection". In: *Comput. Math. Methods Med.* 2017, p. 5271627.

Amoroso, N. et al. (2018). "Deep learning reveals Alzheimer's disease onset in MCI subjects: Results from an international challenge". In: *J. Neurosci. Methods* 302, pp. 3–9.

Andersson, J. L. R., M. Jenkinson, and S. Smith (2010). "Non-linear registration aka Spatial normalisation". In: *FMRIB Technial Report TR07JA2*.

Andersson, J. L. R. and S. N. Sotiropoulos (2016). "An integrated approach to correction for off-resonance effects and subject movement in diffusion MR imaging". In: *NeuroImage* 125, pp. 1063–1078. DOI: 10.1016/j.neuroimage.2015.10.019.

Andersson, J. L., S. Skare, and J. Ashburner (2003). "How to correct susceptibility distortions in spin-echo echo-planar images: application to diffusion tensor imaging". In: *NeuroImage* 20.2, pp. 870–888. DOI: 10.1016/S1053-8119(03)00336-7.

Ashburner, J. (2007). "A fast diffeomorphic image registration algorithm". In: *Neuroimage* 38.1, pp. 95–113.

Ashburner, J. and K. J. Friston (2000). "Voxel-Based Morphometry—The Methods". In: *Neuroimage* 11.6, pp. 805–821.

— (2005). "Unified segmentation". In: *Neuroimage* 26.3, pp. 839–851.

Avants, B. B. et al. (2008). "Symmetric Diffeomorphic Image Registration with Cross-Correlation: Evaluating Automated Labeling of Elderly and Neurodegenerative Brain". In: *Medical image analysis* 12.1, pp. 26–41. DOI: 10.1016/j.media.2007.06.004.

Avants, B. B. et al. (2014). "The Insight ToolKit image registration framework". In: *Front. Neuroinform.* 8, p. 44.

Bäckström, K et al. (2018). "An efficient 3D deep convolutional network for Alzheimer's disease diagnosis using MR images". In: *2018 IEEE 15th International Symposium on Biomedical Imaging (ISBI 2018)*, pp. 149–153.

Baker, M. et al. (2006). "Mutations in progranulin cause tau-negative frontotemporal dementia linked to chromosome 17". In: *Nature* 442.7105, pp. 916–919. DOI: 10.1038/nature05016.

Ballard, C. et al. (2011). "Alzheimer's disease". In: *The Lancet* 377.9770, pp. 1019–1031. DOI: 10.1016/S0140-6736(10)61349-9.

Bankman, I. (2008). *Handbook of Medical Image Processing and Analysis*. Elsevier.

Basaia, S. et al. (2018). "Automated classification of Alzheimer's disease and mild cognitive impairment using a single MRI and deep neural networks". In: *NeuroImage: Clinical*, p. 101645. DOI: 10.1016/j.nicl.2018.101645.

Baskar, D, V. S. Jayanthi, and A. N. Jayanthi (2018). "An efficient classification approach for detection of Alzheimer's disease from biomedical imaging modalities". In: *Multimed. Tools Appl.* Pp. 1–33.

Bateman, R. J. et al. (2012). "Clinical and biomarker changes in dominantly inherited Alzheimer's disease". In: *The New England Journal of Medicine* 367.9, pp. 795–804. DOI: 10.1056/NEJMoa1202753.

Behrens, T. E. J. et al. (2007). "Probabilistic diffusion tractography with multiple fibre orientations: What can we gain?" In: *NeuroImage* 34.1, pp. 144–155. DOI: 10.1016/j.neuroimage.2006.09.018.

Bengio, Y. and Y. Grandvalet (2004). "No Unbiased Estimator of the Variance of K-Fold Cross-Validation". In: p. 17.

Benjamin, D. J. et al. (2018). "Redefine statistical significance". In: *Nature Human Behaviour* 2.1, p. 6. DOI: 10.1038/s41562-017-0189-z.

Benzinger, T. L. S. et al. (2013). "Regional variability of imaging biomarkers in autosomal dominant Alzheimer's disease". In: *Proceedings of the National Academy of Sciences of the United States of America* 110.47, E4502–4509. DOI: 10.1073/pnas.1317918110.

Bermingham, M. L. et al. (2015). "Application of high-dimensional feature selection: evaluation for genomic prediction in man". In: *Sci. Rep.* 5, p. 10312.

Bernal, J. et al. (2018). "Deep convolutional neural networks for brain image analysis on magnetic resonance imaging: a review". In: *Artificial Intelligence in Medicine*. DOI: 10.1016/j.artmed.2018.08.008.

Bertrand, A. et al. (2017). "Early Cognitive, Structural, and Microstructural Changes in Presymptomatic C9orf72 Carriers Younger Than 40 Years". In: *JAMA neurology*. DOI: 10.1001/jamaneurol.2017.4266.

Bhagwat, N. et al. (2018). "Modeling and prediction of clinical symptom trajectories in Alzheimer's disease using longitudinal data". In: *PLoS Comput. Biol.* 14.9, e1006376.

Bishop, C. M. (2009). *Pattern recognition and machine learning*. Corrected at 8th printing 2009. Information science and statistics. New York, NY: Springer. ISBN: 978-0-387-31073-2 978-1-4939-3843-8.

Boer, P.-T. de et al. (2005). "A Tutorial on the Cross-Entropy Method". In: *Ann. Oper. Res.* 134.1, pp. 19–67.

Bonin-Guillaume, S. et al. (2005). "Impact économique de la démence". In: *La Presse Médicale* 34.1, pp. 35–41. DOI: 10.1016/S0755-4982(05)83882-5.

Bourlard, H and Y Kamp (1988). "Auto-association by multilayer perceptrons and singular value decomposition". In: *Biol. Cybern.* 59.4-5, pp. 291–294.

Braak, H and E Braak (1998). "Evolution of neuronal changes in the course of Alzheimer's disease". In: *Ageing and Dementia*. Ed. by K Jellinger, F Fazekas, and M Windisch. Vol. 53. Journal of Neural Transmission. Supplementa. Vienna: Springer Vienna, pp. 127–140.

Broad, R. et al. (2017). "Neurite Orientation Dispersion and Density Imaging (NODDI) highlights axonal degeneration of the motor tracts as the core feature underlying Amyotrophic Lateral Sclerosis. (S53.008)". In: *Neurology* 88.16 Supplement, S53.008.

Brookmeyer, R. et al. (2007). "Forecasting the global burden of Alzheimer's disease". In: *Alzheimers. Dement.* 3.3, pp. 186–191.

Burciu, R. G. et al. (2016). "Free-Water and BOLD Imaging Changes in Parkinson's Disease Patients Chronically Treated with a MAO-B Inhibitor". In: *Human brain mapping* 37.8, pp. 2894–2903. DOI: 10.1002/hbm.23213.

Burciu, R. G. et al. (2017). "Progression marker of Parkinson's disease: a 4-year multi-site imaging study". In: *Brain: A Journal of Neurology* 140.8, pp. 2183–2192. DOI: 10.1093/brain/awx146.

Burns, A. and S. Iliffe (2009a). "Alzheimer's disease". In: *BMJ* 338.feb05 1, b158–b158. DOI: 10.1136/bmj.b158.

Burns, A. and S. Iliffe (2009b). "Dementia". In: *BMJ* 338, b75. DOI: 10.1136/bmj.b75.

Cabral, C. et al. (2015). "Predicting conversion from MCI to AD with FDG-PET brain images at different prodromal stages". In: *Computers in Biology and Medicine* 58, pp. 101–109. DOI: 10.1016/j.compbiomed.2015.01.003.

Cai, S. et al. (2018). "Potential biomarkers for distinguishing people with Alzheimer's disease from cognitively intact elderly based on the rich-club hierarchical structure of white matter networks". In: *Neurosci. Res.*

Cárdenas-Peña, D., D. Collazos-Huertas, and G. Castellanos-Dominguez (2016). "Centered Kernel Alignment Enhancing Neural Network Pretraining for MRI-Based Dementia Diagnosis". In: *Comput. Math. Methods Med.* 2016, p. 9523849.

— (2017). "Enhanced Data Representation by Kernel Metric Learning for Dementia Diagnosis". In: *Front. Neurosci.* 11, p. 413.

Cash, D. M. et al. (2017). "Patterns of grey matter atrophy in genetic frontotemporal dementia: results from the GENFI study". In: *Neurobiology of Aging*. DOI: 10.1016/j.neurobiolaging.2017.10.008.

Chaddad, A, C Desrosiers, and T Niazi (2018). "Deep Radiomic Analysis of MRI Related to Alzheimer's Disease". In: *IEEE Access* 6, pp. 58213–58221.

Chandrashekar, G. and F. Sahin (2014). "A survey on feature selection methods". In: *Computers & Electrical Engineering* 40.1, pp. 16–28. DOI: 10.1016/j.compeleceng.2013.11.024.

Chang, Y. S. et al. (2015). "White Matter Changes of Neurite Density and Fiber Orientation Dispersion during Human Brain Maturation". In: *PLOS ONE* 10.6. Ed. by G. Gong, e0123656. DOI: 10.1371/journal.pone.0123656.

Cheng, D. and M. Liu (2017). "CNNs based multi-modality classification for AD diagnosis". In: *2017 10th International Congress on Image and Signal Processing, BioMedical Engineering and Informatics (CISP-BMEI)*, pp. 1–5. DOI: 10.1109/CISP-BMEI.2017.8302281.

Cheng, D. et al. (2017). "Classification of MR brain images by combination of multi-CNNs for AD diagnosis". In: ed. by C. M. Falco and X. Jiang, p. 1042042. DOI: 10.1117/12.2281808.

Ciresan, D. C. et al. (2011). "Flexible, high performance convolutional neural networks for image classification". In: *IJCAI Proceedings-International Joint Conference on Artificial Intelligence*. Vol. 22. Barcelona, Spain, p. 1237.

Çitak-ER, F., D. Goularas, and B. Ormeci (2017). "A novel Convolutional Neural Network Model Based on Voxel-based Morphometry of Imaging Data in Predicting the Prognosis of Patients with Mild Cognitive Impairment". In: *J. Neurol. Sci. Turk.* 34.1.

Cruts, M. et al. (2006). "Null mutations in progranulin cause ubiquitin-positive frontotemporal dementia linked to chromosome 17q21". In: *Nature* 442.7105, p. 920. DOI: 10.1038/nature05017.

Cruts, M. et al. (2013). "Current insights into the C9orf72 repeat expansion diseases of the FTLD/ALS spectrum". In: *Trends in Neurosciences* 36.8, pp. 450–459. DOI: 10.1016/j.tins.2013.04.010.

Cui, R, M Liu, and G Li (2018). "Longitudinal analysis for Alzheimer's disease diagnosis using RNN". In: *2018 IEEE 15th International Symposium on Biomedical Imaging (ISBI 2018)*, pp. 1398–1401.

Cui, Y. et al. (2012). "Automated detection of amnestic mild cognitive impairment in community-dwelling elderly adults: a combined spatial atrophy and white matter alteration approach". In: *Neuroimage* 59.2, pp. 1209–1217.

Cuingnet, R. et al. (2011). "Automatic classification of patients with Alzheimer's disease from structural MRI: a comparison of ten methods using the ADNI database". In: *Neuroimage* 56.2, pp. 766–781.

Cuingnet, R. et al. (2013). "Spatial and Anatomical Regularization of SVM: A General Framework for Neuroimaging Data". In: *IEEE Trans. Pattern Anal. Mach. Intell.* 35.3, pp. 682–696.

Davidson, Y. et al. (2016). "Neurodegeneration in frontotemporal lobar degeneration and motor neurone disease associated with expansions in *C9orf72* is linked to TDP-43 pathology and not associated with aggregated forms of dipeptide repeat proteins". In: *Neuropathology and Applied Neurobiology* 42.3, pp. 242–254. DOI: 10.1111/nan.12292.

Davidson, Y. S. et al. (2014). "Brain distribution of dipeptide repeat proteins in frontotemporal lobar degeneration and motor neurone disease associated with expansions in C9ORF72". In: *Acta Neuropathologica Communications* 2, p. 70. DOI: 10.1186/2051-5960-2-70.

DeBoy, C. A. et al. (2007). "High resolution diffusion tensor imaging of axonal damage in focal inflammatory and demyelinating lesions in rat spinal cord". In: *Brain: A Journal of Neurology* 130.Pt 8, pp. 2199–2210. DOI: 10.1093/brain/awm122.

DeJesus-Hernandez, M. et al. (2011). "Expanded GGGGCC Hexanucleotide Repeat in Noncoding Region of C9ORF72 Causes Chromosome 9p-Linked FTD and ALS". In: *Neuron* 72.2, pp. 245–256. DOI: 10.1016/j.neuron.2011.09.011.

Demirhan, A. et al. (2015). "FEATURE SELECTION IMPROVES THE ACCURACY OF CLASSIFYING ALZHEIMER DISEASE USING DIFFUSION TENSOR IMAGES". In: *Proc. IEEE Int. Symp. Biomed. Imaging* 2015, pp. 126–130.

Deng, J. et al. (2009). *ImageNet: A large-scale hierarchical image database*.

Desikan, R. S. et al. (2006). "An automated labeling system for subdividing the human cerebral cortex on MRI scans into gyral based regions of interest". In: *NeuroImage* 31.3, pp. 968–980. DOI: 10.1016/j.neuroimage.2006.01.021.

Despotović, I., B. Goossens, and W. Philips (2015). *MRI Segmentation of the Human Brain: Challenges, Methods, and Applications*. Research article. DOI: 10.1155/2015/450341.

Devenney, E. et al. (2014). "Frontotemporal Dementia Associated With the C9ORF72 Mutation: A Unique Clinical Profile". In: *JAMA Neurology* 71.3, pp. 331–339. DOI: 10.1001/jamaneurol.2013.6002.

Dickerson, B. C. et al. (2001). "MRI-derived entorhinal and hippocampal atrophy in incipient and very mild Alzheimer's disease*". In: *Neurobiol. Aging* 22.5, pp. 747–754.

Doan, N. T. et al. (2017). "Dissociable diffusion MRI patterns of white matter microstructure and connectivity in Alzheimer's disease spectrum". In: *Sci. Rep.* 7, p. 45131.

Dolph, C. V. et al. (2017). "Deep learning of texture and structural features for multiclass Alzheimer's disease classification". In: *2017 International Joint Conference on Neural Networks (IJCNN)*, pp. 2259–2266.

Donnelly, C. J. et al. (2013). "RNA toxicity from the ALS/FTD C9ORF72 expansion is mitigated by antisense intervention". In: *Neuron* 80.2, pp. 415–428. DOI: 10.1016/j.neuron.2013.10.015.

Dubey, R. et al. (2014). "ANALYSIS OF SAMPLING TECHNIQUES FOR IMBALANCED DATA: AN N=648 ADNI STUDY". In: *NeuroImage* 87, pp. 220–241. DOI: 10.1016/j.neuroimage.2013.10.005.

Dubois, B. and M. L. Albert (2004). "Amnestic MCI or prodromal Alzheimer's disease?" In: *The Lancet. Neurology* 3.4, pp. 246–248. DOI: 10.1016/S1474-4422(04)00710-0.

Dubois, B. et al. (2007). "Research criteria for the diagnosis of Alzheimer's disease: revising the NINCDS-ADRDA criteria". In: *The Lancet. Neurology* 6.8, pp. 734–746. DOI: 10.1016/S1474-4422(07)70178-3.

Dubois, B. et al. (2014). "Advancing research diagnostic criteria for Alzheimer's disease: the IWG-2 criteria". In: *The Lancet. Neurology* 13.6, pp. 614–629. DOI: 10.1016/S1474-4422(14)70090-0.

Dubois, B. et al. (2016). "Preclinical Alzheimer's disease: Definition, natural history, and diagnostic criteria". In: *Alzheimer's & Dementia: The Journal of the Alzheimer's Association* 12.3, pp. 292–323. DOI: 10.1016/j.jalz.2016.02.002.

Dumoulin, V. and F. Visin (2016). "A guide to convolution arithmetic for deep learning". In:

Duraisamy, B., J. V. Shanmugam, and J. Annamalai (2019). "Alzheimer disease detection from structural MR images using FCM based weighted probabilistic neural network". In: *Brain Imaging Behav.* 13.1, pp. 87–110.

Duyckaerts, C., B. Delatour, and M.-C. Potier (2009). "Classification and basic pathology of Alzheimer disease". In: *Acta Neuropathologica* 118.1, pp. 5–36. DOI: 10.1007/s00401-009-0532-1.

Dyrba, M. et al. (2013). "Robust automated detection of microstructural white matter degeneration in Alzheimer's disease using machine learning classification of multicenter DTI data". In: *PLoS One* 8.5, e64925.

Dyrba, M. et al. (2015a). "Multimodal analysis of functional and structural disconnection in Alzheimer's disease using multiple kernel SVM". In: *Human Brain Mapping* 36.6, pp. 2118–2131. DOI: 10.1002/hbm.22759.

Dyrba, M. et al. (2015b). "Predicting Prodromal Alzheimer's Disease in Subjects with Mild Cognitive Impairment Using Machine Learning Classification of Multimodal Multicenter Diffusion-Tensor and Magnetic Resonance Imaging Data". In: *J. Neuroimaging* 25.5, pp. 738–747.

Eaton-Rosen, Z. et al. (2017). "Investigating the maturation of microstructure and radial orientation in the preterm human cortex with diffusion MRI". In: *NeuroImage* 162, pp. 65–72. DOI: 10.1016/j.neuroimage.2017.08.013.

Ebadi, A. et al. (2017). "Ensemble Classification of Alzheimer's Disease and Mild Cognitive Impairment Based on Complex Graph Measures from Diffusion Tensor Images". In: *Front. Neurosci.* 11, p. 56.

Ellis, K. A. et al. (2009). "The Australian Imaging, Biomarkers and Lifestyle (AIBL) study of aging: methodology and baseline characteristics of 1112 individuals recruited for a longitudinal study of Alzheimer's disease". In: *Int. Psychogeriatr.* 21.4, pp. 672–687.

Ellis, K. A. et al. (2010). *Addressing population aging and Alzheimer's disease through the Australian Imaging Biomarkers and Lifestyle study: Collaboration with the Alzheimer's Disease Neuroimaging Initiative*. Vol. 6. 3.

Erhan, D. et al. (2010). "Why Does Unsupervised Pre-training Help Deep Learning?" In: *J. Mach. Learn. Res.* 11, pp. 625–660.

Eskildsen, S. F. et al. (2013). "Prediction of Alzheimer's disease in subjects with mild cognitive impairment from the ADNI cohort using patterns of cortical thinning". In: *NeuroImage* 65, pp. 511–521. DOI: 10.1016/j.neuroimage.2012.09.058.

Esmaeilzadeh, S. et al. (2018). "End-To-End Alzheimer's Disease Diagnosis and Biomarker Identification: 9th International Workshop, MLMI 2018, Held in Conjunction with MICCAI 2018, Granada, Spain, September 16, 2018, Proceedings". In: *Machine Learning in Medical Imaging*. Ed. by Y. Shi, H.-I. Suk, and M. Liu. Vol. 11046. Lecture Notes in Computer Science. Cham: Springer International Publishing, pp. 337–345.

Estabrooks, A. (2000). "A combination scheme for inductive learning from imbalanced data sets". PhD Thesis. DalTech.

Ewers, M. et al. (2011). "Neuroimaging markers for the prediction and early diagnosis of Alzheimer's disease dementia". In: *Trends Neurosci.* 34.8, pp. 430–442.

Falahati, F., E. Westman, and A. Simmons (2014). "Multivariate Data Analysis and Machine Learning in Alzheimer's Disease with a Focus on Structural Magnetic Resonance Imaging". In: *Journal of Alzheimer's Disease* 41.3, pp. 685–708. DOI: 10.3233/JAD-131928.

Farhan, S., M. A. Fahiem, and H. Tauseef (2014). *An Ensemble-of-Classifiers Based Approach for Early Diagnosis of Alzheimer's Disease: Classification Using Structural Features of Brain Images*. Research article. DOI: 10.1155/2014/862307.

Farooq, A et al. (2017). "A deep CNN based multi-class classification of Alzheimer's disease using MRI". In: *2017 IEEE International Conference on Imaging Systems and Techniques (IST)*, pp. 1–6.

Fellgiebel, A. et al. (2005). "Color-coded diffusion-tensor-imaging of posterior cingulate fiber tracts in mild cognitive impairment". In: *Neurobiol. Aging* 26.8, pp. 1193–1198.

Fellgiebel, A. et al. (2006). "Predicting conversion to dementia in mild cognitive impairment by volumetric and diffusivity measurements of the hippocampus". In: *Psychiatry Res.* 146.3, pp. 283–287.

Ferri, C. P. et al. (2005). "Global prevalence of dementia: a Delphi consensus study". In: *Lancet (London, England)* 366.9503, pp. 2112–2117. DOI: 10.1016/S0140-6736(05)67889-0.

Fischl, B. et al. (1999). "High-resolution intersubject averaging and a coordinate system for the cortical surface". In: *Human Brain Mapping* 8.4, pp. 272–284.

Fischl, B. (2012). "FreeSurfer". In: *NeuroImage* 62.2, pp. 774–781. DOI: 10.1016/j.neuroimage.2012.01.021.

Fisher, R. A. (1992). "The Arrangement of Field Experiments". In: *Breakthroughs in Statistics: Methodology and Distribution*. Ed. by S. Kotz and N. L. Johnson. New York, NY: Springer New York, pp. 82–91. ISBN: 978-1-4612-4380-9. DOI: 10.1007/978-1-4612-4380-9_8.

Floeter, M. K. et al. (2017). "Disease progression in *C9orf72* mutation carriers". In: *Neurology*, 10.1212/WNL.0000000000004115. DOI: 10.1212/WNL.0000000000004115.

Floeter, M. K. and T. F. Gendron (2018). "Biomarkers for Amyotrophic Lateral Sclerosis and Frontotemporal Dementia Associated With Hexanucleotide Expansion Mutations in C9orf72". In: *Frontiers in Neurology* 9. DOI: 10.3389/fneur.2018.01063.

Floeter, M. K. et al. (2016). "Longitudinal imaging in C9orf72 mutation carriers: Relationship to phenotype". In: *NeuroImage: Clinical* 12, pp. 1035–1043. DOI: 10.1016/j.nicl.2016.10.014.

Floris, G. et al. (2015). "Constructional apraxia in frontotemporal dementia associated with the C9orf72 mutation: broadening the clinical and neuropsychological phenotype". In: *Amyotrophic Lateral Sclerosis & Frontotemporal Degeneration* 16.1-2, pp. 8–15. DOI: 10.3109/21678421.2014.959450.

Fonov, V. S. et al. (2009). "Unbiased nonlinear average age-appropriate brain templates from birth to adulthood". In: *Neuroimage* Supplement 1.47, S102.

Fonov, V. et al. (2011). "Unbiased average age-appropriate atlases for pediatric studies". In: *Neuroimage* 54.1, pp. 313–327.

Fonov, V. et al. (2018). "Deep learning of quality control for stereotaxic registration of human brain MRI".

Friese, U. et al. (2010). "Diagnostic utility of novel MRI-based biomarkers for Alzheimer's disease: diffusion tensor imaging and deformation-based morphometry". In: *J. Alzheimers. Dis.* 20.2, pp. 477–490.

Frisoni, G. B. et al. (2010). "3-The clinical use of structural MRI in Alzheimer disease". In: *Nature Reviews Neurology* 6.2, pp. 67–77. DOI: 10.1038/nrneurol.2009.215.

Friston, K. J. et al. (1995). "Analysis of fMRI time-series revisited". In: *Neuroimage* 2.1, pp. 45–53.

Gao, Y. et al. (2015). "MCI Identification by Joint Learning on Multiple MRI Data". In: *Med. Image Comput. Comput. Assist. Interv.* 9350, pp. 78–85.

Glorot, X., A. Bordes, and Y. Bengio (2011). "Deep sparse rectifier neural networks". In: *Proceedings of the fourteenth international conference on artificial intelligence and statistics*, pp. 315–323.

Godenschweger, F. et al. (2016). "Motion correction in MRI of the brain". In: *Physics in Medicine and Biology* 61.5, R32–56. DOI: 10.1088/0031-9155/61/5/R32.

Gomez-Deza, J. et al. (2015). "Dipeptide repeat protein inclusions are rare in the spinal cord and almost absent from motor neurons in C9ORF72 mutant amyotrophic lateral sclerosis and are unlikely to cause their degeneration". In: *Acta Neuropathologica Communications* 3, p. 38. DOI: 10.1186/s40478-015-0218-y.

Gómez-Tortosa, E. et al. (2013). "C9ORF72 hexanucleotide expansions of 20-22 repeats are associated with frontotemporal deterioration". In: *Neurology* 80.4, pp. 366–370. DOI: 10.1212/WNL.0b013e31827f08ea.

Goodfellow, I. (2016). "NIPS 2016 Tutorial: Generative Adversarial Networks". In:

Goodfellow, I. et al. (2016). *Deep learning*. Vol. 1. MIT press Cambridge.

Gorgolewski, K. et al. (2011). "Nipype: a flexible, lightweight and extensible neuroimaging data processing framework in python". In: *Front. Neuroinform.* 5, p. 13.

Gorgolewski, K. J. and R. A. Poldrack (2016). "A Practical Guide for Improving Transparency and Reproducibility in Neuroimaging Research". In: *PLoS Biol.* 14.7, e1002506.

Gorgolewski, K. J. et al. (2016). "The brain imaging data structure, a format for organizing and describing outputs of neuroimaging experiments". In: *Sci Data* 3, p. 160044.

Gorji, H. T. and J Haddadnia (2015). "A novel method for early diagnosis of Alzheimer's disease based on pseudo Zernike moment from structural MRI". In: *Neuroscience* 305, pp. 361–371.

Graña, M et al. (2011). "Computer aided diagnosis system for Alzheimer disease using brain diffusion tensor imaging features selected by Pearson's correlation". In: *Neurosci. Lett.* 502.3, pp. 225–229.

Greve, D. N. and B. Fischl (2009). "Accurate and robust brain image alignment using boundary-based registration". In: *Neuroimage* 48.1, pp. 63–72.

Grussu, F. et al. (2017). "Neurite dispersion: a new marker of multiple sclerosis spinal cord pathology?" In: *Annals of Clinical and Translational Neurology* 4.9, pp. 663–679. DOI: 10.1002/acn3.445.

Gunawardena, K. A.N.N. P., R. N. Rajapakse, and N. D. Kodikara (2017). "Applying convolutional neural networks for pre-detection of alzheimer's disease from structural MRI data". In: IEEE, pp. 1–7. ISBN: 978-1-5090-6546-2. DOI: 10.1109/M2VIP.2017.8211486.

Gutiérrez-Becker, B. and C. Wachinger (2018). "Deep Multi-structural Shape Analysis: Application to Neuroanatomy: 21st International Conference, Granada, Spain, September 16-20, 2018, Proceedings, Part III". In: *Medical Image Computing and Computer Assisted Intervention – MICCAI 2018*. Ed. by A. F. Frangi et al. Vol. 11072. Lecture Notes in Computer Science. Cham: Springer International Publishing, pp. 523–531.

Guyon, I. et al. (2002). "Gene Selection for Cancer Classification using Support Vector Machines". In: *Mach. Learn.* 46.1, pp. 389–422.

Haller, S et al. (2013). "Individual classification of mild cognitive impairment subtypes by support vector machine analysis of white matter DTI". In: *AJNR Am. J. Neuroradiol.* 34.2, pp. 283–291.

Haller, S., K. O. Lovblad, and P. Giannakopoulos (2011). "Principles of classification analyses in mild cognitive impairment (MCI) and Alzheimer disease". In: *J. Alzheimers. Dis.* 26 Suppl 3, pp. 389–394.

Hampel, H. et al. (2014). "Perspective on future role of biological markers in clinical therapy trials of Alzheimer's disease: a long-range point of view beyond 2020". In: *Biochemical Pharmacology* 88.4, pp. 426–449. DOI: 10.1016/j.bcp.2013.11.009.

Hanyu, H. et al. (1998). "Diffusion-weighted MR imaging of the hippocampus and temporal white matter in Alzheimer's disease". In: *Journal of the Neurological Sciences* 156.2, pp. 195–200.

Hardy, J. and D. Allsop (1991). "Amyloid deposition as the central event in the aetiology of Alzheimer's disease". In: *Trends in Pharmacological Sciences* 12, pp. 383–388. DOI: 10.1016/0165-6147(91)90609-V.

He, K. et al. (2016). "Deep residual learning for image recognition". In: *Proceedings of the IEEE conference on computer vision and pattern recognition*, pp. 770–778.

Head, D. et al. (2005). "Frontal-hippocampal double dissociation between normal aging and Alzheimer's disease". In: *Cereb. Cortex* 15.6, pp. 732–739.

Hinton, G. E. and R. S. Zemel (1994). "Autoencoders, Minimum Description Length and Helmholtz Free Energy". In: *Advances in Neural Information Processing Systems 6*. Ed. by J. D. Cowan, G Tesauro, and J Alspector. Morgan-Kaufmann, pp. 3–10.

Ho, T. K. (1995). "Random decision forests". In: *Proceedings of 3rd International Conference on Document Analysis and Recognition*. Vol. 1, 278–282 vol.1. DOI: 10.1109/ICDAR.1995.598994.

Hon, M and N. M. Khan (2017). "Towards Alzheimer's disease classification through transfer learning". In: *2017 IEEE International Conference on Bioinformatics and Biomedicine (BIBM)*, pp. 1166–1169.

Hosseini-Asl, E., G. Gimel'farb, and A. El-Baz (2016). "Alzheimer's Disease Diagnostics by a Deeply Supervised Adaptable 3D Convolutional Network". In:

Hosseini Asl, E. et al. (2018). "Alzheimer's disease diagnostics by a 3D deeply supervised adaptable convolutional network". In: *Front. Biosci.* 23.2, pp. 584–596.

Hua, K. et al. (2008). "Tract probability maps in stereotaxic spaces: analyses of white matter anatomy and tract-specific quantification". In: *NeuroImage* 39.1, pp. 336–347. DOI: 10.1016/j.neuroimage.2007.07.053.

Huang, G. et al. (2017). "Densely connected convolutional networks". In: *Proceedings of the IEEE conference on computer vision and pattern recognition*, pp. 4700–4708.

Hutton, M. et al. (1998). "Association of missense and 5'-splice-site mutations in tau with the inherited dementia FTDP-17". In: *Nature* 393.6686, pp. 702–705. DOI: 10.1038/31508.

Ioffe, S. and C. Szegedy (2015). "Batch Normalization: Accelerating Deep Network Training by Reducing Internal Covariate Shift". In: *arXiv:1502.03167 [cs]*.

Islam, J. and Y. Zhang (2017). "A Novel Deep Learning Based Multi-class Classification Method for Alzheimer's Disease Detection Using Brain MRI Data". In: *Brain Informatics*. Ed. by Y. Zeng et al. Vol. 10654. Lecture Notes in Computer Science. Cham: Springer International Publishing, pp. 213–222.

— (2018). "Brain MRI analysis for Alzheimer's disease diagnosis using an ensemble system of deep convolutional neural networks". In: *Brain Inform* 5.2, p. 2.

Janocha, K. and W. M. Czarnecki (2017). "On Loss Functions for Deep Neural Networks in Classification". In:

Japkowicz, N. and Others (2000). "Learning from imbalanced data sets: a comparison of various strategies". In: *AAAI workshop on learning from imbalanced data sets*. Vol. 68. Menlo Park, CA, pp. 10–15.

Jenkinson, M. and S. Smith (2001). "A global optimisation method for robust affine registration of brain images". In: *Medical Image Analysis* 5.2, pp. 143–156.

Jenkinson, M. et al. (2002). "Improved optimization for the robust and accurate linear registration and motion correction of brain images". In: *NeuroImage* 17.2, pp. 825–841.

Jenkinson, M. et al. (2012). "FSL". In: *Neuroimage* 62.2, pp. 782–790.

Jeurissen, B. et al. (2014). "Multi-tissue constrained spherical deconvolution for improved analysis of multi-shell diffusion MRI data". In: *NeuroImage* 103, pp. 411–426. DOI: 10.1016/j.neuroimage.2014.07.061.

Jezzard, P and R. S. Balaban (1995). "Correction for geometric distortion in echo planar images from B0 field variations". In: *Magn. Reson. Med.* 34.1, pp. 65–73.

Jha, D., J.-I. Kim, and G.-R. Kwon (2017). "Diagnosis of Alzheimer's Disease Using Dual-Tree Complex Wavelet Transform, PCA, and Feed-Forward Neural Network". In: *J. Healthc. Eng.* 2017, p. 9060124.

Jiang, J. et al. (2016). "Gain of Toxicity from ALS/FTD-Linked Repeat Expansions in C9ORF72 Is Alleviated by Antisense Oligonucleotides Targeting GGGGCC-Containing RNAs". In: *Neuron* 90.3, pp. 535–550. DOI: 10.1016/j.neuron.2016.04.006.

Jiskoot, L. (2018). *Neuroimaging and Clinical Biomarkers in the Familial and Sporadic FTD Spectrum – from the Presymptomatic to the Symptomatic Disease Stage*. ISBN: 978-94-028-1164-3.

Jung, W. B. et al. (2015). "Automated Classification to Predict the Progression of Alzheimer's Disease Using Whole-Brain Volumetry and DTI". In: *Psychiatry Investig.* 12.1, pp. 92–102.

Juszczak, P., D Tax, and R. P. W. Duin (2002). "Feature scaling in support vector data description". In: *Proc. ASCI*. Citeseer, pp. 95–102.

Kalavathi, P and V. B. S. Prasath (2016). "Methods on Skull Stripping of MRI Head Scan Images-a Review". In: *J. Digit. Imaging* 29.3, pp. 365–379.

Kamagata, K. et al. (2016). "Neurite orientation dispersion and density imaging in the substantia nigra in idiopathic Parkinson disease". In: *European Radiology* 26.8, pp. 2567–2577. DOI: 10.1007/s00330-015-4066-8.

Kantarci, K et al. (2001). "Mild cognitive impairment and Alzheimer disease: regional diffusivity of water". In: *Radiology* 219.1, pp. 101–107.

Khan, B. K. et al. (2012). "Atypical, slowly progressive behavioural variant frontotemporal dementia associated with C9ORF72 hexanucleotide expansion". In:

Journal of Neurology, Neurosurgery, and Psychiatry 83.4, pp. 358–364. DOI: 10.1136/jnnp-2011-301883.

Klöppel, S. et al. (2008). "Automatic classification of MR scans in Alzheimer's disease". In: *Brain: A Journal of Neurology* 131.Pt 3, pp. 681–689. DOI: 10.1093/brain/awm319.

Kodiweera, C. et al. (2016). "Age effects and sex differences in human brain white matter of young to middle-aged adults: A DTI, NODDI, and q-space study". In: *NeuroImage* 128, pp. 180–192. DOI: 10.1016/j.neuroimage.2015.12.033.

Korolev, S et al. (2017). "Residual and plain convolutional neural networks for 3D brain MRI classification". In: *2017 IEEE 14th International Symposium on Biomedical Imaging (ISBI 2017)*, pp. 835–838.

Kriegeskorte, N. et al. (2009). "Circular analysis in systems neuroscience: the dangers of double dipping". In: *Nat. Neurosci.* 12.5, pp. 535–540.

Krizhevsky, A., I. Sutskever, and G. E. Hinton (2012). "ImageNet Classification with Deep Convolutional Neural Networks". In: *Advances in Neural Information Processing Systems 25*. Ed. by F Pereira et al. Curran Associates, Inc., pp. 1097–1105.

Krogh, A. and J. A. Hertz (1992). "A Simple Weight Decay Can Improve Generalization". In: *Advances in Neural Information Processing Systems 4*. Ed. by J. E. Moody, S. J. Hanson, and R. P. Lippmann. Morgan-Kaufmann, pp. 950–957.

Króliczak, G., B. J. Piper, and S. H. Frey (2016). "Specialization of the left supramarginal gyrus for hand-independent praxis representation is not related to hand dominance". In: *Neuropsychologia* 93.Pt B, pp. 501–512. DOI: 10.1016/j.neuropsychologia.2016.03.023.

Le Ber, I. (2013). "Genetics of frontotemporal lobar degeneration: an up-date and diagnosis algorithm". In: *Revue Neurologique* 169.10, pp. 811–819. DOI: 10.1016/j.neurol.2013.07.014.

Le Ber, I. et al. (2008). "Phenotype variability in progranulin mutation carriers: a clinical, neuropsychological, imaging and genetic study". In: *Brain* 131.3, pp. 732–746. DOI: 10.1093/brain/awn012.

Le Ber, I. et al. (2013). "SQSTM1 mutations in French patients with frontotemporal dementia or frontotemporal dementia with amyotrophic lateral sclerosis". In: *JAMA neurology* 70.11, pp. 1403–1410. DOI: 10.1001/jamaneurol.2013.3849.

Le Bihan, D. et al. (1986). "MR imaging of intravoxel incoherent motions: application to diffusion and perfusion in neurologic disorders". In: *Radiology* 161.2, pp. 401–407. DOI: 10.1148/radiology.161.2.3763909.

Lecun, Y. et al. (1998). "Gradient-based learning applied to document recognition". In: *Proceedings of the IEEE* 86.11, pp. 2278–2324. DOI: 10.1109/5.726791.

LeCun, Y., Y. Bengio, and G. Hinton (2015). "Deep learning". In: *Nature* 521.7553, pp. 436–444.

Ledig, C. et al. (2015). "Robust whole-brain segmentation: application to traumatic brain injury". In: *Med. Image Anal.* 21.1, pp. 40–58.

Lee, S. E. et al. (2016). "Network degeneration and dysfunction in presymptomatic C9ORF72 expansion carriers". In: *NeuroImage : Clinical* 14, pp. 286–297. DOI: 10.1016/j.nicl.2016.12.006.

Lee, W., B. Park, and K. Han (2013). "Classification of diffusion tensor images for the early detection of Alzheimer's disease". In: *Comput. Biol. Med.* 43.10, pp. 1313–1320.

— (2015). "SVM-Based Classification of Diffusion Tensor Imaging Data for Diagnosing Alzheimer's Disease and Mild Cognitive Impairment". In: *Intelligent Computing Theories and Methodologies*. Ed. by D.-S. Huang, K.-H. Jo, and A. Hussain. Vol. 9226. Lecture Notes in Computer Science. Cham: Springer International Publishing, pp. 489–499.

Leemans, A. and D. K. Jones (2009). "The B-matrix must be rotated when correcting for subject motion in DTI data". In: *Magnetic Resonance in Medicine* 61.6, pp. 1336–1349. DOI: 10.1002/mrm.21890.

Lella, E. et al. (2017). "Machine learning for the assessment of Alzheimer's disease through DTI". In: *Applications of Digital Image Processing XL*. Vol. 10396. International Society for Optics and Photonics, p. 1039619.

Lella, E. et al. (2018). "Communicability disruption in Alzheimer's disease connectivity networks". In: *J Complex Netw*.

Leow, A. D. et al. (2007). "Statistical properties of Jacobian maps and the realization of unbiased large-deformation nonlinear image registration". In: *IEEE Trans. Med. Imaging* 26.6, pp. 822–832.

Li, F., D. Cheng, and M. Liu (2017). "Alzheimer's disease classification based on combination of multi-model convolutional networks". In: *2017 IEEE International Conference on Imaging Systems and Techniques (IST)*, pp. 1–5. DOI: 10.1109/IST.2017.8261566.

Li, F., M. Liu, and Alzheimer's Disease Neuroimaging Initiative (2018). "Alzheimer's disease diagnosis based on multiple cluster dense convolutional networks". In: *Comput. Med. Imaging Graph.* 70, pp. 101–110.

Li, F. et al. (2015). "A Robust Deep Model for Improved Classification of AD/MCI Patients". In: *IEEE J Biomed Health Inform* 19.5, pp. 1610–1616.

Li, M. et al. (2014). "Discriminative analysis of multivariate features from structural MRI and diffusion tensor images". In: *Magn. Reson. Imaging* 32.8, pp. 1043–1051.

Li, X. et al. (2016). "The first step for neuroimaging data analysis: DICOM to NIfTI conversion". In: *J. Neurosci. Methods* 264, pp. 47–56.

Lian, C. et al. (2018). "Hierarchical Fully Convolutional Network for Joint Atrophy Localization and Alzheimer's Disease Diagnosis using Structural MRI". In: *IEEE Trans. Pattern Anal. Mach. Intell.*

Lillemark, L. et al. (2014). "Brain region's relative proximity as marker for Alzheimer's disease based on structural MRI". In: *BMC Medical Imaging* 14.1, p. 21. DOI: 10.1186/1471-2342-14-21.

Lin, W. et al. (2018). "Convolutional Neural Networks-Based MRI Image Analysis for the Alzheimer's Disease Prediction From Mild Cognitive Impairment". In: *Front. Neurosci.* 12, p. 777.

Liu, J. et al. (2018a). "Applications of deep learning to MRI images: A survey". In: *Big Data Mining and Analytics* 1.1, pp. 1–18. DOI: 10.26599/BDMA.2018.9020001.

Liu, J. et al. (2016). "Multi-view ensemble learning for dementia diagnosis from neuroimaging: An artificial neural network approach". In: *Neurocomputing* 195, pp. 112–116.

Liu, M. et al. (2018b). "Anatomical Landmark based Deep Feature Representation for MR Images in Brain Disease Diagnosis". In: *IEEE Journal of Biomedical and Health Informatics* PP.99, pp. 1–1. DOI: 10.1109/JBHI.2018.2791863.

Liu, M. et al. (2018c). "Multi-Modality Cascaded Convolutional Neural Networks for Alzheimer's Disease Diagnosis". In: *Neuroinformatics* 16.3-4, pp. 295–308.

Liu, M. et al. (2018d). "Joint Classification and Regression via Deep Multi-Task Multi-Channel Learning for Alzheimer's Disease Diagnosis". In: *IEEE Trans. Biomed. Eng.*

— (2018e). "Landmark-based deep multi-instance learning for brain disease diagnosis". In: *Med. Image Anal.* 43, pp. 157–168.

Liu, S. et al. (2015). "Multimodal neuroimaging feature learning for multiclass diagnosis of Alzheimer's disease". In: *IEEE Trans. Biomed. Eng.* 62.4, pp. 1132–1140.

Loy, C. T. et al. (2014). "Genetics of dementia". In: *The Lancet* 383.9919, pp. 828–840. DOI: 10.1016/S0140-6736(13)60630-3.

Lu, D. and Q. Weng (2007). "A survey of image classification methods and techniques for improving classification performance". In: *International Journal of Remote Sensing* 28.5, pp. 823–870. DOI: 10.1080/01431160600746456.

Lu, D. et al. (2018). "Multimodal and Multiscale Deep Neural Networks for the Early Diagnosis of Alzheimer's Disease using structural MR and FDG-PET images". In: *Sci. Rep.* 8.1, p. 5697.

Maas, A. L., A. Y. Hannun, and A. Y. Ng (2013). "Rectifier nonlinearities improve neural network acoustic models". In: *Proc. icml*. Vol. 30, p. 3.

Mackenzie, I. R. A., P. Frick, and M. Neumann (2014). "The neuropathology associated with repeat expansions in the C9ORF72 gene". In: *Acta Neuropathologica* 127.3, pp. 347–357. DOI: 10.1007/s00401-013-1232-4.

Mackenzie, I. R. A. et al. (2015). "Quantitative analysis and clinico-pathological correlations of different dipeptide repeat protein pathologies in C9ORF72 mutation carriers". In: *Acta Neuropathologica* 130.6, pp. 845–861. DOI: 10.1007/s00401-015-1476-2.

Madabhushi, A. and J. K. Udupa (2005). "Interplay between intensity standardization and inhomogeneity correction in MR image processing". In: *IEEE Trans. Med. Imaging* 24.5, pp. 561–576.

Maggipinto, T. et al. (2017). "DTI measurements for Alzheimer's classification". In: *Physics in Medicine and Biology* 62.6, pp. 2361–2375. DOI: 10.1088/1361-6560/aa5dbe.

Magnin, B. et al. (2009). "Support vector machine-based classification of Alzheimer's disease from whole-brain anatomical MRI". In: *Neuroradiology* 51.2, pp. 73–83. DOI: 10.1007/s00234-008-0463-x.

Mahanand, B. S. et al. (2012). "Identification of brain regions responsible for Alzheimer's disease using a Self-adaptive Resource Allocation Network". In: *Neural Netw.* 32, pp. 313–322.

Mahoney, C. J. et al. (2012a). "Frontotemporal dementia with the C9ORF72 hexanucleotide repeat expansion: clinical, neuroanatomical and neuropathological features". In: *Brain* 135.3, pp. 736–750. DOI: 10.1093/brain/awr361.

Mahoney, C. J. et al. (2012b). "Longitudinal neuroimaging and neuropsychological profiles of frontotemporal dementia with C9ORF72 expansions". In: *Alzheimer's research & therapy* 4.5, p. 41.

Maitra, M. and A. Chatterjee (2006). "A Slantlet transform based intelligent system for magnetic resonance brain image classification". In: *Biomed. Signal Process. Control* 1.4, pp. 299–306.

Marcus, D. S. et al. (2007). "Open Access Series of Imaging Studies (OASIS): cross-sectional MRI data in young, middle aged, nondemented, and demented older adults". In: *J. Cogn. Neurosci.* 19.9, pp. 1498–1507.

Mathew, N. A., R. S. Vivek, and P. R. Anurenjan (2018). "Early Diagnosis of Alzheimer's Disease from MRI Images Using PNN". In: *2018 International CET Conference on Control, Communication, and Computing (IC4)*, pp. 161–164.

McCullagh, P. (2018). *Generalized Linear Models*. Routledge. ISBN: 978-1-351-44584-9.

McKhann, G. et al. (1984). "Clinical diagnosis of Alzheimer's disease Report of the NINCDS-ADRDA Work Group* under the auspices of Department of Health

and Human Services Task Force on Alzheimer's Disease". In: *Neurology* 34.7, pp. 939–939.

McKhann, G. M. et al. (2011). "The diagnosis of dementia due to Alzheimer's disease: recommendations from the National Institute on Aging-Alzheimer's Association workgroups on diagnostic guidelines for Alzheimer's disease". In: *Alzheimer's & Dementia: The Journal of the Alzheimer's Association* 7.3, pp. 263–269. DOI: 10.1016/j.jalz.2011.03.005.

McRobbie, D. W. (2006). *MRI from picture to proton*. Cambridge, UK; New York: Cambridge University Press. ISBN: 978-0-511-34944-7 978-0-511-34849-5 978-0-511-54540-5.

Mechelli, A. et al. (2005). "Voxel-Based Morphometry of the Human Brain: Methods and Applications". In: *Curr. Med. Imaging Rev.* 1.2, pp. 105–113.

Merboldt, K.-D., W. Hanicke, and J. Frahm (1985). "Self-diffusion NMR imaging using stimulated echoes". In: *Journal of Magnetic Resonance (1969)* 64.3, pp. 479–486. DOI: 10.1016/0022-2364(85)90111-8.

Mesrob, L. et al. (2012). "DTI and Structural MRI Classification in Alzheimer's Disease". In: *AMI* 02.02, pp. 12–20.

Misra, C., Y. Fan, and C. Davatzikos (2009). "Baseline and longitudinal patterns of brain atrophy in MCI patients, and their use in prediction of short-term conversion to AD: results from ADNI". In: *NeuroImage* 44.4, pp. 1415–1422. DOI: 10.1016/j.neuroimage.2008.10.031.

Mori, S. et al. (2005). *MRI Atlas of Human White Matter*. Amsterdam: Elsevier.

Mostapha, M. et al. (2018). "Non-Euclidean, convolutional learning on cortical brain surfaces". In: *2018 IEEE 15th International Symposium on Biomedical Imaging (ISBI 2018)*, pp. 527–530. DOI: 10.1109/ISBI.2018.8363631.

Mudher, A. and S. Lovestone (2002). "Alzheimer's disease – do tauists and baptists finally shake hands?" In: *Trends in Neurosciences* 25.1, pp. 22–26. DOI: 10.1016/S0166-2236(00)02031-2.

Müller, M. J. et al. (2005). "Functional implications of hippocampal volume and diffusivity in mild cognitive impairment". In: *Neuroimage* 28.4, pp. 1033–1042.

Müller, M. J. et al. (2007). "Diagnostic utility of hippocampal size and mean diffusivity in amnestic MCI". In: *Neurobiology of Aging* 28.3, pp. 398–403. DOI: 10.1016/j.neurobiolaging.2006.01.009.

Nadeau, C. and Y. Bengio (2000). "Inference for the Generalization Error". In: *Advances in Neural Information Processing Systems 12*. Ed. by S. A. Solla, T. K. Leen, and K Müller. MIT Press, pp. 307–313.

Nair, V. and G. E. Hinton (2010). "Rectified linear units improve restricted boltzmann machines". In: *Proceedings of the 27th international conference on machine learning (ICML-10)*, pp. 807–814.

Nelder, J. A. and R. W. M. Wedderburn (1972). "Generalized Linear Models". In: *Journal of the Royal Statistical Society. Series A (General)* 135.3, p. 370. DOI: 10.2307/2344614.

Neumann, M. et al. (2006). "Ubiquitinated TDP-43 in frontotemporal lobar degeneration and amyotrophic lateral sclerosis". In: *Science (New York, N.Y.)* 314.5796, pp. 130–133. DOI: 10.1126/science.1134108.

Neumann, M. et al. (2007). "TDP-43-positive white matter pathology in frontotemporal lobar degeneration with ubiquitin-positive inclusions". In: *Journal of Neuropathology and Experimental Neurology* 66.3, pp. 177–183. DOI: 10.1097/01.jnen.0000248554.45456.58.

Ning, K. et al. (2018). "Classifying Alzheimer's disease with brain imaging and genetic data using a neural network framework". In: *Neurobiol. Aging* 68, pp. 151–158.

Nir, T. M. et al. (2015). "Diffusion weighted imaging-based maximum density path analysis and classification of Alzheimer's disease". In: *Neurobiol. Aging* 36 Suppl 1, S132–40.

O'Donnell, L. J. and C.-F. Westin (2011). "An introduction to diffusion tensor image analysis". In: *Neurosurgery clinics of North America* 22.2, pp. 185–viii. DOI: 10.1016/j.nec.2010.12.004.

O'Dwyer, L. et al. (2012). "Using support vector machines with multiple indices of diffusion for automated classification of mild cognitive impairment". In: *PLoS One* 7.2, e32441.

Oliveira, F. P. M. and J. M.R. S. Tavares (2014). "Medical image registration: a review". In: *Comput. Methods Biomech. Biomed. Engin.* 17.2, pp. 73–93.

Operto, G. et al. (2016). "CATI: A Large Distributed Infrastructure for the Neuroimaging of Cohorts". In: *Neuroinformatics* 14.3, pp. 253–264. DOI: 10.1007/s12021-016-9295-8.

Ortiz, A. et al. (2016). "Ensembles of Deep Learning Architectures for the Early Diagnosis of the Alzheimer's Disease". In: *Int. J. Neural Syst.* 26.7, p. 1650025.

Panigrahi, A., Y. Chen, and C C. Jay Kuo (2018). "ANALYSIS ON GRADIENT PROPAGATION IN BATCH NORMALIZED RESIDUAL NETWORKS".

Papma, J. M. et al. (2017). "Cognition and gray and white matter characteristics of presymptomaticC9orf72repeat expansion". In: *Neurology* 89.12, pp. 1256–1264. DOI: 10.1212/WNL.0000000000004393.

Parisot, S. et al. (2018). "Disease prediction using graph convolutional networks: Application to Autism Spectrum Disorder and Alzheimer's disease". In: *Med. Image Anal.* 48, pp. 117–130.

Parker, T. D. et al. (2018). "Cortical microstructure in young onset Alzheimer's disease using neurite orientation dispersion and density imaging". In: *Human Brain Mapping* 39.7, pp. 3005–3017. DOI: 10.1002/hbm.24056.

Pasternak, O. et al. (2009). "Free water elimination and mapping from diffusion MRI". In: *Magnetic Resonance in Medicine* 62.3, pp. 717–730. DOI: 10.1002/mrm.22055.

Paszke, A. et al. (2017). "Automatic differentiation in PyTorch".

Pedregosa, F. et al. (2011). "Scikit-learn: Machine Learning in Python". In: *J. Mach. Learn. Res.* 12.Oct, pp. 2825–2830.

Peigneux, P. and M. van der Linden (1999). "Influence of ageing and educational level on the prevalence of body-part-as-objects in normal subjects". In: *Journal of Clinical and Experimental Neuropsychology* 21.4, pp. 547–552. DOI: 10.1076/jcen.21.4.547.881.

Perez, L. and J. Wang (2017). "The Effectiveness of Data Augmentation in Image Classification using Deep Learning". In:

Petersen, R. C. et al. (2010). "Alzheimer's Disease Neuroimaging Initiative (ADNI): clinical characterization". In: *Neurology* 74.3, pp. 201–209.

Pfefferbaum, A. et al. (2010). "Diffusion tensor imaging of deep gray matter brain structures: Effects of age and iron concentration". In: *Neurobiology of Aging* 31.3, pp. 482–493. DOI: 10.1016/j.neurobiolaging.2008.04.013.

Planetta, P. J. et al. (2016). "Free-water imaging in Parkinson's disease and atypical parkinsonism". In: *Brain: A Journal of Neurology* 139.Pt 2, pp. 495–508. DOI: 10.1093/brain/awv361.

Poldrack, R. A. et al. (2017). "Scanning the horizon: towards transparent and reproducible neuroimaging research". In: *Nat. Rev. Neurosci.* 18.2, pp. 115–126.

Popuri, K. et al. (2018). "Gray matter changes in asymptomatic C9orf72 and GRN mutation carriers". In: *NeuroImage: Clinical*. DOI: 10.1016/j.nicl.2018.02.017.

Prasad, G. et al. (2015). "Brain connectivity and novel network measures for Alzheimer's disease classification". In: *Neurobiol. Aging* 36 Suppl 1, S121–31.

Prechelt, L. (2012). "Early Stopping — But When?" In: *Neural Networks: Tricks of the Trade: Second Edition*. Ed. by G. Montavon, G. B. Orr, and K.-R. Müller. Berlin, Heidelberg: Springer Berlin Heidelberg, pp. 53–67.

Qiu, S. et al. (2018). "Fusion of deep learning models of MRI scans, Mini–Mental State Examination, and logical memory test enhances diagnosis of mild cognitive impairment". In: *Alzheimer's & Dementia: Diagnosis, Assessment & Disease Monitoring* 10, pp. 737–749.

Querbes, O. et al. (2009). "Early diagnosis of Alzheimer's disease using cortical thickness: impact of cognitive reserve". In: *Brain: A Journal of Neurology* 132.Pt 8, pp. 2036–2047. DOI: 10.1093/brain/awp105.

Rabinovici, G. D. and B. L. Miller (2010). "Frontotemporal Lobar Degeneration". In: *CNS drugs* 24.5, pp. 375–398. DOI: 10.2165/11533100-000000000-00000.

Raschka, S. (2015). *Python Machine Learning*. Packt Publishing Ltd.

Rathore, S. et al. (2017). "A review on neuroimaging-based classification studies and associated feature extraction methods for Alzheimer's disease and its prodromal stages". In: *Neuroimage* 155, pp. 530–548.

Raut, A and V Dalal (2017). "A machine learning based approach for detection of alzheimer's disease using analysis of hippocampus region from MRI scan". In: *2017 International Conference on Computing Methodologies and Communication (ICCMC)*, pp. 236–242.

Razzak, M. I., S. Naz, and A. Zaib (2018). "Deep Learning for Medical Image Processing: Overview, Challenges and the Future". In: *Classification in BioApps*. Lecture Notes in Computational Vision and Biomechanics. Springer, Cham, pp. 323–350. ISBN: 978-3-319-65980-0 978-3-319-65981-7. DOI: 10.1007/978-3-319-65981-7_12.

Renton, A. E. et al. (2011). "A hexanucleotide repeat expansion in C9ORF72 is the cause of chromosome 9p21-linked ALS-FTD". In: *Neuron* 72.2, pp. 257–268. DOI: 10.1016/j.neuron.2011.09.010.

Reuter, M. et al. (2015). "Head motion during MRI acquisition reduces gray matter volume and thickness estimates". In: *Neuroimage* 107, pp. 107–115.

Ripley, B. D. (1996). *Pattern Recognition and Neural Networks by Brian D. Ripley*. Cambridge University Press.

Rodrigues Cavalcante, K. and P. Caramelli (2009). "Evaluation of the performance of normal elderly in a limb praxis protocol: influence of age, gender, and education". In: *Journal of the International Neuropsychological Society: JINS* 15.4, pp. 618–622. DOI: 10.1017/S1355617709090663.

Rohrer, J. et al. (2013). "Presymptomatic studies in genetic frontotemporal dementia". In: *Revue Neurologique* 169.10, pp. 820–824. DOI: 10.1016/j.neurol.2013.07.010.

Rohrer, J. D. et al. (2015). "Presymptomatic cognitive and neuroanatomical changes in genetic frontotemporal dementia in the Genetic Frontotemporal dementia Initiative (GENFI) study: a cross-sectional analysis". In: *The Lancet Neurology* 14.3, pp. 253–262.

Rolls, E. T., M. Joliot, and N. Tzourio-Mazoyer (2015). "Implementation of a new parcellation of the orbitofrontal cortex in the automated anatomical labeling atlas". In: *Neuroimage* 122, pp. 1–5.

Routier, A et al. (2018). "Clinica: an open source software platform for reproducible clinical neuroscience studies". In: *Annual meeting of the*.

Salvatore, C. et al. (2015). "Magnetic resonance imaging biomarkers for the early diagnosis of Alzheimer's disease: a machine learning approach". In: *Front. Neurosci.* 9, p. 307.

Samper-González, J. et al. (2018). "Reproducible evaluation of classification methods in Alzheimer's disease: framework and application to MRI and PET data". In: DOI: 10.1101/274324.

Sarle, W. S. (1997). "Neural Network FAQ, part 1 of 7". In: *Introduction, periodic posting to the Usenet newsgroup comp. ai. neural-nets URL: ftp://ftp. sas. com/pub/neural/FAQ. html*.

Scherer, D., A. Müller, and S. Behnke (2010). "Evaluation of Pooling Operations in Convolutional Architectures for Object Recognition". In: *Artificial Neural Networks – ICANN 2010*. Springer Berlin Heidelberg, pp. 92–101.

Schmitt, F., M. K. Stehling, and R. Turner (1998). *Echo-Planar Imaging: Theory, Technique and Application*. Berlin Heidelberg: Springer-Verlag. ISBN: 978-3-642-80445-8.

Schneider, T. et al. (2017). "Sensitivity of multi-shell NODDI to multiple sclerosis white matter changes: a pilot study". In: *Functional Neurology* 32.2, pp. 97–101. DOI: 10.11138/FNeur/2017.32.2.097.

Schouten, T. M. et al. (2016). "Combining anatomical, diffusion, and resting state functional magnetic resonance imaging for individual classification of mild and moderate Alzheimer's disease". In: *Neuroimage Clin* 11, pp. 46–51.

Schouten, T. M. et al. (2017). "Individual classification of Alzheimer's disease with diffusion magnetic resonance imaging". In: *Neuroimage* 152, pp. 476–481.

Schuff, N et al. (2009). "MRI of hippocampal volume loss in early Alzheimer's disease in relation to ApoE genotype and biomarkers". In: *Brain* 132.Pt 4, pp. 1067–1077.

Selnes, P. et al. (2013). "Diffusion tensor imaging surpasses cerebrospinal fluid as predictor of cognitive decline and medial temporal lobe atrophy in subjective cognitive impairment and mild cognitive impairment". In: *J. Alzheimers. Dis.* 33.3, pp. 723–736.

Selvikvåg Lundervold, A. and A. Lundervold (2018). "An overview of deep learning in medical imaging focusing on MRI". In: *Zeitschrift für Medizinische Physik*. DOI: 10.1016/j.zemedi.2018.11.002.

Senanayake, U, A Sowmya, and L Dawes (2018). "Deep fusion pipeline for mild cognitive impairment diagnosis". In: *2018 IEEE 15th International Symposium on Biomedical Imaging (ISBI 2018)*, pp. 1394–1997.

Sha, S. J. et al. (2012). "Frontotemporal dementia due to C9ORF72 mutations". In: *Neurology* 79.10, pp. 1002–1011. DOI: 10.1212/WNL.0b013e318268452e.

Shams-Baboli, A and M Ezoji (2017). "A Zernike moment based method for classification of Alzheimer's disease from structural MRI". In: *2017 3rd International Conference on Pattern Recognition and Image Analysis (IPRIA)*, pp. 38–43.

Shattuck, D. W. et al. (2001). "Magnetic resonance image tissue classification using a partial volume model". In: *Neuroimage* 13.5, pp. 856–876.

Shen, T et al. (2018). "Decision Supporting Model for One-year Conversion Probability from MCI to AD using CNN and SVM". In: *2018 40th Annual International Conference of the IEEE Engineering in Medicine and Biology Society (EMBC)*, pp. 738–741.

Shi, J. et al. (2018). "Multimodal Neuroimaging Feature Learning With Multimodal Stacked Deep Polynomial Networks for Diagnosis of Alzheimer's Disease". In: *IEEE J Biomed Health Inform* 22.1, pp. 173–183.

Shmulev, Y., M. Belyaev, and The Alzheimer's Disease Neuroimaging Initiative (2018). "Predicting Conversion of Mild Cognitive Impairments to Alzheimer's Disease and Exploring Impact of Neuroimaging: Second International Workshop, GRAIL 2018 and First International Workshop, Beyond MIC 2018, Held in Conjunction with MICCAI 2018, Granada, Spain, September 20, 2018, Proceedings". In: *Graphs in Biomedical Image Analysis and Integrating Medical Imaging and Non-Imaging Modalities*. Ed. by D. Stoyanov et al. Vol. 11044. Lecture Notes in Computer Science. Cham: Springer International Publishing, pp. 83–91.

Simonyan, K. and A. Zisserman (2014). "Very Deep Convolutional Networks for Large-Scale Image Recognition". In:

Slattery, C. F. et al. (2017). "ApoE influences regional white-matter axonal density loss in Alzheimer's disease". In: *Neurobiology of Aging* 57, pp. 8–17. DOI: 10.1016/j.neurobiolaging.2017.04.021.

Sled, J. G., A. P. Zijdenbos, and A. C. Evans (1998). "A nonparametric method for automatic correction of intensity nonuniformity in MRI data". In: *IEEE Trans. Med. Imaging* 17.1, pp. 87–97.

Smith, S. M. (2002). "Fast robust automated brain extraction". In: *Hum. Brain Mapp.* 17.3, pp. 143–155.

Smith, S. M. et al. (2004). "Advances in functional and structural MR image analysis and implementation as FSL". In: *Neuroimage* 23 Suppl 1, S208–19.

Snowden, J. S. et al. (2006). "Progranulin gene mutations associated with frontotemporal dementia and progressive non-fluent aphasia". In: *Brain: A Journal of Neurology* 129.Pt 11, pp. 3091–3102. DOI: 10.1093/brain/awl267.

Snowden, J. S. et al. (2012). "Distinct clinical and pathological characteristics of frontotemporal dementia associated with C9ORF72 mutations". In: *Brain: A Journal of Neurology* 135.Pt 3, pp. 693–708. DOI: 10.1093/brain/awr355.

Song, S.-K. et al. (2002). "Dysmyelination revealed through MRI as increased radial (but unchanged axial) diffusion of water". In: *NeuroImage* 17.3, pp. 1429–1436.

Song, Y.-K. et al. (2018). "A study of neurite orientation dispersion and density imaging in wilson's disease". In: *Journal of magnetic resonance imaging: JMRI* 48.2, pp. 423–430. DOI: 10.1002/jmri.25930.

Sonnenburg, S. et al. (2007). "The Need for Open Source Software in Machine Learning". In: *J. Mach. Learn. Res.* 8.Oct, pp. 2443–2466.

Spasov, S. E. et al. (2018). "A Multi-modal Convolutional Neural Network Framework for the Prediction of Alzheimer's Disease". In: *Conf. Proc. IEEE Eng. Med. Biol. Soc.* 2018, pp. 1271–1274.

Sperling, R. A. et al. (2011). "Toward defining the preclinical stages of Alzheimer's disease: recommendations from the National Institute on Aging-Alzheimer's Association workgroups on diagnostic guidelines for Alzheimer's disease". In: *Alzheimer's & Dementia: The Journal of the Alzheimer's Association* 7.3, pp. 280–292. DOI: 10.1016/j.jalz.2011.03.003.

Srivastava, N. et al. (2014). "Dropout: a simple way to prevent neural networks from overfitting." In: *Journal of Machine Learning Research* 15.1, pp. 1929–1958.

Stahl, R et al. (2007). "White Matter Damage in Alzheimer Disease and Mild Cognitive Impairment: Assessment with Diffusion-Tensor MR Imaging and Parallel Imaging Techniques1". In: *Radiology*.

Stodden, V., F. Leisch, and R. D. Peng (2014). *Implementing Reproducible Research*. CRC Press.

Suhonen, N.-M. et al. (2015). "Slowly progressive frontotemporal lobar degeneration caused by the C9ORF72 repeat expansion: a 20-year follow-up study". In: *Neurocase* 21.1, pp. 85–89. DOI: 10.1080/13554794.2013.873057.

Suhonen, N.-M. et al. (2017). "Neuropsychological Profile in the C9ORF72 Associated Behavioral Variant Frontotemporal Dementia". In: *Journal of Alzheimer's Disease* 58.2, pp. 479–489. DOI: 10.3233/JAD-161142.

Suk, H.-I., S.-W. Lee, and D. Shen (2014). "Hierarchical Feature Representation and Multimodal Fusion with Deep Learning for AD/MCI Diagnosis". In: *NeuroImage* 101, pp. 569–582. DOI: 10.1016/j.neuroimage.2014.06.077.

— (2015). "Latent feature representation with stacked auto-encoder for AD/MCI diagnosis". In: *Brain structure & function* 220.2, pp. 841–859. DOI: 10.1007/s00429-013-0687-3.

Suk, H.-I. et al. (2017). "Deep ensemble learning of sparse regression models for brain disease diagnosis". In: *Med. Image Anal.* 37, pp. 101–113.

Sullivan, G. M. and R. Feinn (2012). "Effect-size-Using Effect Size—or Why the P Value Is Not Enough". In: *Journal of Graduate Medical Education* 4.3, pp. 279–282. DOI: 10.4300/JGME-D-12-00156.1.

Susumu Mori and J-Donald Tournier (2013). *Introduction to Diffusion Tensor Imaging - 1st Edition*.

Szegedy, C. et al. (2015). "Going deeper with convolutions". In: *Proceedings of the IEEE conference on computer vision and pattern recognition*, pp. 1–9.

Taqi, A. M. et al. (2018). "The Impact of Multi-Optimizers and Data Augmentation on TensorFlow Convolutional Neural Network Performance". In: *2018 IEEE Conference on Multimedia Information Processing and Retrieval (MIPR)*, pp. 140–145.

Tariq, M. et al. (2012). *Scan-rescan reproducibility of neurite microstructure estimates using NODDI*. Proceedings paper. DOI: http://discovery.ucl.ac.uk/1353710/1/Alexander_miua_final.pdf.

Termenon, M et al. (2011). "Alzheimer Disease Classification on Diffusion Weighted Imaging Features". In: *New Challenges on Bioinspired Applications*. Springer Berlin Heidelberg, pp. 120–127.

Thung, K.-H., P.-T. Yap, and D. Shen (2017). "Multi-stage Diagnosis of Alzheimer's Disease with Incomplete Multimodal Data via Multi-task Deep Learning". In: *Deep Learn Med Image Anal Multimodal Learn Clin Decis Support (2017)* 10553, pp. 160–168.

Tournier, J.-D., F. Calamante, and A. Connelly (2012). "MRtrix: Diffusion Tractography in Crossing Fiber Regions". In: *Int. J. Imaging Syst. Technol.* 22.1, pp. 53–66. DOI: 10.1002/ima.22005.

Trafimow, D. et al. (2018). "Manipulating the Alpha Level Cannot Cure Significance Testing". In: *Frontiers in Psychology* 9. DOI: 10.3389/fpsyg.2018.00699.

Tustison, N. J. and B. B. Avants (2013). "35-Explicit B-spline regularization in diffeomorphic image registration". In: *Frontiers in Neuroinformatics* 7. DOI: 10.3389/fninf.2013.00039.

Tustison, N. J. et al. (2010). "N4ITK: improved N3 bias correction". In: *IEEE Trans. Med. Imaging* 29.6, pp. 1310–1320.

Uchida, S. (2013). "Image processing and recognition for biological images". In: *Dev. Growth Differ.* 55.4, pp. 523–549.

Valliani, A. and A. Soni (2017). "Deep Residual Nets for Improved Alzheimer's Diagnosis". In: *Proceedings of the 8th ACM International Conference on Bioinformatics, Computational Biology,and Health Informatics*. ACM, pp. 615–615.

Van Langenhove, T. et al. (2013). "Distinct clinical characteristics of C9orf72 expansion carriers compared with GRN, MAPT, and nonmutation carriers in

a Flanders-Belgian FTLD cohort". In: *JAMA neurology* 70.3, pp. 365–373. DOI: 10.1001/2013.jamaneurol.181.

Van Mossevelde, S. et al. (2017). "Clinical Evidence of Disease Anticipation in Families Segregating a C9orf72 Repeat Expansion". In: *JAMA neurology* 74.4, pp. 445–452. DOI: 10.1001/jamaneurol.2016.4847.

Vanschoren, J. et al. (2014). "OpenML: Networked Science in Machine Learning". In: *SIGKDD Explor. Newsl.* 15.2, pp. 49–60.

Varoquaux, G. et al. (2017). "Assessing and tuning brain decoders: Cross-validation, caveats, and guidelines". In: *NeuroImage* 145, pp. 166–179. DOI: 10.1016/j.neuroimage.2016.10.038.

Vatsavayai, S. C. et al. (2016). "Timing and significance of pathological features in *C9orf72* expansion-associated frontotemporal dementia". In: *Brain* 139.12, pp. 3202–3216. DOI: 10.1093/brain/aww250.

Vemuri, P. and C. R. Jack Jr (2010). "Role of structural MRI in Alzheimer's disease". In: *Alzheimers. Res. Ther.* 2.4, p. 23.

Vemuri, P. et al. (2008). "Alzheimer's disease diagnosis in individual subjects using structural MR images: validation studies". In: *NeuroImage* 39.3, pp. 1186–1197. DOI: 10.1016/j.neuroimage.2007.09.073.

Vos, T. et al. (2016). "Global, regional, and national incidence, prevalence, and years lived with disability for 310 diseases and injuries, 1990–2015: a systematic analysis for the Global Burden of Disease Study 2015". In: *The Lancet* 388.10053, pp. 1545–1602. DOI: 10.1016/S0140-6736(16)31678-6.

Vovk, U., F. Pernus, and B. Likar (2007). "A review of methods for correction of intensity inhomogeneity in MRI". In: *IEEE Trans. Med. Imaging* 26.3, pp. 405–421.

Vu, T. D. et al. (2017). "Multimodal learning using Convolution Neural Network and Sparse Autoencoder". In: *2017 IEEE International Conference on Big Data and Smart Computing (BigComp)*, pp. 309–312.

Vu, T.-D. et al. (2018). "Non-white matter tissue extraction and deep convolutional neural network for Alzheimer's disease detection". In: *Soft Comput* 22.20, pp. 6825–6833.

Walhout, R. et al. (2015). "Brain morphologic changes in asymptomatic C9orf72 repeat expansion carriers". In: *Neurology* 85.20, pp. 1780–1788.

Wang, H. et al. (2019). "Ensemble of 3D densely connected convolutional network for diagnosis of mild cognitive impairment and Alzheimer's disease". In: *Neurocomputing* 333, pp. 145–156.

Wang, Q. et al. (2018a). "The Added Value of Diffusion-Weighted MRI-Derived Structural Connectome in Evaluating Mild Cognitive Impairment: A Multi-Cohort Validation1". In: *J. Alzheimers. Dis.* 64.1, pp. 149–169.

Wang, S.-H. et al. (2018b). "Classification of Alzheimer's Disease Based on Eight-Layer Convolutional Neural Network with Leaky Rectified Linear Unit and Max Pooling". In: *J. Med. Syst.* 42.5, p. 85.

Wang, S. et al. (2017). "Automatic Recognition of Mild Cognitive Impairment from MRI Images Using Expedited Convolutional Neural Networks". In: *Artificial Neural Networks and Machine Learning – ICANN 2017*. Springer International Publishing, pp. 373–380.

Wang, X. et al. (2018c). "Temporal Correlation Structure Learning for MCI Conversion Prediction: 21st International Conference, Granada, Spain, September 16-20, 2018, Proceedings, Part III". In: *Medical Image Computing and Computer Assisted Intervention – MICCAI 2018*. Ed. by A. F. Frangi et al. Vol. 11072. Lecture Notes in Computer Science. Cham: Springer International Publishing, pp. 446–454.

Wee, C.-Y. et al. (2012). "Identification of MCI individuals using structural and functional connectivity networks". In: *Neuroimage* 59.3, pp. 2045–2056.

Wee, C.-Y. et al. (2013). "Prediction of Alzheimer's disease and mild cognitive impairment using cortical morphological patterns". In: *Human Brain Mapping* 34.12, pp. 3411–3425. DOI: 10.1002/hbm.22156.

Wen, D. et al. (2018a). "Deep Learning Methods to Process fMRI Data and Their Application in the Diagnosis of Cognitive Impairment: A Brief Overview and Our Opinion". In: *Front. Neuroinform.* 12, p. 23.

Wen, J. et al. (2018b). "Reproducible evaluation of diffusion MRI features for automatic classification of patients with Alzheimers disease". In:

Wen, J. et al. (2019). "Neurite density is reduced in the presymptomatic phase of C9orf72 disease". In: *J Neurol Neurosurg Psychiatry* 90.4, pp. 387–394. DOI: 10.1136/jnnp-2018-318994.

Wheeler-Kingshott, C. A. M. and M. Cercignani (2009). "About "axial" and "radial" diffusivities". In: *Magnetic Resonance in Medicine* 61.5, pp. 1255–1260. DOI: 10.1002/mrm.21965.

Whitwell, J. L. et al. (2012). "Neuroimaging signatures of frontotemporal dementia genetics: C9ORF72, tau, progranulin and sporadics". In: *Brain* 135.3, pp. 794–806. DOI: 10.1093/brain/aws001.

Whitwell, J. L. et al. (2015). "Brain atrophy over time in genetic and sporadic frontotemporal dementia: a study on 198 serial MRI". In: *European journal of neurology : the official journal of the European Federation of Neurological Societies* 22.5, pp. 745–752. DOI: 10.1111/ene.12675.

Wolz, R. et al. (2011). "Multi-method analysis of MRI images in early diagnostics of Alzheimer's disease". In: *PloS One* 6.10, e25446. DOI: 10.1371/journal.pone.0025446.

Wu, C. et al. (2018). "Discrimination and conversion prediction of mild cognitive impairment using convolutional neural networks". In: *Quant. Imaging Med. Surg.* 8.10, pp. 992–1003.

Wu, M. et al. (2008). "Comparison of EPI Distortion Correction Methods in Diffusion Tensor MRI Using a Novel Framework". In: *Medical Image Computing and Computer-Assisted Intervention – MICCAI 2008*. Ed. by D. Metaxas et al. Vol. 5242. Lecture Notes in Computer Science. Berlin, Heidelberg: Springer Berlin Heidelberg, pp. 321–329.

Xie, S et al. (2006). "Voxel-based detection of white matter abnormalities in mild Alzheimer disease". In: *Neurology* 66.12, pp. 1845–1849.

Xie, Y. et al. (2015). "Identification of Amnestic Mild Cognitive Impairment Using Multi-Modal Brain Features: A Combined Structural MRI and Diffusion Tensor Imaging Study". In: *J. Alzheimers. Dis.* 47.2, pp. 509–522.

Yann, L (1987). "Modeles connexionnistes de lapprentissage". PhD Thesis. PhD thesis, These de Doctorat, Universite Paris 6.

Yao, Y., L. Rosasco, and A. Caponnetto (2007). "On Early Stopping in Gradient Descent Learning". In: *Constr. Approx.* 26.2, pp. 289–315.

Yendiki, A. et al. (2014). "Spurious group differences due to head motion in a diffusion MRI study". In: *NeuroImage* 88, pp. 79–90. DOI: 10.1016/j.neuroimage.2013.11.027.

Zhan, L et al. (2015). "Boosting Classification Accuracy of Diffusion MRI Derived Brain Networks for the Subtypes of Mild Cognitive Impairment Using Higher Order Singular Value Decomposition". In: *Proc. IEEE Int. Symp. Biomed. Imaging* 2015, pp. 131–135.

Zhang, H. et al. (2012). "NODDI: Practical in vivo neurite orientation dispersion and density imaging of the human brain". In: *NeuroImage* 61.4, pp. 1000–1016. DOI: 10.1016/j.neuroimage.2012.03.072.

Zhang, T. and B. Yu (2005). "Boosting with early stopping: Convergence and consistency". In: *Ann. Stat.* 33.4, pp. 1538–1579.

Zhang, Y, M Brady, and S Smith (2001). "Segmentation of brain MR images through a hidden Markov random field model and the expectation-maximization algorithm". In: *IEEE Trans. Med. Imaging* 20.1, pp. 45–57.

Zhang, Y.-T. and S.-Q. Liu (2018). "Individual identification using multi-metric of DTI in Alzheimer's disease and mild cognitive impairment*". In: *Chin. Physics B* 27.8, p. 088702.

Zhang, Y. et al. (2018). "Multivariate Approach for Alzheimer's Disease Detection Using Stationary Wavelet Entropy and Predator-Prey Particle Swarm Optimization". In: *J. Alzheimers. Dis.* 65.3, pp. 855–869.

Zhou, T. et al. (2017). "Feature Learning and Fusion of Multimodality Neuroimaging and Genetic Data for Multi-status Dementia Diagnosis". In: *Mach Learn Med Imaging* 10541, pp. 132–140.

— (2019). "Effective feature learning and fusion of multimodality data using stage-wise deep neural network for dementia diagnosis". In: *Hum. Brain Mapp.* 40.3, pp. 1001–1016.

Zhu, D. et al. (2014). "Connectome-scale assessments of structural and functional connectivity in MCI". In: *Hum. Brain Mapp.* 35.7, pp. 2911–2923.

Zlokovic, R. D.a.B. V. (2007). *Role of the Blood-Brain Barrier in the Pathogenesis of Alzheimers Disease*.